Electron Diffraction Studies of Unsupported Antimony Clusters

A thesis
submitted in partial fulfilment
of the requirements for the Degree
of Doctor of Philosophy in Physics
in the University of Canterbury

by

Martin Kaufmann

Department of Physics and Astronomy
University of Canterbury
2006

Abstract

This thesis contains two main parts: the first part focusses on an electron diffraction study on unsupported antimony (Sb) clusters, while in the second part the design and development of a time-of-flight mass spectrometer (TOFMS) is discussed.

Electron diffraction is an ideal tool to study the structure of clusters entrained in a beam. The main advantage of this technique is the ability to study the clusters *in situ* and in an interaction-free environment. It is therefore not necessary to remove the particles from the vacuum system which would lead to oxidation. Since the particles do not have to be deposited on a sample for further investigation, there is also no substrate which could influence the cluster structure. An additional advantage is the short exposure to the electron beam, thereby minimising the likelihood of damaging the particles.

Sb clusters were produced using an inert-gas aggregation source. To control the cluster properties the source temperature, pressure and type of cooling gas can be adjusted. In the range of source parameters tested, Sb clusters with three different structures were observed: a crystalline structure corresponding to the rhombohedral structure of bulk Sb, an amorphous structure equivalent to the structure of amorphous Sb thin films, and a structure with the same diffraction signature as Sb_4 (Sb evaporates mainly as Sb_4). This last structure was found to belong to large particles consisting of randomly oriented Sb_4 units.

In order to study the size distributions and morphologies of the Sb clusters, the clusters were deposited onto substrates and studied under an electron microscope. The crystalline particles showed a wide variety of strongly faceted shapes. Depending on source conditions, the average cluster diameters ranged from 15 to 130 nm. There was a considerable disagreement between these values and the size estimates from the diffraction results with the latter being smaller by an order of magnitude. This might be due to the existence of domains inside the clusters. The amorphous particles were all found to be spherical with mean sizes between 27 and 45 nm. The Sb_4 particles showed a liquid-like morphology and tended to coalesce easily. Their sizes ranged from 18 to 35 nm.

To obtain an independent method for determining the cluster size, a TOFMS was designed and developed in collaboration with Dr Bernhard Kaiser. However, the TOFMS failed to detect a cluster signal in the original set-up which is most likely due to a defective ioniser and underestimated cluster energies. Further tests were performed in a new vacuum system and mass spectra for palladium clusters were successfully recorded.

Contents

Chapter 1

Introduction

For a long time after discovering that matter consists of atoms, research was limited either to single atoms or to the bulk. Only a few decades ago, the field in-between – the field of clusters – started to attract interest. Clusters are small particles of 2 to about 10^5 atoms and bridge the gap between quantised states in atoms and molecules on one side and continuous states in the bulk on the other side. There is, of course, no definite upper limit to the number of atoms in a cluster, as it depends on the properties under consideration. The limit can be defined as the size at which particular properties become indistinguishable from the bulk properties. The fact that some of these properties differ widely from the bulk values makes research on clusters particularly interesting: the melting point of small gold [1] or sodium [2] clusters, for example, is greatly reduced. The band gap of silicon has been observed to be size-dependent as well [3]. Furthermore, it has been shown that inert metals such as gold show strong catalysis if the particle size is reduced [4]. Most of these differences can be explained through the dominance of quantum effects at small scales and the influence of the surface on the clusters. In the case of bulk material, the number of atoms on the surface is negligible compared to the number of atoms inside. For clusters, however, the fraction of surface atoms F_S becomes important.

For a pseudo-spherical cluster it is given by the following expression [5]:

$$F_S = 4 \cdot N^{-\frac{1}{3}} \tag{1.1}$$

where N is the number of atoms per cluster. Accordingly, a cluster of 100 atoms has more than 85% of its atoms on the surface, while a cluster of 100 000 atoms still has almost 10% on the surface. This has a huge impact on many properties of clusters, since the atoms on the surface have fewer nearest neighbours and are therefore less strongly bound.

The size-dependent behaviour of may cluster properties offers the opportunity to produce clusters with predetermined features which can be fine-tuned. Figure 1.1 shows a schematic representation of the dependence of a cluster property G on the number of atoms per cluster N. On the upper end of the size scale it might be possible to extrapolate certain cluster properties from the bulk value $G(\infty)$. In this region, the cluster size effects follow a smooth trend. At the lower end of the scale, however, these properties do not follow the same trends. Instead, they show significant deviations. These deviations usually oscillate around the general trend and are caused by quantum size effects and surface effects [6].

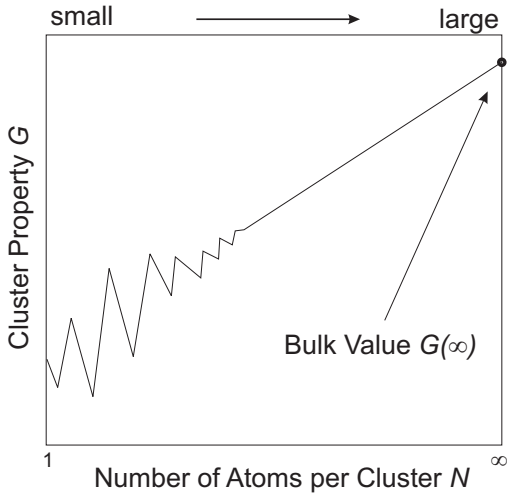

Figure 1.1: The size dependence of cluster property G on the number of atoms per cluster N. After [6].

The study of clusters can be compared to the study of bulk surfaces as in both cases the influence of surface atoms is crucial. The low coordination number of surface atoms can lead to strain and rearrangement on the surface. The structure of a particle directly influences its electronic properties which in turn affect the general properties. Determining the structure of a cluster therefore helps to understand many of its characteristics.

There are several different ways to study the cluster structure. Most techniques rely on depositing the clusters on a substrate to study them either under an electron microscope or by using a diffraction technique. The main disadvantage of most of these methods is the interaction between the substrate and the clusters which can alter their structure. It is also possible that the clusters fragment on impact or diffuse and aggregate on the surface to form new clusters. To avoid these problems it is necessary to probe the clusters while they are still unsupported in the vacuum. A technique which allows this is electron diffraction from a dense cluster beam crossed by high energy electrons. By analysing the signal of the scattered electrons, conclusions about the structure of the clusters can be drawn.

The topic of this thesis is the study of the structure and possible phase transitions of antimony (Sb) clusters. The clusters are produced in an inert-gas aggregation (IGA) source and are then analysed by a high energy electron diffractograph. Structure analysis is only one small part of the fast-growing field of cluster science. More information on other aspects can be found in [5, 7, 8].

In the following section the structure of clusters is discussed in detail. This is followed by a section describing previous electron diffraction studies of unsupported clusters. The third section introduces Sb and reviews the current knowledge of its cluster structure. The chapter finishes with an outline of the thesis.

1.1 The Structure of Clusters

As previously mentioned, the structure of a cluster is heavily influenced by the fraction of atoms on the surface. The smaller a cluster is, the larger the

fraction of surface atoms relative to its volume is. The surface free energy γ of a cluster or a crystal is related to the energy W required to break the cluster along a crystal plane [9]:

$$\gamma = \frac{W}{2S} \tag{1.2}$$

where S is the area of the crystal face which is exposed. The thermodynamic equilibrium shape of a cluster can be achieved by minimising its total surface energy F [10]:

$$F = \int \gamma \, \mathrm{d}A \tag{1.3}$$

where A is the total surface area. This equilibrium shape can only be reached if the particle is relatively small, since the kinetic processes necessary to change the shape of a large particle and reach equilibrium require too much time. Furthermore, particles in a dense vapour have no chance to reach equilibrium at all because it is more likely for them to assume a shape based on kinetic growth than their equilibrium shape [10].

For a liquid, the equilibrium shape is a sphere. Clusters, however, can assume faceted shapes even if the resulting surface area is enlarged, since the surface free energy γ varies for different crystal planes. To determine the equilibrium shape, a geometrical method to minimise (1.3) was developed by Wulff [11]: vectors with a length relative to the surface free energy γ for each facet are drawn from the origin in the direction of each crystal plane. At the end of these vectors, perpendicular planes are constructed which form a polyhedron geometrically similar to the equilibrium shape.

As the Wulff shape only minimises the surface energy and not the total energy of a particle, it is possible for small particles to assume a shape different to the Wulff shape. This is achieved by introducing strain in the crystal structure as in the case of the so-called multiply twinned particles (MTP) which are based on a face-centred cubic (fcc) structure and are formed of tetrahedra [13]. Common examples for MTPs are icosahedra and decahedra shown in Figure 1.2. Both these structures show a five-fold

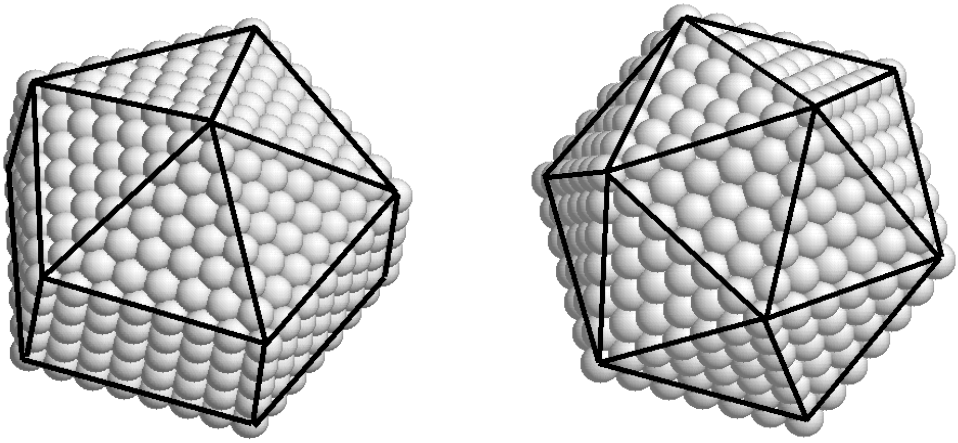

Figure 1.2: Examples of multiply twinned particles: decahedron (left) and icosahedron. After [12].

symmetry which is not seen in macroscopic particles. This is due to the fact that the five-fold symmetry is not a translational symmetry and therefore requires non-crystalline packing. The icosahedron consists of 20 tetrahedra touching at one point at the centre of the structure. However, as tetrahedra are not space-filling, the icosahedral structure is highly strained [14] which is also a reason why there is no icosahedral bulk structure. The decahedron is formed by five tetrahedra sharing a common edge. However, the resulting body is not filled completely either, as there is still a gap between two connecting faces. The only way of achieving a perfect decahedron is to allow the tetrahedra to deform which in turn leads to strain in the resulting structure.

Since the surface energy is of great importance for polyhedral particles and since they have such a well-defined shape, it is energetically unfavourable to add single atoms to the faces of such a particle during growth. To retain the shape, a whole layer of atoms, a so-called shell, is required.[1] A filled shell leads to an increased stability of the particle by reducing its total

[1]Depending on the shape, it is not always required to have a whole new shell, as long as the original symmetry is retained.

energy. For every cluster shape there is a characteristic series of numbers of atoms required to construct the basic shape as well as the consecutive layers. These numbers are called *magic numbers* – or more accurately *geometric* magic numbers. This is to avoid confusion with the *electronic* magic numbers which are due to filled electronic shells. Both the geometric and the electronic shell structure can be observed experimentally using a mass spectrometer. Depending on the type of experiment, a filled shell appears in a mass spectrum as either a peak or a dip [15].

Since the five-fold symmetry of the MTPs discussed above is not a valid bulk structure, there has to be a stage during the growth process of a cluster where the phase changes from an MTP to the bulk structure. This rearrangement is due to the competition between internal strain and surface energy, as previously mentioned. If the fraction of surface atoms is low enough, the decreased surface energy of an MTP structure loses its importance and the strain-free crystal structure takes over. At which particle size this transition happens depends on the material: for aluminium a transition to fcc has been observed for particles with less than 1000 atoms [5], while sodium clusters with tens of thousands of atoms were found to be icosahedral [14]. Electron diffraction on unsupported clusters is one of the preferred methods to study this transition.

1.2 Electron Diffraction Studies on Unsupported Metal Clusters

As discussed above, electron diffraction is the technique of choice to study the structure of unsupported clusters. The background of this technique will be described in detail in Chapter 3. An overview of the results of previous studies and their importance for the present work is presented in the following.

Many electron diffraction experiments on clusters were done on rare gas clusters, while there are only limited results available for metal clusters. For a review of electron diffraction studies on unsupported clusters in general, refer to Bartell [16]. The first – and for a long time the only – group under-

taking electron diffraction studies on unsupported metal clusters was that of Stein *et al.* [17–20]. They studied the structure of lead (Pb), bismuth (Bi), indium (In), silver (Ag), and Sb clusters. The clusters were produced in an inert-gas aggregation (IGA) source. In this source, metal is evaporated and the hot metal vapour is quenched by a flow of cold inert gas. This leads to regions of supersaturation which allow clusters to be formed. The cluster growth stops once the particles are swept out of the source chamber by the inert gas. The first metal studied by Stein *et al.* was In. They investigated clusters between 40 and 80 Å diameter and observed a structural change from tetragonal (which is the bulk structure of In) to fcc at a diameter of around 50 to 60 Å [18].[2] For Pb the clusters had similar sizes and the observed structure was fcc over the whole size range (the same as the bulk structure) [17]. Upon closer examination, they found that a mixture of fcc and liquid clusters fitted the diffraction data of smaller clusters better [20]. Bi clusters between 60 and 95 Å were studied and the structure was found to be rhombohedral as for the bulk [18]. The silver clusters with a diameter of 40 to 110 Å showed a bulk-like fcc structure on the upper end of the scale and a deviation from the bulk structure for smaller particles. They assumed this was due to partially liquid or amorphous clusters [19]. The patterns for Sb clusters were too weak to gain any detailed information about the structure, but two different phases were observed [20]. The first phase showed crystalline features and was achieved by adding inert gas to improve cooling of the clusters. For the second phase, Sb was evaporated without additional cooling gas and a pattern with liquid or amorphous features was recorded. These experiments will be discussed in detail in the next section.

With Stein's support, a group at Ecole Polytechnique Fédérale de Lausanne (EPFL) built an electron diffraction apparatus where they studied Ag, copper (Cu), and germanium (Ge) clusters [21–26]. The first experiments on Ag clusters of 20 to 110 Å diameter showed an fcc structure for the larger clusters and a mixture of different structures (mainly fcc and decahedra) for smaller ones [21]. More in-depth studies, however, came

[2] Although the Ångström unit ($1\,\text{Å} = 10^{-10}\,\text{m}$) is not an SI unit, it is widely used in the context of crystallography.

to the conclusion that the cluster structure is more dependent on the temperature than on the size. They investigated 30 to 110 Å diameter clusters and found a change from fcc to icosahedra [22–25]. In case of Cu, they studied 30 to 70 Å diameter clusters and observed a change from fcc to icosahedra at 38 Å diameter in accordance with molecular dynamics simulations [24, 26, 27]. The experiments on Ge led to diffraction patterns with a single weak but reproducible peak and did not allow any further conclusions about the cluster structure to be drawn [24].

Further electron diffraction studies on Bi and Sb were undertaken by Sun *et al.* [28]. They formed clusters by pure vapour ejection from a nozzle source. In the case of Sb, they also added helium to improve cooling. A liquid state for both Bi and Sb was reported but the patterns were very weak and no further conclusions could be drawn. The Sb results will be discussed in more detail in the next section.

The same equipment that was used by the group at EPFL in Switzerland was then moved to the University of Canterbury in New Zealand. Here two further studies were undertaken: the first one on lead (Pb) and zinc (Zn) clusters [12] and the second one on Bi [29]. Pb clusters between 20 and 70 Å diameter were observed. The small particles showed a mainly icosahedral structure, while at approximately 55 Å there was a change to a mainly decahedral structure. In contrast to all other experiments undertaken with this equipment, the structural change was not caused by a change in source temperature or pressure but by the type of cooling gas used. With helium (He) the smaller icosahedral particles were observed and with argon (Ar) the larger decahedral ones. No fcc phase (bulk) was detected. For Zn it was not possible to generate a high-intensity cluster beam needed for the diffraction experiments. The Bi study showed large clusters with diameters between 70 and 230 Å and it was impossible to reduce the cluster sizes even using a very wide range of source conditions. Most of the clusters detected had the rhombohedral structure of bulk Bi, but clusters with an amorphous or liquid structure were also observed. As in the Pb study, this transition depended on the type of inert gas used. Using He led to mainly amorphous particles, while changing to Ar gave rise to crystalline clusters.

In another project, which is not directly related to our research, an ion trap was used to mass-select cluster ions which were then probed by

electron diffraction [30–33]. The clusters investigated were C_{60}^+, $(CsI)_nCs^+$ (n = 30–39) and more recently Ag_n (n = 36–46, 55). While ion trapping is a slow procedure and the scattering intensities are usually very low, it has two major advantages over the standard electron diffraction experiment on a continuous beam: it allows the exact size as well as the temperature of the trapped ions to be determined. In all the other experiments described above, the clusters in the beam have always a broad size distribution and the temperature can only be estimated.

1.3 Antimony

Apart from the few studies previously mentioned, there is no detailed information about the structure of antimony (Sb) clusters available. Since Sb is part of the same group in the periodic table as Bi and sinc e they both share the same bulk structure, a comparison to the previous study on Bi clusters is expected to lead to new insights into both elements. Sb is also an interesting element in its own right. Sb vapour, for instance, consists mainly of tetramers and not monomers and dimers as in most other cases. Furthermore, Sb thin films show an amorphous structure which is semiconducting (see below). This might lead to new cluster structures which have not yet been observed. In the next section, the general properties of Sb are discussed. This is followed by a review of previous studies on Sb clusters.

1.3.1 General Properties of Antimony

The properties of Sb are reviewed in [34], and all data is reported here is from this review unless otherwise noted. Sb is a brittle, silvery metal with a density of $6.68\times10^3\,\mathrm{kg\cdot m^{-3}}$ when solid and $6.45\times10^3\,\mathrm{kg\cdot m^{-3}}$ when liquid [35].[3] The melting point of Sb is 630.6°C (903.8 K) and the boiling point 1587°C (1860 K). The temperature-dependence of the vapour pressure is an important characteristic for the cluster production. For Sb 10 Pa of vapour pressure (a pressure at which clusters are commonly expected

[3] Unlike in the case of Bi, the volume of liquid Sb decreases when freezing.

to form) is reached at 603°C compared to 768°C for Bi [34] (despite the melting point of Bi being only 271.5°C).

Sb is a semi-metal and part of the group VA in the periodic table (together with nitrogen (N), phosphorus (P), arsenic (As) and Bi). It has an electrical resistivity of $39\times10^{-8}\,\Omega$m at 273 K (compared to $107\times10^{-8}\,\Omega$m for Bi and $1.5\times10^{-8}\,\Omega$m for Cu). There are two stable isotopes: ^{121}Sb with a natural abundance of 57.2% and ^{123}Sb with an abundance of 42.8%. The atomic mass is 121.76 g·mol^{-1}.

Sb Allotropes

The bulk structure of metallic Sb (also known as 'grey' Sb) is rhombohedral and the unit cell resembles a cube stretched along a body diagonal with two atoms per unit cell. The Sb crystal structure consists of puckered six-membered rings which form two-layered structures as shown in Figure 1.3. The structural data for Sb is given in Table 1.1. For comparison, this table also displays the data for Bi. Across the periodic table, the rhombohedral structure is not very common: apart from Sb and Bi, only arsenic (As), mercury (Hg), and samarium (Sm) show this structure. In addition to the rhombohedral structure, Sb also shows two high pressure modifications: at 5 GPa the structure changes to a simple cubic structure and above 9 GPa to a hexagonal close-packed (hcp) structure [36].

Apart from the rhombohedral structure, there is a second known allotrope called 'black' Sb which corresponds to 'red' phosphorus and 'black'

Table 1.1: Structural data for Sb and Bi at room temperature. After [36].

	Sb	Bi
Lattice constant a (Å)	4.5067	4.746
Lattice angle α (°)	57.11	57.23
Bond length (Å)	2.908	3.072
Bond angle ϑ (°)	95.60	95.45
Interlayer distance (Å)	3.355	3.529
Atomic volume (Å^3)	30.21	35.39

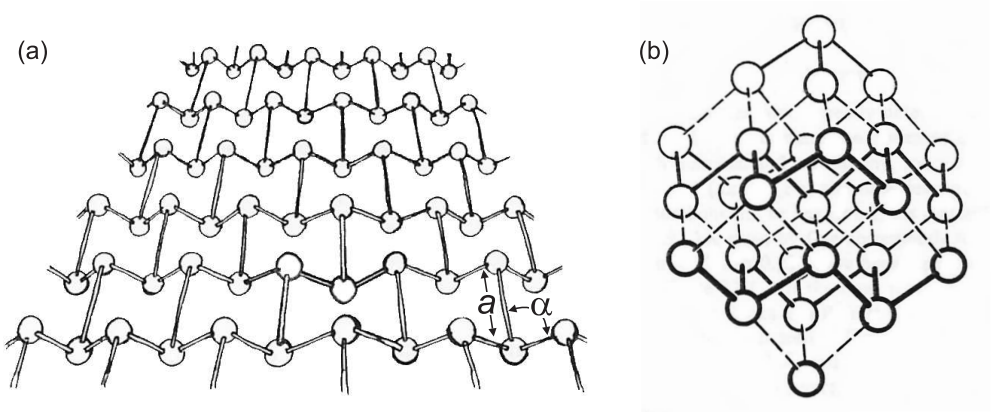

Figure 1.3: Schematics of the rhombohedral structure of Sb. (a) Double layer consisting of puckered rings. The lattice constant a and the angle α are marked (after [37]). (b) Several double layers stacked on top of each other. The solid lines indicate intralayer bonds, the dotted lines interlayer contacts (after [36]).

arsenic. It has an amorphous structure and is usually obtained by depositing Sb vapour on a cooled sample [38–41]. If the sample is heated up or if the deposited layer exceeds a certain thickness, the structure changes to the ordinary rhombohedral structure [42, 43]. The amorphous phase has a density of $5.57\times10^3\,\mathrm{kg\cdot m^{-3}}$ (i.e. 17% less dense than the rhombohedral structure) and is a semiconductor. The average bond length is similar to the bond length of the crystalline phase (2.9 Å) and the average bond angle is 96° [37]. The so-called 'explosive' phase has the same structure as the amorphous phase [42, 44]. Amorphous solids in general will be discussed in more detail in Chapter 3.

When Sb is evaporated, the vapour consists mainly of tetramers with virtually no contribution from monomers, dimers or trimers. At 800 K the intensity ratio for Sb_4:Sb_3:Sb_2:Sb_1 was found to be 77:6:8:9 [45]. However, there is no known allotrope of Sb consisting of Sb_4 units which would correspond to 'white' phosphorus and 'yellow' arsenic. White P and yellow As are both thought to have a cubic structure, but the structural information available is not conclusive as both phases are unstable and decompose under an X-ray beam [36]. There is one recent study, where small ordered

areas are reported in amorphous Sb thin films on molybdenum disulfide (MoS_2) substrates. These areas are attributed to a cubic arrangement of Sb_4 molecules [46].

1.3.2 Previous Studies on Sb Clusters

Little is known about the structure of Sb clusters. In the following, earlier studies on Sb clusters are presented in an overview, starting with small Sb clusters and moving on to electron diffraction and microscopy studies on Sb clusters. Finally, a selection of previous experiments on amorphous Sb clusters will be presented.

Small Sb Clusters and Magic Numbers

As previously mentioned, when Sb is evaporated into a vacuum, the vapour consists predominantly of Sb_4 tetramers and virtually no monomers: In a time-of-flight mass spectrometer Sattler *et al.* observed the ratio for Sb_4:Sb_3:Sb_2:Sb_1 to be 77:6:8:9 at 800 K and no higher masses could be detected [45]. Only after adding He, clusters with a higher mass could be observed. For these higher masses, magic numbers were detected (see Section 1.1). The magic numbers for Sb were 8, 36, 52 and 84 which correspond to 2, 9, 13 and 21 Sb_4 units [47]. Sattler *et al.* also presented possible models for these magic clusters based mainly on geometrical considerations. The basis for all models are the Sb_4 building blocks. In the case of Sb_8, a structure is suggested where the faces of two tetrahedra are in contact and rotated by 60°. For Sb_{36}, Sb_{52} and Sb_{84} clusters, models based on an Sb_{20} pyramid were suggested where Sb_4 units are attached to the pyramid faces. For Sb_{36} there is one, for Sb_{52} two, and for Sb_{84} three Sb_4 units per face. In a more recent study, Rayane *et al.* observed Sb_{4n} clusters up to about Sb_{200} and while they found Sb_{36} to be magic, the results for 52 and 84 were much less obvious than in Sattler's work [48, 49]. It is worth mentioning that they did not find any magic numbers for Bi at all. In a mass spectrum recorded in an unrelated study shortly afterwards, the peaks for Sb_{36}, Sb_{52}, and Sb_{84} clearly stand out [50]. In an additional experiment, Geusic *et al.* found the magic number and size distribution to be strongly charge-dependent [51].

For small Sb clusters, there are also some results from theoretical studies available: Kumar and Sundararajan used *ab initio* molecular dynamics calculations to investigate the atomic and electronic structure of Sb_n (n = 2–8 and 12) [52, 53]. They found that a regular tetrahedron has the lowest energy for Sb_4, but for Sb_8 and especially for Sb_{12} a combination of tetrahedron and bent rhombus could play an important role as well. The lowest energy structure for Sb_8 was found to be equivalent to the geometric model suggested by Sattler. Because of limited computing power it was not possible to continue to higher masses. The structures of the magic configurations (n = 36, 52, and 84) would be of particular interest. Later theoretical studies for Sb_n ($n \leq 4$ [54–56] and $n \leq 6$ [57]) confirmed the tetrahedral structure for Sb_4 but determined slightly different values for the bond lengths.

Electron Diffraction Studies on Sb Clusters

To our knowledge there are only two previous electron diffraction studies on unsupported Sb clusters. As mentioned above, the first study was undertaken by Stein *et al.* [20]. Figure 1.4(a) shows the three diffraction patterns recorded during this study: pattern (1) was recorded using 1 Torr of Ar gas for cooling, while for pattern (2) no cooling gas was added. Pattern (3) is the diffraction signal from a polycrystalline Sb thin film for comparison. It is not known at what source temperature these patterns were recorded. The first pattern shows only weak peaks, but it is evident that the peak positions match the positions of the bulk sample. However, the pattern is too weak to draw further conclusions about the exact structure and size of the particles. The second pattern has a different shape with three broad peaks. Stein *et al.* attributed this pattern to amorphous clusters.

The patterns from Sun *et al.* [28] are shown in Figure 1.4(b). Instead of Ar, He was used as cooling gas. Setting the source temperature to 1100°C and increasing the He pressure from 0 to 1.3×10^{-3} Torr gave rise to three patterns with similar features but increasing peak intensities. They concluded that the clusters were in a liquid state and that the atomic order was increased with improved cooling.

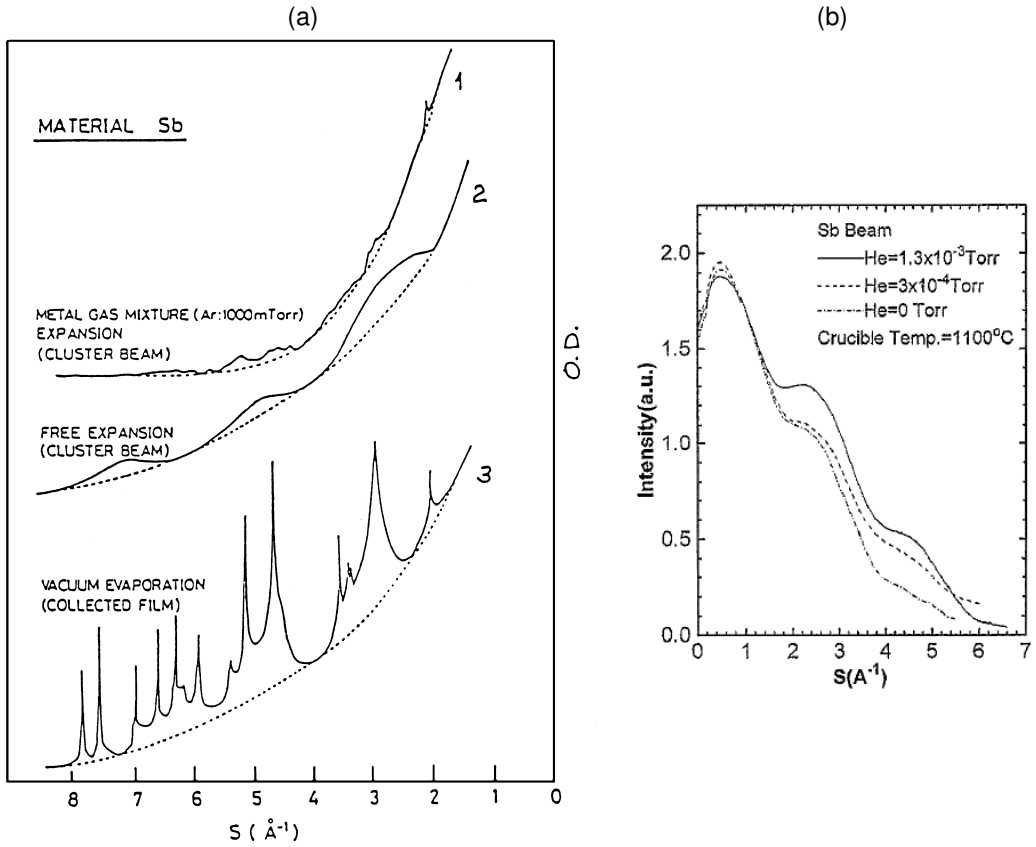

Figure 1.4: Diffraction patterns of Sb clusters from two previous studies. (a) Patterns from Stein *et al.* [20] (pattern (3) is the diffraction signal from a polycrystalline thin film for comparison). (b) Patterns from Sun *et al.* [28]. Note that in both cases the scattering parameter s is defined differently than in the present work. Their values are larger by a factor of 2π than the values used in this thesis.

Microscopy Studies on Sb Clusters

While the structure of clusters can also be studied using high-resolution microscopes such as a high-resolution transmission electron microscope (HRTEM), the results cannot be compared directly to the electron diffraction results on unsupported particles. For an HRTEM study it is necessary to deposit clusters onto a substrate and in most cases it requires the sample to be removed from vacuum for the transfer to the microscope. As mentioned before, the interaction between the clusters and the substrate might lead to a change in structure or even to fragmentation. If the clusters are exposed to air, they are also likely to oxidise. On the other hand, an HRTEM has a major advantage over electron diffraction on a cluster beam: under a microscope, single particles can be observed, while the cluster beam studies always average over the whole ensemble. Connected to this is of course the danger of a non-representative selection in a microscopy study.

There are only a limited number of HRTEM studies on Sb particles available. Yamamoto *et al.* deposited clusters onto a heated amorphous carbon substrate and observed the growth of large square pyramids [58]. Since these pyramids only grow on the substrate, it is impossible to determine the structure of the particles before deposition.

In an extensive study, Otaki observed and classified ten different types of particles grown in a gas-evaporation source (smoke source) [59] (quoted in [60]). In this source, metal is evaporated in an Ar atmosphere with a pressure between 1 and 50 Torr. The ten different crystal habits are listed in Table 1.2. The pressure used for these particular experiments was 50 Torr but there is no information available about the source temperature. Note that the same habits were also observed for Bi, particularly particles of type 2, while for Sb the particles of type 1 prevailed.

In a third study, Sb powder was evaporated in a collimated HRTEM beam and deposited *in situ* [61]. It was therefore not necessary to transfer the samples in air. A mixture of crystalline and amorphous particles was observed. The crystalline particles had a mean size of approximately 50 nm and the structure corresponded to the Sb bulk structure. Mainly wedge-shaped particles with {110}, {111} and {112} planes as their surfaces were found and these surfaces were determined to be free from lattice relaxation

Table 1.2: Crystal habits of Sb particles observed in [59].

No.	Shape
1	Trigonal pyramid bounded by three $\{100\}$ and one (111)
1a	No. 1 truncated by $(\overline{1}\overline{1}\overline{1})$
1b	No. 1 truncated by one or more of $\{\bar{1}00\}$
1c	No. 1 truncated by $(\overline{1}\overline{1}\overline{1})$ and one or more of $\{\bar{1}00\}$
1d	No. 1 truncated by (111), $\{\bar{1}00\}$ and $\{100\}$
2	Sphere
2a	Polyhedron bounded by two $\{111\}$, six $\{100\}$ and six $\{110\}$
3a	Twin with a twin plane (100)
3b	Twin with a twin plane $(\bar{1}22)$
3c	Twin with a twin plane (111)

and superstructure. Some particles also showed stacking faults. It is, however, not clear whether these particles grew on the substrate or whether they existed already before deposition.

Amorphous Sb Clusters

There are no electron diffraction studies on unsupported amorphous Sb clusters available. There are, however, many studies on supported clusters. Most of these studies investigated the crystallisation of deposited amorphous particles and related phenomena. Many of the observed effects were first found in experiments on amorphous Sb thin films such as the dependence of crystallisation and conductivity on the film thickness [62–68]. All studies found a critical film thickness which depends on the nature and temperature of the sample and on the deposition rate. Since amorphous Sb is a semi-conductor and crystalline Sb a semi-metal, there is an obvious change in the temperature-dependent conductivity characteristics when changing from one state to the other.

For amorphous Sb clusters most studies found similar results to the ones for thin films. However, the critical thickness seems to be reduced for the deposited clusters by up to an order of magnitude and it is possible to produce continuous films which are stable at room temperature [61, 69–75].

While many reports include diffraction rings characteristic for amorphous solids, there is unfortunately no detailed information about the structure available. It is therefore not possible to confirm whether the observed structures are equivalent to the amorphous bulk phase.

It is important to note that the term *amorphous* can be ambiguous when describing micrographs or diffraction rings. If it is not explicitly stated, it can refer to either the amorphous structure observed for bulk Sb described above or a different non-crystalline structure which does not give rise to sharp diffraction rings or lattice fringes. In the present work, a second amorphous phase is observed which shows similar diffraction characteristics but is clearly distinguishable when comparing the positions of the diffraction rings.

1.4 Outline of the Thesis

In the following, an outline of the remaining chapters is presented.

In Chapter 2 the experimental equipment used for the electron diffraction study is introduced. It consists of a cluster source, an electron diffractograph and a sampling device; all components are explained in detail. There are also detailed instructions for the operation of the equipment. The last part outlines the analysis of the micrographs.

Chapter 3 introduces the electron diffraction theory in a first part including a digression about amorphous solids in general. Based on the theory, a series of calculated diffraction patterns is presented. In a second part, the analysis of the experimental patterns is described which contains the data preparation as well as the size analysis based on the diffraction patterns.

Chapter 4 contains the results and analysis from the electron diffraction study on Sb clusters. The presentation of the results is divided into three parts according to the type of cooling gas used (Ar, He, and a He/Ar mixture). In a second part, the diffraction patterns are analysed and the results discussed in detail. The third part contains an independent study on the morphology of deposited clusters. The micrographs for different

morphologies are presented and the size information determined from the samples is compared to the results from the diffraction patterns.

In Chapter 5 the time-of-flight (TOF) mass spectrometer built for this study is discussed. After an introduction to mass spectrometry in general and TOF mass spectrometry in particular, the design of the spectrometer used in this work is presented. It is followed by a discussion of the ion optics simulations used to optimise the device. In the last part of the chapter, the experiments performed with the TOF mass spectrometer are discussed.

Chapter 6 is the final chapter of this thesis and reviews the previous chapters. It also contains an outlook on further work in the field of electron diffraction and mass spectrometry on clusters.

References

[1] P. Buffat and J. P. Borel, Phys. Rev. A **13**, 2287 (1976).

[2] H. Haberland *et al.*, Phys. Rev. Lett. **94**, 035701 (2005).

[3] T. van Buuren, L. N. Dinh, L. L. Chase, W. J. Siekhaus, and L. J. Terminello, Phys. Rev. Lett. **80**, 3803 (1998).

[4] M. Haruta, Catal. Today **36**, 153 (1997), and references therein.

[5] R. L. Johnston, *Atomic and Molecular Clusters*, Masters Series in Physics and Astronomy, Taylor & Francis, 2002.

[6] J. Jortner, Z. Phys. D: Atom. Mol. Cl. **24**, 247 (1992).

[7] H. Haberland, editor, *Clusters of Atoms and Molecules*, volume 52 of *Springer Series in Chemical Physics*, Springer-Verlag, 1994.

[8] W. Eberhardt, Surf. Sci. **500**, 242 (2002).

[9] A. Pimpinelli and J. Villain, *Physics of Crystal Growth*, Cambridge University Press, 1998.

[10] C. Herring, The use of classical macroscopic concepts in surface-energy problems, in *Structure and Properties of Solid Surfaces*, edited by R. Gomer and C. S. Smith, The University of Chicago Press, 1953.

[11] G. Wulff, Z. Kristallogr. **34**, 449 (1901).

[12] M. Hyslop, *Electron Diffraction Studies of Unsupported Clusters*, PhD thesis, University of Canterbury, 2002.

[13] S. Ino, J. Phys. Soc. Jpn. **21**, 364 (1966).

[14] T. P. Martin, Phys. Rep. **273**, 199 (1996).

[15] R. L. Johnston, Philos. T. Roy. Soc. A **356**, 211 (1998).

[16] L. S. Bartell, Chem. Rev. **86**, 491 (1986), and references therein.

[17] A. Yokozeki, J. Chem. Phys. **68**, 3766 (1978).

[18] A. Yokozeki and G. D. Stein, J. Appl. Phys. **49**, 2224 (1978).

[19] B. G. de Boer and G. D. Stein, Surf. Sci. **106**, 84 (1981).

[20] G. D. Stein, *Metal cluster beams and electron diffraction: Deviations from the bulk state of matter*, unpublished, 1982.

[21] M. Flüeli, *Observation des Structures Anormales de Petites Particules d'Or et d'Argent par Microscopie Eléctronique à Haute-Résolution et Diffraction d'Eléctrons par un Jet d'Agrégats d'Argent*, PhD thesis, Ecole Polytechnique Fédérale de Lausanne, 1989.

[22] B. D. Hall, *An Installation for the Study of Unsupported Ultrafine Particles by Electron Diffraction with Application to Silver: Observation of Multiply Twinned Particle Structures*, PhD thesis, Ecole Polytechnique Fédérale de Lausanne, 1991.

[23] B. D. Hall, M. Flüeli, R. Monot, and J.-P. Borel, Phys. Rev. B **43**, 3906 (1991).

[24] D. Reinhard, *Croissance et Stabilité d'Agrégats d'Argent et de Cuivre, Etudiés en Jets Moléculaires par Diffraction d'Electrons à Haute Energie*, PhD thesis, Ecole Polytechnique Fédérale de Lausanne, 1996.

[25] D. Reinhard, B. Hall, D. Ugarte, and R. Monot, Phys. Rev. B **55**, 7868 (1997).

[26] D. Reinhard, B. D. Hall, P. Berthoud, S. Valkealahti, and R. Monot, Phys. Rev. Lett. **79**, 1459 (1997).

[27] D. Reinhard, B. D. Hall, P. Berthoud, S. Valkealahti, and R. Monot, Phys. Rev. B **58**, 4917 (1998).

[28] L. Sun, G. Takaoka, J. Matsuo, and I. Yamada, Mater. Sci. Eng. A **217**, 15 (1996).

[29] A. Wurl, *Electron Diffraction Studies of Unsupported Bismuth Clusters*, PhD thesis, University of Canterbury, 2003.

[30] M. Maier-Borst, D. B. Cameron, M. Rokni, and J. H. Parks, Phys. Rev. A **59**, 3162 (1999).

[31] S. Krückeberg, D. Schooss, M. Maier-Borst, and J. H. Parks, Phys. Rev. Lett. **85**, 4494 (2000).

[32] X. Xing *et al.*, Phys. Rev. B **72**, 081405 (2005).

[33] D. Schooss *et al.*, Nano Lett. **5**, 1972 (2005).

[34] D. R. Lide, editor, *CRC Handbook of Chemistry and Physics*, CRC Press, 84th edition, 2003.

[35] L. Wang, Q. Wang, A. Xian, and K. Lu, J. Phys.: Condens. Mat. **15**, 777 (2003).

[36] J. Donohue, *The Structures of the Elements*, John Wiley & Sons, 1974.

[37] G. N. Greaves, S. R. Elliott, and E. A. Davis, Adv. Phys. **28**, 49 (1979).

[38] J. A. Prins, Nature **131**, 760 (1933).

[39] J. A. Prins, Nature **136**, 299 (1935).

[40] H. Hendus, Z. Phys. **119**, 265 (1942).

[41] H. Levinstein, J. Appl. Phys. **20**, 306 (1949).

[42] H. Richter, H. Berckhemer, and G. Breitling, Z. Naturforsch. A **9**, 236 (1954).

[43] G. Fuchs *et al.*, Thin Solid Films **204**, 107 (1991).

[44] H. Krebs and R. Steffen, Z. Anorg. Allg. Chem. **327**, 224 (1964).

[45] K. Sattler, J. Mühlbach, and R. Recknagel, Phys. Rev. Lett. **45**, 821 (1980).

[46] T. M. Bernhardt, B. Stegemann, B. Kaiser, and K. Rademann, Angew. Chem. Int. Edit. **42**, 199 (2003).

[47] K. Sattler, J. Mühlbach, P. Pfau, and R. Recknagel, Phys. Lett. **87A**, 418 (1982).

[48] D. Rayane *et al.*, Z. Phys. D: Atom. Mol. Cl. **12**, 217 (1989).

[49] D. Rayane *et al.*, J. Chem. Phys. **91**, 3100 (1989).

[50] G. Fuchs *et al.*, Philos. Mag. B **63**, 715 (1991).

[51] M. E. Geusic, R. R. Freeman, and M. A. Duncan, J. Chem. Phys. **89**, 223 (1988).

[52] V. Kumar, Phys. Rev. B **48**, 8470 (1993).

[53] V. Sundararajan and V. Kumar, J. Chem. Phys. **102**, 9631 (1995).

[54] L.-S. Wang, Y. T. Lee, D. A. Shirley, K. Balasubramanian, and P. Feng, J. Chem. Phys. **93**, 6310 (1990).

[55] K. Balasubramanian, K. Sumathi, and D. G. Dai, J. Chem. Phys. **95**, 3494 (1991).

[56] H. Zhang and K. Balasubramanian, J. Chem. Phys. **97**, 3437 (1992).

[57] B. Reddy and P. Jena, Chem. Phys. Lett. **288**, 253 (1998).

[58] Y. Yamamoto, Y. Tanaka, and R. Suganuma, Jpn. J. Appl. Phys. **21**, 829 (1982).

[59] T. Okazaki, J. Jpn. Assoc. Cryst. Growth **9**, 175 (1982), in Japanese.

[60] R. Uyeda, Crystallography of Metal Smoke Particles, in *Morphology of Crystals*, edited by I. Sunagawa, chapter 6, Terra Scientific Publishing Company, 1987.

[61] T. Isshiki, K. Nishio, H. Saijo, and M. Shiojiri, Thin Solid Films **237**, 155 (1994).

[62] J. Hauser, Phys. Rev. B **9**, 2623 (1974).

[63] C. Ghosh and B. P. Varma, J. Phys. D: Appl. Phys. **7**, 1773 (1974).

[64] A. Kinbara, M. Ohmura, and A. Kikuchi, Thin Solid Films **34**, 37 (1976).

[65] A. J. Mackintosh, R. T. Phillips, and A. D. Yoffe, Physica B **117**, 1001 (1983).

[66] M. Hashimoto, Thin Solid Films **116**, 373 (1984).

[67] N. Kaiser, Thin Solid Films **116**, 259 (1984).

[68] V. M. Kuzmenko, A. N. Vladychkin, and Y. V. Navozenko, JETP Lett. **57**, 658 (1993).

[69] P. Jensen *et al.*, Appl. Phys. Lett. **59**, 1421 (1991).

[70] G. Fuchs *et al.*, Phys. Rev. B **44**, 3926 (1991).

[71] P. Melinon *et al.*, Phys. Rev. B **44**, 12562 (1991).

[72] P. Jensen *et al.*, J. Phys. I **2**, 365 (1992).

[73] S. Iwama and K. Mihama, Nanostruct. Mater. **6**, 305 (1995).

[74] K. Tanaka and S. Iwama, Nanostruct. Mater. **9**, 121 (1997).

[75] K. Tanaka, S. Iwama, and K. Mihama, Jpn. J. Appl. Phys. 2 **37**, L669 (1998).

Chapter 2

Experimental Equipment

In this chapter, the experimental equipment used for the present work will be introduced. The following sections explain the individual parts of the experimental apparatus and the experimental procedure in detail. The time-of-flight mass spectrometer (TOFMS) will be discussed in Chapter 5.

The experimental equipment consists of a cluster source, a high energy electron gun, an electron detector, and a sampling device. The apparatus was originally built at Ecole Polytechnique Fédérale in Lausanne (EPFL), Switzerland, and is described in more detail in [1–4]. It was then moved to the University of Canterbury, New Zealand, where the detector was replaced by an improved model.

Figure 2.1 shows a schematic of the experimental equipment. The clusters are generated in an inert-gas aggregation source. The mixture of clusters and inert gas is pumped through two pumping stages into the diffraction chamber where it is probed by a high energy electron beam. As the clusters are randomly oriented in the beam, the scattered electrons give rise to a Debye-Scherrer diffraction pattern. This diffraction pattern is recorded by a detector consisting of two linear diode arrays (LDA). Additionally, the clusters can be deposited on various types of samples for further studies *in situ* or outside of the system.

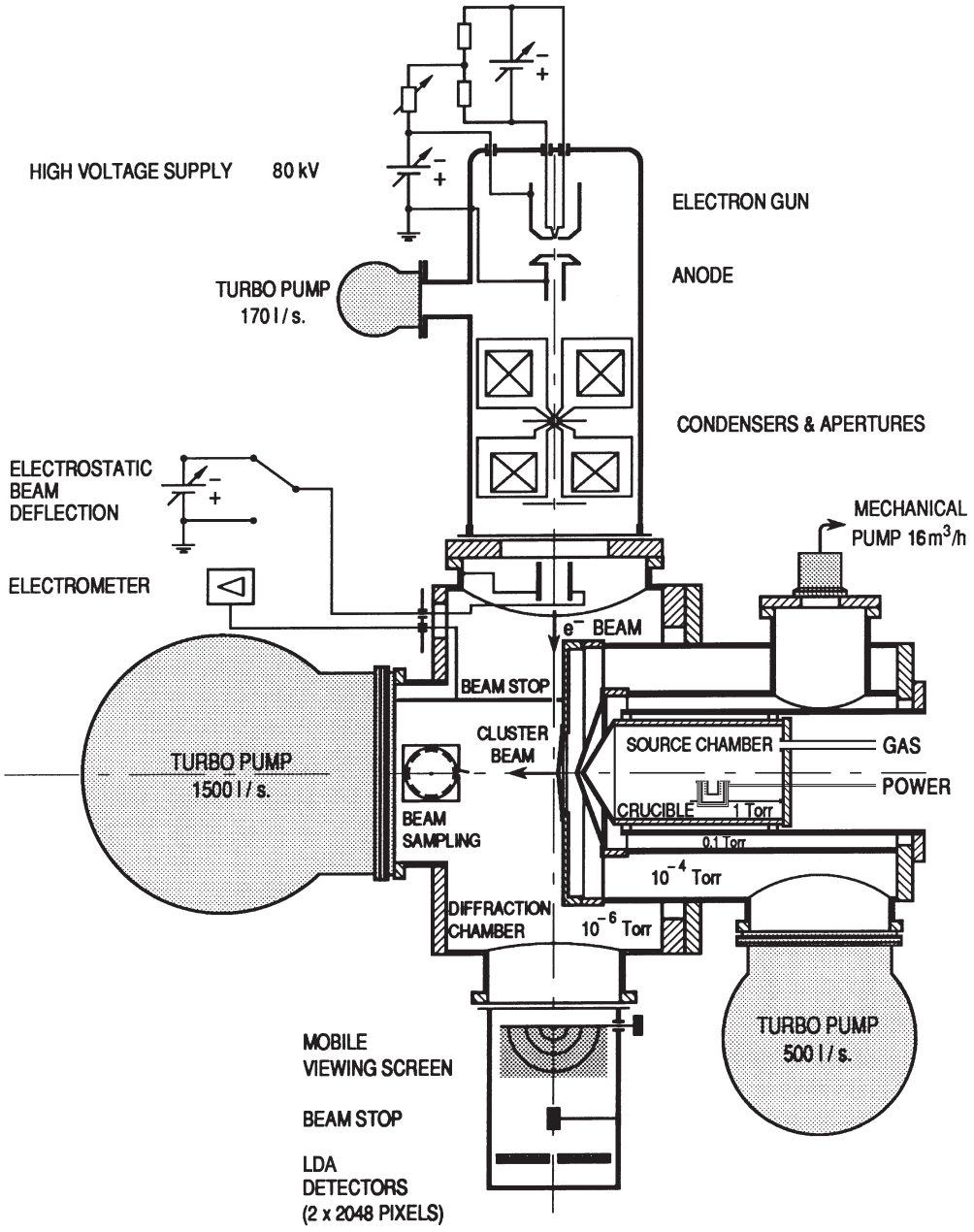

Figure 2.1: Schematic of the experimental equipment. After [5].

2.1 Cluster Source

The cluster source is based on a Sattler-type source [6] which uses the inert-gas aggregation (IGA) technique for cluster production. The metal is resistively heated in a crucible. The hot metal evaporates into a flow of cool inert gas which leads to supersaturation. This allows the formation of small clusters through homogeneous nucleation [7]. The clusters then grow by adsorption from the vapour phase or by collision with other clusters. This process comes to an end when the clusters are pushed out of the growth region by the gas flow.

2.1.1 Homogeneous Nucleation Theory

As the homogeneous nucleation theory is based on many complex processes, it has not been possible to generate a theoretical model that would predict the performance of the source quantitatively. The most relevant part of the nucleation theory for the present work is the equation relating the nucleation rate I to the temperature of the cooled vapour T [7]:

$$I = q\frac{n^2}{\rho}\sqrt{\frac{2\sigma m}{\pi}}e^{-\Delta F^*/k_\mathrm{B}T} = q\frac{p}{\rho k_\mathrm{B}T}\sqrt{\frac{2\sigma m}{\pi}}n^* \tag{2.1}$$

where q is the condensation coefficient, n the number of monomers per unit volume, ρ the density of a droplet, σ its surface tension, m its mass, ΔF^* the maximum free energy, k_B the Boltzmann constant, p the pressure of the supersaturated vapour, and n^* the number of critically-sized droplets. Following this equation, the nucleation rate is directly proportional to the vapour pressure of the metal at a certain evaporation temperature. Therefore, the higher the temperature of the heated metal is, the higher the nucleation rate. Figure 2.2 shows the nucleation rate as a function of the vapour temperature after cooling for the metals used in the present work and in the two previous studies [5, 8]. The maximum in nucleation rate in this plot is caused by the temperature dependence of the number of critically-sized droplets n^* in (2.1). The plot also helps to understand some important issues about the nucleation process of different metals. Firstly, the nucleation

rate differs widely for different metals. Secondly, as the maximum of each of these curves corresponds to the ideal temperature of the cooled vapour, it implies that the nucleation conditions for Bi and Pb are more favourable than for Zn. In fact, as our source is only water-cooled, the minimum vapour temperature is around 300 K, while the maximum of the curve for Zn lies around 240 K. This would explain why it was nigh impossible to achieve high nucleation rates for Zn in our system [8]. It might also account for the low rate for Sb in the present work compared to Bi. Additionally, a higher nucleation rate leads to smaller clusters, since the increased number of critically-sized droplets compete for the limited volume of metal vapour. This would account for the relatively large Sb clusters found in the present study (see Chapter 4).

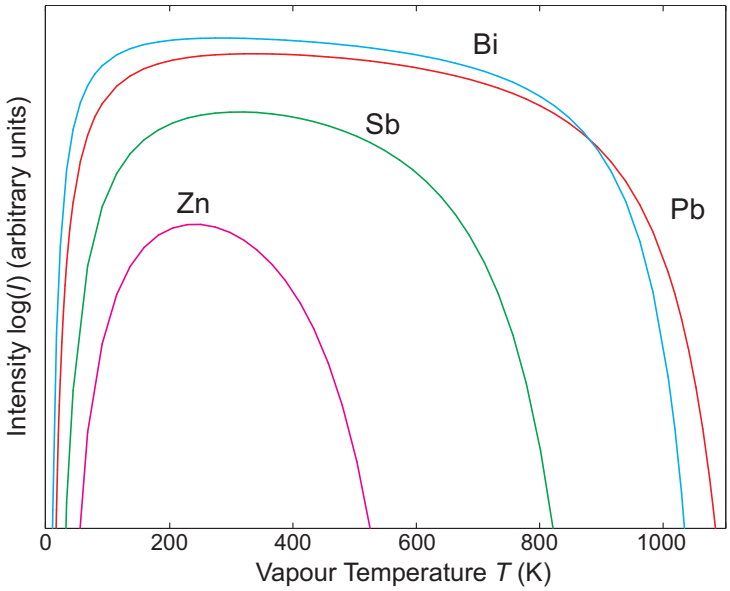

Figure 2.2: The nucleation rate I as a function of the vapour temperature T for the metals Zn, Sb, Bi and Pb. Note that the nucleation rate is normalised to the maximum value for Bi and the rate is plotted on a logarithmic scale. After [5].

2.1.2 Design of the Cluster Source

Figure 2.3 shows a schematic of the cluster source. The walls of the source chamber are water-cooled to keep them at a constant temperature. The arrangement of crucible, filament and heat shields sits on support rods which are attached to the source backplate. This backplate can be removed to allow access to the source chamber for cleaning, refilling and repairs. The backplate itself is water-cooled as well and there are feedthroughs for the thermocouple, the heating, the gas inlet, and a pressure gauge. The source chamber is pumped by two differential pumping stages forcing the mixture of gas and clusters through a nozzle and out of the source chamber. These pumping stages – separated by two further nozzles – also remove most of the inert gas and lead to the formation of a cluster beam. After leaving the second stage, the cluster beam then enters the diffraction chamber.

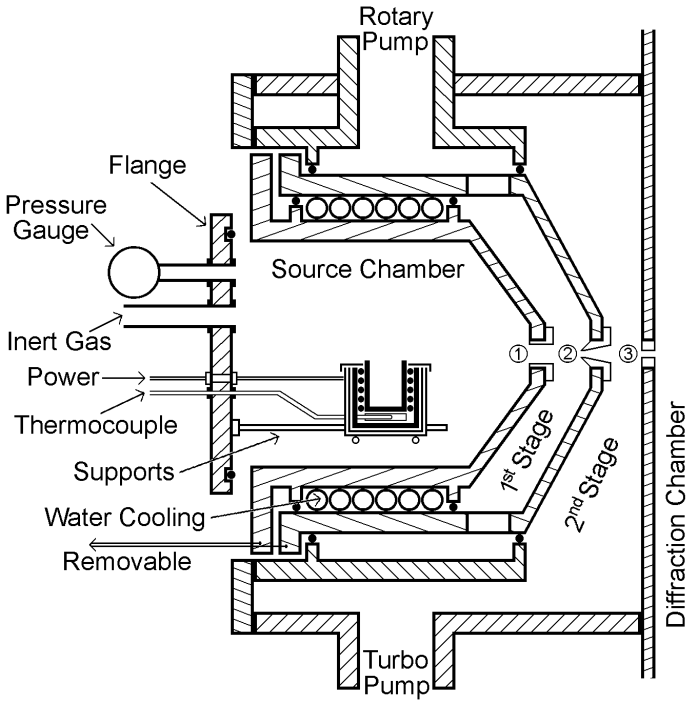

Figure 2.3: Schematic of the inert-gas aggregation source and pumping stages. The numbers 1–3 denote the nozzles described in Table 2.1. After [8].

Crucible Arrangement

The crucible arrangement is shown in Figure 2.4 and 2.5. The crucible itself is made of boron nitride (BN) and is heated by a tungsten filament that is wrapped around it. The filament has to be shaped in such a way as to minimise the resulting magnetic field which would disturb the electron beam in the diffraction chamber. For the cluster production, high-purity metal shots are used.[1] There is a hole in the base of the crucible for the thermocouple.[2] The crucible and filament are put in an alumina cup for electrical insulation which is surrounded by two tantalum heat shields. This entire set-up is covered by a tantalum lid. When using a high-temperature thermocouple, the temperature of the crucible can be ramped up to 1400°C. For the present work, however, the temperature never exceeded 900°C.

Nozzles

The geometry of the nozzles at the exit of the source chamber and between the pumping stages is crucial for the cluster production, as it determines the characteristics of the gas flow as well as the source pressure and there-

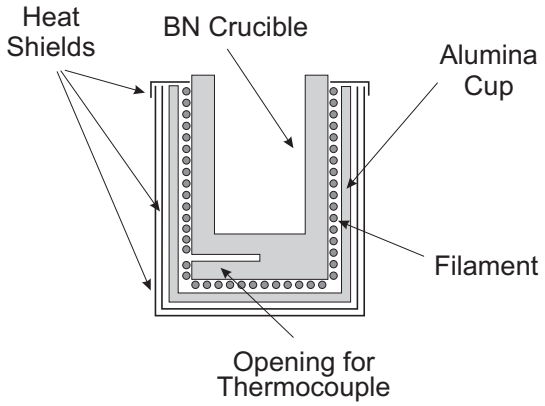

Figure 2.4: Schematic of the crucible arrangement.

[1] The Sb used in this study has a purity of 99.999% and was supplied by Kamis Inc.

[2] The thermocouples used were type K (low temperature) and type C (high temperature) from Omega.

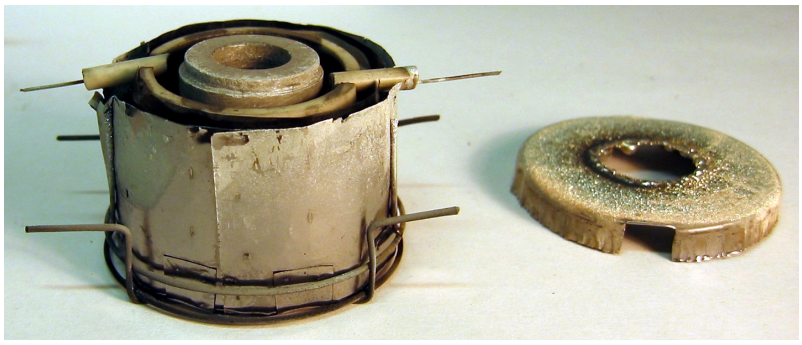

Figure 2.5: Crucible arrangement consisting of boron nitride crucible, tungsten filament, alumina cup, tantalum heat shields, and lid (on the right).

fore the cluster properties. Table 2.1 shows the specifications of the nozzles used during the present work. The term *collector* is used for a conical nozzle aligned so that the concave side is presented to the beam, while the term *skimmer* is used for the alignment where the beam enters the convex side of the nozzle.

Table 2.1: Properties of nozzles used in the experiments. Nozzle numbers as indicated in Figure 2.3. The first and third nozzle were made of graphite, the second of graphite or aluminium.

Nozzle	Geometry	Length (mm)	Diameter (mm)
1	cylindrical	9–24	0.8–3.5
2	conical (skimmer/collector)	4–6	1.5
3	cylindrical	2	1.5

During all the experiments, the third nozzle was never changed, while for the second nozzle, the 4 mm long model was used for most experiments. While the second nozzle was used as a skimmer for most of the time, is was also tested as a collector. However, no obvious changes in the cluster beam were observed. The first nozzle was the one changed the most; most experiments, however, were done using either the one with 2.5 or 3.5 mm diameter and a length of 24 mm. These particular nozzles were chosen because they produced the most consistent results. It was found that shorter nozzles or nozzles with smaller diameter failed to generate a

cluster beam with high enough intensity for the diffraction experiments. Usually, the nozzle with a larger diameter (3.5 mm) was chosen to produce Sb_4 clusters, as the larger diameter is more suitable for the higher gas flow rates required. The generation of crystalline clusters was found to be more consistent when using a smaller diameter nozzle (2.5 mm). It is, however, important to note that even choosing the same parameters for two subsequent experiments (i.e. gas type, gas flow rate, temperature, nozzle type) would not necessarily lead to the same experimental results. The system always required a certain amount of fine-tuning to achieve satisfactory experimental conditions.

Gas Flow Control

The inert-gas flow can be controlled accurately by using two flow controllers[3] which allow a choice of either helium (He) or argon (Ar) to be used individually or as a mixture. The type of gas and the total gas flow control the source chamber pressure for any given set of nozzles used. During an experiment the pressure in the source chamber can be changed from around 1 to 10 Torr for Ar and up to around 20 Torr for He. Outside this range it was found to be virtually impossible to achieve a high enough cluster beam intensity for the diffraction experiments. The pressure in the first stage is kept below 0.1 Torr by a rotary pump, while the pressure in the second stage varies between 1×10^{-5} and 2×10^{-4} Torr and is pumped by a turbo pump. The pressure in the diffraction chamber is typically between 1×10^{-6} and 5×10^{-6} Torr during an experiment. The pressure in the second stage is a limiting factor during experiments as the gas flow rate has to be limited to avoid overloading the turbo pump.

2.2 Electron Diffractograph

A schematic of the electron diffractograph is shown in Figure 2.6. It consists of an electron source, optical elements such as lenses and apertures as well

[3] Two controllers from MKS Instruments, type 1179A, were used.

as a detector. In the following, the individual components are explained in detail.

2.2.1 Electron Source

The electron source is a 100 kV electron gun which is taken from a Philips EM300 Transmission Electron Microscope (TEM) together with the optics down to the second condenser lens. The acceleration voltage can be adjusted in steps of 20 kV up to 100 kV. It is desirable to use the highest acceleration voltage available to increase the signal to noise ratio and to minimise dynamic diffraction effects (see Chapter 3). The disadvantage, however, is a loss of information for small scattering angles as the diffraction rings get smaller for higher voltages. For our experiments the acceleration voltage was always set to 80 kV and the beam current to between 2 and 3 µA. This setting is a compromise between maximising the intensity of the diffraction pattern and maximising the lifetime of the electron gun filament. Using this set-up, the resulting scattering parameter range is 0.25 Å^{-1} to 1.4 Å^{-1}.

After leaving the second condenser lens, the electron beam passes through a beam blanking device. This device consists of two metal plates parallel to the beam direction and a graphite plate with a small aperture perpendicular to the beam. To blank the beam, 400 V are applied to the two metal plates, thereby diverting the beam into the graphite plate. As the graphite plate is connected to an electrometer, blanking the beam also allows measurement of the beam current. If the beam blanking is turned off, there is no voltage applied to the plates and the beam passes through the aperture.

Just below the beam blanking stage the electron beam crosses the cluster beam and the electrons are scattered by the clusters. This process is described in detail in Chapter 3. There is also the possibility of moving a set of calibration samples into the electron beam. These samples consist of standard transmission electron microscope (TEM) grids onto which a thin polycrystalline film of a known material is deposited. For the present study

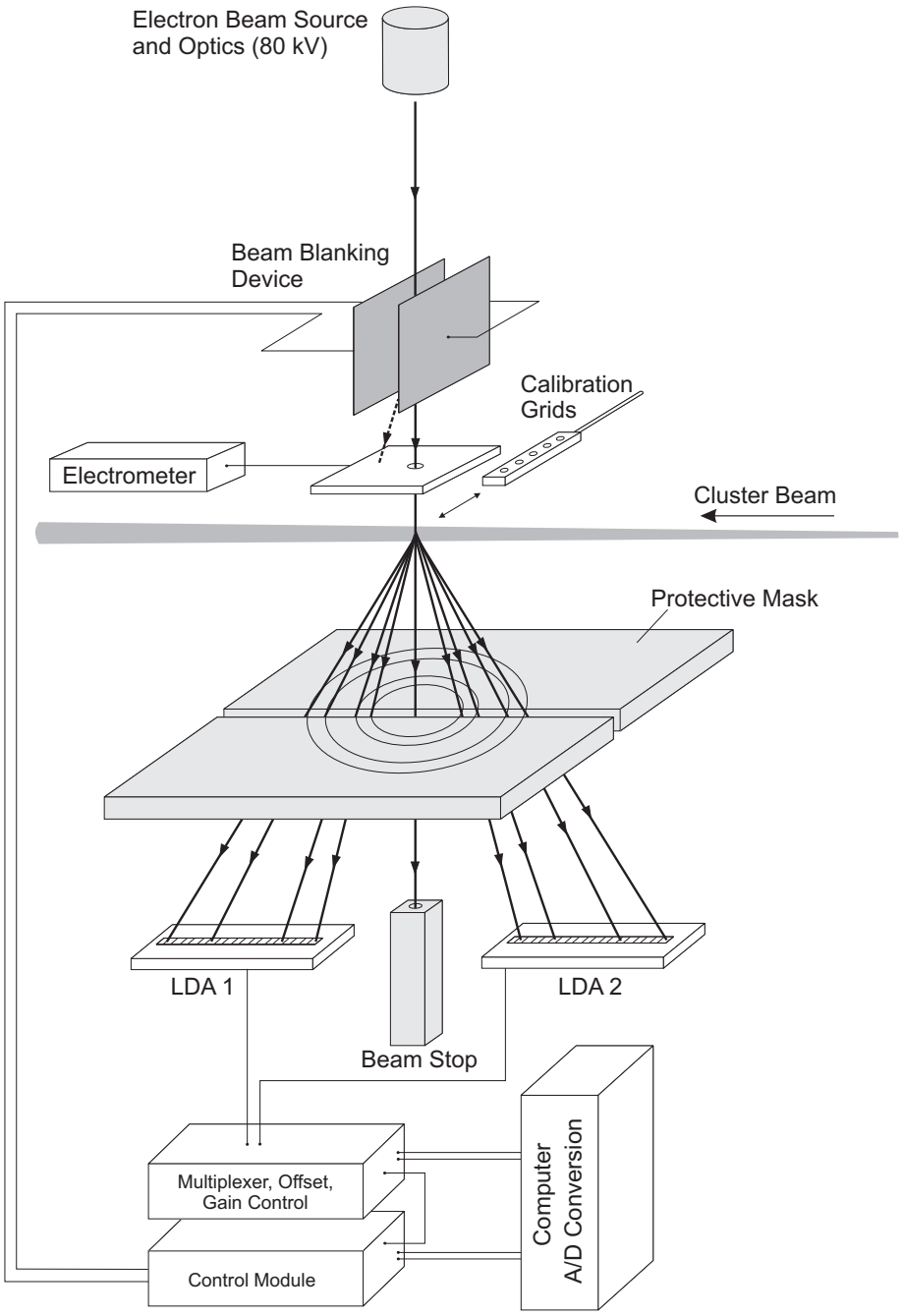

Figure 2.6: Schematic of the electron diffractograph (not to scale). After [5].

gold, aluminium and thallium chloride (TlCl) are used.[4] These samples allow calibration of the experimental diffraction patterns.

2.2.2 Detector

Finally, the electron beam hits the detector. The detector has been replaced for the previous study. The design and the electronics of the new system are described in detail in [5]. The detector itself consists of two linear diode arrays (LDA)[5] which are mounted perpendicular to the incoming electrons and on a diameter of the Debye-Scherrer diffraction rings. Each chip has 2048 pixels which each cover an area of 13 µm by 13 µm. The sensors are diffused p-n junction photodiodes where incident high-energy electrons create electron-hole pairs. The resulting electrons are integrated and stored as charge in a capacitor near the photodiode. At the end of each cycle, the charge in each diode is switched through a transfer gate to an analogue shift register where it is read out. The odd and even pixels are read out through shift registers on opposite sides. To avoid impact on the sensitive transfer gates by high-energy electrons, a protective mask is mounted on top of the chips. Despite this mask, some electrons still hit the transfer gates and are measured as additional charge. It is therefore important to align the mask properly to avoid getting a disproportionate signal for either odd or even pixels. The LDA chips are cooled by two Peltier elements to decrease the dark current. The hot side of these elements is connected to the water-cooled aluminium base plate of the vacuum system. Depending on the water temperature (which mainly depends on the season), the chips can be cooled down to $-12°C$ in summer and $-17°C$ in winter. To further minimise the influence of dark current, for every diffraction pattern a dark-current pattern is generated by reading out the registers with the beam blanking device turned on. This dark-current pattern is then subtracted from the raw pattern to get the final diffraction pattern.

[4] The Al and TlCl samples are commercially available from Electron Microscopy Sciences. The Au sample was made at EPFL.

[5] The chips used are from EG&G Reticon, type RL2048DAU-111.

2.3 Sampling Device

After crossing the electron beam, the clusters continue down the diffraction chamber where they can be deposited onto a sample for further analysis in a microscope. There is also a quartz crystal deposition rate monitor to determine the cluster beam intensity during an experiment.

Figure 2.7 shows a close-up of the sample arm with the built-in shutter. The shutter protects the samples and the deposition rate monitor from unwanted cluster deposition. To control the exposure time, the speed of the rotating shutter can be adjusted, allowing clusters to be deposited only during the time the slot in the shutter is in front of the sample. The whole sample turret can be moved in and out of the beam and manually rotated around its axis to select a sample for deposition. Several different sample holders can be fitted to the arm. The most commonly used sample holder is a rotary turret with flat faces. Up to eight solid SiN, SiO_2 or graphite samples can be attached to these faces and exposed to the cluster beam.

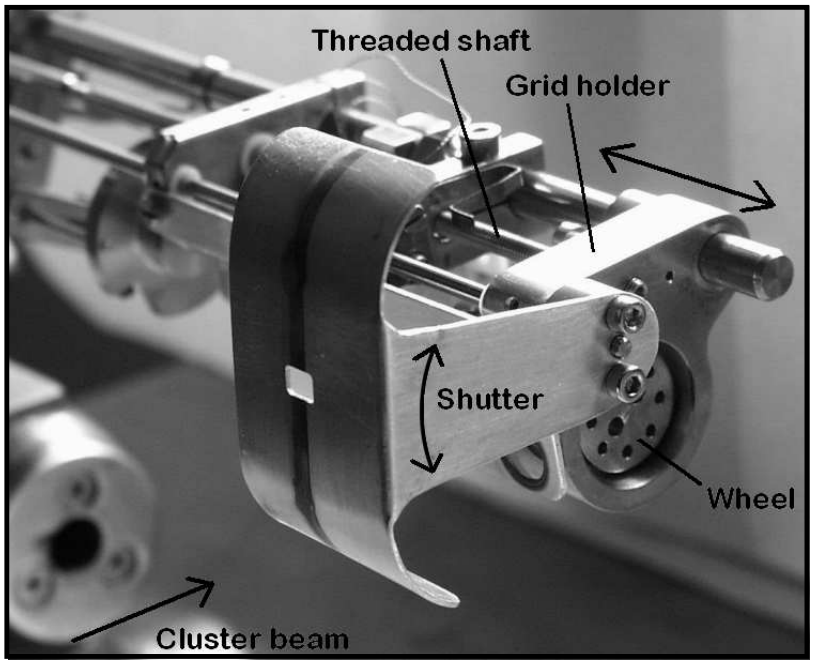

Figure 2.7: The sample arm with the built-in rotating shutter. After [8].

A similar system exists for eight TEM grids which are round copper grids with a thin amorphous carbon layer on top.[6] After depositing clusters onto these samples, they are taken out of the system and transferred to a field emission scanning electron microscope (FE-SEM) or a TEM for further analysis (see Section 2.5).

The quartz crystal deposition rate monitor[7] is situated further downstream just behind the sample arm. The deposition rate R_{dep} is determined by measuring the oscillation frequency of a quartz crystal over time. The more material is deposited onto the crystal, the lower the frequency. The monitor is mainly used to tune the cluster source and compare different source parameter settings. It is also used to calculate the exposure time for depositing onto samples.

2.4 Experimental Procedure

There is a standard procedure for the experiments which varies only slightly. The main steps of this procedure are the following:

- The source chamber, the crucible and the nozzles are thoroughly cleaned.
- The crucible is refilled with metal pellets and put in place.
- The source chamber is put into the system.
- The pumps are turned on and the system is left pumping overnight.
- The high voltage for the electron gun is slowly ramped up to 80 kV (over about 45 minutes). After reaching the desired voltage, the beam current is set to around 2 µA and the system is left to stabilise for about an hour.
- The inert gas flow and the crucible heating are turned on.

[6] The TEM grids used were provided by ProSciTech (model # GSCu300C).
[7] The deposition rate monitor used is from Sycon Instruments, type STM-100/MF.

- The electron beam has to be aligned. There is a full alignment procedure which has to be done after a long system downtime or after replacing the electron gun filament and a shorter daily alignment.
  - Full alignment: There is a needle on the calibration sample arm which can be moved in front of the third nozzle (where the electron beam is going to hit the cluster beam). Before putting the source in, the needle has to be aligned with the nozzle, thereby marking the position of the cluster beam entering the diffraction chamber. The shadow of this needle can be seen on the phosphorescent screen and the electron beam can be adjusted accordingly.
  - Daily alignment: Before every run the position of the condenser lenses and the apertures have to be centred relative to the electron beam and the beam has to be focussed.
- After a long system downtime or after cleaning the detector, the position of the detector has to be aligned relative to the electron beam. For this procedure, the calibration samples are moved into the electron beam. The whole detector can now be moved until the two LDAs show exactly the same pattern, i.e. the main peak in each pattern is at exactly the sample pixel number. In this position the LDAs run through the centre of the Debye-Scherrer diffraction rings. In this set-up, however, the information of the second LDA is redundant. Therefore, the detector can be shifted out along the LDA axis to increase the detection range, since the combined information of the two shifted LDAs will add up to a bigger detection range.
- The protective mask on top of the detector transfer gates has to be adjusted to avoid getting a disproportionate signal for either odd or even pixels.
- Diffraction patterns from two of the calibration samples (usually TlCl and Al) are recorded.
- The system is now ready for experiments. During an experiment, the source parameters such as crucible temperature, gas flow rate and

gas composition (Ar/He mixture) are varied and diffraction patterns recorded for interesting conditions. A diffraction pattern usually consists of 4000 exposure and readout cycles. The number of cycles is chosen to reduce the noise as much as possible while keeping the time for a run short to minimise the influence of a change in source conditions. The exposure time is chosen to maximise the signal while at the same time avoid overexposure in individual pixels and minimise damage to the chips.

- If interesting conditions are observed, clusters are deposited onto samples. As the number of available samples is limited (seven TEM grids or SEM samples), it is impossible to deposit clusters for every single diffraction pattern.
- After the experiment, the crucible heating is turned off. Even though the two pumping stages remove most of the carrier gas, the scattering intensity from the gas is still significant compared to the intensity from the cluster beam. To remove the gas background, a series of diffraction patterns is recorded at the same gas background pressure in the diffraction chamber but with the cluster beam off.
- For comparison and to check for consistency, calibration patterns from the TlCl and Al samples are recorded again.
- After the temperature in the source has dropped to room temperature, the pumps are shut down and the system is vented.
- The samples are removed and transferred to an electron microscope.

2.5 Analysis of FE-SEM and HRTEM Images

In this work, clusters are studied under an electron microscope primarily to gain independent insight into the size distribution of the clusters in the beam. Most of the samples were analysed using a Raith 150 field emission scanning electron microscope (FE-SEM) available in the Electrical and Computer Engineering Department. The FE-SEM was mainly used for practical

reasons: Firstly, it is a digital system which allows recording of an almost unlimited number of images without having to wait for the development of the film. Secondly, it enables loading of a great number of samples at the same time. As all the previous studies in our group used a transmission electron microscope (TEM) to determine the cluster size distribution, it was necessary to compare the FE-SEM results to TEM results. For this reason, the JEOL JEM-2010 high resolution TEM (HRTEM) at Victoria University in Wellington was used. The main advantages of this system over the TEMs at the University of Canterbury are the following: firstly, it is a digital system and secondly, as the resolution is considerably higher than that of the FE-SEM and the local TEMs, it allows the detection of clusters which might be too small to be seen on the other microscopes. At the same time, it is possible to take high resolution images of single clusters to compare the structural information to the information gained from the diffraction patterns. As the FE-SEM permits the use of TEM grids, only these samples were used for all the comparison runs. Figure 2.8 shows examples of an FE-SEM image and an HRTEM image respectively. The most evident difference is that the HRTEM image is a bright-field image (the clusters are shown as dark spots), while the FE-SEM image is a secondary electron image (the clusters are shown as bright spots).

The image analysis method used in this work has been originally developed by Hall [2] and implemented by Hyslop [8] and Wurl [5]. It consists of a series of Matlab scripts and runs through the following steps:

- The image is prepared by removing the scale bar and additional information not required for the analysis. The HRTEM images are inverted to bright-field.

- The image is processed with a mean and a median filter to minimise the noise. A background image is calculated by interpolating the greyscale histogram level for small sections of the image. This background image is then subtracted from the filtered image to get a smoother background.

- A suitable threshold level is determined. This step has to be done manually as the contrast between the clusters and the background

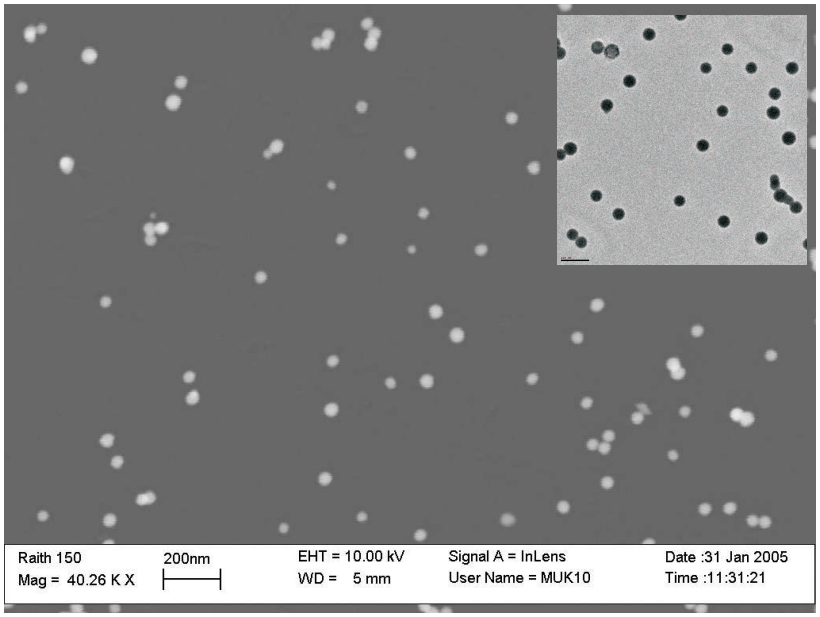

Figure 2.8: Samples of size distribution images. The main image shows an FE-SEM micrograph of amorphous Sb clusters and the inset an HRTEM image of the same sample (on the same scale).

is too small to achieve a reliable automatic fit. If the threshold level is chosen too low, the clusters appear too big and background noise starts to become visible. If it is too high, the cluster size is underestimated.

- Having prepared the image for analysis, it is now scanned automatically for clusters. If a cluster is found, its area A and perimeter P are calculated. To exclude the possibility that several small clusters which have landed close together are counted as one big cluster, the measure of circularity or compactness C is introduced:

$$C = \frac{4\pi \cdot A}{P^2} \tag{2.2}$$

The compactness of a circle equals 1 while all other geometric shapes

have smaller values. All clusters with a compactness smaller than 0.7 were disregarded in the analysis.

- As all the remaining clusters are now roughly circular, for each cluster a diameter can be calculated corresponding to the diameter of a circle with the same area.

- All clusters smaller than 5 nm were disregarded as this is about the resolution limit of the FE-SEM. This is a valid assumption for the present work, as the HRTEM study did not show any clusters below this threshold (see Chapter 4).

- Examples of the histograms are displayed in Figure 2.9 comparing results from FE-SEM and HRTEM images. The histograms at the bottom of this figure show the volume-weighted distribution which is expected to agree more closely with the mean diameter determined from the diffraction patterns (see Section 3.4.2) as the diffraction intensity depends on the number of atoms per particle and not on the area of the particle [9]. As the detector of the HRTEM in Wellington is considerably smaller compared to the one from the FE-SEM at Canterbury, the HRTEM size distribution is less representative. This explains the absence of clusters larger than 100 nm in the HRTEM size distribution.

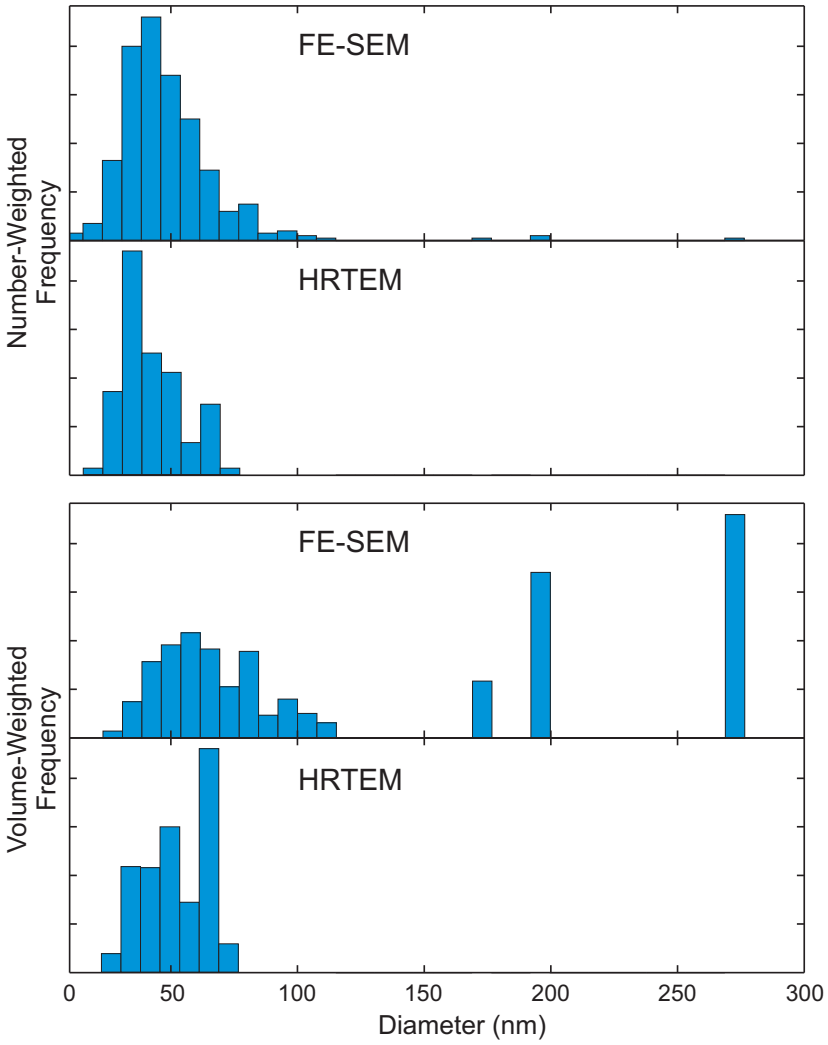

Figure 2.9: Comparison of diameter distribution from FE-SEM and HRTEM images for one particular sample. Number-weighted (top) and volume-weighted distribution (bottom).

References

[1] M. Flüeli, *Observation des Structures Anormales de Petites Particules d'Or et d'Argent par Microscopie Eléctronique à Haute-Résolution et Diffraction d'Eléctrons par un Jet d'Agrégats d'Argent*, PhD thesis, Ecole Polytechnique Fédérale de Lausanne, 1989.

[2] B. D. Hall, *An Installation for the Study of Unsupported Ultrafine Particles by Electron Diffraction with Application to Silver: Observation of Multiply Twinned Particle Structures*, PhD thesis, Ecole Polytechnique Fédérale de Lausanne, 1991.

[3] B. D. Hall, M. Flüeli, D. Reinhard, J.-P. Borel, and R. Monot, Rev. Sci. Instrum. **62**, 1481 (1991).

[4] D. Reinhard, *Croissance et Stabilité d'Agrégats d'Argent et de Cuivre, Etudiés en Jets Moléculaires par Diffraction d'Electrons à Haute Energie*, PhD thesis, Ecole Polytechnique Fédérale de Lausanne, 1996.

[5] A. Wurl, *Electron Diffraction Studies of Unsupported Bismuth Clusters*, PhD thesis, University of Canterbury, 2003.

[6] K. Sattler, J. Mühlbach, and R. Recknagel, Phys. Rev. Lett. **45**, 821 (1980).

[7] J. E. McDonald, Homogeneous Nucleation of Vapor Condensation, in *Homogeneous Nucleation Theory*, edited by F. F. Abraham, pages 225–256, Academic Press, 1974.

[8] M. Hyslop, *Electron Diffraction Studies of Unsupported Clusters*, PhD thesis, University of Canterbury, 2002.

[9] B. D. Hall, J. Appl. Phys. **87**, 1666 (2000).

Chapter 3

Electron Diffraction and Analysis

For almost a hundred years one of the preferred methods to study the structure of bulk material, molecules, clusters and even atoms has been the diffraction method. While optical microscopy only gives information about the size and morphology of a particle, diffraction techniques allow fast and straight-forward characterisation of the crystal structure including the crystal size and its purity. The disadvantage of the diffraction technique, however, is the indirect nature of the observation. Only comparison with theoretical models allows the interpretation of an experimental diffraction pattern. X-ray diffraction was the first diffraction technique to be discovered thereby forming the theoretical basis for all other diffraction methods. The subsequent discovery of electron diffraction led to the realisation that many different particle sources can be used for diffraction experiments. The three most commonly used techniques for structure analysis are X-ray, electron, and neutron diffraction. While all three methods are based on the same theory, the main difference lies in the way the particles interact with atoms. X-rays have a wavelengths of about 1 Å which is of the same order of magnitude as the interatomic distances in a crystal. They are scattered by the electrons surrounding the core and are not influenced by the positive charge of the nucleus. Therefore, X-ray diffraction produces an electron density map of the subject. Electrons, on the other

hand, are scattered by the electrostatic potential of the electron cloud and the nucleus through Coulomb interaction which – for most materials – is stronger than X-ray diffraction. Electrons are also easily absorbed by matter. The shape of the electrostatic potential is similar to the electron density distribution, although it falls off less steeply when moving away from an atom. Since neutrons have no electric charge, they are only very faintly influenced by the electron cloud. However, they do interact with the delta-function potential of the nucleus. For this reason, neutron diffraction – in contrast to X-ray and electron diffraction – is very insensitive to the type of atoms in the sample. However, neutron diffraction can be used to distinguish between isotopes and to detect spin differences which would be impossible with both X-ray and electron diffraction. For studies on cluster beams, electron diffraction has several advantages over the other two diffraction methods [1]: Electrons are scattered more strongly than X-rays or neutrons, electron beams can be focused better for a higher resolution, and a higher beam intensity is reached more easily which leads to a higher signal-to-noise ratio.

The next section gives an introduction to general diffraction theory. This is followed by a digression about amorphous solids in general. The subsequent section contains calculations of diffraction patterns from various model structures. The chapter ends with a section explaining the analysis of the experimental diffraction patterns.

3.1 Diffraction Theory

Diffraction by matter – regardless of the type of radiation used – consists of two processes shown in Figure 3.1: In a first step, the electrons (in case of electron diffraction) are scattered by individual atoms A and B. In a second step, these scattered waves interfere with each other leading to an interference pattern. It is therefore very similar to the double-slit interference experiment. Instead of the two slits, the interference centres are pairs of atoms which scatter electrons [1]. Whenever the path difference is equal to a wavelength, it leads to constructive interference on the detector. If it is equal to half a wavelength, the result is destructive interference. In case

of a crystal, there is a huge number of scattering centres which contribute to the interference pattern and the individual scattering signals have to be summed up.

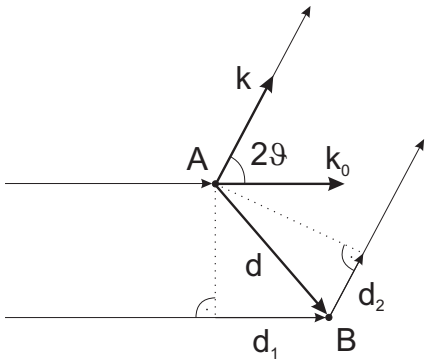

Figure 3.1: Schematic of the diffraction process: scattering by the two atoms A and B leads to interference between the resulting waves. After [2].

3.1.1 Scattering Parameter

Because of the path difference described above, there is a phase shift ψ between the incident wave and the scattered wave. For a given direction of the incident wave, the interference pattern only depends on the position of the two atoms A and B and therefore on the different path lengths of the two scattering processes. The path of the wave scattered by atom B will be longer by $\boldsymbol{\delta} = \mathbf{d_1} + \mathbf{d_2}$ where $\mathbf{d_1}$ equals the projection of $\mathbf{d}$ onto the incoming wave and $\mathbf{d_2}$ the projection onto the scattered wave ($\mathbf{d_2}$ is negative because the angle between $\mathbf{k}$ and $\mathbf{d}$ is obtuse) [2]:

$$\mathbf{d_1} = \mathbf{k_0} \cdot \mathbf{d} \tag{3.1}$$

$$\mathbf{d_2} = -\mathbf{k} \cdot \mathbf{d} \tag{3.2}$$

$$\Rightarrow \quad \boldsymbol{\delta} = -\mathbf{d} \cdot (\mathbf{k} - \mathbf{k_0}) \tag{3.3}$$

This allows the phase difference to be calculated:

$$\psi = \frac{2\pi\,\boldsymbol{\delta}}{\lambda} = -2\pi\,\mathbf{d}\,\frac{\mathbf{k} - \mathbf{k_0}}{\lambda} \tag{3.4}$$

where λ is the electron wavelength. The vector $\mathbf{s} = (\mathbf{k} - \mathbf{k_0})/\lambda$ is introduced [2]. The relationship between $\mathbf{s}$, $\mathbf{k}$, and $\mathbf{k_0}$ can be seen in Figure 3.2.

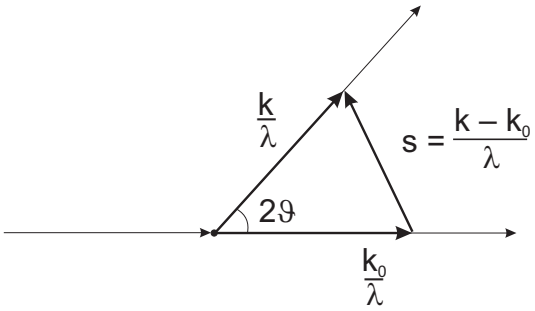

Figure 3.2: The relationship between the vectors $\mathbf{s}$, $\mathbf{k}$, and $\mathbf{k_0}$. After [2].

If the scattering angle between $\mathbf{k}$ and $\mathbf{k_0}$ is given as 2ϑ, the length of $\mathbf{s}$ can be calculated:

$$|\mathbf{s}| = s = \frac{2\sin\vartheta}{\lambda} \tag{3.5}$$

Depending on the definition of the scattering angle, different relations for s can be found in the literature, i.e. $s = \sin\vartheta/\lambda$ or $s = 4\pi\sin\vartheta/\lambda$. In this thesis, however, (3.5) is used. s is called the scattering parameter and is an important element of the diffraction theory.

3.1.2 Diffraction from Crystals

In a diffraction experiment there are usually more than two scattering sites involved. A crystal, for instance, is a three-dimensional periodic arrangement of scattering sites where each scattering site is a member of a Bravais lattice. When a scattering site is hit by an incoming wave, the scattered wave is sent out as a sphere of reflection. The resulting scattering pattern is a regular pattern of spots at all the positions where the individual spheres of reflection interfere constructively. This is equivalent to the Laue condition which states that constructive interference will occur provided that the change in wave vector $\mathbf{s} = \frac{\mathbf{k}-\mathbf{k_0}}{\lambda}$ is a vector of the reciprocal lattice [3].

3.1.3 Diffraction from Clusters

Diffraction from clusters in a molecular beam follows the same principle as described in the last section. However, instead of being stationary and embedded in a crystal structure, the clusters are randomly oriented in the beam. As a consequence, the interference pattern is not the dot pattern described above, but rather consists of concentric rings around the axis of the electron beam, giving rise to the so-called Debye-Scherrer diffraction pattern. The distance between these haloes is inversely proportional to the distance between the atoms in the clusters: widely spaced atoms lead to closely spaced rings and vice versa. The resulting diffraction pattern for the cluster beam is the sum of all the individual interference patterns of pairs of atoms in all the clusters. As long as all the clusters have the same structure and are of roughly the same size, it is relatively straightforward to derive size and structure from such a diffraction pattern. Under typical experimental conditions, however, the cluster sizes in the beam show strong variations and there is even the possibility of a mixture of different structures. To analyse the experimental diffraction patterns, a series of diffraction patterns has to be calculated, starting with the most likely structure and size of the clusters. These calculated patterns are then compared to the experimental ones. The underlying theory will be described over the next two sections. In the first section, the kinematic theory will be introduced which is based on the assumption that secondary scattering can be neglected. The subsequent section discusses the dynamic theory where secondary scattering is incorporated.

Kinematic Theory

The kinematic theory is based on the Born approximation which assumes that the scattered waves are considerably weaker than the primary waves. In this case, the secondary waves are too weak to scatter again. Consequently, every atom in the cluster scatters by a wave of the same amplitude, as if there were no attenuation of the incident wave as it passes through the cluster. This approximation is valid if the clusters are relatively small (see below). The kinematic theory can be expressed by the

Debye equation which allows the scattering intensity I to be calculated as a function of the scattering parameter s [2]:

$$I_N(s) = I_0 N f^2(s) \left(1 + \frac{D}{N} \sum_{n \neq m} \frac{\sin(2\pi s r_{mn})}{2\pi s r_{mn}}\right) \tag{3.6}$$

where I_0 is the intensity of the incident beam, N the number of atoms in a cluster, $f(s)$ the atomic scattering factor, D the Debye-Waller factor, and r_{mn} the distance between atom m and atom n. Note that the Debye equation only depends on the interatomic distances and does not require a crystal structure. As long as the positions of all atoms are known, it can also be used to calculate patterns for amorphous and liquid patterns. The atomic scattering factor $f(s)$ and the Debye-Waller factor D will be explained in detail in the following.

The atomic scattering factor (also called form factor) differs for electrons and X-rays. The X-ray scattering factor is given by the following expression [4]:

$$f_x(s) = 4\pi \int_0^\infty r^2 \rho(r) \frac{\sin(2\pi s r)}{2\pi s r} \, \mathrm{d}r \tag{3.7}$$

where r is the atomic radius and $\rho(r)$ the electron density of the atom. For most elements, the resulting X-ray scattering factors can be found in tabulated form [4]. The X-ray and the electron scattering factor are connected through the Mott formula [4]:

$$f_{el}(s) = \frac{me^2}{2h^2} \left(\frac{Z - f_x(s)}{s^2}\right) \tag{3.8}$$

where m is the relativistic mass of the electron, e the electron charge, h Planck's constant, and Z the atomic number. Figure 3.3 displays the characteristics of the two form factors using Sb as an example (note that the values are normalised). By applying (3.8) it can be shown that the atomic scattering factor for electrons is typically 10^4 times stronger than the X-ray scattering factor [5].

In the Debye equation (3.6) the scattering intensity is proportional to the square of the scattering factor, $f^2(s)$. It represents the differential cross sec-

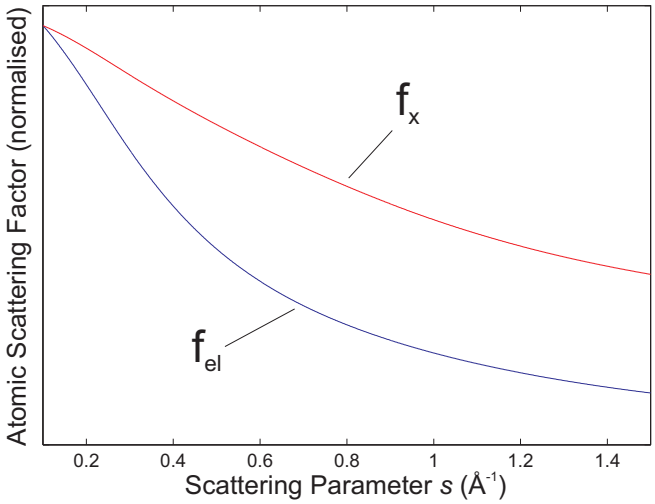

Figure 3.3: The characteristics of the electron and X-ray form factors f_{el} and f_{x} for Sb in dependence of the scattering parameter s at 80 kV electron energy. The values are normalised for comparison. Data from [4].

tion of a single atom, equivalent to the probability of the incident electron hitting an atom.

The Debye-Waller factor D in (3.6) represents the influence of displacement disorder (mainly thermal motion) on the cluster structure. Through thermal vibrations, the atoms in a cluster are slightly displaced around their original positions. These displacements of the scattering centres have two effects on the diffraction pattern [2]: firstly, the peak intensities are decreased and secondly, the general background of the pattern is increased. The integrated intensity of the whole patterns stays constant and there is no broadening of the diffraction peaks. If the displacements are isotropic, the Debye-Waller factor can be written in the following form:

$$D = \exp\left(-\frac{4\pi^2 s^2}{3}(\Delta r)^2\right) \tag{3.9}$$

where Δr is the root-mean-square (rms) displacement of the atoms from their equilibrium position at a given temperature. According to this equation, the weakening of the diffraction peaks is stronger at higher scattering

angles. Compared to X-ray diffraction, this effect is less pronounced for electrons as the electron scattering factor drops off more steeply at higher scattering angles (see Figure 3.3). To calculate the Debye factor, it is necessary to know the rms displacement as a function of the temperature. According to the theory of the specific heat of solids, the rms displacement can be written in the following form [2]:

$$(\Delta r)^2 = \frac{9\hbar^2 T}{m k_B \Theta^2} \left(\frac{1}{4}\frac{\Theta}{T} + \phi\left(\frac{\Theta}{T}\right) \right) \tag{3.10}$$

where $\hbar$ is Planck's constant, T the temperature of the experiment, m the atomic mass, k_B Boltzmann's constant, Θ the Debye characteristic temperature, and the function $\phi(\frac{\Theta}{T})$ is given by

$$\phi\left(\frac{\Theta}{T}\right) = \frac{T}{\Theta}\int_0^{\Theta/T} \frac{y}{e^y - 1}\,\mathrm{d}y \tag{3.11}$$

As the whole expression

$$\frac{1}{4}\frac{\Theta}{T} + \phi\left(\frac{\Theta}{T}\right) \tag{3.12}$$

is equal to unity within 3% for $T > \Theta$ [2], the rms displacement can be written in the form

$$(\Delta r)^2 = \frac{9\hbar^2 T}{m k_B \Theta^2} \tag{3.13}$$

The importance of the Debye-Waller factor in the present work will be discussed in Section 3.3.1.

Dynamic Theory

The kinematic theory described above is only an approximation and does not take into account multiple scattering nor attenuation of the incident waves. In reality, the primary waves lose intensity as they pass through the cluster, thereby creating a refractory beam. When the path through the cluster is long enough, the ratio of the intensities of the primary wave and the scattered wave is independent of its thickness. This threshold is called the dynamical equilibrium. For X-ray diffraction this threshold lies

at around 0.1 mm [6]. Given the fact that electron scattering is considerably more intense than X-ray scattering, the limit for electron diffraction is substantially lower. Depending on electron energy and element, the kinematic theory starts to show deviations from the experiment for clusters as small as 10 nm in diameter. A method to account for dynamic effects was developed by Bartell [7–9] and tested for argon and gold clusters. It essentially adds corrective terms to the kinematic theory to include secondary scattering effects. The advantage of this method is that it can be applied to arbitrary structures, not only to crystals. It also allows the diffraction pattern to be calculated directly. However, it was only tested on clusters with up to 135 atoms. A more refined method which is based on the multislice technique [10] has been developed by Hall [11]. It was used to calculate dynamic diffraction patterns for gold and silver clusters between 15 and 55 Å with face-centred-cubic (fcc) and icosahedral structure at 40 and 100 kV electron energy. Comparing the results to the kinematic theory, the following conclusions can be drawn: Dynamic diffraction leads mainly to an overall reduction of the scattering intensity, particularly in the first peaks. This reduction is strongest for bigger and heavier clusters, for lower electron energies and for clusters with a higher crystalline order (for icosahedral clusters the difference was much smaller than for fcc clusters).

While there is an obvious difference between the dynamic and kinematic theory, it is not trivial to estimate the impact on the diffraction patterns for Sb. Sb is slightly heavier than Ag but considerably lighter than Au, so there should be less influence compared to Au. However, the clusters in this study are all larger than 55 Å and the electron energy is only 80 kV. The effect of the rhombohedral structure of Sb can only be estimated. As the multislice method is computationally intensive and as it would have been very time-consuming to develop a new software package to account for the Sb structure, it was decided to concentrate on the time-of-flight mass spectrometer (see Chapter 5). However, by only considering the kinematic approximation, it is evident that the amount of information that can be extracted from the diffraction patterns is limited. As the signal-to-noise ratio of the experimental diffraction patterns in the present work is too low to allow detailed analysis by fitting to calculated patterns, the

effect of dynamic diffraction on the present analysis is minimal, and the decision not to perform detailed calculations seems to be justified.

3.2 Amorphous Solids in General

In contrast to crystals, non-crystalline (or amorphous) materials possess a certain degree of randomness (see Figure 3.4). It is important to note, however, that the structure of amorphous materials is not completely random in a statistical sense (unlike the atomic arrangement for a gas as shown in Figure 3.4(c)). In fact, amorphous solids display a very non-random short-range order but lack a periodic long-range order. In a crystalline solid the bond lengths and nearest-neighbour separations are *exactly* equal whereas in an amorphous solid they are only *nearly* equal. The same holds true for the bond angles: in an amorphous solid they are randomly distributed around the crystalline value and the width of the distribution is a measure of stress in the amorphous structure.

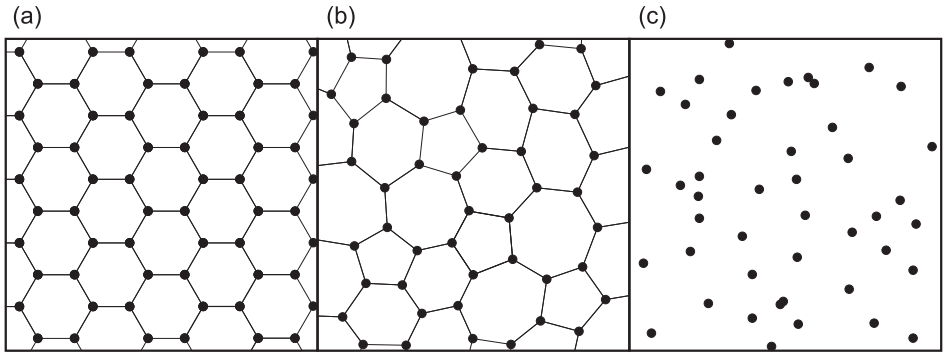

Figure 3.4: 2D atomic arrangements in (a) a crystalline solid, (b) an amorphous solid, and (c) a gas. After [12].

3.2.1 Radial Distribution Function

The radial distribution function (RDF) is an important tool for understanding the amorphous structure in general and comparing calculations to experimental results. Starting from an arbitrary atom in a structure, the RDF,

$J(r) = 4\pi r^2 \rho(r)$, is defined such that $J(r)$ gives the probability of finding a neighbouring atom at a distance between r and $r + \mathrm{d}r$ [13]. The function $\rho(r)$ is basically a pair correlation function which is large at distances with many atoms and small otherwise. Figure 3.5 shows a schematic construction of the density function $\rho(r)$ from a 2D amorphous structure. The integrated area of the first peak corresponds to the number of nearest neighbours, i.e. the coordination number.

In the case of a crystalline structure the RDF theoretically leads to a series of delta peaks at the position of the nearest neighbours, the next-nearest neighbours and so on. (In reality, even at a low temperature the peaks have a finite width due to thermal motion.) The RDF of an amorphous structure, however, shows an intrinsic broadening of all the peaks because the interatomic distances are distributed around an average value.

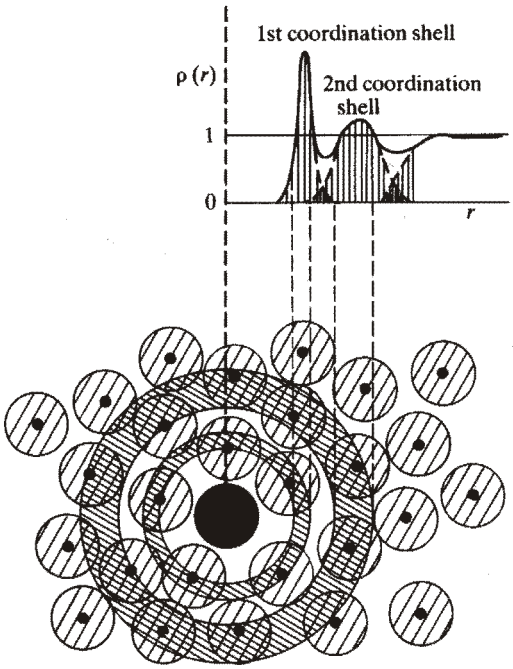

Figure 3.5: A schematic construction of the density function $\rho(r)$ from a 2D amorphous structure. After [13].

Figure 3.6 shows a comparison of different RDFs for a crystalline structure, an amorphous structure and a gas.

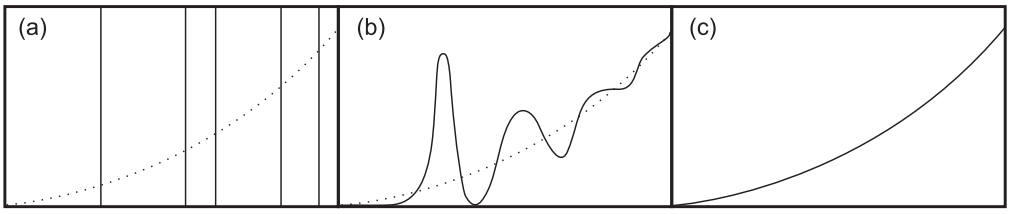

Figure 3.6: Radial distribution functions of (a) a crystalline structure, (b) an amorphous structure, and (c) a gas. The dotted lines indicates the average density to which the RDF tends at large r. After [12].

If the RDF is constructed in 3D, all the peaks beyond the first peak receive contributions from higher coordination shells as well. Another important point is that the RDF is a 1D representation of a 3D structure. Therefore, the construction of an RDF always leads to a loss of structural information and it is possible to have two different structures with indistinguishable RDFs [13].

3.2.2 Fourier Transform

The importance of the RDF for the diffraction theory is based on the fact that it can be determined from a diffraction pattern by Fourier transform. Thus, there is a direct connection between the experimental observation in reciprocal space (diffraction pattern) and the structural information in real space (RDF). Using the RDF introduced in the last section, the Debye equation (3.6) can be rewritten as [14]

$$I_N(s) = I_0 f^2(s) \left(N + \int_0^\infty 4\pi r^2 \left[\rho(r) - \rho_a\right] \frac{\sin(2\pi s r)}{2\pi s r} \, \mathrm{d}r \right) \tag{3.14}$$

where ρ_a is the average density of the sample. Since the experimental scattering intensity $I(s)$ is only measured over a limited range of s-values,

the inverse Fourier transformation of (3.14) takes the form [15]

$$P(r) = \beta r \int_{s_{\min}}^{s_{\max}} s \left[\frac{I(s)}{\alpha f^2(s)} - 1 \right] \sin(2\pi s r)\, \mathrm{d}s\, s \tag{3.15}$$

where α and β are parameters that have to be estimated. If the range of s-values is wide, this expression is a good approximation of the RDF $J(r)$. In our experiments, however, s is only measured between 0.25 and 1.2 Å^{-1}, hence, $P(r)$ can differ considerably from the RDF. It is also important to note that $P(r)$ is no longer restricted to positive values only.

3.2.3 Diffraction from Amorphous Solids

Although the basic scattering process is the same for amorphous materials as for crystals, the resulting diffraction patterns differ considerably. Electron or X-ray diffraction from amorphous materials does not give rise to several sharp rings as in the case of randomly oriented crystals. Instead, only a few diffuse haloes are observed. The small number of rings is due to the lack of long-range order and the diffuseness is due to the distribution in bond lengths and angles.

Using the Fourier transform procedure described above, it is possible to gain information about the structure of the amorphous particles. The position of the first peak r_1 in the RDF corresponds to the average bond length of the amorphous structure. The integrated area of the first peak indicates the coordination number.[1] The position of the second peak r_2 corresponds to the next-nearest-neighbour distance and – together with r_1 – defines the bond angle ϑ [13]:

$$\vartheta = 2 \arcsin\left(\frac{r_2}{2r_1}\right) \tag{3.16}$$

In amorphous materials the second peak is usually wider than the first peak indicating a spread in bond angles of about $\pm 10\%$ [16].

[1] The area of each of the subsequent peaks would also indicate the coordination number of the respective shell. As described above, it has to be considered however, that all the peaks beyond the first one also have higher order contributions.

3.3 Calculating Diffraction Patterns

The Debye equation (3.6) described above has to be modified to allow efficient calculation of the diffraction patterns which can then be compared to experimental patterns. The computationally most intensive part is the calculation of the sine functions for all the interatomic distances. To speed this step up, a histogram $H(r)$ is introduced into which all interatomic distances are binned. Equation (3.6) will then take on the following form:

$$I_N(s) = f^2(s)\left(1 + \frac{D}{N}\sum_r \frac{\sin(2\pi sr)}{2\pi sr}\,2H(r)\right) \tag{3.17}$$

The intensity of the experimental pattern has to be scaled to fit the calculated pattern. The choice of the bin size is a trade-off between computing time and accuracy. If the bin size is chosen too big, systematic errors are introduced [17]. The Debye-Waller factor, D, given in (3.9) can be written as [18]

$$D = \exp(-s^2\gamma^2) \quad \text{with} \quad \gamma^2 = \frac{4\pi^2}{3}(\Delta r)^2 \tag{3.18}$$

Replacing $(\Delta r)^2$ by the expression from (3.13) leads to

$$\gamma^2 = \frac{4\pi^2}{3}\frac{9\hbar T}{mk_B\Theta^2} = \frac{3h^2}{mk_B\Theta^2}\,T = a \cdot T \tag{3.19}$$

As the Debye characteristic temperature for Sb is 200 K [3] and Δr is given in Å, γ^2 can be approximated by the following expression:

$$\gamma^2 = a \cdot T \simeq 0.00118 \cdot T \tag{3.20}$$

3.3.1 Examples of Calculated Diffraction Patterns

This section contains a collection of calculated diffraction patterns. In the first part patterns of crystalline Sb clusters are shown, followed by patterns for Sb_4 tetramers, clusters of Sb_4 tetramers, and liquid Sb clusters. At the end of the section, a pattern for amorphous Sb is shown which is not

calculated but based on previous experimental studies. This collection of patterns is provided in order to compare with experimental results.

Bulk Sb for Comparison

For comparison, Figure 3.7 shows the peak positions of the rhombohedral bulk Sb structure. The data for the peak positions, the intensity and the Miller indices are taken from [19]. The Miller indices are given in the notation used for a rhombohedral cell, not a hexagonal cell. The conversion between these two systems is explained in [20]. In this thesis, only the rhombohedral notation is used.

Diffraction Patterns of Crystalline Sb Clusters

All diffraction patterns in this section are calculated using the adjusted Debye equation (3.17). Initially, a rhombohedral lattice based on the bulk values of Sb [21] is created from which the respective shapes are cut

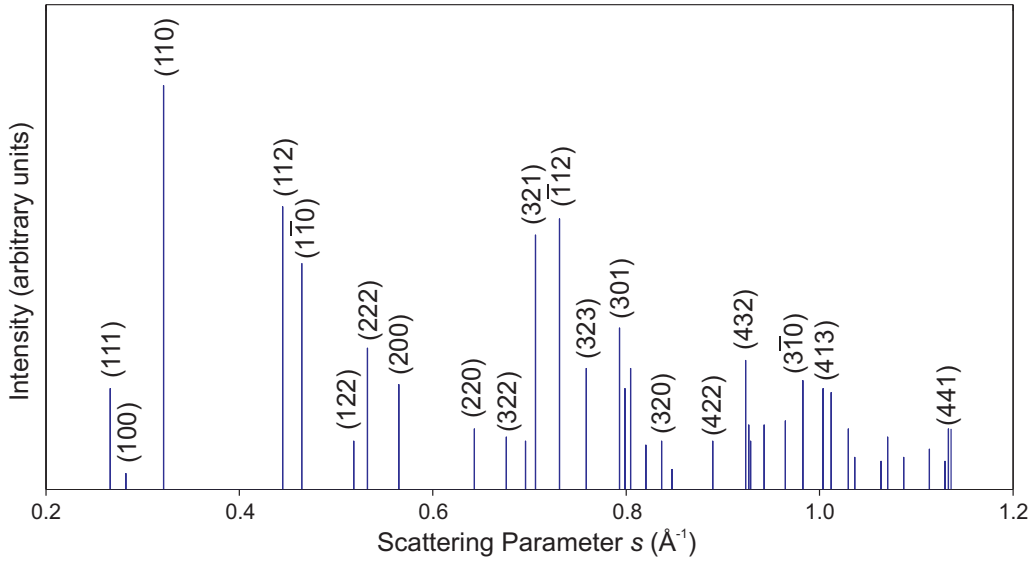

Figure 3.7: Powder diffraction pattern for bulk Sb with the Miller indices (based on the rhombohedral structure) for the most important peaks with their relative X-ray intensity. Data from [19].

out. The Debye-Waller factor was calculated for room temperature (295 K) which leads to $\gamma^2 = 0.35$. This value was used for all calculations except for Figure 3.10 where the Debye-Waller factor is varied. Where the size or diameter of a cluster is given, it is determined by measuring the *largest* interatomic distance.[2] To enable a comparison of the individual patterns, all patterns in a set are scaled so that the intensities of the highest peak are equal.

The influence of the cluster size on the diffraction pattern is shown in Figure 3.8. The clusters are all spherical. With increasing cluster size, more details in the diffraction patterns become visible but the peak positions remain constant. Additionally, the diffuse background is reduced. Because the effect of increasing the cluster size is so evident, it can be used to determine the cluster size by analysing the diffraction pattern (see Section 3.4.2).

The cluster shape has a distinct influence on the diffraction pattern. Figure 3.9 shows four examples of different cluster shapes. The cluster sizes were chosen so that all clusters contain a similar number of atoms. In Figure 3.9(a) the cluster facets are defined by one type of planes (six $\{100\}$) and in Figure 3.9(b) they are defined by two different types, namely six $\{011\}$ and two $\{111\}$ where the $\{111\}$ planes are three quarters of the distance of the $\{011\}$ planes away from the centre of the crystal. The cluster in Figure 3.9(c) has a hexagonal shape which is defined by six $\{1\bar{1}0\}$ and two $\{111\}$ planes where the $\{111\}$ surfaces are half as far from the centre of the clusters as the $\{1\bar{1}0\}$ surfaces. Figure 3.9(d) shows a tetragonal cluster which is defined by three $\{100\}$ planes and one $\{111\}$ plane. As reported in Section 1.3.2, this shape has been observed by Okazaki for Sb particles [22]. From these four examples, it is clear that the shape of a cluster is an important factor in determining the relative peak intensities, especially of the second and third main peak.

Figure 3.10 shows the influence of the cluster temperature on the diffraction patterns. The solid line represents a Debye-Waller factor of 1 which is equivalent to a temperature of 0 K ($\gamma^2 = 0$). The dotted line is calculated for a temperature of 900 K ($\gamma^2 = 1.06$) which is just below the melting point

[2] Note that all other definitions of the cluster size would lead to smaller values.

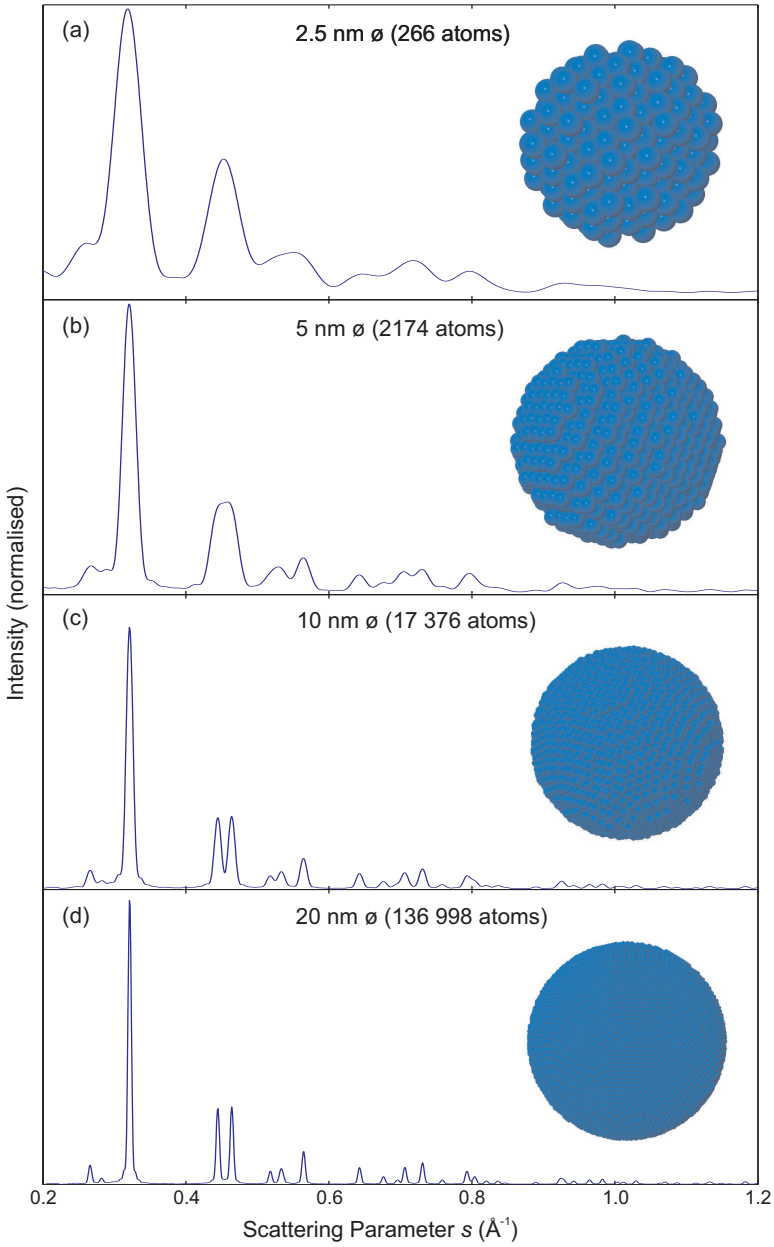

Figure 3.8: Diffraction patterns calculated for a series of different cluster sizes. The clusters are all spherical and have the rhombohedral structure of bulk Sb.

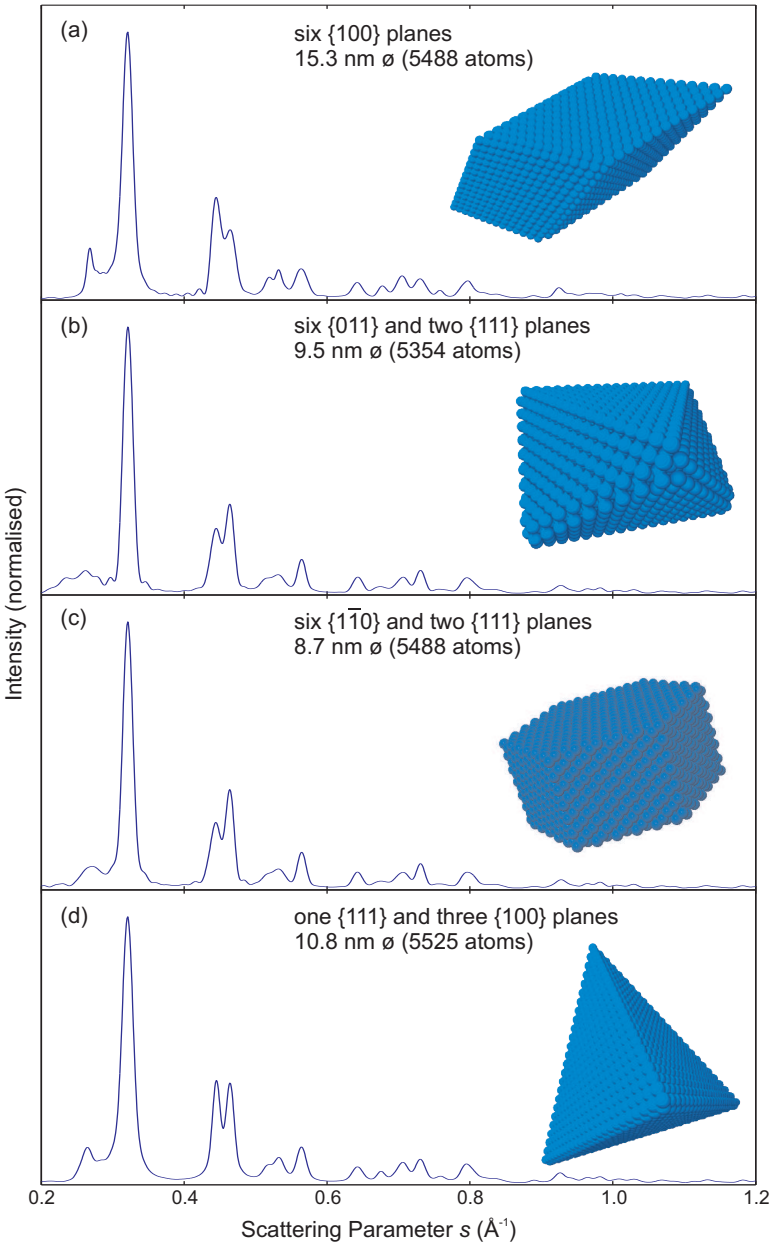

Figure 3.9: Diffraction patterns calculated for a series of different shapes. The clusters all have the rhombohedral structure of bulk Sb and are faceted by (a) six {100} planes, (b) six {011} and two {111} planes, (c) six {1$\bar{1}$0} and two {111} planes, and (d) one {111} and three {100} planes.

of bulk Sb (903.8 K). As discussed in Section 3.3, the higher temperatures lead to a weakening of the peaks at higher *s*-values and increase the background over the whole range of scattering parameters. The differences, however, are minute and will not be detectable in an experimental diffraction pattern. An exact match of the experimental temperature is therefore not required and the choice of 295 K for the calculated patterns is justified.

Diffraction Patterns of Sb_4 Molecules and Sb_4 Clusters

One of the distinct properties of Sb is the fact that it evaporates mainly in tetramers (Sb_4), rather than in monomers and dimers (Sb_1 and Sb_2). It is therefore to be expected that at least some experimental diffraction patterns display an influence of scattering from Sb_4 molecules. The dotted line in Figure 3.11 shows the diffraction pattern of a single Sb_4 molecule. The structural information for the Sb_4 units is taken from [23]. As it has to be considered that these tetramers form amorphous clusters by condensing

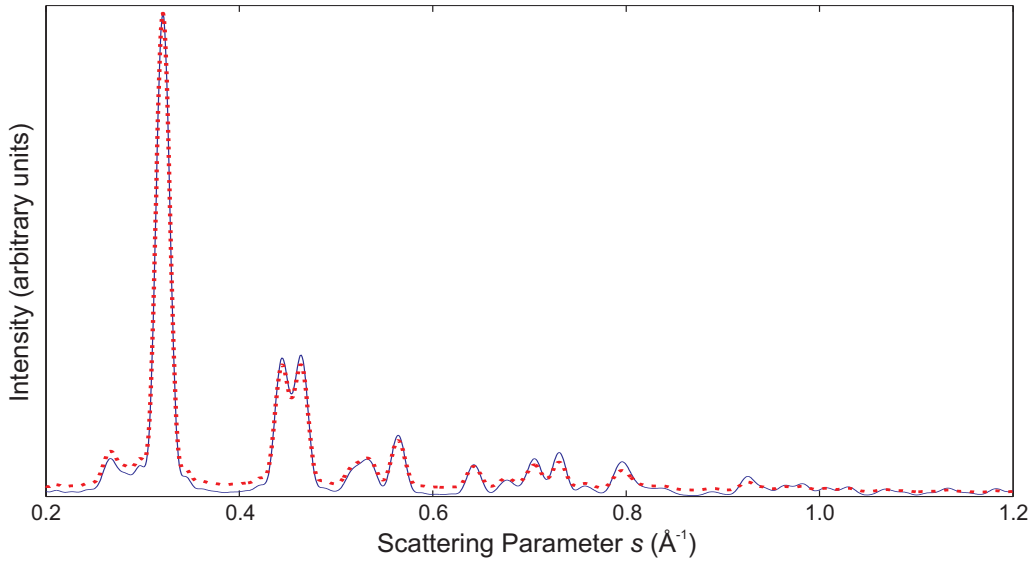

Figure 3.10: Diffraction patterns calculated for two different temperatures. The solid line represents a cluster temperature of 0 K while for the dotted line the cluster temperature is increased to 900 K.

without crystallising, a diffraction pattern for a 10 nm cluster consisting of randomly oriented Sb_4 units has been calculated (solid line). Unfortunately, the difference between the two patterns is very small which makes it impossible to distinguish between these two particles.

Phosphorus (P) and arsenic (As) – Sb's neighbouring elements in group V of the periodic table – both evaporate mainly as tetramers as well, however, unlike the case of Sb, they both also have bulk modifications made of tetramers: 'white' P and 'yellow' As. Both modifications are thought to have a cubic structure but the structural information available is not conclusive as both phases are unstable and decompose under X-ray illumination [24]. Therefore, no calculated patterns of these structure were included in this section.

As discussed in Section 1.3, Sattler *et al.* observed magic numbers for Sb clusters at 8, 36, 52, and 84 [25]. They also presented models of the geometry of these magic clusters. All models are based on Sb_4 building blocks. In the case of Sb_8, a structure with two tetrahedra which are in contact with

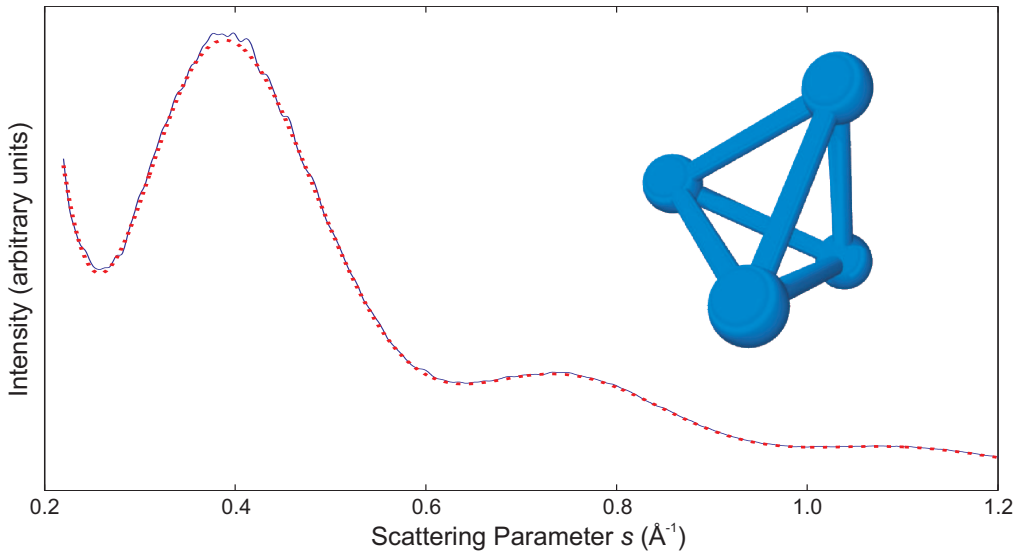

Figure 3.11: Diffraction patterns calculated for an Sb_4 molecule (dotted line) and a 10 nm cluster consisting of randomly oriented Sb_4 units (solid line).

one of their faces and twisted by 60° is suggested. Subsequent molecular dynamics studies found such a geometry to be the lowest energy structure amongst all their calculations [26]. For Sb_{36}, Sb_{52}, and Sb_{84} clusters, models based on an Sb_{20} pyramid were suggested where Sb_4 units are attached to the pyramid faces. For Sb_{36} there is one, for Sb_{52} two, and for Sb_{84} three Sb_4 units per face.

Figure 3.12 shows the calculated diffraction patterns of these four models. The bond length for the Sb_4 units in these models is taken from [23], while the separation distance between the two tetramers in the Sb_8 cluster is taken from [26].

Diffraction Patterns of Liquid Sb Clusters

Because of a lack of direct structural information for liquid Sb clusters, it was not possible to calculate diffraction patterns using the same procedure as previously described. It was therefore necessary to use a model which was developed by Zou *et al.* [27, 28]. This model is based on the hard sphere

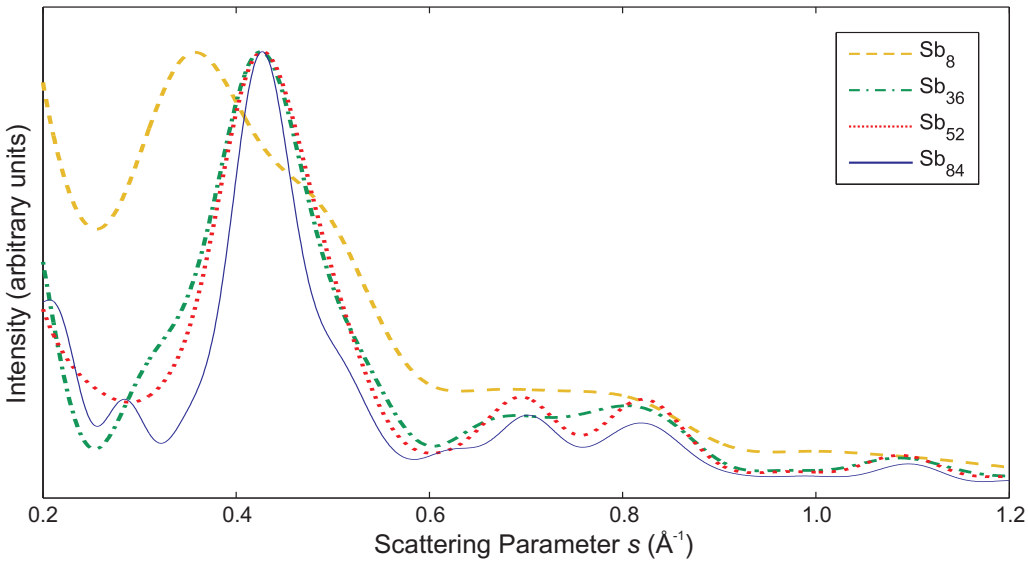

Figure 3.12: Diffraction patterns calculated for the four models of Sb_8, Sb_{36}, Sb_{52}, and Sb_{84} suggested by Sattler *et al.* [25].

(HS) model of Ashcroft and Lekner [29] extending it for non-simple liquid metals like Bi, Ga, Sb, and Sn. The diffraction patterns of these non-simple metals show a characteristic shoulder on the right hand side of the main peak which is not visible for simple liquid metals (e.g. Al, In, Tl, and Pb). To account for this shoulder, the original HS model was extended to include two types of spheres, A and B, where species A and B correspond to long and short interatomic distances. These spheres are arranged randomly in groups (clusters) of the same type within the liquid. Hence, the whole liquid consists of a mixture of these two types of clusters and is therefore also called hard sphere cluster (HSC) model. This model is based on the fact that metals such as Sb have a double structure with three nearest and three next-nearest neighbours. While it is not expected that this structure is retained upon melting, it is possible that there are still two separate groups of long and short interatomic distances in the liquid phase. The HSC model gives the following expression to calculate the structure factor (scattering intensity of the whole structure):

$$F(s) = (1 - x)F_{\mathrm{A}}(s) + xF_{\mathrm{B}}(s) \tag{3.21}$$

where x is the percentage of spheres of type B in the liquid and F_{A} and F_{B} are the scattering factors given by the HS model for each type individually. These two terms only depend on the hard sphere diameter and the packing density of the two different types of spheres. All these parameters (including x) are temperature dependant. For Sb this model has been fitted to experimental neutron diffraction data [30] and the five parameters (hard sphere diameter and packing density of the two types of spheres as well as the relative percentage of the two species) have been derived for temperatures of 660°C and 800°C [27, 28].

For clusters with a diameter of more than approximately 20 nm the HSC model can be directly used to calculate the diffraction pattern. For smaller clusters it is essential to take effects due to the finite volume into account. This can be achieved by calculating the convolution between the structure function and the function for a sphere [18]. Figure 3.13 shows the diffraction patterns for a 1 nm and a 20 nm liquid Sb cluster at 660°C. The diffraction pattern for the bigger cluster clearly shows the shoulder to the

right of the main peak. The difference between the diffraction patterns at 660°C and 800°C is negligible.

Diffraction Patterns of Amorphous Clusters

The structure of amorphous solids is similar to that of liquids but it is less homogeneous and more rigidly packed as the thermal vibration of the atoms is weaker. However, as discussed in Section 3.2, amorphous solids display a very non-random short-range order but lack a periodic long-range order. As in the case of liquid Sb clusters, there is no structural information available for amorphous Sb clusters that could be used for direct calculation of the diffraction patterns. There are, however, extensive experimental diffraction results available for amorphous Sb [31–34].

The pattern in Figure 3.14 is the experimental pattern from Richter *et al.* [33]. The pattern was originally recorded using X-ray diffraction and the intensity had to be converted to match the electron form factor (see Figure 3.3). The samples used in this experiment were Sb thin films and are

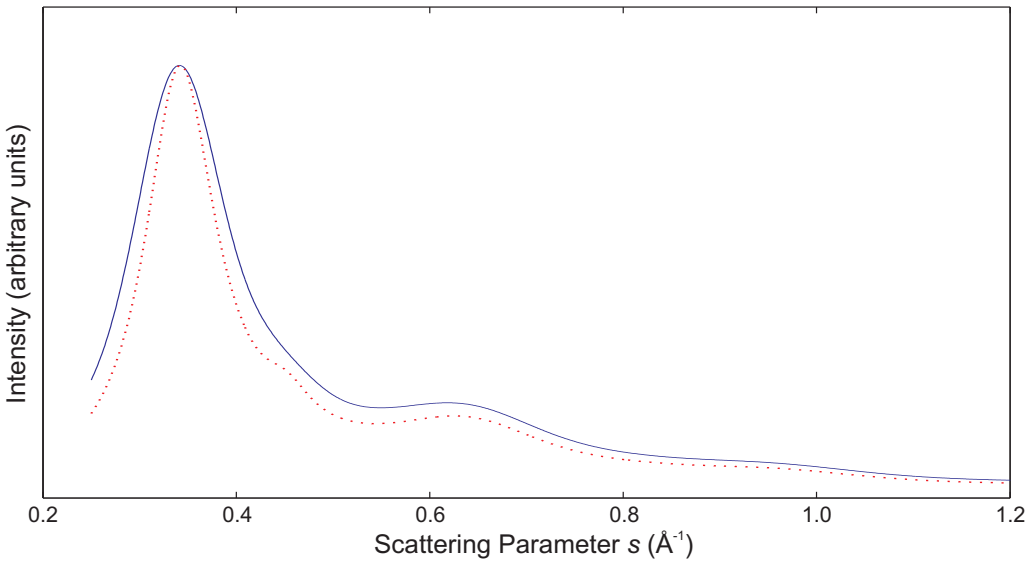

Figure 3.13: Diffraction patterns calculated for liquid Sb at 660°C. The solid line corresponds to a 1 nm cluster, the dotted line to a 20 nm cluster.

as such not directly comparable to clusters. As discussed in the previous section for liquid clusters, however, the difference between large clusters (at least 10 nm diameter) and thin films is expected to be marginal. On first glance, the general appearance of this pattern is similar to the liquid pattern in Figure 3.13, but on closer examination there are very distinct differences: the peak positions do not match and the peaks in the amorphous pattern are more pronounced.

It is interesting to compare the patterns for Sb_4, amorphous and liquid Sb to the two patterns shown in the introduction from Stein *et al.* and Sun *et al.* (see Figure 1.4). Stein *et al.* concluded that their pattern was due to amorphous clusters, while Sun *et al.* attributed their pattern to liquid clusters. If the peak positions of these two pattern are compared to the patterns presented in this chapter, it is evident that both patterns were most likely due to Sb_4 – either individual tetramers or in the form of larger particles.

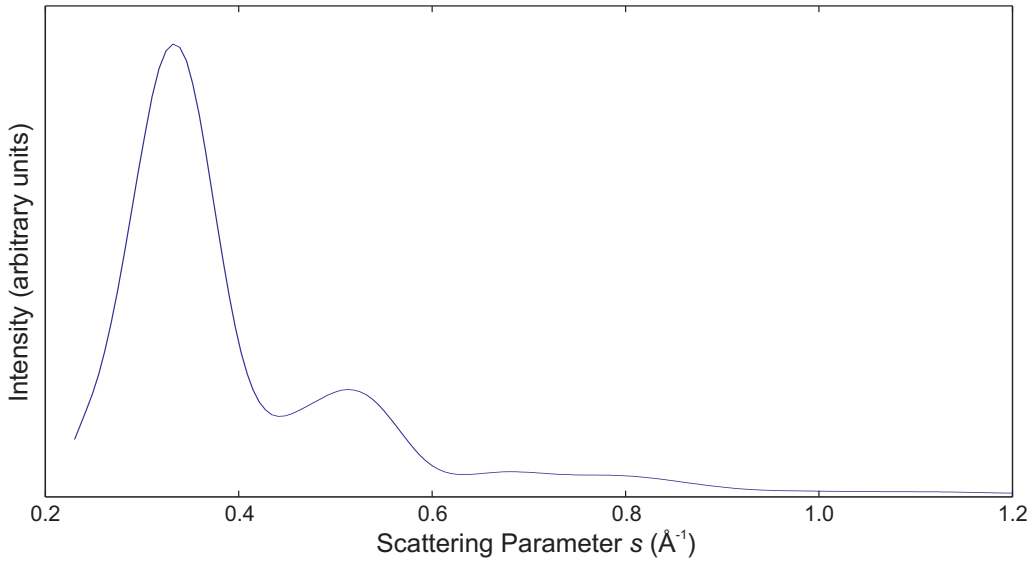

Figure 3.14: Experimental diffraction pattern for amorphous Sb thin film. The data is a scanned plot from [33] which was digitised, filtered and converted to the electron diffraction form factor.

3.4 Analysis of Experimental Diffraction Patterns

As described in Section 2.2, during an experiment the diffraction rings are recorded by two LDA chips situated on a diameter of the Debye-Scherrer haloes. Each chip consists of 2048 individual pixels, each recording the charge at a particular scattering angle. In theory, the accumulated pattern of one chip looks like one of the diffraction pattern shown in Figure 3.8. The raw experimental pattern, however, looks quite different, as can be seen in Figure 3.15. This discrepancy is mainly due to the scattering of the carrier gas which is not fully removed by the two pumping stages. The following section describes the procedure necessary to prepare the experimental diffraction pattern for analysis. It is followed by a section explaining different ways of extracting information about the cluster size from experimental patterns.

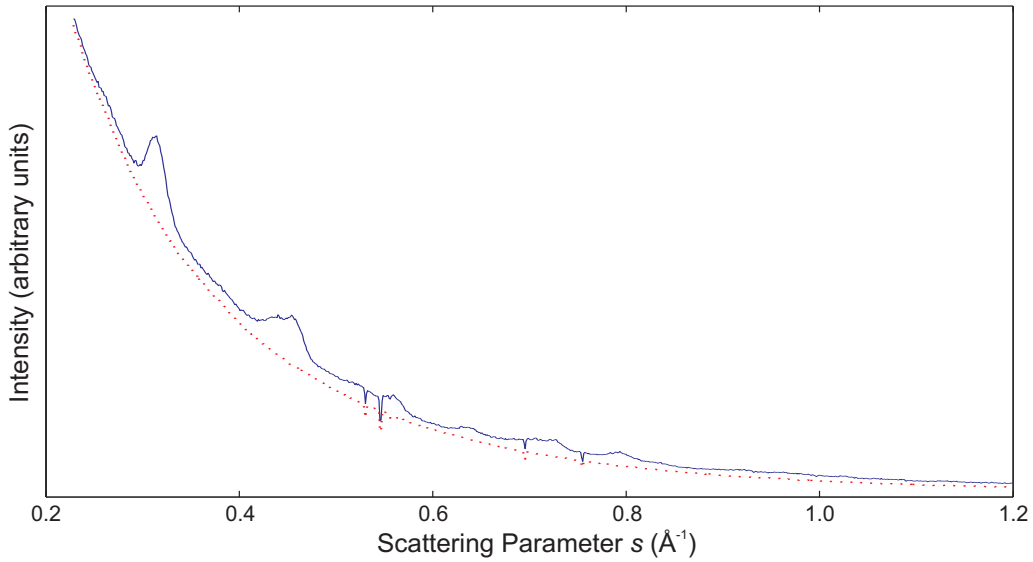

Figure 3.15: Raw diffraction pattern before the gas background is subtracted. The dotted line indicates the gas background.

3.4.1 Data Preparation

The raw data recorded during an experiment consists of an intensity value for every pixel. The pixel numbers have to be translated into scattering parameter values s to compare the experimental diffraction patterns to calculated ones. Additionally, the detector chips most probably do not run exactly through the centre of the scattering rings. The basic situation before conversion and adjustment can be seen in Figure 3.16. Before and after every experiment, a set of calibration patterns is recorded. For these calibration patterns polycrystalline Al and TlCl films are used which show diffraction peaks at known scattering parameter values. The following equation describes the calibration procedure (using the definitions from Figure 3.16) [18]:

$$\left(\frac{s}{c}\right)^2 = (wn)^2 + 2bwn + (d^2 + b^2) \tag{3.22}$$

For calibration, only the interdependence between scattering parameter s and pixel number n is important:

$$s^2 = An^2 + Bn + C \tag{3.23}$$

The parameters A, B, and C can be determined by a least-square fitting procedure using the known peak positions of the calibration patterns.

In a second step, the background signal due to scattering of the carrier gas has to be removed. Immediately after every experiment a set of background diffraction patterns is recorded while there are no clusters in the diffraction chamber. For every experimental cluster diffraction pattern there has to be a gas diffraction pattern at exactly the same diffraction chamber pressure. However, even if the same base pressure is chosen, differences in intensity between the cluster pattern and the gas pattern are observed. The reason for the differences lies in the fact that the electron beam intensity varies over the course of an experiment. To adjust for this inconsistency, the gas pattern is scaled slightly before it is subtracted from the cluster pattern. The resulting diffraction pattern is shown in Figure 3.17.

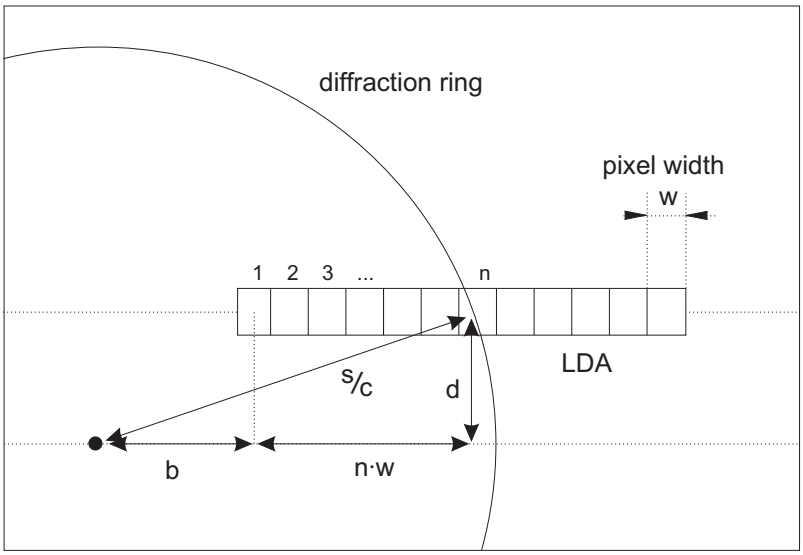

Figure 3.16: Calibration of the detector chips. The chip can be offset in two directions, b and d respectively. w is the pixel width and n the pixel number where one of the diffraction peaks lies. The factor c converts the physical distance on the detector to the scattering parameter s. After [18].

3.4.2 Size Analysis

After the diffraction pattern has gone through the preparatory procedure outlined above, it is ready for analysis. From an ideal diffraction pattern (high intensity, high signal-to-noise ratio) information about cluster size, cluster structure, lattice parameters and even cluster shape can be extracted. In this work, however, the signal-to-noise ratio of crystalline diffraction patterns was too low for very detailed analysis and only cluster size analysis was carried out. In the following two sections, two different techniques to determine the cluster size are discussed. The first is based on the Scherrer equation and the second on the radial distribution function (RDF) obtained by inverting the diffraction pattern. The subsequent section discusses the influence of disorder and domains on the size estimates.

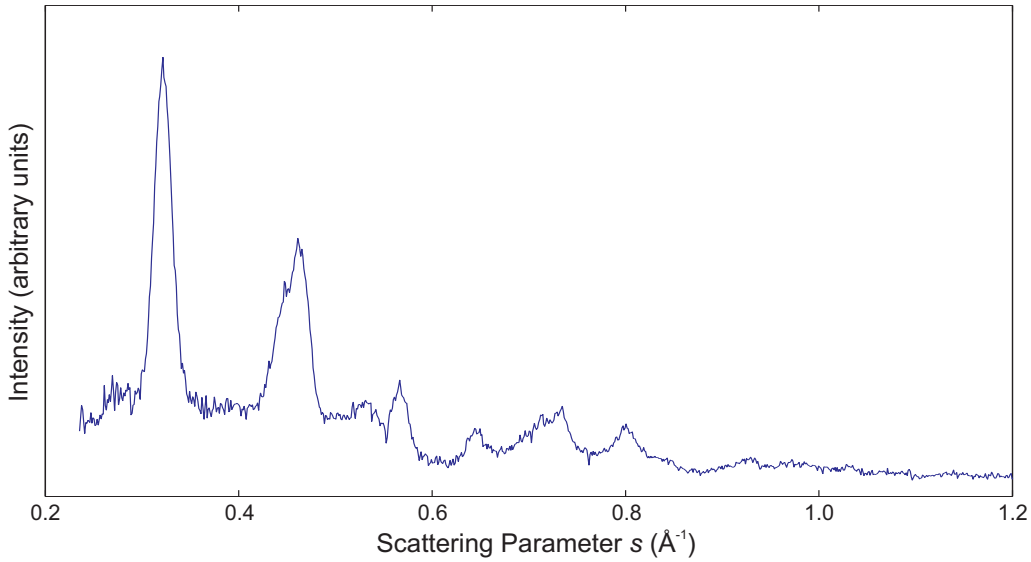

Figure 3.17: Resulting diffraction pattern after the gas background has been subtracted from the raw pattern in Figure 3.15.

The Scherrer Equation

If the cluster size decreases, the diffraction rings broaden due to the limited number of scattering centres. This phenomenon can be used to estimate the cluster size. The Scherrer equation correlates the peak width to the cluster size [6, 14, 18]:

$$L = \frac{K}{\sqrt{(\Delta s)^2 - (\Delta s_0)^2}} \tag{3.24}$$

where L is the size of the cluster, Δs the full width at half maximum (FWHM) of a chosen diffraction peak (in Å^{-1}), Δs_0 the instrumental peak broadening, and K the Scherrer factor which depends on the shape of the cluster. K is usually set to around 0.9 for cubic crystals [14] and given as being close to unity for most crystals [14, 35]. The instrumental peak broadening is explained in the next section in further detail.

It is important to note that the Scherrer equation is only an estimate and deviations from the actual cluster size are to be expected for the following reasons: Firstly, as mentioned above, the shape factor K can vary. Secondly,

the shape of the diffraction peaks has a crucial influence on the result. If the peak shape does not follow a Gaussian distribution, the equation would need adjusting. Lastly, the Scherrer equation does not account for strain or defects in the clusters, as disordered particles broaden the diffraction peaks additionally. Two further disadvantages are that the Scherrer equation does only apply to crystalline particles and that it fails completely if the clusters consist of domains. The effect of domains will be discussed towards the end of this chapter.

Instrumental Peak Broadening

In addition to the peak broadening due to the particle size, there is always an inherent instrumental broadening as a result of the finite spot size of the electron beam, the path length through the cluster beam or imperfect focussing. In theory, it is possible to correct for this effect by measuring the peak width on a calibration sample with large grains using the same conditions as for a cluster experiment. In our study, however, this procedure cannot be applied for two reasons: Firstly, the diffraction intensity of the calibrations patterns is very high compared to the cluster diffraction intensity. It is therefore necessary to use an additional aperture which reduces the electron beam spot size, thereby influencing the peak broadening. Secondly, as the calibration samples are considerably thinner than the cluster beam, this would reduce the peak broadening. Adding these two effects together, it is obvious that the peak broadening would be substantially underestimated.

Nevertheless, it is possible to estimate the instrumental peak broadening [18]. According to Reinhard [36], the electron beam used in this study has a diameter of 250 µm when crossing the cluster beam and 90 µm at the detector. The latter is the important value and leads to a peak broadening of $3.8\times10^{-3}\,\text{Å}^{-1}$ at 80 kV. The path length h through the cluster beam is approximately 1.5 mm (diameter of the third nozzle) which results in an additional broadening [18]:

$$b = h \cdot \tan(2\vartheta) \tag{3.25}$$

As this equation depends on the scattering angle ϑ, it also depends on

the scattering parameter s. The Scherrer equation is mostly applied to the first peak which is at $s \simeq 0.32\,\text{Å}^{-1}$ for Sb. For this s-value and at 80 kV the peak broadening amounts to $0.85\times10^{-3}\,\text{Å}^{-1}$. The lower and upper limit of scattering parameter values in an experimental diffraction pattern are 0.25 and $1.4\,\text{Å}^{-1}$ respectively. For these values the peak broadening is 0.68×10^{-3} and $3.75\times10^{-3}\,\text{Å}^{-1}$ respectively. Adding up the influence of the electron beam spot size and the path length through the cluster beam, the instrumental peak broadening at the position of the first Sb peak amounts to about $4.7\times10^{-3}\,\text{Å}^{-1}$ at 80 kV. For comparison: the experimental peak width is approximately $2\times10^{-2}\,\text{Å}^{-1}$ (FWHM).

Fourier Inversion

Because of the previously outlined disadvantages of the Scherrer equation, a different approach to determine the particle size from the diffraction patterns has been tested: the Fourier inversion method. As discussed in Section 3.2, the RDF of a sample can be determined from an experimental diffraction pattern by Fourier transform. Equation (3.15) shows the relationship between the diffraction pattern and the RDF. As noted before, $P(r)$ is only a good approximation of the RDF if the diffraction pattern was measured over a wide range of s-values. Unfortunately, the experimental patterns are only recorded in the range from 0.25 to $1.2\,\text{Å}^{-1}$, hence, $P(r)$ can differ considerably from the RDF.

An example of the Fourier inversion is shown in Figure 3.18. It is based on a Fourier analysis of a diffraction pattern which was previously obtained from (3.6) using the calculated structure of a spherical Sb cluster with 10 nm diameter. The diffraction pattern itself is not shown here but it corresponds to the pattern in Figure 3.8(c). In Figure 3.18(a) the original (known) histogram of interatomic distances of this structure is shown. The Fourier transform $P(r)$ was calculated using (3.15) and the result is displayed in Figure 3.18(b). Drawing the envelope of $P(r)$, the cluster size can be estimated quite accurately. In the case of an experimental pattern, this estimate is considerably less obvious as the noise introduces additional oscillations. To attenuate these oscillations, a modification function $M(s)$ can

be introduced:

$$P(r) = \beta r \int_{s_{\min}}^{s_{\max}} sM(s) \left[\frac{I(s)}{\alpha f^2(s)} - 1 \right] \sin(2\pi sr)\, \mathrm{d}s \tag{3.26}$$

This function should lessen the influence of high s-values as they are the least accurate. One of the most commonly used modification functions is the pseudo-temperature function $M(s) = e^{-a^2 s^2}$ [14]. As the pseudo-temperature function leads to a loss in resolution, the Lanczos function is preferred [15]:

$$M(s) = \frac{\sin(2\pi sb)}{2\pi sb} \quad \text{with} \quad b = \frac{1}{2s_{\max}} \tag{3.27}$$

Figure 3.18(c) shows the Fourier transform calculated with the Lanczos function as modification function. The influence of the Lanczos function on the oscillations beyond the cluster diameter is evident when comparing it to Figure 3.18(b).

To address some of the shortcomings of the standard Fourier inversion method, Wurl developed a new variant called the constrained inversion method [18]. In this method, three constraints are given for the Fourier transform: The solution $P(r)$ should be positive for all r, it should be zero below the first peak in the RDF and it should be zero for all r larger than the largest cluster in the sample volume. This new technique reduces the sensitivity to noise and increases the resolution of the resulting RDF. The disadvantage is the much longer computation time compared to the standard method. Tests done for the present study, however, seemed to indicate that the constrained method fails for noisy diffraction patterns from very large clusters. It was therefore not used for the size analysis.

Effects of Domains and Disorder

One of the crucial issues when determining the size of clusters is the existence of lattice defects which can divide a cluster in several domains. As the crystal structure is interrupted at the domain boundaries, the diffraction pattern of such a cluster resembles a diffraction pattern of a series of

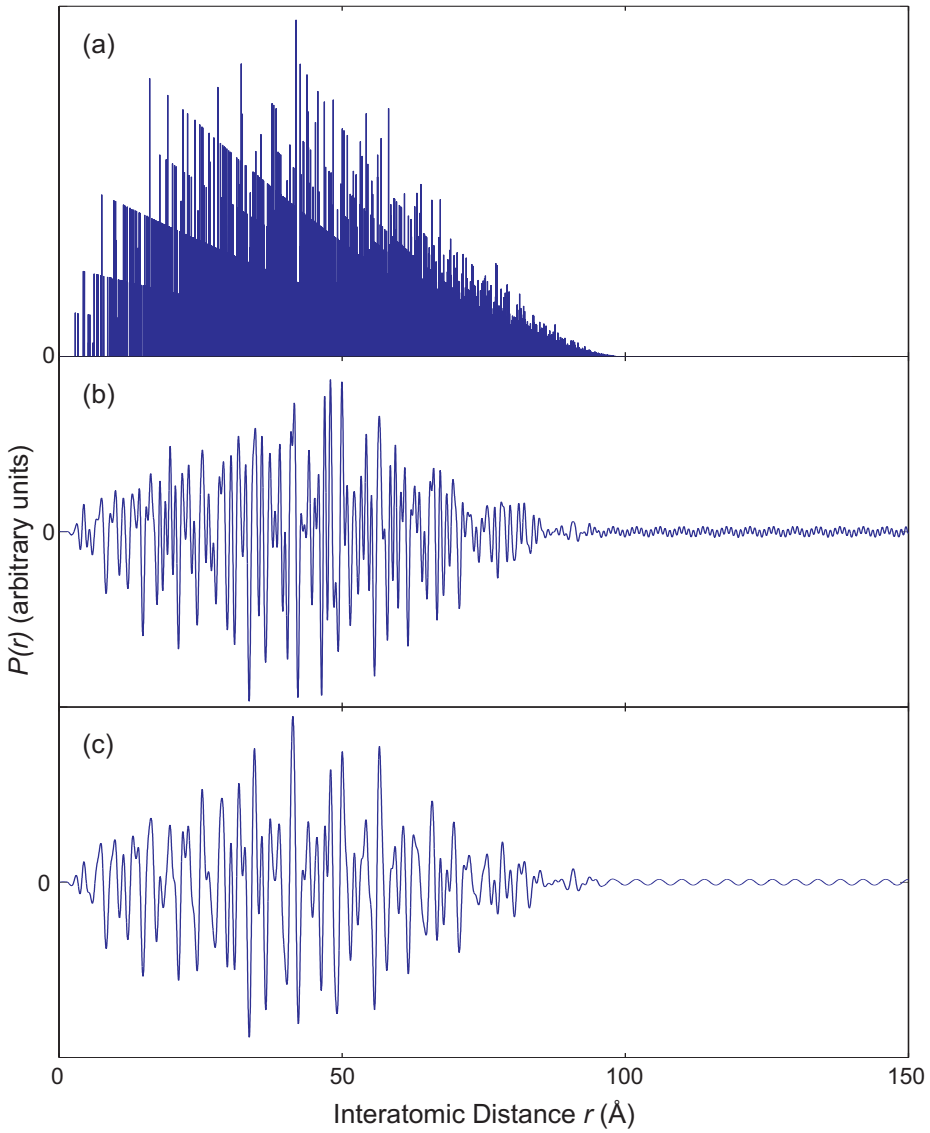

Figure 3.18: (a) Histogram of interatomic distances of an Sb cluster with 10 nm diameter. (b) The inverse Fourier transform of the calculated diffraction pattern based on (a) (without modification function). (c) The inverse Fourier transform using the Lanczos function as modification function.

smaller clusters with different orientations relative to each other [18, 37, 38]. When trying to determining the cluster size using the Scherrer equation, the result reflects the size of the individual domains rather than the true cluster size as observed by a TEM. However, the inversion process introduced in the last section is expected to be more sensitive to the whole cluster size than to the domain size [15, 39].

3.5 Conclusions

The present chapter was focussed on the diffraction theory with particular emphasis on electron scattering by crystals. Most importantly, the Debye equation was introduced to calculate diffraction patterns and it was applied to a series of structures like rhombohedral crystals, liquid and amorphous materials.

The second part of the chapter explained the analysis of the experimental diffraction patterns, starting with the data preparation procedure and ending with a discussion about different techniques to determine the particle size from diffraction patterns.

References

[1] L. S. Bartell, Chem. Rev. **86**, 491 (1986).

[2] A. Guinier, *X-Ray Diffraction in Crystals, Imperfect Crystals, and Amorphous Bodies*, W. H. Freeman and Company, 1963.

[3] N. W. Ashcroft and N. D. Mermin, *Solid State Physics*, Saunders College Publishing, 1976.

[4] D. Rez, P. Rez, and I. Grant, Acta Crystallogr. A **50**, 481 (1994).

[5] B. Fultz and H. James, *Transmission Electron Microscopy and Diffractometry of Materials*, Springer-Verlag, 2001.

[6] T. B. Rymer, *Electron Diffraction*, Methuen & Co Ltd, 1970.

[7] L. S. Bartell, J. Chem. Phys. **63**, 3750 (1975).

[8] L. S. Bartell, B. Raoult, and G. Torchet, J. Chem. Phys. **66**, 5387 (1977).

[9] B. R. Miller and L. S. Bartell, J. Chem. Phys. **72**, 800 (1980).

[10] P. A. Stadelmann, Ultramicroscopy **21**, 131 (1987).

[11] B. D. Hall, D. Ugarte, D. Reinhard, and R. Monot, J. Chem. Phys. **103**, 2384 (1995).

[12] R. Zallen, *The physics of amorphous solids*, Wiley Classics Library, John Wiley & Sons, 1998.

[13] S. R. Elliott, *Physics of Amorphous Materials*, Longman Scientific & Technical, 1989.

[14] B. E. Warren, *X-Ray Diffraction*, Dover Publications, 1990.

[15] B. D. Hall, D. Zanchet, and D. Ugarte, J. Appl. Crystallogr. **33**, 1335 (2000).

[16] G. N. Greaves, S. R. Elliott, and E. A. Davis, Adv. Phys. **28**, 49 (1979).

[17] B. D. Hall, *An Installation for the Study of Unsupported Ultrafine Particles by Electron Diffraction with Application to Silver: Observation of Multiply Twinned Particle Structures*, PhD thesis, Ecole Polytechnique Fédérale de Lausanne, 1991.

[18] A. Wurl, *Electron Diffraction Studies of Unsupported Bismuth Clusters*, PhD thesis, University of Canterbury, 2003.

[19] P. Bayliss, L. G. Berry, M. E. Mrose, and D. K. Smith, editors, *Mineral Powder Diffraction File*, JCPDS, 1980.

[20] E. A. Wood, *Crystal orientation manual*, page 75, Comlumbia University Press, 1963.

[21] R. W. G. Wyckoff, *Crystal structures*, Interscience Publishers, 1963.

[22] T. Okazaki, J. Jpn. Assoc. Cryst. Growth **9**, 175 (1982), in Japanese.

[23] B. Reddy and P. Jena, Chem. Phys. Lett. **288**, 253 (1998).

[24] J. Donohue, *The Structures of the Elements*, John Wiley & Sons, 1974.

[25] K. Sattler, J. Mühlbach, P. Pfau, and R. Recknagel, Phys. Lett. **87A**, 418 (1982).

[26] V. Kumar, Phys. Rev. B **48**, 8470 (1993).

[27] X.-W. Zou, Z.-Z. Jin, and Y.-J. Shang, Phys. Status. Solidi. B **139**, 365 (1987).

[28] X.-W. Zou, Z.-Z. Jin, and Y.-J. Shang, Phys. Status. Solidi. B **142**, 9 (1987).

[29] N. W. Ashcroft and J. Lekner, Phys. Rev. **145**, 83 (1966).

[30] Y. Waseda, *The structure on non-crystalline materials*, McGraw-Hill, 1980.

[31] J. A. Prins, Nature **131**, 760 (1933).

[32] H. Hendus, Z. Phys. **119**, 265 (1942).

[33] H. Richter, H. Berckhemer, and G. Breitling, Z. Naturforsch. A **9**, 236 (1954).

[34] H. Krebs and R. Steffen, Z. Anorg. Allg. Chem. **327**, 224 (1964).

[35] C. Hammond, *The Basics of Crystallography and Diffraction*, Oxford University Press, 1997.

[36] D. Reinhard, *Croissance et Stabilité d'Agrégats d'Argent et de Cuivre, Etudiés en Jets Moléculaires par Diffraction d'Electrons à Haute Energie*, PhD thesis, Ecole Polytechnique Fédérale de Lausanne, 1996.

[37] B. D. Hall, J. Appl. Phys. **87**, 1666 (2000).

[38] M. Hyslop, *Electron Diffraction Studies of Unsupported Clusters*, PhD thesis, University of Canterbury, 2002.

[39] D. Zanchet, B. D. Hall, and D. Ugarte, J. Phys. Chem. B **104**, 11013 (2000).

Chapter 4

A Study of Antimony Clusters

This chapter presents the results and analysis from an electron diffraction study on antimony (Sb) clusters. The presentation of the results is divided into three parts according to the type of cooling gas used for the experiment: for the first part, Ar was used, for the second He and for the third a mixture of the two gases. This is followed by the analysis and discussion of the diffraction results. The last section of this chapter describes the microscopy studies on deposited Sb clusters: this section presents the different morphologies of supported Sb clusters and the results of the cluster size analysis. These size averages are then compared to the results from the diffraction patterns.

4.1 Results of the Diffraction Experiments

The results are divided into three groups: for the first group, only Ar was used as cooling gas, for the second only He, and for the third a mixture of Ar and He. The diffraction patterns displayed in the following sections are representative for the conditions observed during the experiment unless otherwise noted. All the diffraction patterns collected in one figure were recorded during one experimental run. The individual patterns are prepared from the raw data as described in Section 3.4.1. All patterns are

scaled to have the same intensity of the highest peak (but note that deposition rate figures given in Table 4.4 allow an estimate of relative intensities). The detailed source conditions, together with the results from the size analysis, are shown in Table 4.4 at the end of the chapter.

During an experimental run, three main parameters can be adjusted: The temperature of the crucible T_C, the type of cooling gas (Ar or He), and the source inlet gas flow rate (and thereby the inert-gas pressure in the source P_G which increases with increasing flow rate). Together with the geometry of the nozzles (see Section 2.1.2), these parameters influence the nucleation conditions and thus the cluster properties.

During some of the diffraction experiments, clusters were deposited on SiO_2 or SiN substrates or on TEM grids to obtain information about the size distribution of the clusters in the beam and the morphology of the resulting cluster films. The size analysis procedure is described in Section 2.5. This procedure only works if the cluster density on the samples is low. If the clusters are overlapping, they have to be analysed manually. The size information gained from microscopy studies will be compared to the results from the Scherrer equation (see Section 3.4.2).

4.1.1 Experiments using Ar as Cooling Gas

During the diffraction experiments in which Ar was used as the source cooling gas, cluster production was controlled using two parameters: the crucible temperature T_C and the gas flow rate. The temperature range used for these experiments was 600°C to 825°C and the range of Ar flow rates was 50 to 200 sccm. The resulting source pressure ranged from 2 to 10 mbar.

Increasing Gas Flow Rate

For the first part of this study, the source temperature was left constant for a whole run while the gas flow rate was increased. The three resulting series of diffraction patterns are shown in Figure 4.1, 4.2, and 4.3. The diameter of the first nozzle was 2.5 mm for the first and last run and 3.5 mm for the run

in-between. Between the runs, the temperature was increased from 625°C to 650°C and finally to 675°C.

The general features are similar in all three runs: at Ar flow rates up to approximately 100 sccm two broad peaks are observed at $s \simeq 0.33\,\text{Å}^{-1}$ and at $s \simeq 0.52\,\text{Å}^{-1}$. These peak positions do not match the crystalline diffraction patterns shown in Section 3.3.1 and the general shape resembles diffraction patterns from amorphous solids or liquids. Increasing the gas flow rate leads to a split in the second peak, while the first peak gets narrower. This can be best seen in Figure 4.3(c). At the same time, the deposition rate R_{dep} generally drops significantly which results in patterns with more noise. When the flow rate is further increased, the peaks become narrower again and new peaks appear at higher s-values, while the deposition rate increases again but not to the same level as before (except for Figure 4.2). The resulting patterns are consistent with the calculated

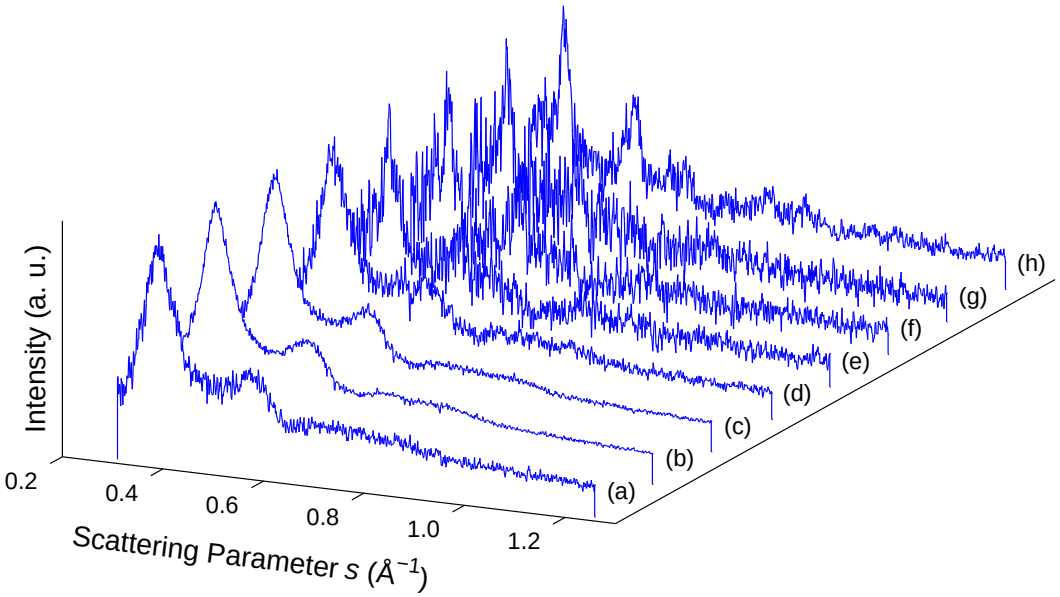

Figure 4.1: Diffraction patterns of Sb clusters using Ar as cooling gas and increasing the gas flow rate from (a) 58 sccm to (h) 170 sccm. The temperature is left constant at 625°C. Refer to Table 4.4 for details. (Note: the increase in noise in pattern (e) to (h) is due to the low deposition rate in these experiments.)

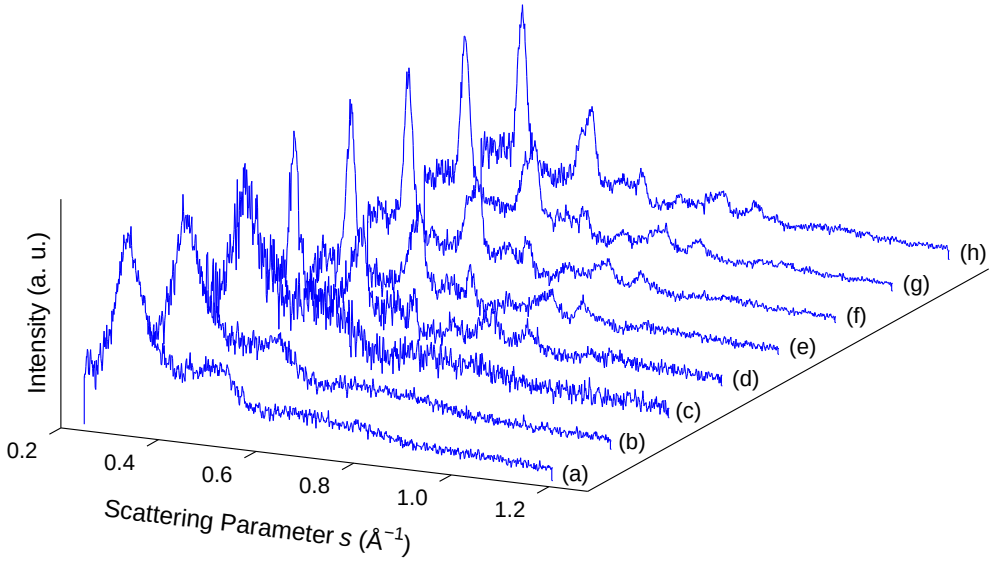

Figure 4.2: Diffraction patterns of Sb clusters using Ar as cooling gas and increasing the gas flow rate from (a) 90 sccm to (h) 180 sccm. The temperature is left constant at 650°C. Refer to Table 4.4 for details.

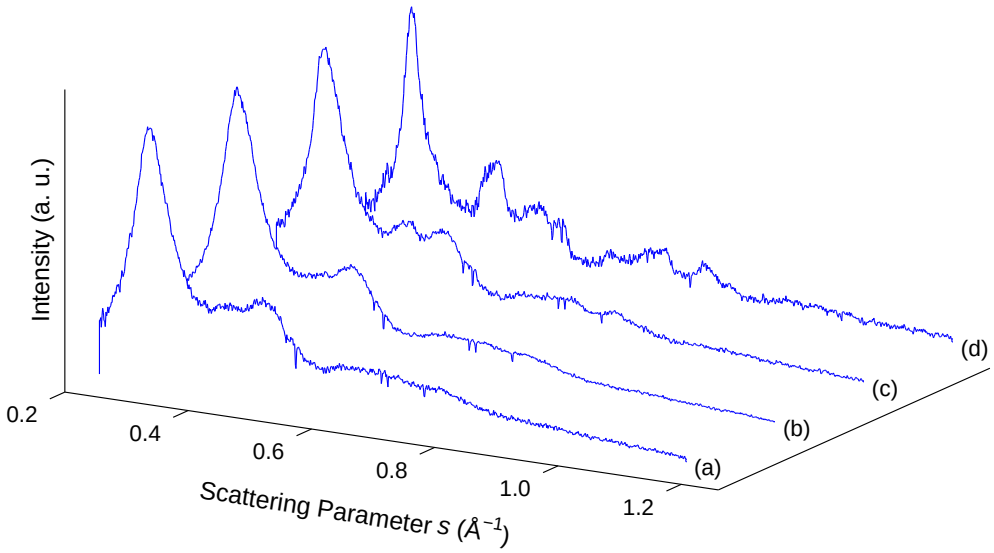

Figure 4.3: Diffraction patterns of Sb clusters using Ar as cooling gas and increasing the gas flow rate from (a) 82 sccm to (d) 122 sccm. The temperature is left constant at 675°C. Refer to Table 4.4 for details.

diffraction patterns for clusters with the symmetry of bulk rhombohedral Sb shown in Section 3.3.1. Further increasing the gas flow rate, does not change the peak shapes noticeably (see Figure 4.2).

If the gas flow rate is decreased below 50 sccm, the deposition rate usually drops below 5 Ås^{-1} which leads to very weak and noisy diffraction patterns. The upper limit of the gas flow rate is defined by the maximum load on the turbo pumps. Depending on the nozzle diameter, the Ar gas flow rate can usually not be increased beyond 150–200 sccm.

Increasing Source Temperature

In a second set of experiments, the Ar gas flow rate was left constant while the source temperature was increased. The results from these runs are shown in Figure 4.4 and 4.5. The first run presents an overview over a wide temperature range while the second one focusses on a smaller range of temperatures. For the first run, the gas flow rate was left at 82 sccm while the temperature was increased in steps of 50 K from 675°C to 825°C. The gas flow rate in the second run remained at 80 sccm and the temperature was increased in steps of 25 K from 675°C to 775°C. For both runs, the diameter of the first nozzle was 2.5 mm.

Increasing the source temperature leads to a similar result as increasing the gas flow rate: at temperatures below 700°C there are two broad peaks as shown in Figure 4.4(a). Increasing the temperature leads to the appearance of new and narrower peaks (see Figure 4.4(d)). The resulting diffraction patterns are again consistent with patterns from the bulk rhombohedral structure. It should be noted that this change from a liquid or amorphous structure to the crystalline structure depends on the choice of a suitable gas flow rate. If the gas flow rate is higher to start with, the diffraction patterns at low temperature would be crystalline already as in the previous section.

The crystalline patterns in Figure 4.5 do not show any obvious changes in shape with increasing temperature. The background of the patterns, however, is increased for higher temperatures. This is particularly evident in Figure 4.5(e) at high s-values where the intensity is still significantly above the baseline. This behaviour can also be observed in Figure 4.4(d).

The deposition rates in the first run were considerably higher than in

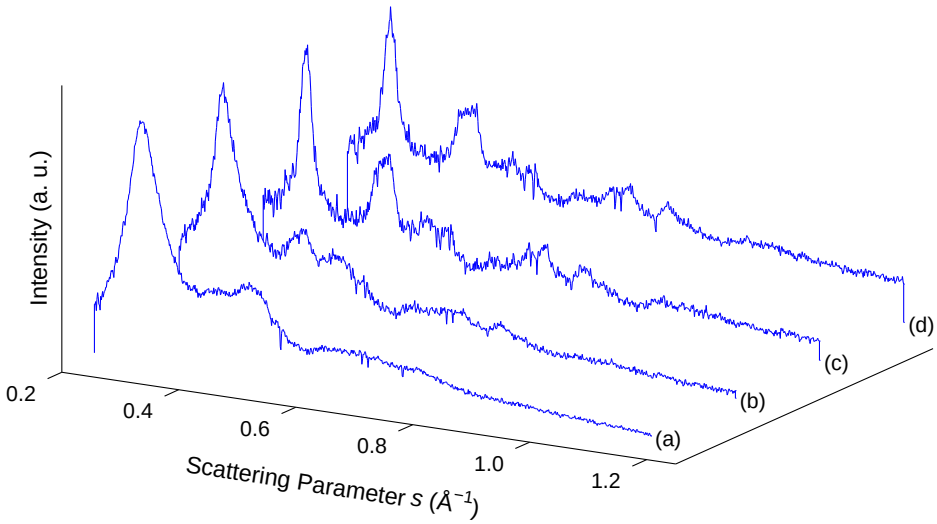

Figure 4.4: Diffraction patterns of Sb clusters using Ar as cooling gas and increasing the temperature in steps of 50 K from (a) 675°C to (d) 825°C. The gas flow rate is left constant at 82 sccm. Refer to Table 4.4 for details.

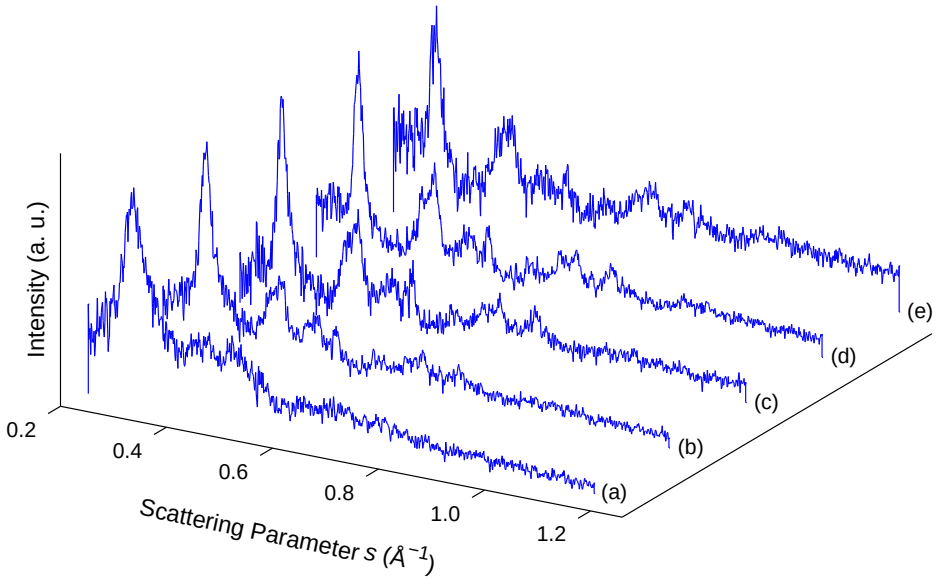

Figure 4.5: Diffraction patterns of Sb clusters using Ar as cooling gas and increasing the temperature in steps of 25 K from (a) 675°C to (e) 775°C. The gas flow rate is left constant at 80 sccm. Refer to Table 4.4 for details.

the second run as can be seen from the low noise patterns in Figure 4.4. It is therefore important to note that the same source conditions would not necessarily lead to a diffraction pattern of the same intensity. The overall evolution of the patterns, however, was always reproducible.

It was not possible to record diffraction patterns below 625°C because of low deposition rates (the pattern at this temperature is very similar to the one shown in Figure 4.4(a)). It would have been possible to increase to temperature beyond 825°C. However, even at 825°C the material in the source evaporates at a very high rate leading to transient source conditions.

4.1.2 Experiments using He as Cooling Gas

The second set of experiments was carried out using He as the source cooling gas. The range of source temperatures used for these measurements was between 650°C and 750°C. The gas flow rates, however, had to be significantly greater than for Ar in order to reach sufficiently high cluster beam intensities (see below for a detailed discussion of the deposition rates achieved). A suitable range was found between 300 and 1500 sccm. The reason for this behaviour lies in the fact that He is lighter than Ar and is therefore less efficient in cooling the hot metal vapour. This is due to the fact that the energy exchanged during collisions between inert gas and metal atoms is higher for inert gas atoms with a higher molecular weight [1]. Due to the higher gas flow rates, the resulting source pressure range was significantly higher with values between 5 and 25 mbar. As in the case of Ar, the source temperature is left constant while the gas flow rate is increased and its effect on the diffraction patterns observed. However, there are no patterns with constant gas flow rate and increasing temperature. Over the narrow temperature range where it was possible to record patterns there was no evolution observed. Below 650°C – in fact even below 700°C – the diffraction intensity was very weak. Above 750°C, the source conditions became unstable - possibly due to the high gas flow rates. Even at 700°C, the high gas flow rates frequently caused blocking of one of the nozzles. This is also the reason why there is hardly any size distribution data from cluster deposition (see below).

Increasing Gas Flow Rate

In this part, two different runs are presented to show the influence of an increasing He gas flow on the diffraction patterns. For the patterns in Figure 4.6, the source temperature was kept at 700°C and the gas flow rate increased from 500 to 1454 sccm. The run shown in Figure 4.7 was recorded at 750°C with a gas flow rate between 570 and 1454 sccm. In both cases, the diameter of the first nozzles was 3.5 mm. Note that the patterns in this figure are sorted by decreasing instead of increasing flow rate. This was done for all remaining figures in this section to improve readability of the individual patterns.

The evolution in both runs follows a similar trend: at a He flow rate below approximately 800 sccm the diffraction patterns in Figure 4.6(e–g) show a broad main peak at $s \simeq 0.40\,\text{Å}^{-1}$ and a weaker broad peak at $s \simeq 0.75\,\text{Å}^{-1}$. These patterns again resemble diffraction patterns from amorphous solids or liquids as in the last section, however, the main peak is

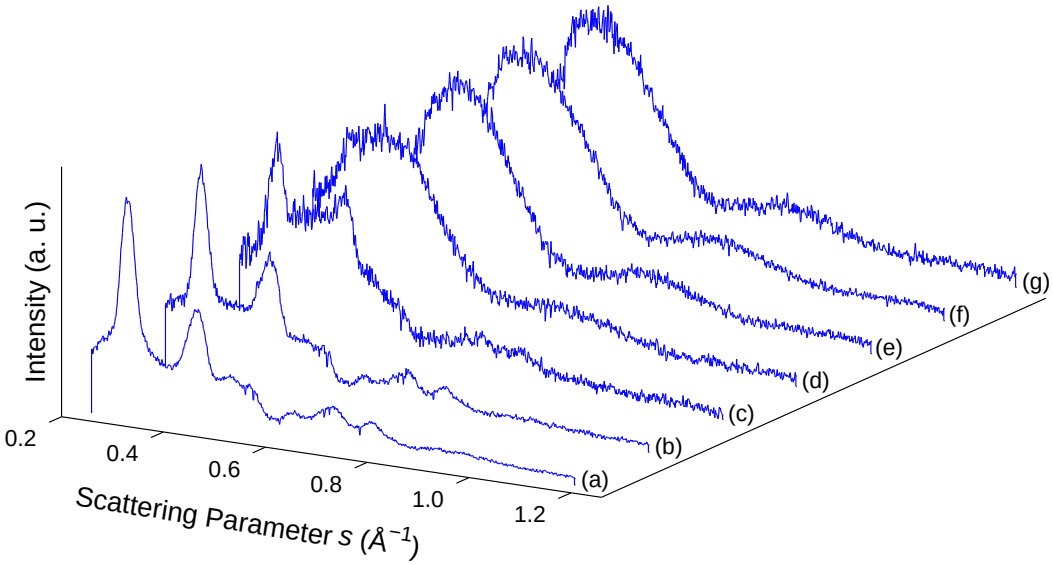

Figure 4.6: Diffraction patterns of Sb clusters using He as cooling gas and decreasing the gas flow rate from (a) 1454 sccm to (g) 500 sccm. The temperature is left constant at 700°C. Refer to Table 4.4 for details.

clearly broader and at a higher *s*-value than the main peak in Figure 4.3(a). Increasing the He flow rate leads to a split in the first peak as shown in Figure 4.6(c). When the flow rate is further increased, peaks are observed which are consistent with rhombohedral clusters (Figure 4.6(a)). The intermediate pattern in Figure 4.6(c) is clearly due to a mixture of the amorphous structure observed at low flow rates and the crystalline structure at high flow rates.

If the temperature is increased to 750°C, the same evolution can be observed as can be seen in Figure 4.7, however, the change from an amorphous to a crystalline structure occurs at a higher gas flow rate. Additionally, the resulting crystalline pattern in Figure 4.7(a) has narrower peaks than the one in Figure 4.6(a) which is due to large cluster sizes in the beam.

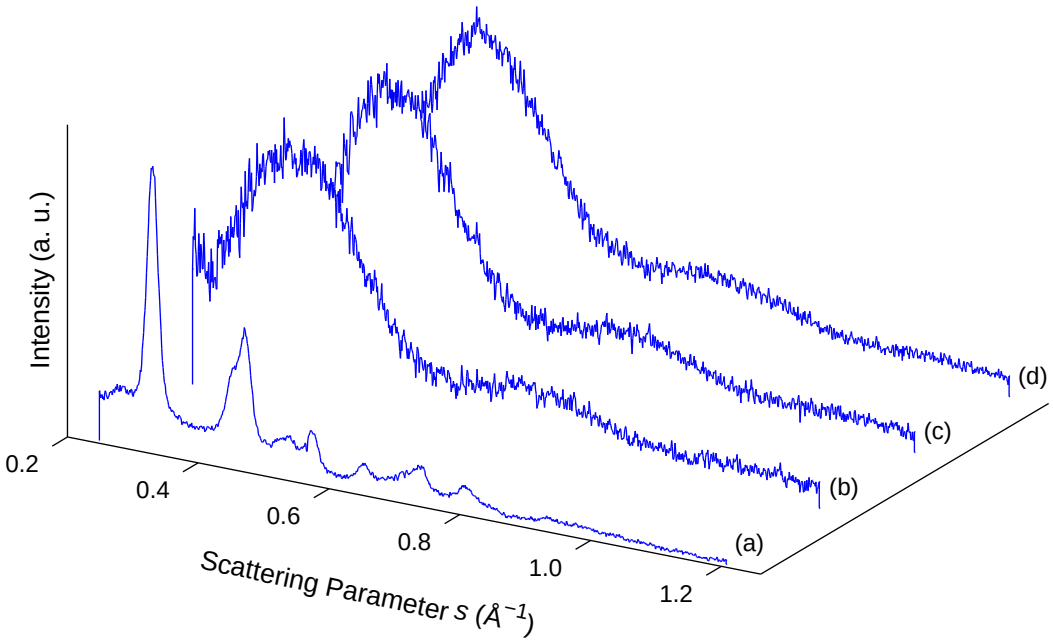

Figure 4.7: Diffraction patterns of Sb clusters using He as cooling gas and decreasing the gas flow rate from (a) 1454 sccm to (d) 570 sccm. The temperature is left constant at 750°C. Refer to Table 4.4 for details.

This is particularly evident in the second peak which starts to split in Figure 4.7(a) but not in Figure 4.6(a).

The deposition rates for low He gas flow rates are very low, typically well below 5 Ås^{-1}. As soon as the patterns change into crystalline ones, the deposition rates increase, sometimes to values beyond 100 Ås^{-1}. However, the crystalline pattern in Figure 4.6(a) was recorded with an apparent deposition rate of only 4 Ås^{-1}, although the signal-to-noise ratio seems to be very high – comparable to the pattern in Figure 4.7(a) where the deposition rate was given as 90 Ås^{-1}. There is no obvious explanation for this phenomenon, except perhaps a faulty deposition rate monitor or a misalignment of the cluster beam.

As discussed above, the lower limit of the He gas flow rates at around 500 sccm was determined by the required deposition rate to record a pattern with sufficient intensity. The upper limit of 1454 sccm is the limit of the flow controller used in these experiments. As the source conditions become very unstable at such a high gas flow rate, there is no need to achieve higher flow rates.

4.1.3 Experiments using a He/Ar Mixture as Cooling Gas

In the third and final set of experiments a mixture of He and Ar was used as source cooling gas. The total gas flow rate was left constant and only the relative contributions of He and Ar adjusted. As discussed in the last section, for a pure He gas flow the flow rate has to be at least 500 sccm to achieve a sufficiently high diffraction intensity. Starting with this value, the Ar content could be increased to approximately 20% before the limit of the second-stage turbo pump was reached. The resulting source pressures were in the range of 5 to 20 mbar. As in the last section, the temperature range for these experiments was 650°C to 700°C.

In this section, three different runs are presented showing the influence of changing the He/Ar mixture on the diffraction patterns. The first run is shown in Figure 4.8 and was recorded at a source temperature of 700°C and a total gas flow rate of 550 sccm. For the second run – displayed in Figure 4.9 – the same temperature was used but the total gas flow rate was increased slightly to 600 sccm. While the first run presents an overview of

the observed changes, for the second run the Ar contribution was increased in smaller steps to study the observed transition in more detail. Figure 4.10 shows the third run which was recorded under rather different conditions, namely a source temperature of 750°C and a total flow rate of 800 sccm. Between 0% and 10% Ar content, no additional patterns were recorded for all runs. Beyond 10%, the Ar content was increased in 5% steps in the first and third run and in 2% steps in the second run. The diameter of the first nozzle was 3.5 mm for all runs.

For all three runs, the effect of an increase in Ar content leads to similar characteristics in the diffraction patterns. If no Ar is added to the He flow, the patterns are equivalent to the patterns shown in Figure 4.6(e)–(g) and 4.7(d) in the last section. Adding up to 10% of Ar does not lead to

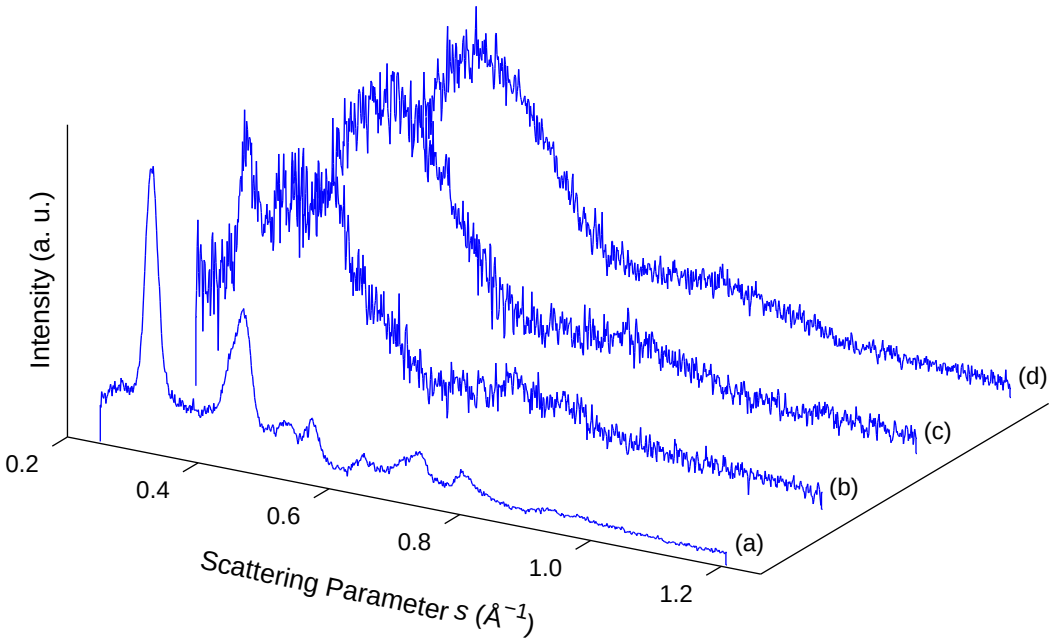

Figure 4.8: Diffraction patterns of Sb clusters using a He/Ar mixture as cooling gas. The total gas flow is left constant at 550 sccm and the relative Ar content is decreased from (a) 20% to (d) 0%. The source temperature is set to 700°C. Refer to Table 4.4 for details.

any visible changes in the shape of the patterns for the first two runs as seen in Figure 4.8(c) and (d) as well as 4.9(f) and (g). Due to the higher total flow rate in the third run, already at 10% there is a mixture of the aforementioned amorphous structure and the crystalline structure of bulk Sb observable (Figure 4.10(c)). This change only occurs for an Ar content of around 15% in the first and second run. If the Ar content is further increased towards 20%, only the crystalline pattern is visible (Figure 4.8(a), 4.9(a), and 4.10(a)). These crystalline patterns are very similar in the first two runs. In the third run, however, an equivalent crystalline pattern is already observed at 15% Ar content and the pattern shown for 20% has distinctly narrower peaks. This is most evident in the splitting of the second peak at $s \simeq 0.45\,\text{Å}^{-1}$. Narrower diffraction peaks indicate the presence of larger particles in the cluster beam.

The observed cluster beam intensities were similar to the ones in the

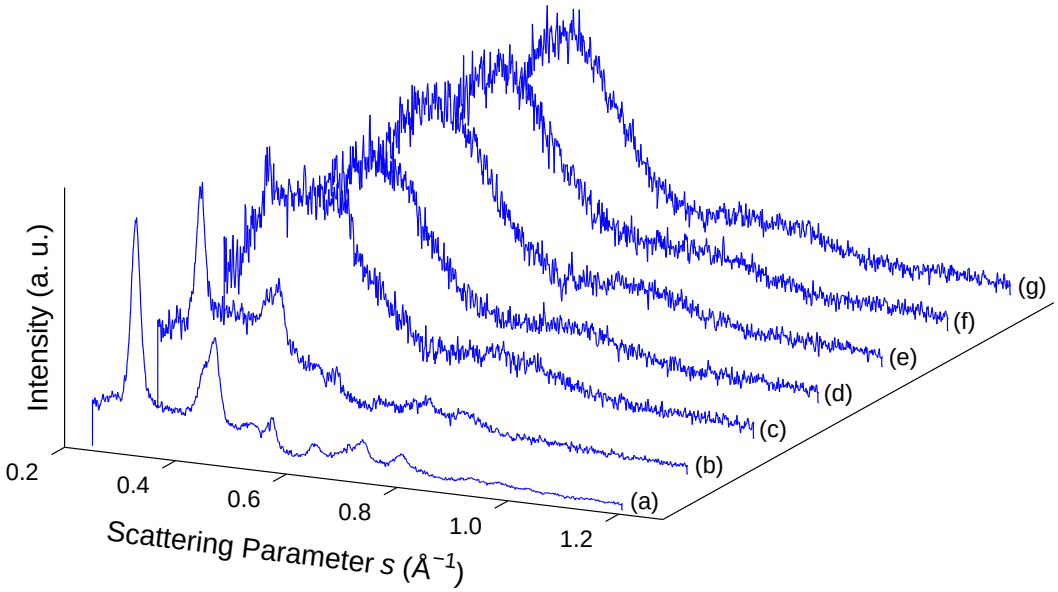

Figure 4.9: Diffraction patterns of Sb clusters using a He/Ar mixture as cooling gas. The total gas flow is left constant at 600 sccm and the relative Ar content is decreased from (a) 20% to (g) 0%. The source temperature is set to 700°C. Refer to Table 4.4 for details.

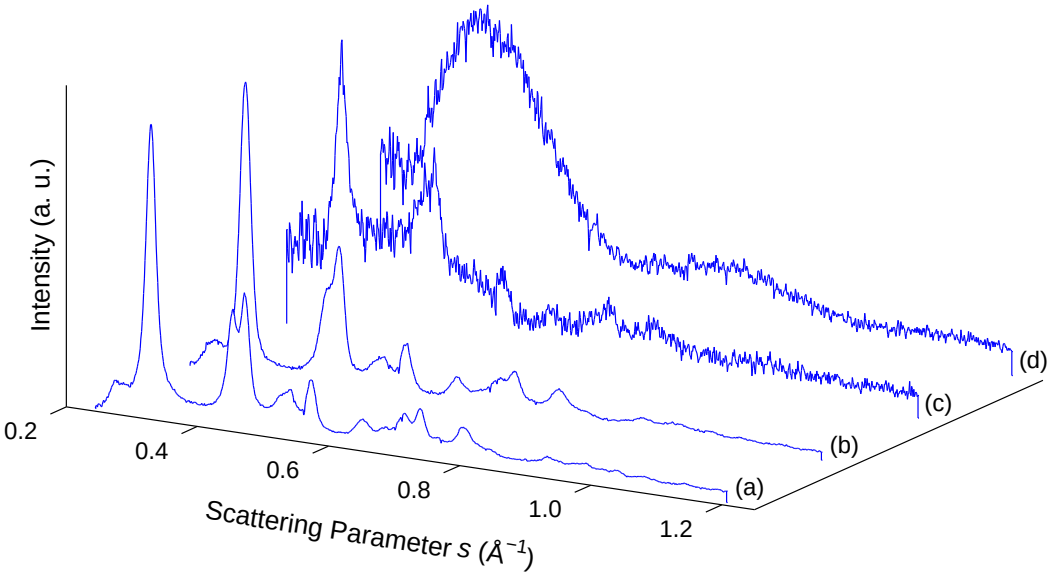

Figure 4.10: Diffraction patterns of Sb clusters using a He/Ar mixture as cooling gas. The total gas flow is left constant at 800 sccm and the relative Ar content is decreased from (a) 20% to (d) 0%. The source temperature is set to 750°C. Refer to Table 4.4 for details.

last section: For the first two runs, deposition rates well below 5 Ås^{-1} were measured for low Ar content. The mixed and crystalline patterns were recorded with higher rates of up to 70 Ås^{-1}. For the third run, the deposition rates were higher throughout: rising from 3.6 Ås^{-1} for 0% up to 170 Ås^{-1} for 20% Ar content.

4.1.4 General Observations about the Diffraction Intensity

When comparing the results of the present study to results of previous studies on the experimental equipment [2, 3], it is evident that the signal-to-noise ratio of the diffraction patterns presented here is – apart from some exceptions – considerably lower than in the previous studies. In the following, two different aspects are discussed: the first issue is the difference in observed deposition rates between the previous study on Bi

and the present one. The second issue regards the expected difference in scattering intensity between Bi and Sb.

In the diffraction study on Bi clusters [3], deposition rates of well over $100\,\text{Å s}^{-1}$ were observed regularly, whereas in the present study, the rates were mostly in the range between 5 and $50\,\text{Å s}^{-1}$ and only very rarely over $100\,\text{Å s}^{-1}$. A possible explanation of this discrepancy is given in Section 2.1: according to the homogeneous nucleation theory, a higher nucleation rate over a wider range of source temperatures is expected for Bi compared to Sb. It is therefore expected to be easier to achieve high deposition rates over a wider range of source parameters for Bi than for Sb. It has to be noted, however, that the relationship between the measured deposition rate and the recorded diffraction intensity on the detector is not as straightforward as expected. An extreme example has been mentioned in Section 4.1.2: the crystalline patterns in both figures in this section were recorded with diffraction intensities within 10% of each other, while the deposition rates varied between 4 and $90\,\text{Å s}^{-1}$.

If it is assumed for the moment that there is a direct and reproducible relationship between the measured deposition rate and the diffraction intensity, there is still an inherent difference in scattering intensity to be expected between Bi and Sb. This is due to the scattering cross section being related to the atomic weight of the sample. The relationship between the cross section σ and the atomic number Z is given as $\sigma \sim Z^2$ [4]. This would mean that the scattering intensity for Bi is approximately 2.6 times higher than the intensity for Sb.

Combining these two issues helps to understand why it is harder to achieve diffraction patterns with a high signal-to-noise ratio for Sb than it is for Bi [3] or Pb [2].

4.2 Analysis of the Diffraction Experiments

The analysis of the diffraction patterns is split up into three sections: in the first section, the diffraction patterns from crystalline clusters are analysed, followed by two sections about the two different types of non-crystalline structures observed during the experiments. The first type was found to

correspond to the structure of amorphous Sb. The second type was identified to be equivalent to Sb_4. In each of these three parts, the experimental diffraction patterns are compared to calculated patterns presented in Section 3.3.1. At the end of this section, there is an additional part investigating the background which is present in many diffraction patterns.

4.2.1 Crystalline Patterns

All the diffraction patterns from crystalline particles presented in the last section are very similar in appearance. The peak positions in all patterns are in good agreement with the calculated patterns for particles with the rhombohedral structure of bulk Sb presented in Section 3.3.1. Figure 4.11 shows the experimental pattern from Figure 4.10 together with the calculated pattern from Figure 3.9(b). The shape of the latter is not spherical but faceted by six {011} and two {111} planes. As discussed in Section 3.3.1, the shape of the cluster does not influence the peak positions in the diffraction pattern, only the relative peak intensities. The relative peak intensities are best studied using the second and third peaks between $s \simeq 0.4$ and $0.5\,\text{Å}^{-1}$. As demonstrated in Section 3.3.1, a spherical cluster shape leads to about the same peak intensity for these two peaks. However, the second of the two peaks is consistently higher in all experimental diffraction patterns. The relative intensity is matched by the calculated pattern from the particle with the shape mentioned above. While this shape is not the only shape which gives rise to the peak intensity distribution observed in the experiments, it has to be considered as a possible shape. If the second and third diffraction peak are not separated at all, it is impossible to determine the cluster shape accurately. Additionally, it has to be kept in mind that the diffraction patterns represent the whole cluster ensemble which is likely to contain a wide range of different shapes.

Figure 4.12 presents a selection of the crystalline diffraction patterns observed in this study. The vertical grey lines indicate the positions of the stronger peaks for the rhombohedral structure of bulk Sb [5]. It is evident that all patterns are in good agreement with these values. The most obvious difference between all the patterns – apart from the signal-to-noise ratio – is the difference in peak widths. As discussed in Section 3.4.2, the peak width

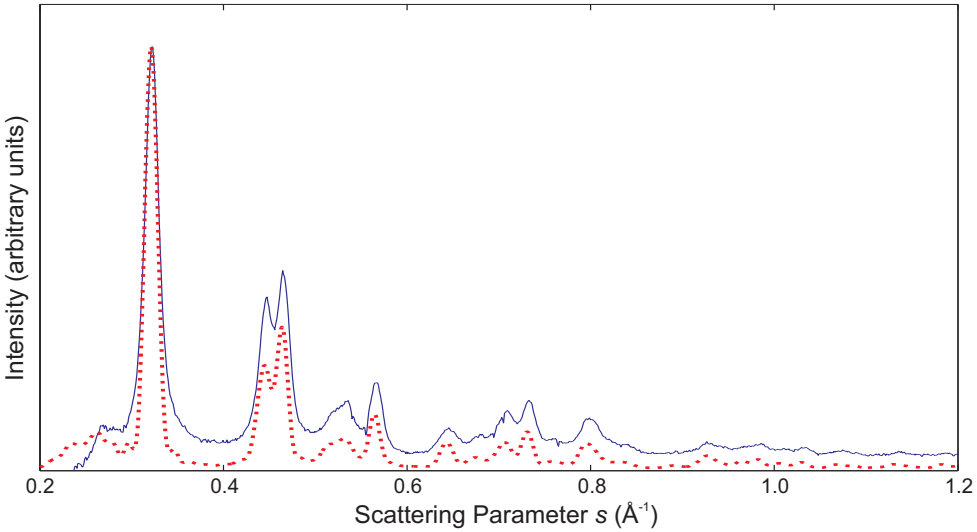

Figure 4.11: Comparison of experimental and calculated patterns from crystalline clusters. The calculated pattern (dotted line) is based on a rhombohedral Sb cluster with six {011} and two {111} planes cut out and a diameter of 9.5 nm (see Figure 3.9). The experimental pattern corresponds to the pattern in Figure 4.10(a).

can be correlated to the average particle size using the Scherrer equation. The results from the analysis of the Scherrer equation will be presented in a separate section together with the results from microscopy studies towards the end of this chapter.

Apart from cluster shape and size, it is also possible to draw conclusions from the diffraction patterns about the structure of the particles. In previous studies on Pb [2], Cu [6] and Ag [6, 7] clusters, calculated patterns of model structures have been fitted to the experimental patterns to determine the exact structure of the particles. This approach could not be followed in the present study for various reasons: First of all, the lack of tested potentials for Sb makes it impossible to use molecular dynamics simulations to create realistic models for Sb clusters. Secondly, there are also no geometric models for Sb available which include defects. Additionally, it is expected that the use of the kinematic diffraction theory introduces errors for large clusters. It would therefore be necessary to develop the means to calculate diffraction patterns based on the dynamic theory to be able to fit realistic

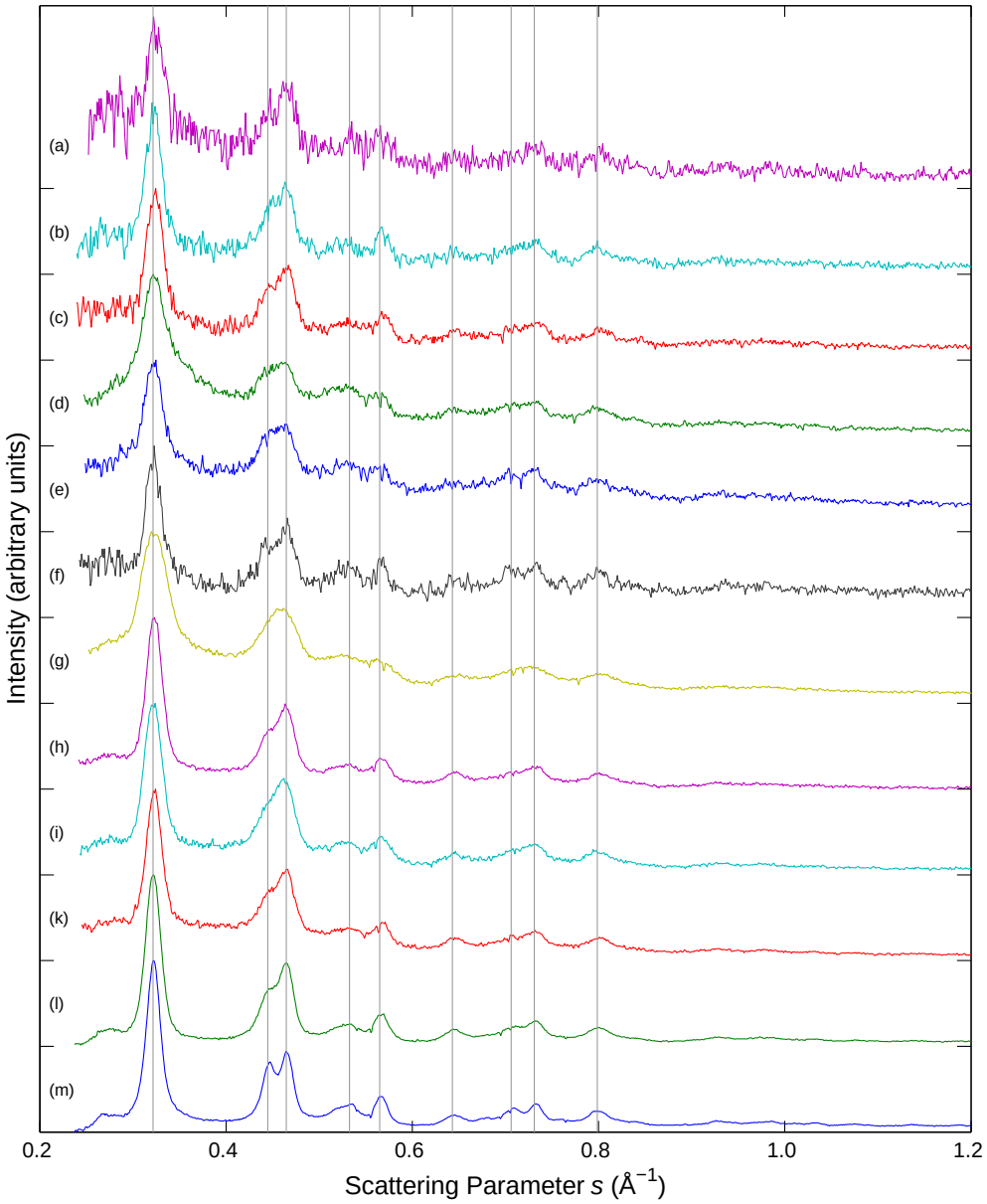

Figure 4.12: Overview of experimental crystalline diffraction patterns. The patterns correspond to the patterns in (a) Figure 4.1(h), (b) Figure 4.2(e), (c) Figure 4.2(h), (d) Figure 4.3(d), (e) Figure 4.4(c), (f) Figure 4.5(d), (g) Figure 4.6(a), (h) Figure 4.7(a), (i) Figure 4.8(a), (k) Figure 4.9(a), (l) Figure 4.10(b), (m) Figure 4.10(a). The vertical grey lines indicate the positions of the strongest peaks for rhombohedral bulk Sb [5].

models to the experimental data. Lastly, the low signal-to-noise ratio of the diffraction patterns in this study would lead to fits of questionable quality. Even without fitting of model structures it is still possible to gain an insight into the structure of the clusters observed in this study.

Determination of Lattice Parameters

For diffraction patterns from crystalline clusters it is interesting to see whether the lattice parameters deviate from the bulk values. Once the peak positions are known and indexed with the Miller indices (see Figure 3.7), the lattice parameters, i.e. lattice constant a and angle α, can be calculated [8]:

$$s^2 = \frac{1}{a^2}\left(\frac{(1+\cos\alpha)[(h^2+k^2+l^2)-(1-\tan^2(\frac{\alpha}{2}))(hk+kl+lh)]}{1+\cos\alpha-2\cos^2\alpha}\right) \quad (4.1)$$

where s is the scattering parameter of one particular peak and h, k and l its Miller indices. Note that this equation is only valid for a rhombohedral structure.

To solve (4.1) at least two peak positions have to be determined as accurately as possible. The main peak (Miller indices (110)) was used as the first peak for all the analysed patterns. The obvious choice for the second peak was the peak at $s \simeq 0.45\,\text{Å}^{-1}$. However, as described above, this peak consists of two individual peaks which are merged in most experimental patterns: the (112) and the $(1\bar{1}0)$ peak. Since the $(1\bar{1}0)$ peak is stronger in all patterns, it was chosen for this analysis but the determination of the peak position is less accurate than for the main peak because of the influence of the additional peak. As an alternative second peak, the (200) peak at $s \simeq 0.55\,\text{Å}^{-1}$ was chosen which is not influenced by other peaks and is clearly visible in most patterns. The results for all the crystalline patterns shown in Figure 4.12 are displayed in Table 4.1. Where there are no values given for certain peak positions, this means that there was too much noise to determine the position accurately. The mean values of 4.47 Å for a and 57.6° resp. 57.5° for α (for the two pairs of peaks) are in good agreement with the values for bulk Sb at room temperature which are given as 4.51 Å and 57.1° [9].

Table 4.1: Peak positions of the (110), (1$\bar{1}$0), and (200) peaks in the experimental diffraction patterns shown in Figure 4.12 and the resulting lattice parameters a and α calculated from two pairs of peaks independently. The bulk values are taken from [9].

Fig.	Peak Positions (Å^{-1})			Lattice Parameters a, α (Å, °)			
	(110)	(1$\bar{1}$0)	(200)	(110)/(1$\bar{1}$0)		(110)/(200)	
4.1(h)	0.3246	–	–	–	–	–	–
4.2(e)	0.3223	0.4662	0.5677	4.503	56.89	4.519	56.53
4.2(h)	0.3237	0.4658	0.5671	4.453	57.64	4.452	57.69
4.3(d)	0.3246	0.4616	0.5614	4.382	59.25	4.347	60.30
4.4(c)	0.3228	0.4633	–	4.453	57.99	–	–
4.5(d)	0.3226	0.4644	0.5671	4.472	57.58	4.497	56.94
4.6(a)	0.3237	0.4601	0.5624	4.393	59.31	4.390	59.38
4.7(a)	0.3229	0.4664	0.5678	4.485	57.12	4.494	56.91
4.8(a)	0.3219	0.4651	0.5664	4.504	57.02	4.515	56.76
4.9(a)	0.3228	0.4657	0.5666	4.480	57.28	4.479	57.30
4.10(b)	0.3217	0.4657	0.5668	4.518	56.75	4.530	56.46
4.10(a)	0.3221	0.4661	0.5663	4.507	56.86	4.502	56.96
			Average	4.468	57.61	4.472	57.52
			Standard deviation	0.045	0.91	0.060	1.29
			Bulk values	4.507	57.11		

In principle, the lattice parameter of a cluster depends on the size of the cluster and its temperature and so knowing the lattice parameter would allow determination of these two parameters. However, the deviation of the experimental data from the bulk value is very small compared to the uncertainty of the measurement described above. It is therefore only possible to conclude that the crystalline clusters in this study are structurally indistinguishable from the bulk material.

4.2.2 Amorphous Patterns

The diffraction patterns with an amorphous or liquid appearance which were observed in experiments where Ar was used as cooling gas were first compared to the calculated patterns from liquid clusters shown in

Section 3.3. In Figure 4.13 the experimental pattern from Figure 4.3(b) is compared to the calculated pattern from a liquid cluster from Figure 3.13. It is evident that these two patterns to not agree. Even the position of the main peak does not match and the second and third peak are found at completely different *s*-values.

In a next step, the experimental patterns were compared to diffraction patterns from amorphous Sb thin films found in the literature [10–13]. These patterns were recorded using X-ray diffraction and the intensity had to be converted to match the electron form factor (see Section 3.1.3). In Figure 4.14 the same experimental pattern as in the last figure is compared to a pattern from Richter *et al.* [10]. The agreement between these two patterns is significantly better than in the comparison to the liquid pattern. The peak positions are accurately matched and only the relative peak intensity of the first and second peak is distinctly different. Since all amorphous patterns observed in the first part of this study (using Ar as cooling gas) are

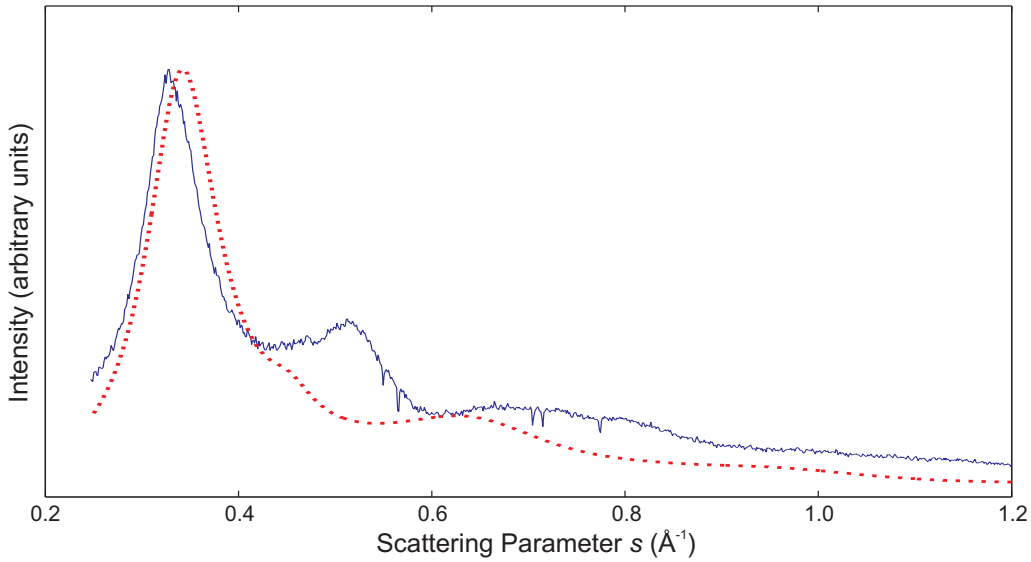

Figure 4.13: Comparison of experimental pattern and calculated pattern from a liquid Sb cluster (dotted line). The calculated pattern corresponds to a 20 nm cluster at 660°C as shown in Figure 3.13. The experimental pattern corresponds to the pattern in Figure 4.3(b).

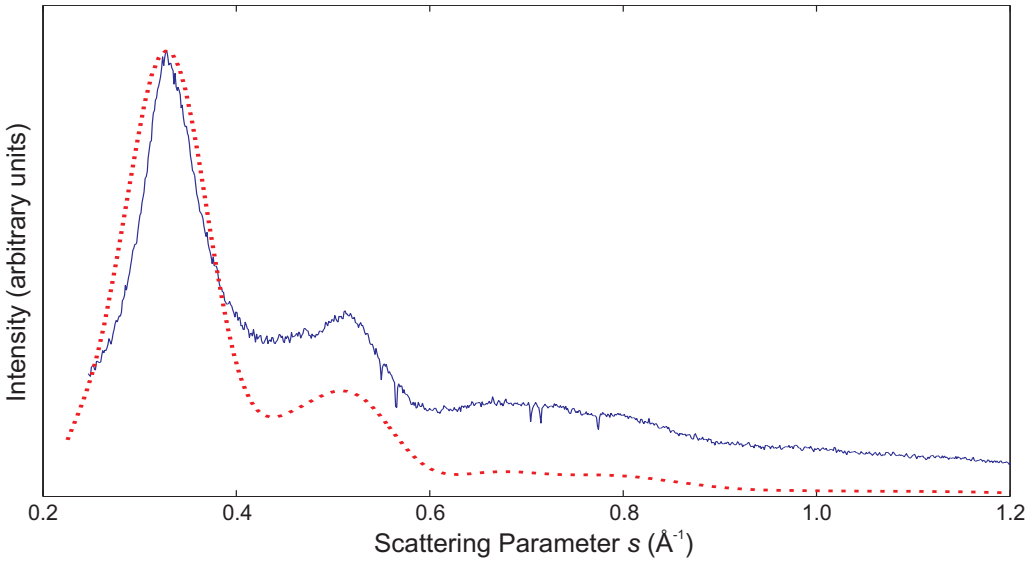

Figure 4.14: Comparison of experimental pattern and pattern from Sb thin films (dotted line) [10]. The experimental pattern corresponds to the pattern in Figure 4.3(b).

very similar to the one shown in this comparison, it can be concluded that the structure of these clusters is consistent with the structure of amorphous Sb thin films.

It is noteworthy that the peak width in diffraction patterns of amorphous particles does not allow any conclusion about the particle size. The broadening of the peak is due to the inherent distribution of interatomic distances in amorphous solids (see Section 3.2 for details).

Determination of Bond Length and Bond Angle

For diffraction patterns from amorphous particles, it is possible to determine the bond length and the bond angle of the structure. This is achieved by calculating the radial distribution function (RDF) by Fourier transform as described in Section 3.2.2. Figure 4.15 shows the first part of the RDF (up to 10 Å) corresponding to the experimental diffraction pattern displayed in the last two figures.

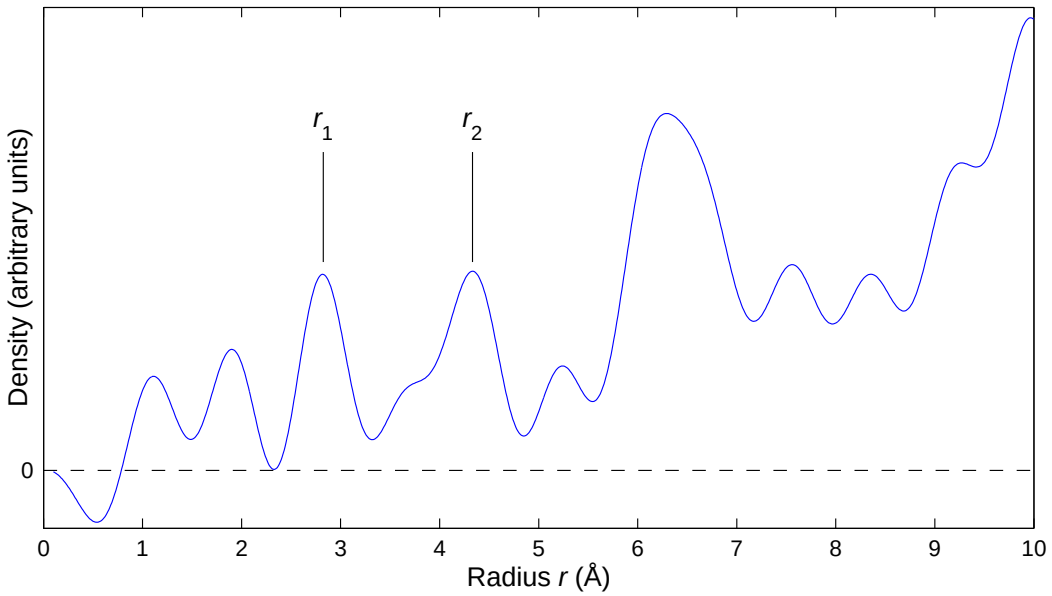

Figure 4.15: RDF determined by Fourier inversion of the experimental diffraction pattern for amorphous clusters shown in Figure 4.3(b). The peaks marked with r_1 and r_2 correspond to the nearest and next-nearest-neighbour distance.

There was no modification function used to calculate this RDF to avoid a loss of resolution. All the peaks well below the crystalline bond length are due to the limited range of scattering parameters and noise in the diffraction pattern.[1] The first peak beyond this value corresponds to the nearest neighbour distance, i.e. the bond length, marked r_1 in Figure 4.15. The position of the second peak corresponds to the next-nearest-neighbour distance, marked r_2. These two values allow the determination of the bond angle using (3.16). Table 4.2 shows the values for r_1, r_2 and the bond angle ϑ for a selection of experimental diffraction patterns from amorphous particles. The average bond length has been calculated to be 2.82 ± 0.01 Å and the average bond angle to be $100.7° \pm 1.3°$. Compared to the values given in the literature for amorphous Sb thin films (2.90 Å for the bond length and 96° for the angle [14]), the calculated bond length does not agree very well

[1] Although the bond length of an amorphous solid is expected to differ from its crystalline counterpart, the difference is not expected to be considerable. Choosing the crystalline value as a rough approximation is therefore valid.

and also the bond angle is significantly different. The deviation of the bond angle is mainly due to the uncertainty of the bond length, since the calculated value for r_2 is very close to the value found in the literature.

Table 4.2: Nearest and next-nearest-neighbour distances as well as bond angle determined by Fourier inversion of amorphous diffraction patterns from Figure 4.1 to 4.5. The literature values are taken from [14].

Figure	Peak Positions r_1 (Å^{-1})	r_2 (Å^{-1})	Bond Angle ϑ (°)
4.1(b)	2.817	4.346	100.93
4.1(c)	2.808	4.350	101.51
4.2(a)	2.833	4.287	98.33
4.3(a)	2.799	4.339	101.63
4.3(b)	2.826	4.331	100.04
4.5(a)	2.807	4.356	101.75
Average	2.815	4.335	100.70
Standard deviation	0.013	0.025	1.32
Literature values	2.90	4.31	96

4.2.3 Sb_4 Patterns

The diffraction patterns with amorphous appearance which were observed when He or a He/Ar mixture was used as cooling gas (Figure 4.6 to 4.10) are markedly different from the ones discussed in the previous section. They do not match the liquid pattern presented in Figure 4.13 either. Since Sb evaporates mainly in tetramers rather than monomers and dimers as discussed in Section 1.3.1, it is to be expected that some diffraction patterns display an influence of scattering from Sb_4 molecules. To test this, a diffraction pattern was calculated for Sb_4 with a structure based on *ab initio* calculations [15]. Figure 4.16 shows a comparison of this pattern and the experimental pattern shown in Figure 4.6(e). All the features of the experimental pattern seem to be well represented by the calculated pattern.

While it seems obvious that the experimental patterns are due to scattering on a beam of Sb_4 units, it might also be possible that there are

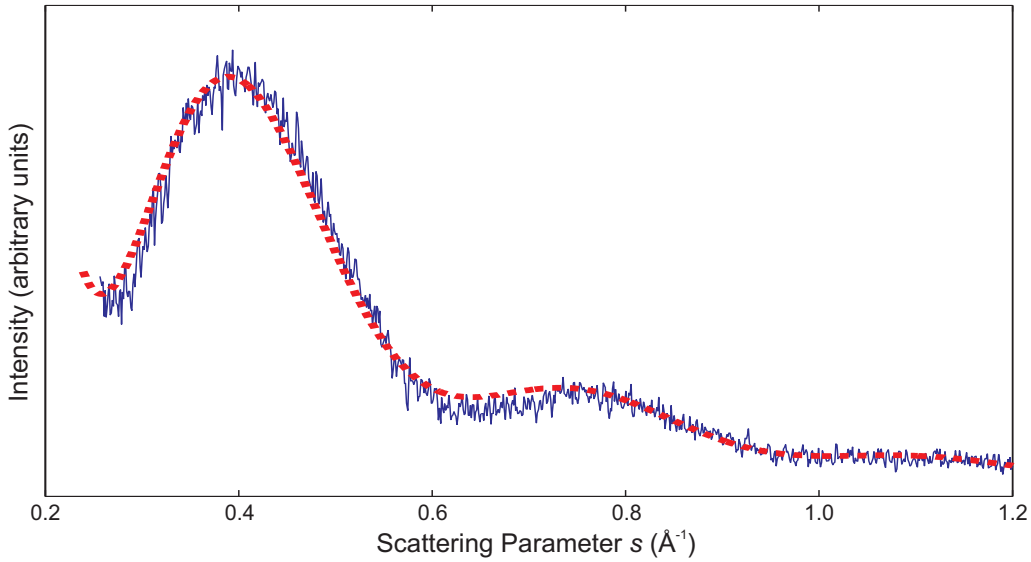

Figure 4.16: Comparison of experimental and calculated Sb_4 patterns. The calculated pattern (dotted line) is based on a theoretical model [15] and the experimental pattern corresponds to the pattern in Figure 4.6(e).

larger clusters consisting of randomly oriented tetramers in the beam as discussed in Section 3.3.1. The diffraction method is not suitable to distinguish between single Sb_4 units and large Sb_4 clusters as was shown in Figure 3.11. This is due to the fact that the large Sb_4 clusters consist of randomly oriented particles and do not show a long-range order. To gather more information about these particles, it is necessary to use an independent technique. Studying the morphology of deposited clusters is one way of solving this issue. This will be discussed in more detail below. Another possibility would be the use of a mass spectrometer which is the topic of the next chapter.

Determination of Bond Length

As in the case of amorphous clusters described above, it is also possible to determine the bond length for Sb_4 particles. In a first step, the RDF has to

be determined by inverting the diffraction pattern. The RDF for the pattern used in the comparison above is shown in Figure 4.17.

In contrast to the RDF for amorphous particles presented in the previous section, for Sb_4 there is only one peak of importance. This peak corresponds to the nearest-neighbour distance or bond length and is marked with r_1 in the figure. This is due to the fact that every atom in an Sb_4 unit has just three nearest neighbours which are all the same distance away from each other. Independent of whether the Sb_4 unit is on its own or whether it is part of a larger cluster with a random arrangement of Sb_4 units, there are no next-nearest neighbours at a well-defined distance. All the further peaks visible in Figure 4.17 are therefore introduced by the inversion process.

For a selection of Sb_4 diffraction patterns, the bond lengths were determined as shown in Table 4.3. The average bond length has been calculated to be 2.82 ± 0.02 Å. This is in reasonable agreement with the value of 2.85 Å found in the literature for a theoretical Sb_4 model [15].

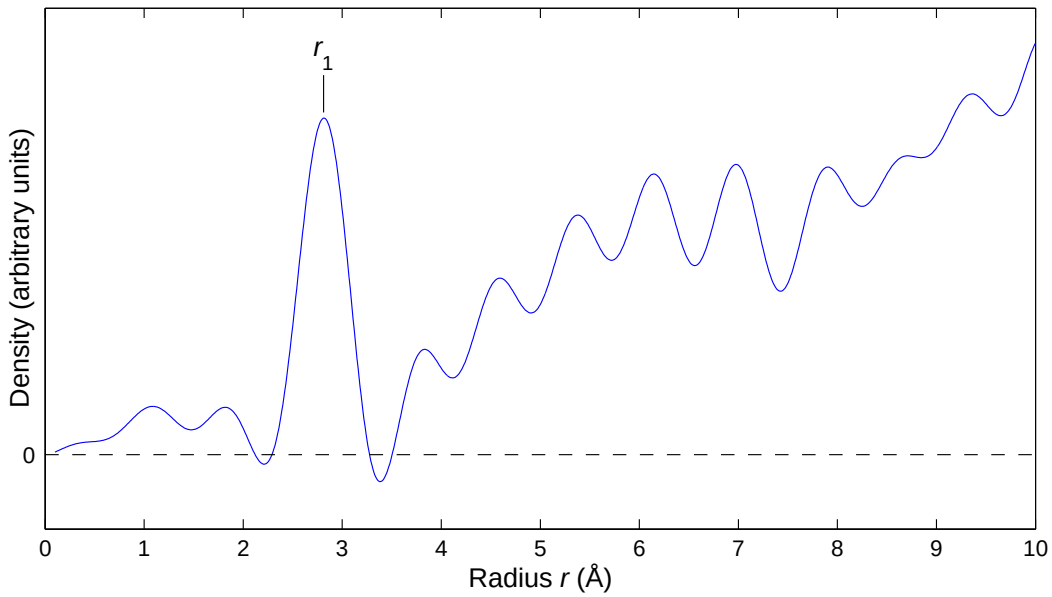

Figure 4.17: RDF determined by Fourier inversion of the experimental diffraction pattern for Sb_4 clusters shown in Figure 4.6(e). The peak marked with r_1 corresponds to the nearest-neighbour distance.

Table 4.3: Nearest-neighbour distance determined by Fourier inversion of Sb_4 diffraction patterns from Figure 4.6 to 4.10. The literature value is taken from [15].

Figure	Peak Position r_1 (Å^{-1})
4.6(g)	2.824
4.6(e)	2.811
4.7(d)	2.835
4.7(c)	2.841
4.8(d)	2.829
4.8(c)	2.834
4.9(g)	2.816
4.9(f)	2.789
4.10(d)	2.805
Average	2.821
Standard deviation	0.017
Literature value	2.85

4.2.4 Background of Experimental Diffraction Patterns

In the diffraction patterns from crystalline clusters, there is a background visible which is not present in the calculated patterns based on the Debye equation. Although the background differs in intensity, it is visible in all crystalline patterns presented in this chapter. It can be best seen in Figure 4.11. In this figure, the intensity of the experimental pattern is scaled to match the calculated pattern. However, the background is visible over the whole spectrum. It has to be noted that the slope of this background is different from the slope of the gas background which is subtracted already. It is therefore not possible to correct this by scaling the gas background before subtraction as this would influence the overall shape of the pattern. As can be seen in Figure 4.4 and 4.5, the background is stronger the higher the source temperature is. There are several possible explanations for this phenomenon:

- As described in Section 3.1.3, an increase in cluster temperature leads to an increase in background while the peak intensities for higher

s-values are reduced due to displacement disorder. However, this increase in background is minor compared to the observed background in the experimental patterns as can be seen in Figure 3.10. The two patterns in this figure are calculated for a temperature of 0 K and 900 K which is the largest difference in temperature possible for solid Sb clusters,[2] but due to noise, this increase in background would not be distinguishable in our diffraction patterns.

- The existence of planar disorder (e.g. stacking faults) leads to an increase in background comparable to the effects of an increase in temperature described above [16]. Without the knowledge of possible disordered structures for Sb clusters it is difficult to estimate the effect on the diffraction patterns.

- It is possible that the cluster beam contains a certain number of small Sb molecules like Sb_1, Sb_2 and Sb_3. Especially for higher source temperature it is expected that the fraction of Sb_4 is greatly reduced and Sb_1 and Sb_2 are more important [17]. These molecules would add a scattering signal similar to that of the inert carrier gas. The exact diffraction curves for Sb_1, Sb_2 and Sb_3 are shown in Figure 4.18.[3] This additional contribution could account for at least a part of the background in the diffraction patterns and would also explain why the background is stronger for higher source temperatures.

- Following on from the last argument, it has to be considered that the crystalline diffraction patterns contain additional scattering intensity from amorphous or Sb_4 particles. Particularly around the transition from one phase to the other, a mixture of two structures is to be expected. Additionally, the presence of individual Sb_4 particles in the beam cannot be discounted at any time. Figure 4.19 shows the influence of additional amorphous and Sb_4 scattering intensity on a crystalline pattern. The experimental pattern is the same as in the

[2] The likely decrease of the melting temperature for small clusters is not considered in this example.

[3] The structural information for Sb_2 and Sb_3 was taken from [15].

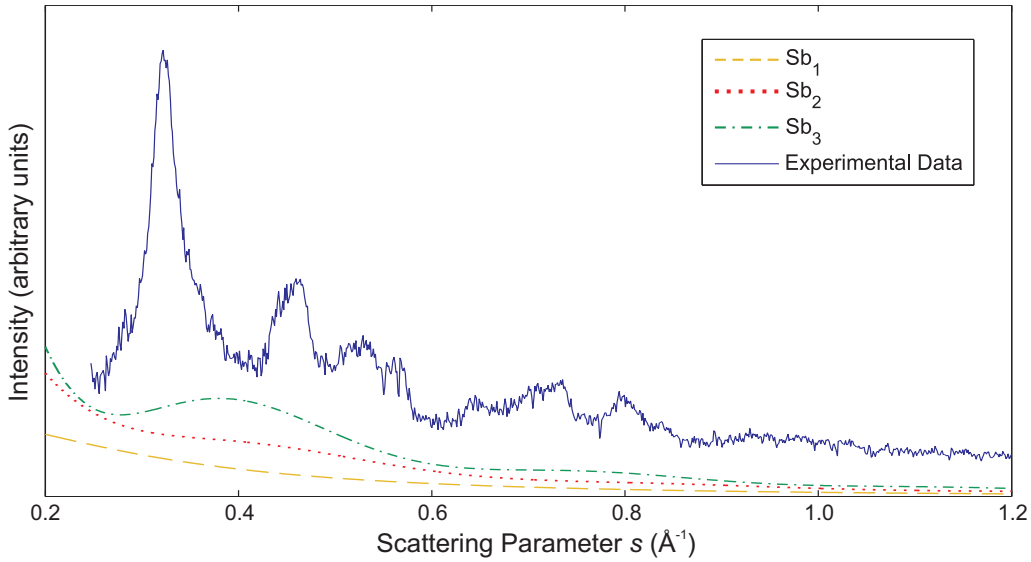

Figure 4.18: The influence of scattering from Sb_1, Sb_2 and Sb_3 on the background of a diffraction pattern. The structural data for Sb_2 and Sb_3 is taken from [15]. The experimental pattern corresponds to Figure 4.3(d).

last figure and is compared in Figure 4.19(a) to the calculated pattern of a crystalline Sb cluster with 6.9 nm diameter and the same structure described in Section 4.2.1. In Figure 4.19(b) 70% of the normalised scattering intensity for amorphous particles is added to the calculated pattern from (a). This leads to a broadening of the base of the main peak similar to that observed in the experimental pattern. The background in the high s-range is not increased noticeably. In Figure 4.19(c) 50% of the Sb_4 scattering intensity is added to the calculated pattern from (a) which adds a strong background to the whole pattern. Finally, in Figure 4.19(d), the two previous figures are combined (with the same relative ratios) giving rise to a pattern which follows the experimental pattern very closely in the first half of the displayed s-range, while it is too weak in the second half.

- Experimental issues cannot be excluded from this discussion. As discussed in Section 3.4, the diffraction patterns of the carrier gas are not recorded after every individual pattern but rather at the end of each

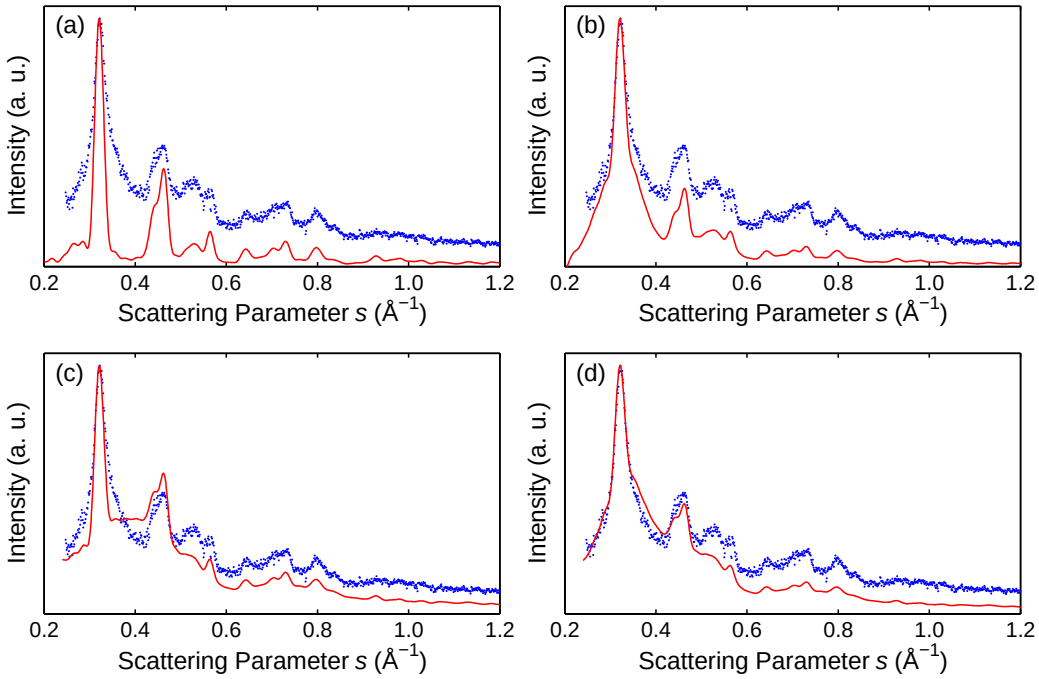

Figure 4.19: The influence of additional amorphous and Sb_4 scattering intensity on a crystalline pattern. The dotted line in all patterns corresponds to the experimental pattern in Figure 4.3(d). (a) The solid line represents a 6.9 nm diameter Sb cluster with the structure described in Section 4.2.1. (b) 70% normalised amorphous scattering intensity is added to the calculated pattern in (a). (c) 50% normalised Sb_4 scattering intensity is added to the calculated pattern in (a). (d) A mixture of all three phases with the ratios as before. The amorphous pattern is taken from [10] and the structural data for Sb_4 is taken from [15].

run, once the source heating is turned off. This is due to the fact that it is impossible in the current set-up to interrupt the cluster beam intermittently to record a background pattern without the influence of cluster scattering. During the course of a run, the experimental conditions have been observed to change, most notably the electron beam intensity. While a change in electron beam intensity should have the same influence across the whole range of scattering parameters, it cannot be discounted that secondary effects lead to an uneven effect on the scattering intensity.

To summarise, there are several possible explanations for the observed background in the scattering patterns, all of which are difficult to prove or disprove. The background is most likely caused by the concurrence of several different effects such as planar disorder, the existence of additional particles in the cluster beam as well as additional experimental effects.

4.3 FE-SEM and HRTEM Studies of Deposited Clusters

To obtain information about the cluster size distribution and their morphology, clusters were deposited on SiO_2 and SiN substrates as well as TEM grids. These samples were then studied under an FE-SEM or an HRTEM. In the following section, the morphology of the three different cluster structures observed in this work is described. This is followed by a section about the size analysis of the deposited clusters compared to the size analysis of the diffraction patterns.

4.3.1 Morphology of Supported Sb Clusters

Depositing clusters of the three different structures described in the previous sections leads to three distinctly different morphologies on the samples. Firstly, FE-SEM and HRTEM images for crystalline clusters are shown followed by FE-SEM images for amorphous clusters and clusters

consisting of Sb_4 units. For the last two species there are no HRTEM included as the high-resolution images did not show any additional information. This will be explained in detail in the corresponding sections.

The morphologies presented in this section are representative for the vast majority of the morphologies observed during the present study. However, due to the huge variety of cluster shapes and sizes encountered, especially for crystalline clusters, the selection shown here cannot cover all the observed shapes. Furthermore, setting the source conditions to exactly the same parameters as described here does not guarantee to obtain the same morphology. While the general characteristics are usually reproducible, the finer details are not.

Crystalline Clusters

From all three species studied in this work, the crystalline clusters show the broadest range of morphologies. Figure 4.20 presents a series of FE-SEM images of crystalline clusters deposited under different source conditions. The clusters in Figure 4.20(a) and (b) are from two consecutive depositions in the same run where the Ar gas flow rate was increased from 158 to 191 sccm while the source temperature remained constant at 750°C. In both images, the clusters show a variety of different shapes and are all strongly faceted. It is evident that, in this example, a higher gas flow rate leads to smaller clusters. This is due to the fact that clusters spend less time in the source chamber if the gas flow rate is increased.

For the clusters presented in Figure 4.20(c) there was a mixture of He and Ar used as cooling gas. The exact source conditions were 87 sccm Ar and 496 sccm He at a source temperature of 700°C. The cluster shapes in this example are very similar to the ones observed in the first two images and the cluster size lies between the two extremes of Figure 4.20(a) and (b).

Figure 4.20(d) shows the influence of a low Ar flow rate and a high source temperature on the morphology. The size of these clusters is dramatically increased compared to the last three examples (note the different scale bar in this example).

Because of the limited resolution of the FE-SEM, a number of samples were also studied under an HRTEM. With an HRTEM it is possible to

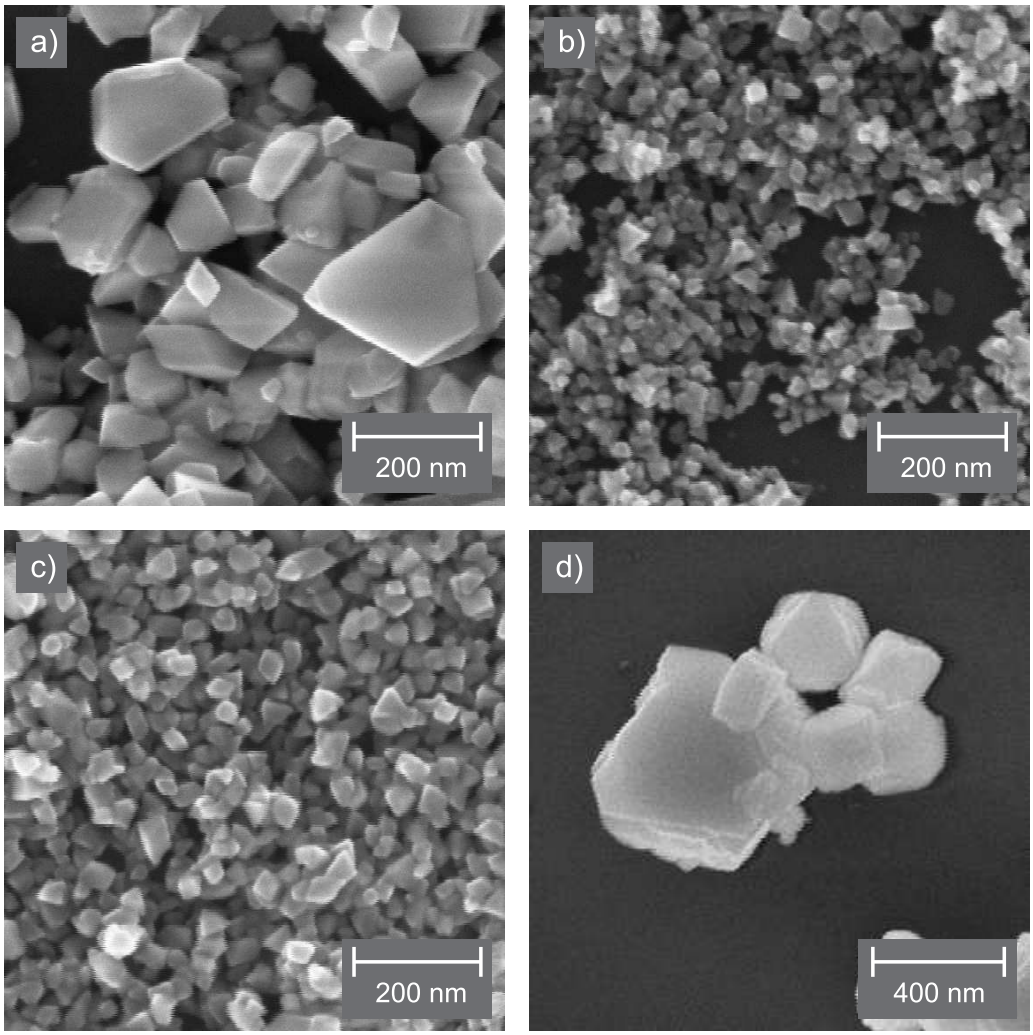

Figure 4.20: FE-SEM images of clusters corresponding to crystalline diffraction patterns. The source conditions used were (a) 750°C and 158 sccm Ar; (b) 750°C and 191 sccm Ar (same run as (a)); (c) 700°C, 87 sccm Ar and 496 sccm He; (d) 825°C and 82 sccm Ar (corresponding to Fig. 4.4(d)).

see lattice fringes that enable a determination of whether the clusters are single-crystalline or whether they contain domains. Figure 4.21 shows a collection of four HRTEM images from crystalline clusters. It is worth mentioning, however, that the absence of lattice fringes on a HRTEM image does not necessarily imply that the particles are non-crystalline. It could also mean that the lattice planes are not oriented properly relative to the electron beam or that the optics of the microscope was not focussed.

The cluster in Figure 4.21(a) has a single-crystalline core which is surrounded by an amorphous layer. This amorphous layer is most likely due to oxidation. As the samples have to be transferred from the deposition chamber to the microscope, it is inevitable that oxidation occurs. In all examples studied, the amorphous layer has a thickness of approximately 2 nm. A previous study also observed an amorphous oxide layer around Sb clusters [18], although in this study, the oxide layer crystallised under electron beam irradiation into an Sb_2O_3 structure. This behaviour is not observed in the present work.

Figure 4.21(b) displays a particle with triangular cross section consisting of multiple domains. At least four different domains are visible; the domain boundaries, however, are not well defined and it is not possible to determine whether twin planes exist. There is an amorphous layer visible around this particle as well.

Figure 4.21(c) and (d) show two examples of clusters sticking together. These two images are from the same sample. In the first case, an area of coalescence is visible between the two particles and the amorphous layers have merged. In the second case, however, the two clusters merely stick together without any further interaction. It is worth mentioning that the clusters in these two images were deposited under conditions which gave rise to an amorphous diffraction pattern (the sample corresponds to the pattern in Figure 4.5(a)). It has been known for some time that amorphous Sb thin film crystallise either spontaneously after a certain time or under the influence of an electron beam [10, 11, 19]. This would explain why clusters with a spherical shape which usually correspond to the amorphous phase (see below) display lattice fringes.

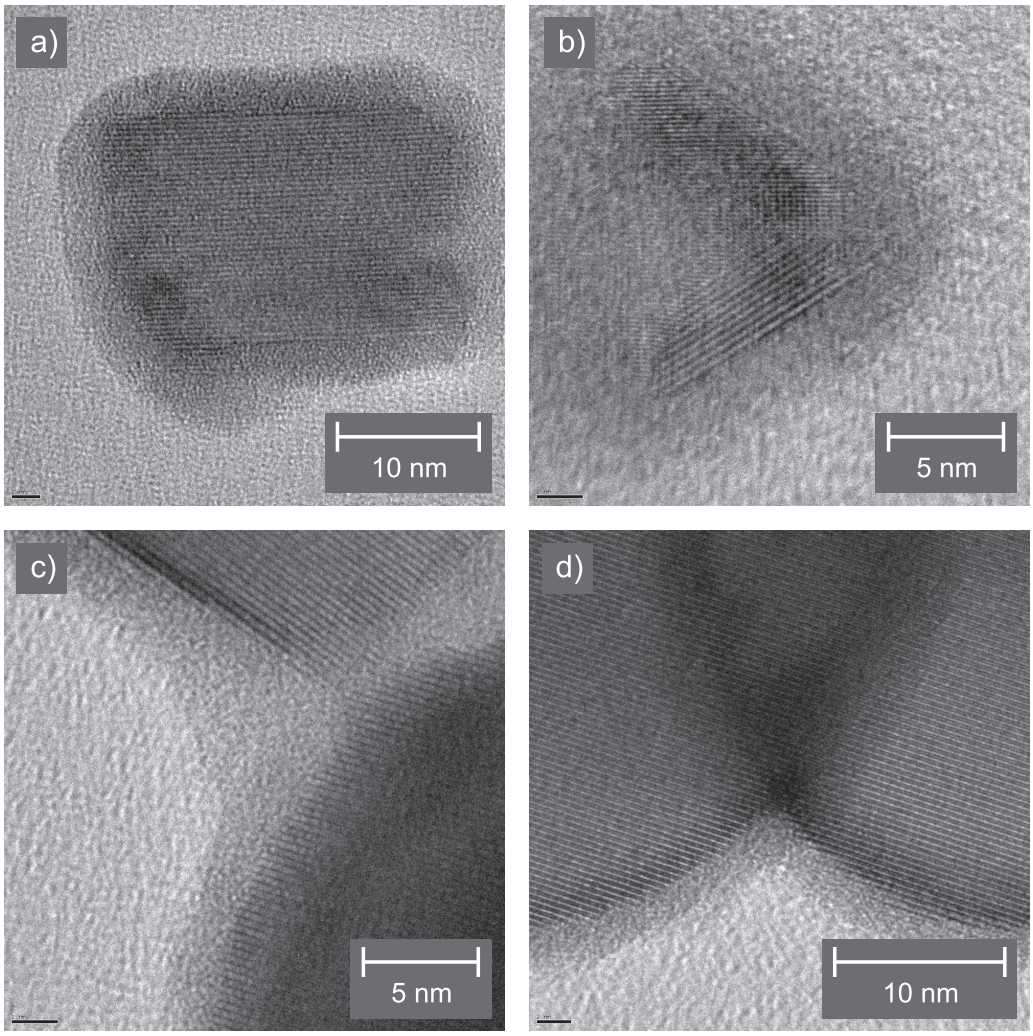

Figure 4.21: HRTEM images of individual Sb clusters showing crystal lattices and oxide layers.

Amorphous Clusters

The amorphous clusters formed at low temperatures and low Ar flow rates are shown in Figure 4.22. These clusters are spherical and have a narrow size distribution with a mean size of around 40 nm (see below for a detailed discussion of the cluster sizes). As observed in a previous study, the majority of these clusters bounce off the substrate's surface [20]. Clumps of clusters such as those shown in Figure 4.22(a) and (b) most likely arise due to the fact that they only stick to the surface when they hit either a surface defect or another cluster. A higher coverage of amorphous particles leads to an appearance as shown in Figure 4.22(c). Rather than forming a continuous film, the clusters form well-separated, evenly sized islands.

Figure 4.22(d) shows an example of a mixture of amorphous and crystalline particles. Although the diffraction pattern shown in Figure 4.3(d) which corresponds to this sample shows distinct crystalline features, there is a significant number of spherical particles visible. While it is not possible to determine whether these spherical particles are indeed amorphous in the cluster beam, they are identical in appearance to the ones shown in Figure 4.22(a) and (b) and distinctly different to the crystalline particles displayed in Figure 4.20. It has been mentioned before that some of the spherical particles turn out to be crystalline under the HRTEM, although it is assumed that they are amorphous in the beam and crystallise on the substrate. If they are still amorphous in the cluster beam, it would have an influence on the cluster size estimate based on the diffraction patterns. This issue will be discussed in more detail below.

As mentioned above, there are no HRTEM images of amorphous clusters included for two reasons: Firstly, high resolution images of amorphous particles do not contain any information about the structure of these particles, since the structure lacks long range order which would be visible as lattice fringes. Secondly, an image of a cluster without lattice fringes does not allow the conclusion that the particle is not crystalline. As discussed above, this is due to the fact that lattice fringes can only be detected under an electron microscope if the crystal planes are properly aligned relative to the electron beam.

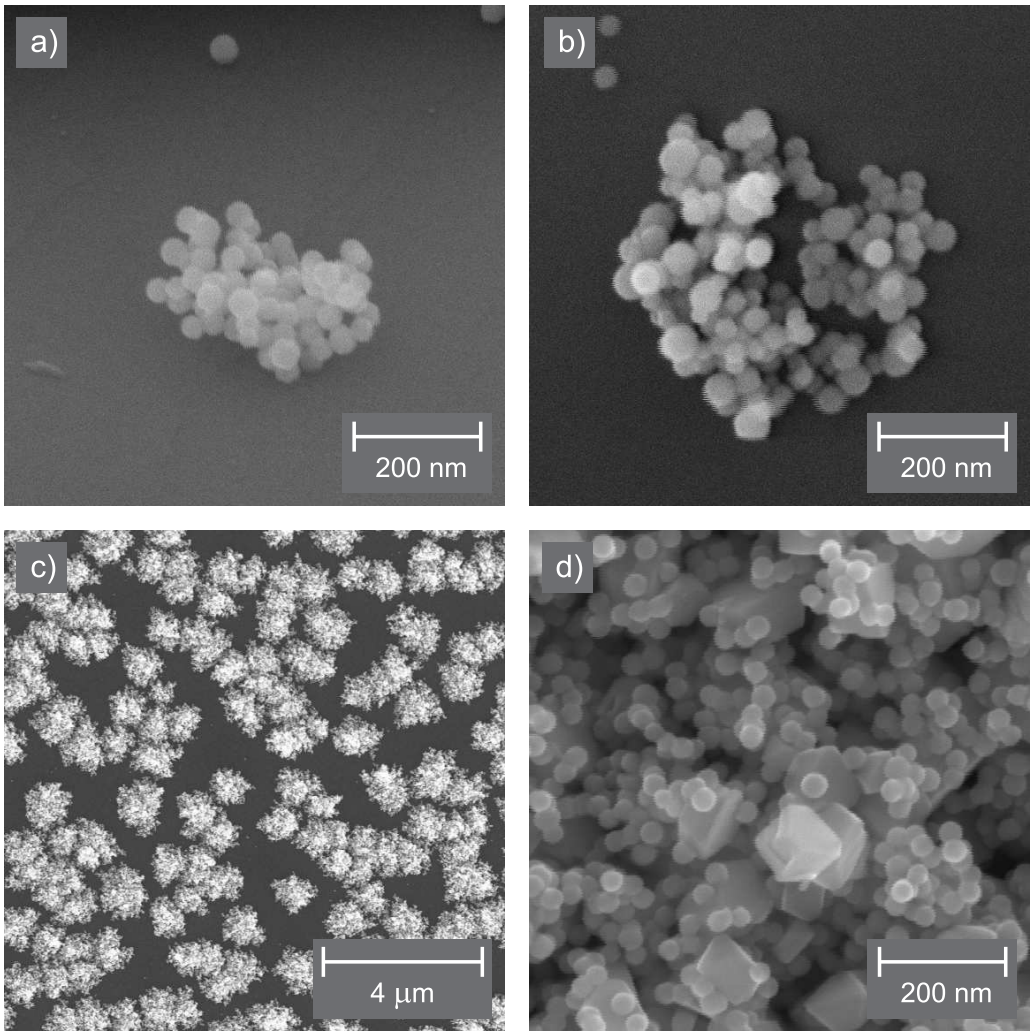

Figure 4.22: FE-SEM images of amorphous clusters. The source conditions used were (a) 625°C and 77 sccm Ar (corresponding to Fig. 4.1(b)); (b) 675°C and 82 sccm Ar (corresponding to Fig. 4.3(a)); (c) 650°C and 82 sccm Ar; (d) 675°C and 122 sccm Ar (corresponding to Fig. 4.3(d)).

Sb_4 Clusters

FE-SEM images of clusters which give rise to diffraction patterns corresponding to those of Sb_4 are shown in Figure 4.23. In Figure 4.23(a) a low-density area with individual, well-separated particles is visible. Figure 4.23(b) is from the same sample but closer towards the centre of the cluster beam spot. In this image, most particles have merged but the original shape is still visible. There are almost no small particles present as in Figure 4.23(a) leading to the assumption that these small particles have already coalesced with the larger ones. The clusters in Figure 4.23(c) are from a different sample but from the same run as the ones above. This image shows individual clusters sitting in a second layer above a dense interconnected lower layer of clusters and was recorded in the centre of the cluster beam. The sample in Figure 4.23(d) features V-grooves which were etched into the substrate before the clusters were deposited. This allows the morphology to be studied at an angle without having to tilt the microscope stage. The clusters in this image are similar to the ones in Figure 4.23(b) on the plateau between the grooves but are still individual particles on the slope – although some coalescence is evident.

These results, and especially the morphology shown in Figure 4.23(c), are not consistent with the deposition of Sb_4 molecules. It appears, therefore, that the particles in the beam have a mean diameter of approximately 30 nm and consist of randomly oriented Sb_4 units. The lack of long-range order in such a particle and the absence of correlation between neighbouring Sb_4 units would lead to a diffraction pattern which is almost identical to that of isolated Sb_4 particles. This has been checked by calculating a diffraction pattern for 10 nm particles composed of randomly assembled Sb_4 units and indeed the diffraction patterns are almost identical to these of isolated Sb_4 tetramers (see Figure 3.11).

There are no HRTEM images of Sb_4 particles included in this section for the same reasons outlined for amorphous clusters.

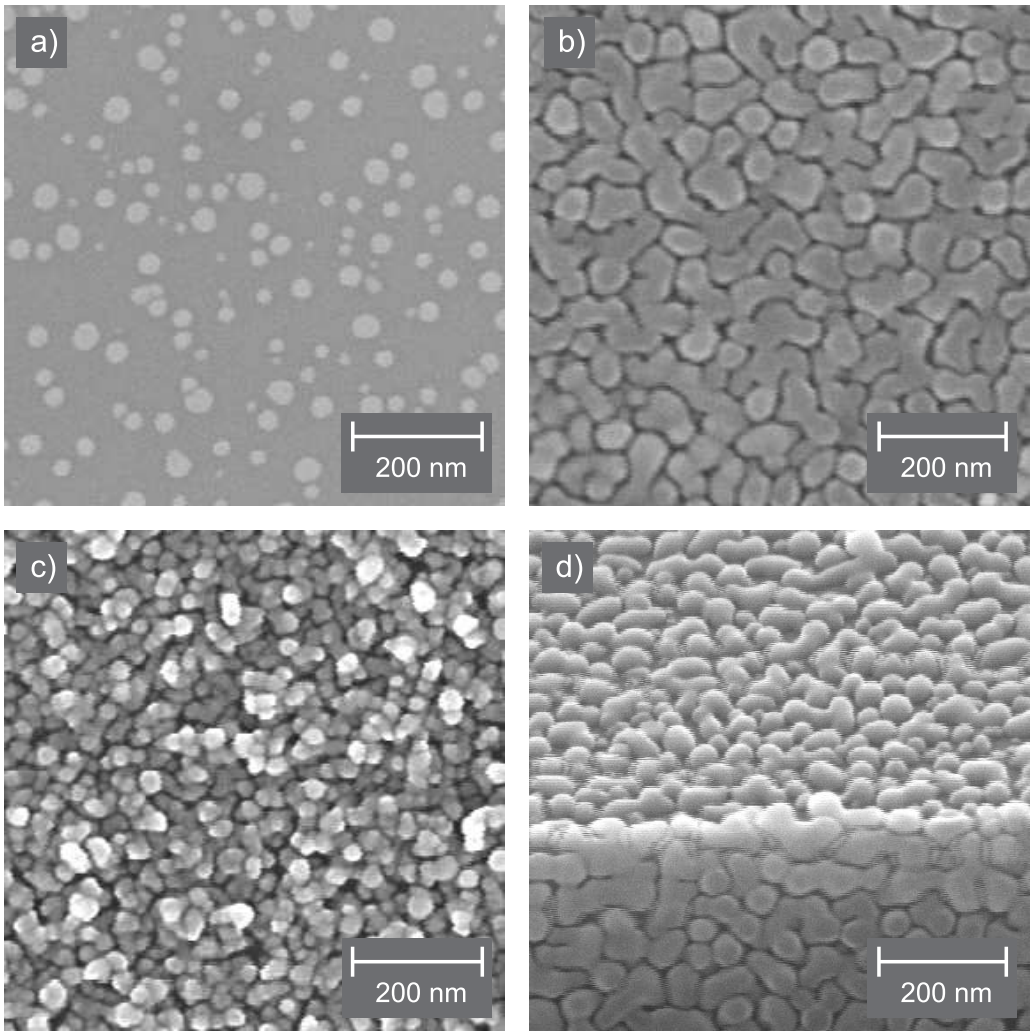

Figure 4.23: FE-SEM images of Sb_4 clusters. The source conditions used were (a) 700°C and 750 sccm He (corresponding to Fig. 4.6(e)); (b) same sample as in (a), closer to the centre of the cluster beam spot; (c) 700°C and 500 sccm He (corresponding to Fig. 4.6(g)), very high coverage; (d) 700°C, 60 sccm Ar and 750 sccm He (corresponding to Fig. 4.9(f)), deposited on sample with V-grooves (the V-groove wall is shown in the top half of the image and the plateau in the bottom half).

4.3.2 Size Analysis of Sb Clusters

Three different methods were used to determine the size of the clusters observed in this study: the microscopy method using FE-SEM and HRTEM, the Scherrer equation and the inversion method. All these techniques were discussed in detail in earlier sections and in the following they will only be mentioned briefly to explain how each method was applied to the experimental data. At the end of this section a table with all the experimental conditions and results will be presented.

Microscopy

The cluster size distribution of the particles shown in the last section is determined using the procedure described in Section 2.5. The FE-SEM was mainly used for this procedure, as the higher resolution of the HRTEM was not required. Some samples, however, were studied under the HRTEM as well to check for smaller clusters below the detection limit of the FE-SEM and to confirm that these two systems lead to the same result. Since the size averages from the FE-SEM and the HRTEM agreed well (see Section 2.5 and in particular Figure 2.9) and since the smallest clusters found with the HRTEM were about 5 nm in diameter, the choice of mainly using the FE-SEM is justified.

Scherrer Equation

For crystalline clusters, the Scherrer equation was used as an alternative method to determine the mean cluster size as discussed in Section 3.4.2. The additional background observed in the experimental diffraction patterns (see Section 4.2.4) is subtracted first. In a next step, a Gaussian distribution is fitted to the main peak and the FWHM of this distribution is determined. Finally, the particle size is calculated using (3.24) as described in the corresponding section (the factor K is set to unity and the instrumental peak broadening Δs_0 to $4.7\times10^{-3}\,\text{Å}^{-1}$). It is noteworthy that the Scherrer equation is only an estimate and is expected to lead to incorrect results if the cluster beam consists of a mixture of crystalline as well as non-crystalline particles.

Inversion Method

The inversion method as described in Section 3.4.2 has also been used for size analysis. Figure 4.24 shows four examples of RDFs calculated for a selection of experimental diffraction patterns. The data in Figure 4.24(a) and (b) correspond to the crystalline clusters shown in Figure 4.20(a) and (b), respectively. While the two FE-SEM images show considerably different size distributions for the two samples, an estimate based on the inversion results would lead to a mean cluster size of approximately 70 nm for both figures. It is worth noting that both RDFs show large oscillations below 10 nm.

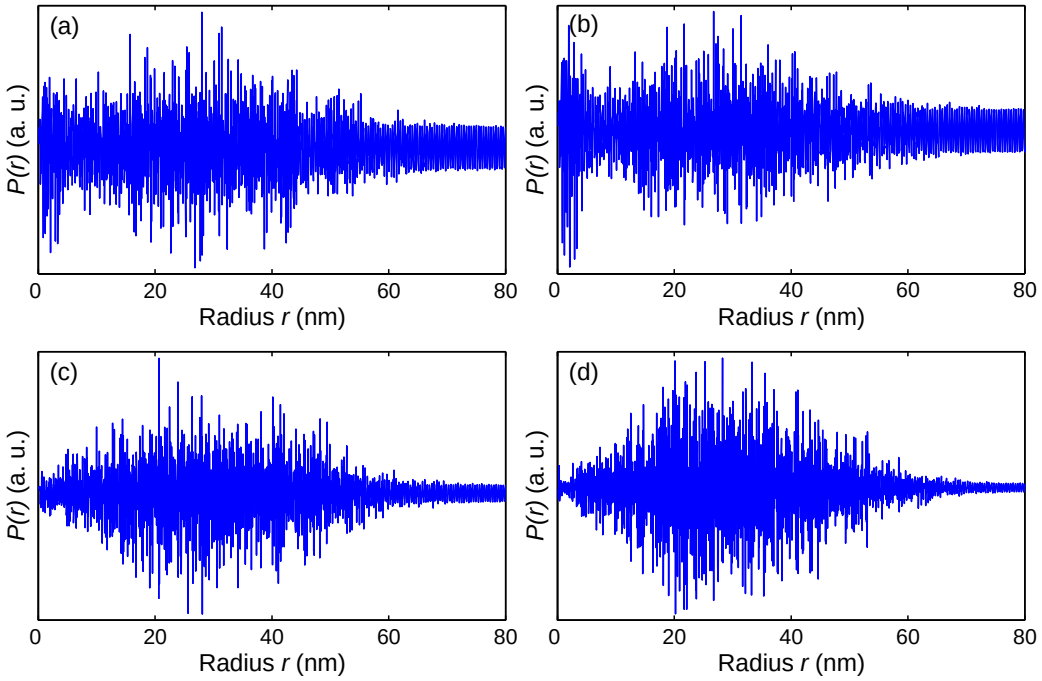

Figure 4.24: Comparison of the inversion method for crystalline, amorphous and Sb_4 clusters. The RDFs correspond to (a) crystalline clusters as shown in Figure 4.20(a); (b) crystalline clusters as shown in Figure 4.20(b); (c) amorphous clusters giving rise to the diffraction pattern in Figure 4.5(a); (d) Sb_4 clusters giving rise to the diffraction pattern in Figure 4.8(d). The Lanczos function was used as modification function for all the calculations.

The RDF in Figure 4.24(c) corresponds to the amorphous diffraction pattern displayed in Figure 4.5(a). As in the case of the crystalline clusters, a size estimate based on this RDF would lead to a value of about 70 nm. This is also true for the last RDF shown in Figure 4.24(d) which is based on the Sb_4 diffraction pattern in Figure 4.8(d). Not only the four presented RDFs but also all the other diffraction patterns analysed by the inversion method led to a size estimate in the range of 60 to 70 nm. This is in total disagreement with the results from the FE-SEM study which show a wide range of mean cluster sizes.

In two previous studies [2, 3], the inversion method was used successfully for cluster diameters up to approximately 10 nm, however, most of the diffraction patterns in these studies had a higher signal-to-noise ratio than those in the present work. There are several possible reasons why the inversion method does not produce meaningful results in the present work: firstly, as described in Section 3.4.2, the range of scattering parameters recorded during an experiment is limited, leading to the appearance of additional oscillations. Secondly, the signal-to-noise ratio of the patterns was rather low, again introducing errors. And thirdly, the large clusters observed in this study introduce a considerable amount of complexity into the inversion process. Hence, the inversion results are not discussed further.

Experimental Conditions and Results

All the results from the size analysis together with the source conditions for each run are presented in Table 4.4. The source temperature T_C and the gas flow rates are the source parameters which can be controlled directly; the source pressure P_G depends on the gas flow rate, the nozzle diameter and to some extent the temperature and cannot be adjusted independently. The deposition rate monitor is not considered to be very accurate and therefore the deposition rate R_{dep} gives only a rough indication of the cluster beam intensity (see also Section 4.1.4). The nozzle diameter quoted in the table corresponds to the diameter of the first nozzle and cannot be changed during a run (see Section 2.1 for more details). The size estimates listed here are obtained through two independent procedures:

the first method determines the cluster size from FE-SEM images (see Section 2.5), while the second one uses the Scherrer equation which calculates the mean diameter based on the diffraction patterns (see Section 3.4.2). The results from the FE-SEM measurements are given as number-weighted and volume-weighted mean diameter. The volume-weighted measure is expected to agree more closely to the size information gained from the diffraction patterns. Because of the limited number of samples which can be mounted inside the vacuum chamber, there are not FE-SEM size estimates available for all experiments presented here. The Scherrer equation can only be used for crystalline patterns and could not be applied to some patterns with low signal-to-noise ratio. The uncertainty for the results from the Scherrer equation is about 30% [4] and for the FE-SEM size measurements about 10%. The last column in the table denotes the type of diffraction pattern observed for each measurement: crystalline, amorphous, Sb_4 or a mixture of two of these structures. This classification does not, however, take into account that some of the crystalline diffraction patterns might contain a background due amorphous or Sb_4 particles (see Section 4.2.4 for more information).

Discussion of General Trends and Size Estimates

In this section, the general trends as well as the size estimates shown in Table 4.4 are discussed. The discussion is divided into three parts according to the structure of the clusters. To refer to a specific section in Table 4.4, the numbering of the diffraction pattern figures is used. This is, however, only a means of identifying the corresponding experimental conditions and is not intended as a link to the original diffraction patterns.

It is noteworthy that all the measurements shown in this table (pressure, deposition rate, and especially size estimates) cannot be considered to be representative for runs with similar source conditions, as it proved to be very difficult to achieve the same results even in two consecutive runs using exactly the same settings. Note that the volume-weighted diameter can be influenced considerably by a single very large cluster. It was possible, however, to recreate the general trends with changing source parameters as described in Section 4.1.1 to 4.1.3.

Table 4.4: Experimental conditions and size distribution estimates for the runs from Figure 4.1 to 4.10 and 4.20. T_C stands for the source temperature, P_G for the source pressure and R_{dep} for the deposition rate. For the size estimates, three values are given – if available: the first two are from FE-SEM images (number-weighted and volume-weighted mean diameter) and the third is determined from the diffraction patterns using the Scherrer equation. The last column denotes whether the diffraction pattern shows crystalline (C), amorphous (A) or Sb_4 (S) characteristics (or a mixture of two types). The data at the bottom without figure number is include because it contains additional size estimates not available in the previous runs.

Figure	T_C	Flow Rate (sccm)		P_G	R_{dep}	Nozzle ∅	Size Estimates (nm)			Pattern
	(°C)	Ar	He	(mbar)	(Ås^{-1})	(mm)	SEM mean	SEM vol.	Scherrer	
4.1(a)	625	58	–	3.5	9.1	2.5	32	38	–	A
4.1(b)	625	77	–	4.3	41	2.5	38	39	–	A
4.1(c)	625	92	–	5.0	21	2.5	27	28	–	A
4.1(d)	625	105	–	5.6	6.9	2.5	26	27	–	AC
4.1(e)	625	119	–	6.2	6.6	2.5	42	50	–	C
4.1(f)	625	130	–	6.7	3.4	2.5	–	–	–	C
4.1(g)	625	149	–	7.5	1.4	2.5	–	–	–	C
4.1(h)	625	170	–	8.2	5.3	2.5	34	53	4.0	C
4.2(a)	650	90	–	2.9	7.3	3.5	–	–	–	A
4.2(b)	650	100	–	3.1	7.6	3.5	–	–	–	A
4.2(c)	650	110	–	3.4	4.8	3.5	–	–	–	AC
4.2(d)	650	140	–	4.1	5.8	3.5	–	–	4.2	C
4.2(e)	650	150	–	4.4	11	3.5	–	–	4.6	C
4.2(f)	650	160	–	4.6	33	3.5	–	–	4.7	C
4.2(g)	650	170	–	4.8	39	3.5	–	–	4.6	C
4.2(h)	650	180	–	5.1	38	3.5	–	–	4.5	C
4.3(a)	675	82	–	4.8	18	2.5	39	42	–	A
4.3(b)	675	100	–	5.6	23	2.5	–	–	–	A
4.3(c)	675	111	–	6.2	21	2.5	33	37	–	AC
4.3(d)	675	122	–	6.7	8.5	2.5	42	61	3.2	C
4.4(a)	675	82	–	4.8	18	2.5	39	42	–	A
4.4(b)	725	82	–	5.1	25	2.5	93	215	–	AC

Table 4.4: (continued)

Figure	T_C (°C)	Flow Rate (sccm) Ar	He	P_G (mbar)	R_{dep} (Ås^{-1})	Nozzle ∅ (mm)	Size Estimates (nm) SEM mean	SEM vol.	Scherrer	Pattern
4.4(c)	775	82	–	5.5	21	2.5	101	203	3.7	C
4.4(d)	825	82	–	6.2	39	2.5	92	184	3.8	C
4.5(a)	675	80	–	4.8	5.0	2.5	49	62	–	A
4.5(b)	700	80	–	5.4	9.4	2.5	52	62	3.9	C
4.5(c)	725	80	–	5.1	5.8	2.5	60	93	4.2	C
4.5(d)	750	80	–	5.8	11	2.5	68	93	4.8	C
4.5(e)	775	80	–	6.3	14	2.5	111	180	4.5	C
4.6(a)	700	–	1454	15.9	4.0	3.5	–	–	3.0	C
4.6(b)	700	–	1250	14.1	5.5	3.5	–	–	–	SC
4.6(c)	700	–	1125	13.3	2.4	3.5	–	–	–	SC
4.6(d)	700	–	1000	12.2	2.8	3.5	–	–	–	SC
4.6(e)	700	–	750	9.7	2.9	3.5	20	21	–	S
4.6(f)	700	–	600	8.0	3.6	3.5	–	–	–	S
4.6(g)	700	–	500	7.3	2.7	3.5	21	24	–	S
4.7(a)	750	–	1454	17.1	90	3.5	–	–	4.9	C
4.7(b)	750	–	1170	14.5	3.2	3.5	–	–	–	S
4.7(c)	750	–	711	10.1	2.2	3.5	–	–	–	S
4.7(d)	750	–	570	8.6	1.9	3.5	–	–	–	S
4.8(a)	700	110	440	9.1	28	3.5	14	17	4.4	C
4.8(b)	700	82	467	9.0	5.6	3.5	14	17	–	SC
4.8(c)	700	55	495	8.7	0.9	3.5	21	24	–	S
4.8(d)	700	0	550	8.2	1.4	3.5	23	26	–	S
4.9(a)	700	120	480	10.2	69	3.5	28	31	4.8	C
4.9(b)	700	108	492	10.2	23	3.5	21	23	–	SC
4.9(c)	700	96	504	10.2	4.7	3.5	19	23	–	SC
4.9(d)	700	84	516	10.2	2.1	3.5	26	32	–	S

Table 4.4: (continued)

Figure	T_C (°C)	Flow Rate (sccm) Ar	He	P_G (mbar)	R_{dep} (Ås^{-1})	Nozzle ∅ (mm)	Size Estimates (nm) SEM mean	SEM vol.	Scherrer	Pattern
4.9(e)	700	72	528	10.2	1.4	3.5	35	39	–	S
4.9(f)	700	60	540	10.2	1.1	3.5	20	22	–	S
4.9(g)	700	0	600	9.5	1.2	3.5	25	26	–	S
4.10(a)	750	160	640	15.4	109	3.5	47	123	5.2	C
4.10(b)	750	120	680	14.4	167	3.5	26	31	4.9	C
4.10(c)	750	80	720	13.4	6.5	3.5	32	43	–	SC
4.10(d)	750	0	800	11.5	3.6	3.5	21	23	–	S
4.20(a)	750	158	–	5.5	25	3.5	73	91	4.8	C
4.20(b)	750	191	–	6.5	56	3.5	26	29	5.0	C
	700	–	550	8.2	1.4	3.5	23	26	–	S
	700	–	1125	13.3	4.3	3.5	23	25	–	SC
	700	–	1454	16.1	7.7	3.5	19	22	3.9	C
	650	80	–	4.6	64	2.5	41	44	–	A
	650	120	–	6.3	26	2.5	48	64	4.1	C
	700	0	500	7.5	7.4	3.5	18	20	–	S
	700	100	400	9.1	114	3.5	30	37	4.6	C
	675	78	–	4.5	7.0	2.5	45	51	–	A
	675	101	–	5.6	2.8	2.5	38	79	–	A
	675	122	–	6.5	1.5	2.5	83	116	4.8	C
	725	78	–	4.7	7.1	2.5	73	112	4.0	C
	775	78	–	5.1	11	2.5	131	171	5.7	C

The size information of the mixed phases will not be discussed in detail since it can be considered to be a convolution of the two size distributions for each separate phase. Table 4.5 presents the size averages calculated for the three structures independently.

Table 4.5: Size averages according to cluster structure for the data in Table 4.4.

Cluster Structure	Size Averages (nm)		
	SEM mean	SEM vol.	Scherrer
amorphous	38	48	–
Sb_4	24	26	–
crystalline	57	87	4.4

Amorphous Clusters

Amorphous diffraction patterns are observed for temperatures between 625°C and 675°C and Ar gas flow rates of up to 100 sccm and are identified with the letter A in Table 4.4 (see Figure 4.1, 4.2, 4.3, 4.4 and 4.5). If the temperature and flow rate are increased further, mainly crystalline clusters are produced (marked with the letter C in Table 4.4). Note that the gas flow rate and not the source pressure is crucial for the change to crystalline particles: in Figure 4.2 the change is observed between 100 and 110 sccm, even though the source pressure is considerably lower than in the other runs (because of a wider first nozzle). It is not possible to produce amorphous clusters using He as source cooling gas, independent of the parameter range.

The average cluster diameter for amorphous particles is given as 38 nm for the number-weighted diameter and 48 nm for the volume-weighted diameter (see Table 4.5). The mean sizes are not influenced by changing source conditions and the size distribution is narrow with almost all mean values in the range of 30 to 40 nm.

Sb_4 Clusters

Sb_4 clusters are observed for a temperature range of 700°C to 750°C, for He gas flow rates of up to approximately 1000 sccm (see Figure 4.6 and 4.7)

and for He/Ar mixtures with up to around 10% Ar content (see Figure 4.8, 4.9 and 4.10) and are marked with the letter S in Table 4.4. For higher values for these parameters, crystalline particles are found. The flow rate threshold for the change from Sb_4 to crystalline is temperature dependent: at 700°C, increasing the flow rate already leads to crystalline features in the pattern at 1000 sccm (see Figure 4.6), while at 750°C the pattern recorded with a flow rate of 1170 sccm still shows Sb_4 features (see Figure 4.7). The limit of Ar content, on the other hand, is dependent on the total flow rate: the higher the flow rate is, the lower the Ar content has to be before a change is observed (Figure 4.9 and 4.10).

As in the case of amorphous clusters, the particle size range is narrow and the average values for all the runs are 24 nm for the number-weighted and 26 nm for the volume-weighted mean diameter. There is no discernible trend for the cluster sizes for different source parameters.

Crystalline Clusters

Crystalline clusters show the widest variety of shapes and sizes and are observed over a broad range of source parameters. When Ar is used as the source cooling gas, flow rates above 120 sccm (see Figure 4.1, 4.2 and 4.3) and temperatures beyond 750°C (see Figure 4.4 and 4.5) invariably lead to the production of crystalline clusters. If the cooling gas is switched to pure He, crystalline clusters are only observed for very high flow rates of around 1400 sccm (see Figure 4.6(a) and 4.7(a)). Adding Ar to the cooling gas allows crystalline clusters to be detected as soon as the Ar content reaches 15 to 20% depending on the total gas flow rate (see Figure 4.8(a), 4.9(a), 4.10(a) and (b)).

Using the FE-SEM method, the average size of crystalline particles in this study has been determined to be 57 nm for the number-weighted and 87 nm for the volume-weighted diameter. This average value, however, is misleading since the measured sizes depend strongly on the experimental conditions. For an increasing Ar gas flow rate, a trend to smaller clusters is observed (see Figure 4.20(a) and (b)). The reason for this behaviour is that for higher flow rates the particles spend less time in the nucleation region. This also explains the fact that the use of an He/Ar mixture leads to small

particles since the total flow rates in this case are very high (see Figure 4.8 and 4.9). However, the opposite trend is observed in Figure 4.10 which might be due to the increased source temperature of this run. For high source temperatures, the increased amount of evaporated material leads to larger clusters (see Figure 4.4 and 4.5).

Using the Scherrer equation to determine the mean cluster size leads to significantly differing values. The overall average size estimate is only 4.4 nm.[4] Additionally, most trends described above cannot be observed in the Scherrer results. While a previous study using the same equipment also reported a discrepancy between the two results, the difference was considerably smaller [3]. It is worth mentioning that the results from the Scherrer equation agree well with the results from a comparison of the experimental patterns with the calculated ones. It is evident from the patterns in Figure 3.8 that the second and third peak start to split at cluster sizes between 5 and 10 nm. Since most experimental diffraction patterns do not show two separate peaks, this comparison would lead to the assumption that the clusters have a diameter of approximately 5 nm.

There are five possible explanations for the disagreement between the results from the Scherrer equation and the results from the FE-SEM study:

Firstly, the clusters might be smaller in the beam but grow on the substrate through aggregation. This can be ruled out due to the morphology of the film (see Figure 4.20); the loose-packed 3D structure is consistent with the random deposition of large crystalline particles but inconsistent with diffusion and aggregation of smaller clusters [21]. Diffusion is also unlikely, since the rms roughness of the samples used is too high (e.g. approximately 2–5 nm for SiO_2 samples used in this study). This has been tested by varying the deposition time – and thereby the coverage – for a set of experimental conditions and then comparing the mean sizes. The conditions used were low and high Ar flow rate (corresponding to the transition from amorphous to crystalline clusters) as well as low He flow rate and He/Ar mixture (corresponding to the transition from Sb_4 to crystalline clusters). The results of these two transitions are presented in Table 4.6.

[4] Note that the results from the Scherrer equation are expected to be closer to the volume-weighted diameter.

While the first column seems to indicate a slight increase in cluster size with increasing coverage, the second one shows a decrease. The two remaining columns show no significant changes. In general, there is no trend discernible which would support the argument that the clusters grow on the substrate through aggregation.

Table 4.6: Size averages for different deposition times for the transitions from amorphous (A) to crystalline (C) and from Sb_4 (S) to crystalline clusters. Only the number-weighted averages are listed.

Deposition	Size Averages (nm)			
Time (a. u.)	A	C	S	C
1	35	59	17	31
2	41	48	18	30
4	41	45	17	34

Secondly, as described in Section 3.4.2, it is well established that diffraction patterns reflect the structure of domains rather than that of the whole cluster. However, the majority of clusters studied by HRTEM were single-crystalline, although some clusters clearly consist of individual domains as can be seen in Figure 4.21(b). It is therefore to be expected that there is some disagreement between the size information from microscopy data and from the Scherrer equation. It has to be noted that the presence of domains would also render the discussion about the cluster shape invalid (see Section 4.2.1). In this case, the shape determined by the diffraction patterns would correspond to the shape of the domains and not the shapes of the particles themselves.

Thirdly, many FE-SEM images show that there is a mixture of crystalline and amorphous particles, even when the diffraction pattern shows strong crystalline features (see Figure 4.22(d)). As the peaks in the diffraction pattern from amorphous particles occur at similar scattering angles to the main peaks for crystalline particles, the resultant peak broadening most likely invalidates the use of the Scherrer equation and the comparison with calculated patterns. However, it would still be possible to distinguish large crystalline clusters from amorphous clusters as can be seen in Figure 4.25. If half or less than half of the clusters are amorphous, the pattern is clearly

dominated by the crystalline signal with narrow peaks (Figure 4.25(a) and (b)). If considerably more than half of the clusters are amorphous, however, the contribution from amorphous scattering takes over (Figure 4.25(c)). In an experiment it might be very hard to distinguish pattern (c) from a purely amorphous pattern.

Fourthly, the influence of oxidation has to be considered. The HRTEM images in Figure 4.21 clearly show that there is an amorphous oxide layer around the crystal lattice of all the clusters. The thickness of this layer is in the order of 2 nm. While this obviously has an influence on the size estimate results from the FE-SEM images, it does not explain the huge difference between the two methods.

Finally, a further possibility is that the diffraction peak width is limited by the resolution of the instrument. This would also explain why the results from the Scherrer equation do not show the same trends for changing

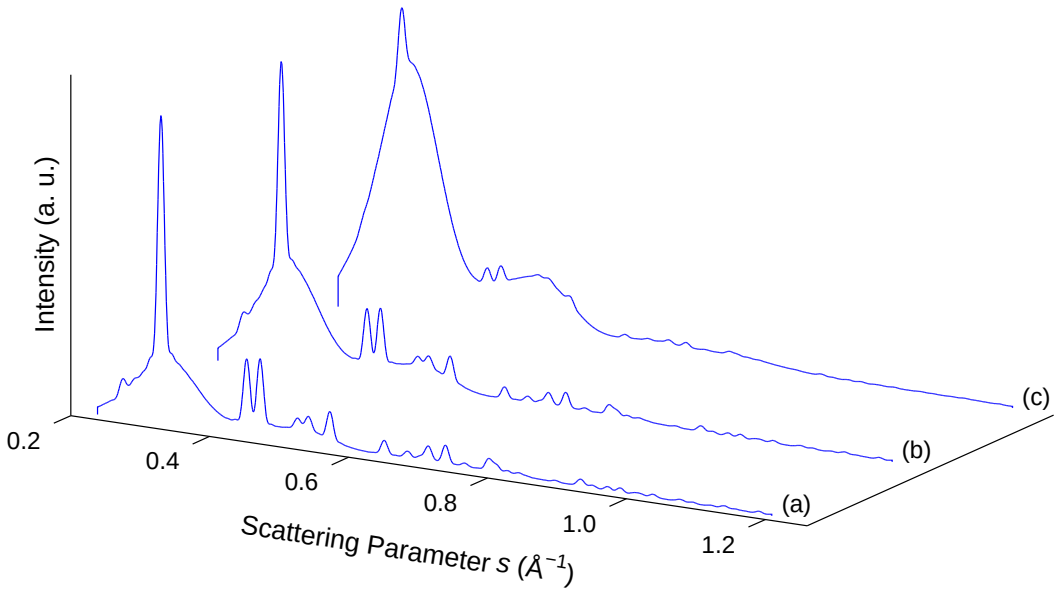

Figure 4.25: Calculated diffraction patterns from a mixture of amorphous and 10 nm crystalline particles. (a) 20% amorphous particles. (b) 50% amorphous particles. (c) 80% amorphous particles. The amorphous scattering pattern from Figure 3.14 has been used for these calculations.

source conditions as the size estimate from the deposited clusters. The polycrystalline films used for calibration of the diffraction patterns can be used to determine whether the instrument is able to resolve peaks for larger particles. While the exact size of the crystallites on the these films is not known, it can be assumed that they are considerably larger than 5 nm. Figure 4.26 shows the diffraction pattern from a polycrystalline Al sample which was used for calibration. These diffraction peaks in this pattern are obviously considerably narrower than the peaks in the patterns from clusters. To determine the size of the crystallites, the Scherrer equation was employed as described in Section 3.4.2. This results in a crystallite size for this particular pattern of 21 nm. While this measurement cannot be used to determine how accurate the results of the Scherrer equation in the present study are, it is evident that the instrumental resolution is high enough to record peaks corresponding to crystallite with a diameter of more than 20 nm.

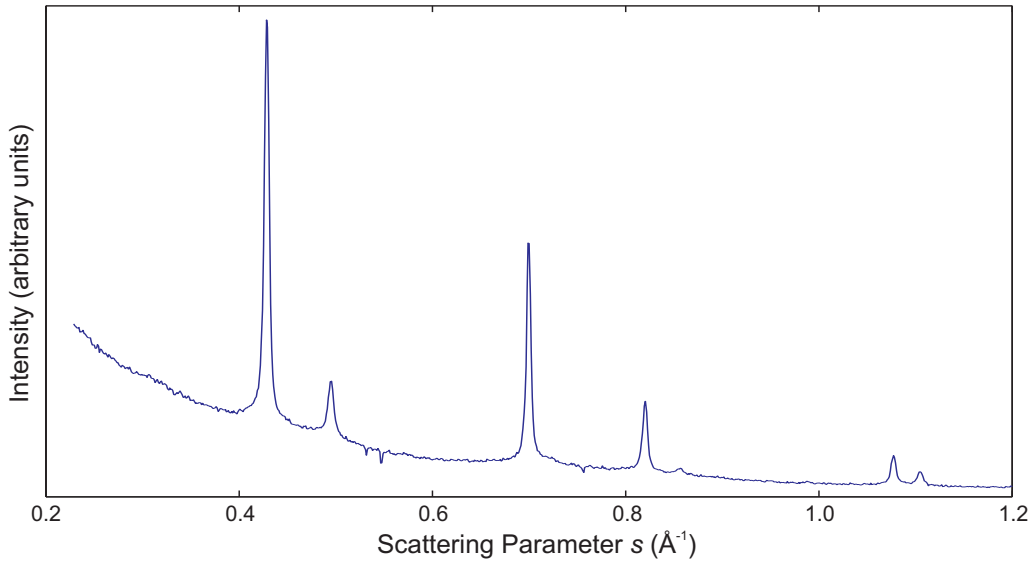

Figure 4.26: Diffraction pattern from a polycrystalline Al sample.

4.4 Conclusions

In the present chapter, the results from electron diffraction studies on Sb clusters as well as their size estimates and morphologies are presented. The electron diffraction patterns reveal three different structures: crystalline clusters, amorphous clusters, and clusters consisting of randomly oriented Sb_4 units. These three structures will be discussed below in more detail.

Using Ar as cooling gas, a transition from an amorphous to a crystalline structure was observed while increasing the source inlet gas flow rate or the temperature. The amorphous structure is in agreement with the structure found for Sb thin film deposition [10–13], although the bond length is smaller and the average bond angle larger than expected. A possible explanation might be the presence of compression in the clusters due to the effect of surface tension. The size distribution of all the amorphous samples investigated in this study is fairly narrow and lies between 30 and 40 nm. They all have a very regular spherical shape and do not adhere to the sample surface very well.

When He and a He/Ar mixture were used as the source inlet cooling gas, a transition from Sb_4 to crystalline diffraction patterns was observed for increasing flow rates or increasing Ar content. The measured bond length agrees well with the value from a theoretical model for Sb_4. FE-SEM images suggest, however, that individual tetramers are not present in the beam but rather large clusters consisting of randomly oriented Sb_4 units. While structures composed of tetramers have been known to exist for a long time for As as well as P, an analogous structure for bulk Sb or Sb nanoparticles has never been observed before. On average, the Sb_4 particles were the smallest particles observed with mean cluster sizes between 20 and 30 nm.

Since no diffraction patterns were observed which correspond to the structures proposed by Sattler [22] (see Figure 3.12), the packing of Sb tetramers to form a compact crystalline structure can be ruled out in the present experiments. Instead, on the basis of the data reported here, it appears that Sattler's mass spectra might be better explained using a model which incorporates a random (amorphous or liquid) packing of tetramers. It should be noted, however, that Sattler's experiments focussed on very

small Sb particles (up to Sb_{240}), while the clusters in our study had mean sizes of at least 20 nm and so direct comparison is problematic.

Crystalline clusters were observed for all types of cooling gas, whether pure Ar, pure He or a mixture of both was used. Increasing the source temperature, the gas flow rate or the Ar content (in case of a mixture of He and Ar) usually led to the formation of crystalline clusters. The structure of these clusters is in good agreement with the bulk structure. Since the signal-to-noise ratio was rather low, it was not possible to draw further conclusions about potential lattice contractions or about the temperature of the clusters. All crystalline diffraction patterns displayed a distinct background even after subtracting the scattering background due to the carrier gas. Several possible explanations have been discussed and the two most likely reasons seem to be the presence of small Sb molecules in the beam as well as lattice defects in the crystalline clusters.

The FE-SEM images show the crystalline clusters as strongly faceted particles with a wide size distribution. HRTEM images indicate that they are mostly single-crystalline. Furthermore, an amorphous oxide layer of approximately 2 nm thickness was visible in the HRTEM images. Although this layer could only be observed for the crystalline particles, it can be assumed that it also surrounds amorphous clusters as well as particles consisting of Sb_4 units. In these two cases, it would be very difficult to distinguish between the cluster structure and the oxide layer, since both are amorphous.

For crystalline clusters, the Scherrer equation was used as an additional method to estimate the particle size. However, the information from the microscopy images and from the Scherrer equation vary widely. According to the Scherrer equation, the crystalline particles in the present study have an average diameter of 3 to 5 nm, while the size distributions measured from the FE-SEM images range from at least 15 to more than 100 nm. The two methods also disagree on whether different source conditions have any influence on the cluster size. While the results from the Scherrer equation are all very similar, independent of source conditions, the analysis of the FE-SEM images seems to indicate several trends: the smallest crystalline clusters (between 15 and 35 nm diameter) are observed whenever He or a mixture of He and Ar was used as cooling gas. Using only Ar and

increasing the flow rate led to clusters in the range of 40 to 90 nm. The largest clusters were produced using high crucible temperatures and Ar as cooling gas. In this case, average cluster sizes of more than 100 nm were observed. This is in agreement with previous studies on Ag, Pb, and Bi clusters which found an increase in cluster size for higher source temperature and a decrease for higher flow rates and for a lower molecular weight of the cooling gas [2, 3, 7].

Several possible explanations for the disagreement in the cluster size estimates between the FE-SEM images and the Scherrer equation haven been discussed. The most likely reasons are the presence of domains as well as defects inside the clusters. To get a better understanding of this issue it would be very helpful to have a third method available which would allow the cluster size to be measured *in situ* but independent of the electron diffraction system. In the next chapter, the time-of-flight mass spectrometer is introduced which could provide such an alternative method.

References

[1] N. Wada, Jpn. J. Appl. Phys. **7**, 1287 (1968).

[2] M. Hyslop, *Electron Diffraction Studies of Unsupported Clusters*, PhD thesis, University of Canterbury, 2002.

[3] A. Wurl, *Electron Diffraction Studies of Unsupported Bismuth Clusters*, PhD thesis, University of Canterbury, 2003.

[4] T. B. Rymer, *Electron Diffraction*, Methuen & Co Ltd, 1970.

[5] P. Bayliss, L. G. Berry, M. E. Mrose, and D. K. Smith, editors, *Mineral Powder Diffraction File*, JCPDS, 1980.

[6] D. Reinhard, *Croissance et Stabilité d'Agrégats d'Argent et de Cuivre, Etudiés en Jets Moléculaires par Diffraction d'Electrons à Haute Energie*, PhD thesis, Ecole Polytechnique Fédérale de Lausanne, 1996.

[7] B. D. Hall, *An Installation for the Study of Unsupported Ultrafine Particles by Electron Diffraction with Application to Silver: Observation of Multiply Twinned Particle Structures*, PhD thesis, Ecole Polytechnique Fédérale de Lausanne, 1991.

[8] K. Andrews, D. Dyson, and S. Keown, *Interpretation of Electron Diffraction Patterns*, Adam Hilger Ltd, 1971.

[9] J. Donohue, *The Structures of the Elements*, John Wiley & Sons, 1974.

[10] H. Richter, H. Berckhemer, and G. Breitling, Z. Naturforsch. A **9**, 236 (1954).

[11] J. A. Prins, Nature **131**, 760 (1933).

[12] H. Hendus, Z. Phys. **119**, 265 (1942).

[13] H. Krebs and R. Steffen, Z. Anorg. Allg. Chem. **327**, 224 (1964).

[14] G. N. Greaves, S. R. Elliott, and E. A. Davis, Adv. Phys. **28**, 49 (1979).

[15] B. Reddy and P. Jena, Chem. Phys. Lett. **288**, 253 (1998).

[16] A. Guinier, *X-Ray Diffraction in Crystals, Imperfect Crystals, and Amorphous Bodies*, W. H. Freeman and Company, 1963.

[17] J. Kordis and K. A. Gingerich, The Journal of Chemical Physics **58**, 5141 (1973).

[18] G. Fuchs *et al.*, Philos. Mag. B **63**, 715 (1991).

[19] H. Levinstein, J. Appl. Phys. **20**, 306 (1949).

[20] J. G. Partridge *et al.*, Nanotechnology **15**, 1382 (2004).

[21] P. Melinon *et al.*, Phys. Rev. B **44**, 12562 (1991).

[22] K. Sattler, J. Mühlbach, P. Pfau, and R. Recknagel, Phys. Lett. **87A**, 418 (1982).

Chapter 5

Time-of-Flight Mass Spectrometer

This chapter focusses on time-of-flight (TOF) mass spectrometry. The first part presents a general overview of various types of mass spectrometers followed by an in-depth study of time-of-flight mass spectrometers (TOFMS) in particular. For this thesis, a TOFMS for cluster analysis has been designed, built and tested. This is described in detail in a second part of this chapter starting with a detailed presentation of all the components involved including the ioniser and two different types of detectors. It is followed by an introduction to the ion optics simulation software used to model the TOFMS. Finally, the results of experiments on gas as well as cluster beams and the comparison to simulations are presented.

5.1 Mass Spectrometers in General

Mass spectrometers are a powerful tool used to identify atoms or molecules by measuring the ratio of mass to charge. They usually consist of three main parts: an ion source where the material is ionised, an analyser where the ions are separated according to their mass-to-charge ratio m/z, and a detector to record the ions.

Three of the main techniques used for mass analysis are explained in more detail below.

5.1.1 Magnetic Analyser

An ion with mass m and charge ze (where e is the electronic charge and z is the number of charges) is accelerated in a potential V to a kinetic energy $zeV = \frac{1}{2}mv^2$. In a magnetic field B which is perpendicular to the flight path of the ion it gets deflected by the Lorentz force F as shown in Figure 5.1 [1]:

$$F = zevB \tag{5.1}$$

The ion therefore flies in a circle with radius r which is defined by the equilibrium of centripetal and Lorentz force:

$$F = \frac{mv^2}{r} = zevB \tag{5.2}$$

which leads to the following equation for the ratio of mass to charge:

$$\frac{m}{z} = \frac{rB}{v} = \frac{eB^2r^2}{2V} \tag{5.3}$$

If a group of ions is let into the analyser, all ions are forced on different circles according to their mass-to-charge ratio. By varying the magnetic field B while leaving the acceleration potential V constant or by varying

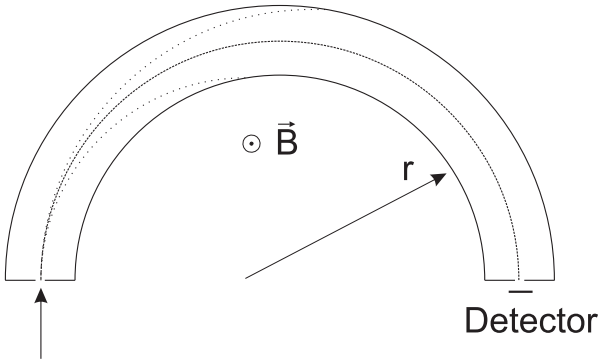

Figure 5.1: Schematic of a magnetic analyser: positively charged particles are flying into the analyser from the left hand side and the magnetic field points towards the reader. After [1].

V while leaving B constant, it is possible to detect ions with a specific m/z value. By scanning through a large range of B or V values a full mass spectrum can be recorded.

The main advantages of magnetic analysers are the high mass resolution and the sensitivity for heavy particles. The disadvantages are size and cost of the apparatus, the slow scan speed if the magnetic field is varied (because of hysteresis), and time required to record a whole spectrum. Magnetic analysers work best with a continuous particle beam and are not suited for pulsed sources or ionisation methods.

5.1.2 Quadrupole Analyser

A quadrupole analyser consists of four parallel rods (see Figure 5.2). A constant DC voltage U and a superimposed AC voltage $V\cos(\omega t)$ of opposite polarity are applied between opposite pairs of the rods. Ideally the rods have a hyperbolic shape to create a homogeneous quadrupole field but in practice, a cylindrical shape is typically chosen. The ions fly through the analyser along the x-axis. Their flight path is influenced by the variable field in the yz-plane. The different voltages can be adjusted so that only ions with a certain mass-to-charge ratio are able to pass through. All other ions fly on unstable trajectories which do not lead to the detector. The quadrupole analyser is mainly used as a mass selector. In this case the DC voltage and the amplitude of the AC voltage is varied relative to each other while the frequency stays constant.

The benefits of quadrupole analysers are their compactness and low cost, while the drawbacks are the limited resolution, the reduced sensitivity for higher masses, and the time required to record a whole spectrum. As in the case of magnetic analysers, they are also not suited for pulsed beams. To achieve the highest possible mass resolution, the shape of the rods has to be hyperbolic and it has to be machined to high precision.

5.1.3 Time-of-Flight Analyser

In a time-of-flight analyser, ions are accelerated in an electric field, travel through a field-free drift region and are registered by a detector. As lighter

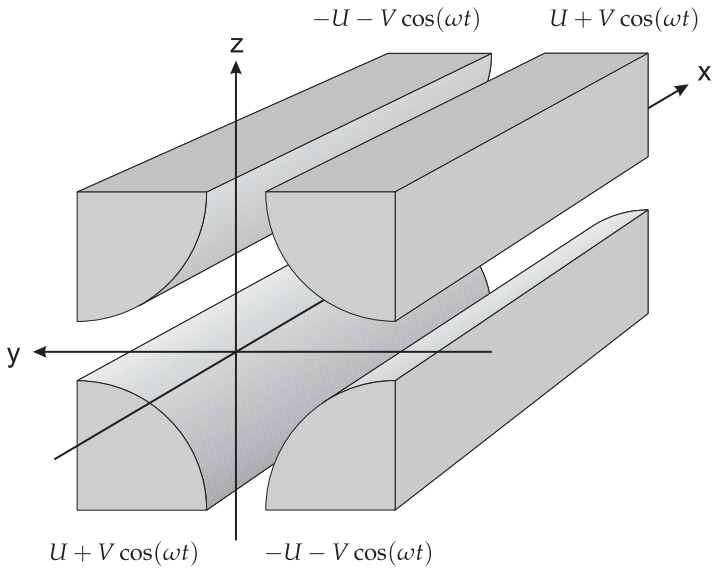

Figure 5.2: Schematic of a quadrupole analyser: Parts of the analyser rods are shown together with the corresponding fields. After [1].

ions reach higher velocities during acceleration than heavier ions, they require less time to arrive at the detector. Measuring the time differences at the detector allows the relative mass of the ions to be determined. A detailed description of this type of mass spectrometer is found in the following section.

5.2 Time-of-Flight Mass Spectrometer in Detail

A basic time-of-flight mass spectrometer (TOFMS) consists of an ion source and an accelerating field on one side of an evacuated tube and a detector on the other side (see Figure 5.3).

The TOFMS is operated in a pulsed mode where either the ion source or the field of the acceleration region is pulsed. This pulse serves as a starting point for the time measurement. In the acceleration region, the lighter ions – as well as the multiply charged ones – reach a higher velocity than the heavier or singly charged ions. The kinetic energy of an ion with mass m is

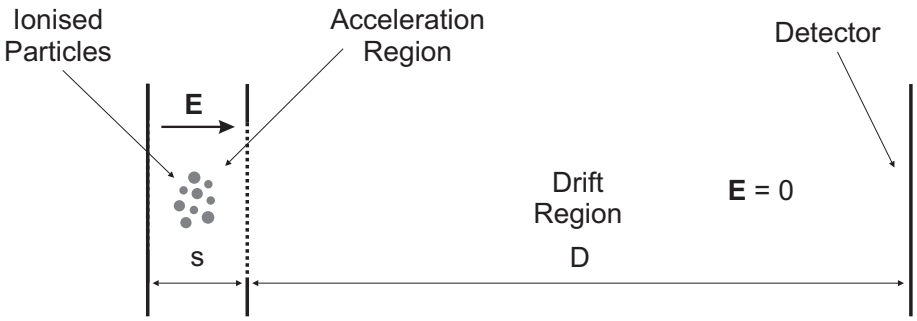

Figure 5.3: Basic layout of a time-of-flight mass spectrometer. Ionised particles are accelerated by an electric field E in the first region s and fly through the field-free drift region D.

given by the following equation (assuming that the particles are stationary before they are accelerated) [2]:

$$E_{\text{kin}} = \frac{1}{2}mv^2 = zeV \tag{5.4}$$

where V is the potential applied to the acceleration region. Consequently, the ion velocity in the drift tube is given by the following equation:

$$v = \sqrt{\frac{2zeV}{m}} \tag{5.5}$$

Thus, the ion velocity is inversely proportional to the square root of the mass-to-charge ratio. The time of flight for a drift tube with length D is then given by:

$$t = \frac{D}{v} = D\sqrt{\frac{m}{2zeV}} \tag{5.6}$$

Note that this equation is only an approximation for the flight times of the ions as it neglects the time spent in the acceleration region.

For each ion, the flight time is recorded by the detector. This time is proportional to the square root of the mass-to-charge ratio. If the flight times of at least two ions with known mass and charge are determined, (5.6) allows calibration of the mass spectrometer. The calibration function

is given by the following expression:

$$t = A \cdot \sqrt{\frac{m}{z}} + B \tag{5.7}$$

The offset B contains the delay time of electronics and detector as well as the finite rise-time of the pulsed field [3].

The two main advantages of a TOFMS compared to other mass spectrometers are the high mass range and the speed with which a complete spectrum can be recorded. In a conventional TOFMS, the mass range is only limited by the high-mass sensitivity of the detector. In contrast to most other mass spectrometers, a TOFMS is able to record a whole spectrum at once. A duty cycle of at least several kHz is possible. An additional advantage is the ability to record one complete spectrum per acceleration pulse. Most other mass spectrometers work mainly as mass filters and allow only the ions of a specific mass-to-charge ratio to reach the detector. In order to record a full spectrum, the mass analyser has to scan through the whole range of possible parameters. The efficiency of a TOFMS is especially important if the number of ions is limited or the properties of the ion beam change quickly. In the latter case, the TOFMS allows, for example, observation of the influence of source parameters on the mass spectrum in real-time. A third advantage is that the accuracy of a TOFMS depends mostly on the electronic components and not on the stability of magnetic fields or the precision of mechanical parts. The pulsed nature of a TOFMS also makes it more suitable for applications with pulsed particle sources.

For a long time, the main disadvantage, on the other hand, was the limited resolution of a TOFMS compared to other spectrometers. However, there are two designs which address this drawback: the first, the so-called reflectron, uses an electrostatic mirror or reflector at the end of the flight tube [4], while in the second design an additional acceleration region is included between the acceleration region and the drift tube [5]. This design is named after its developers, Wiley and McLaren, and will be discussed in detail below.

5.2.1 Resolution of a TOFMS

To fully understand the advantage of the Wiley-McLaren system, a few general properties of TOF spectrometers have to be considered first. Ideally, all ions start from the same point or at least in a plane parallel to the detector. Additionally, they would also have no initial velocity in the direction of the drift tube. In this ideal system the flight time would be exactly the same for all ions with the same mass-to-charge ratio, and the resolution would only be defined by the detector and the electronics. In practice, however, the resolution is limited by a number of factors described below.

Definition of Resolution

The resolution of a mass spectrometer is the ability to distinguish an ion of mass m from one of mass $m + \Delta m$. It is defined by the following expression [6]:

$$R = \frac{m}{\Delta m} \tag{5.8}$$

To measure the resolution of an experimental spectrum, the definition has to be translated into the time domain. The relationship between the mass and the time of flight was given in (5.7) as $m = At^2$ where A is a constant (assuming no offset). The time derivative of this expression is given by

$$\frac{\mathrm{d}m}{\mathrm{d}t} = 2At \tag{5.9}$$

For finite intervals, this leads to $\Delta m = 2At\Delta t$. The resolution in (5.8) can therefore be written as

$$R = \frac{m}{\Delta m} = \frac{t}{2\Delta t} \tag{5.10}$$

There are several definitions for the distinction between two peaks: according to one definition, a peak of time $t + \Delta t$ can be distinguished from a peak of time t if the height of the valley between these two peaks is at most half of the height of the two peaks (50% valley definition; see Figure 5.4). An alternative and much stronger definition requires the height of the valley to be at most 10% of the peak height (10% valley definition). In TOF mass spectrometry the 50% valley definition is commonly used which

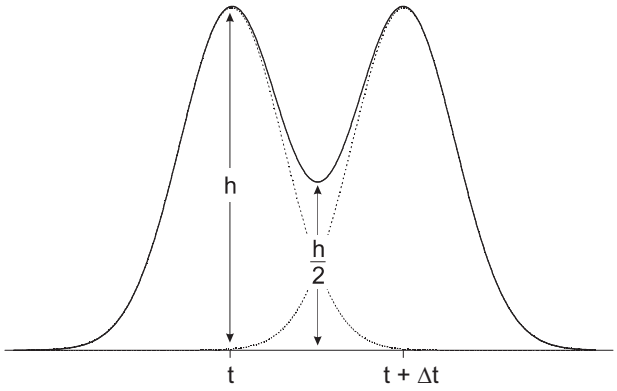

Figure 5.4: Resolution of a mass spectrometer: 50% valley definition. After [1].

leads to a resolution which is about twice as good compared to the 10% definition [6]. In the case of only one peak, Δt is defined as the full width at half maximum (FWHM) which is equivalent to the 50% valley definition.

In practice, the resolution of a TOFMS is limited for several reasons, the three main factors being the initial space, time and kinetic energy distributions of the ions in the acceleration region. These three effects will be discussed in more detail below. Additional effects are non-ideal electric fields and the response time of detector and electronics.

Time Distribution

The initial time distribution is the maximum time difference between the ionisation of any two particles. The time difference stays constant during the whole time of flight and its influence on the resolution is given by (5.10). To improve the resolution in this case, the time of flight can be increased by decreasing the acceleration voltage or by extending the drift region (e.g. using a reflectron). Alternatively, an ionisation method with shorter pulse times can be used (e.g. laser desorption ionisation) or the particles can be ionised outside the acceleration region. The latter method is widely used for cluster beam applications as some particle sources generate already ionised clusters. The time distribution then only depends on the rise time of the pulsed acceleration field.

Space Distribution

The initial space distribution is due to the variation of starting positions of ions of the same mass. An ion which starts closer to the drift region spends less time in the acceleration region and receives less kinetic energy than an ion formed further away from the drift region. Since the latter ion is accelerated to a higher velocity, it will eventually overtake the slower ion. The location at which the two ions with starting positions $s = s_0 \pm \frac{1}{2}\delta s$ (where s_0 is the average initial starting position) pass each other can be calculated by the following expression [7]:

$$\left(\frac{\mathrm{d}t}{\mathrm{d}s}\right)_{s_0} = 0 \tag{5.11}$$

This condition is fulfilled if $D = 2s_0$ [7] and the location is called the space focus plane. A design which follows this condition would have to use a very short drift tube (in practice, they are typically between half a metre and several metres long) or a very long acceleration region. A long acceleration region is not practical since the field would be greatly weakened (assuming that the acceleration voltage would remain constant). A short drift region, on the other hand, leads to short flight times which would worsen the influence of an initial time spread as described above. Additionally, the whole TOF spectrum is compacted into a shorter time range which requires an improved digitiser resolution.

The initial space distribution is a particular problem for molecular beam experiments where the TOFMS is mounted in the direction of the beam. Since particles are continually entering the acceleration region, there is a wide spread in initial starting positions leading to a low resolution. It is, however, possible to change the orientation of the whole TOFMS so that it is orthogonal to the beam direction (this set-up is called orthogonal acceleration TOFMS or oa-TOFMS). The initial space distribution then only depends on the dimensions of the beam in the direction of the TOFMS and can be controlled using a lens or a collimator at the entrance to the TOFMS. This particular set-up is used in the present study and will be discussed in Section 5.3.

Kinetic Energy Distribution

The distribution of initial kinetic energies in the direction of the TOFMS axis influences the velocities of the ions in the drift region. In the worst case, two ions have the same kinetic energy but opposite direction, one pointing towards the detector and the other one away from it. The latter ion has to be decelerated to zero first before being accelerated towards the detector, passing through the starting point again with the same kinetic energy as the former ion. The time it takes to reach this point is called the turn-around time. This time difference will remain constant until the two ions reach the detector leading to a decreased resolution. The turn-around time can be reduced by increasing the field of the acceleration region. Its influence can also be lessened by extending the drift region as the situation is equivalent to the time distribution discussed above.

The case where the two ions have different velocities but the same direction has to be treated individually. Here, a longer flight time would decrease the resolution. A possible solution is the use of a reflectron which can correct for different velocities. However, this method does not correct for the turn-around time [8]. For both cases, the so-called *time-lag focussing* technique can be applied where a time delay between ionisation and acceleration is introduced. During this time, the ions spread out and the resulting spatial distribution can be compensated as described in the last section. The ideal time delay, however, is mass dependent and this method does therefore not work over the whole mass spectrum [6].

It is noteworthy that the reduction of the initial energy distribution and space distribution require opposite measures: While a low acceleration voltage can compensate for space distribution, a high acceleration voltage is required to compensate for the energy distribution [9]. Hence the best resolution will be achieved through a compromise between reducing the initial energy and space distribution. For a conventional linear TOFMS (without ion reflector), it has been shown analytically that the Wiley-McLaren TOFMS discussed below reaches the highest possible reduction of energy distribution [10].

For molecular beams, the use of orthogonal acceleration reduces the influence of initial energy distribution as the velocity spread perpendicular

to the beam is negligible compared to the spread of cluster velocities in the direction of the beam.

5.2.2 The Wiley-McLaren TOFMS

As mentioned above, the Wiley-McLaren TOFMS contains two acceleration regions instead of only one, while all other components stay the same as in a conventional TOFMS. Figure 5.5 shows a schematic of a Wiley-McLaren TOFMS. This figure also shows an additional post-acceleration region between the end of the drift region and the detector which was omitted in Figure 5.3.

The second acceleration region is particularly beneficial for reducing the initial spatial distribution discussed in the last section. It is located at the space focus plane, thereby acting as a virtual ion source. This second region adds two new parameters – namely the length of the second region and the ratio of the two acceleration fields – which allow space focussing with a more favourable geometry than in the original set-up with only one acceleration region. The effect of the additional acceleration region on the resolution is discussed in detail below.

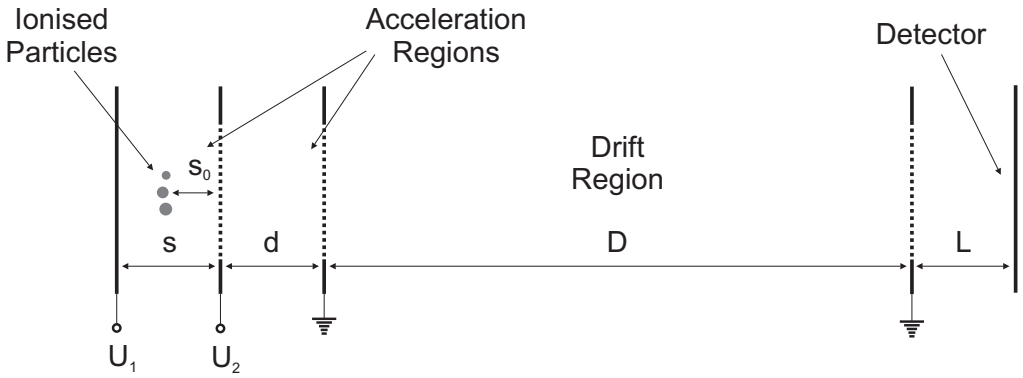

Figure 5.5: Schematic of a Wiley-McLaren TOFMS with two acceleration regions s and d, a drift region D, and a post-acceleration region L. s_0 is the average starting position of the ions. U_1 and U_2 are the voltages applied to the first and second acceleration region.

Calculation of Time-of-Flight

The total time of flight of an ion of mass m and charge z is equal to the sum of the individual times of all the regions:

$$t = t_s + t_d + t_D \tag{5.12}$$

Note that the time of the last region, t_L, has been omitted as it is negligible in most cases. Refer to Figure 5.5 and Table 5.1 for the nomenclature used for the calculations. If the electric fields of the two acceleration regions are given by

$$E_s = \frac{U_1 - U_2}{s} \quad \text{and} \quad E_d = \frac{U_2}{d} \tag{5.13}$$

the individual flight times can be calculated using (5.6) [7]:

$$t_\mathrm{s} = \frac{\sqrt{2m}}{zeE_\mathrm{s}} \left(\sqrt{zeE_\mathrm{s}s_0 + W_0} \pm \sqrt{W_0} \right) \tag{5.14}$$

$$t_\mathrm{d} = \frac{\sqrt{2m}}{zeE_\mathrm{d}} \left(\sqrt{zeE_\mathrm{s}s_0 + zeE_\mathrm{d}d + W_0} - \sqrt{zeE_\mathrm{s}s_0 + W_0} \right) \tag{5.15}$$

$$t_\mathrm{D} = D\sqrt{\frac{m}{2(zeE_\mathrm{s} + zeE_\mathrm{d} + W_0)}} \tag{5.16}$$

W_0 is the initial kinetic energy and its sign in (5.14) depends on the initial direction of the particle along the TOFMS axis. If the initial energy is set to zero, the total flight time can be written as

$$t = \sqrt{\frac{m}{2ze(E_\mathrm{s}s + E_\mathrm{d}d)}} \left(2s_0\sqrt{k} + \frac{2d\sqrt{k}}{\sqrt{k}+1} + D \right) \tag{5.17}$$

where k is defined as

$$k = \frac{E_\mathrm{s}s_0 + E_\mathrm{d}d}{E_\mathrm{s}s_0} \tag{5.18}$$

As discussed above, space focussing can be achieved by setting

$$\left(\frac{\mathrm{d}t}{\mathrm{d}s} \right)_{s_0} = 0 \tag{5.19}$$

which leads to

$$D = 2s_0 k^{3/2} \left(1 - \frac{1}{k + \sqrt{k}} \frac{d}{s_0}\right) \tag{5.20}$$

Once the geometry of the TOFMS is defined, this equation can be solved numerically to determine the optimal k.

Table 5.1: TOFMS nomenclature used in this work.

Quantity	Symbol	Description
Mass	m	ion mass
Charge	e	charge of electron
	z	number of electron charges
Distance	s	distance of first acceleration region
	s_0	average ion starting position
	d	distance of second acceleration region
	D	drift distance
	L	distance of post-acceleration region (between end of drift tube and detector)
Time	t	total time of flight
	t_s	time of flight in first acceleration region
	t_d	time of flight in second acceleration region
	t_D	time of flight in drift tube
	t_L	time of flight in post-acceleration region
Potential	U_1	potential of first electrode
	U_2	potential of second electrode
	U_det	potential of detector
Electric field	E_s	electric field of first acceleration region
	E_d	electric field of second acceleration region
	E_det	electric field of post-acceleration region
Energy	W_0	initial kinetic energy of ion

5.3 Design

The following section describes the TOFMS which has been built for this study. Most of the design, set-up and installation were done in collaboration with Dr Bernhard Kaiser from the Humboldt University in Berlin. The design is based on the Wiley-McLaren set-up described above. The position of the TOFMS relative to the cluster source and electron beam for diffraction experiments is shown in Figure 5.6.[1] As the TOFMS replaces the sampling device described in Section 2.3, they cannot be used at the same time. The spectrometer axis is perpendicular to the cluster beam axis. As discussed above, this design reduces the initial energy distribution significantly compared to a coaxial design. However, it would not have been possible to position the spectrometer on axis, as the space further downstream is used by one of the turbo pumps (see Figure 2.1).

Figure 5.7 shows a schematic of the actual set-up. All size information corresponding to this schematic are given in Table 5.2. The dimensions of the two acceleration regions were kept short to achieve high field strengths without having to switch very high acceleration voltages. However, it would be very straightforward to adjust the relative distances of these two regions. The flight tube is relatively short with a length of 417 mm. However, a high resolution is not crucial to determine the average cluster masses of interest here. It is more important to achieve a high throughput. Since the TOFMS is mounted orthogonally, increasing the drift tube length would lead to a loss of signal.

5.3.1 Acceleration and Drift Regions

The outer dimensions of the spectrometer are restricted by the flange it is mounted to. The inner diameter of this flange (ISO63) is 70 mm and the distance between the flange and the centre of the cluster beam is 257 mm. The two acceleration regions and the drift region are shown in Figure 5.8.

[1] The TOFMS and the electron diffraction experiment are not meant to be run completely simultaneously as the electric fields of the TOFMS could disturb the electron scattering. It is envisaged that alternate mass spectra and electron diffraction patterns would be obtained.

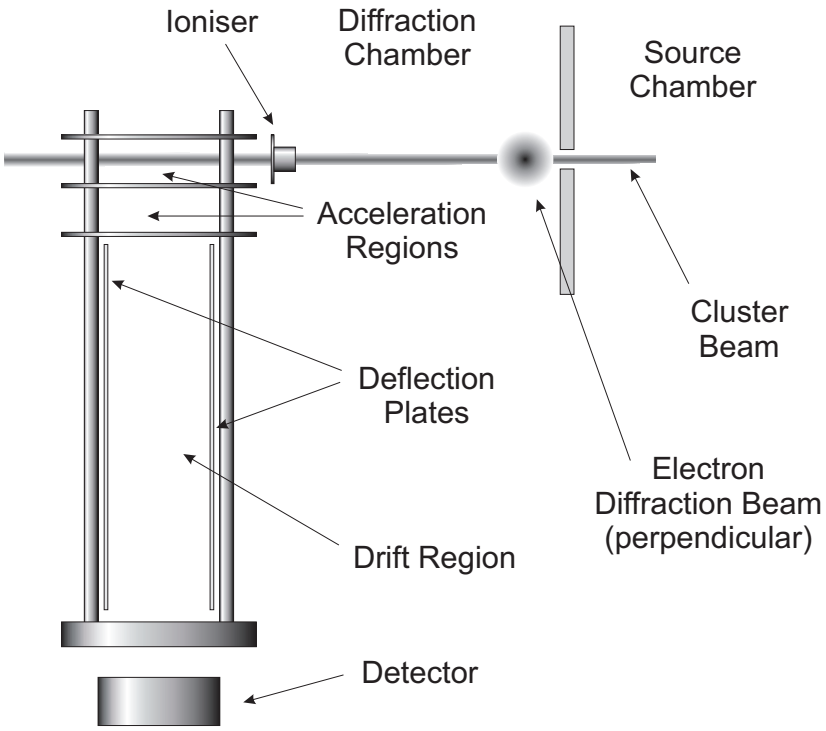

Figure 5.6: Top view of vacuum chamber and TOFMS (not to scale).

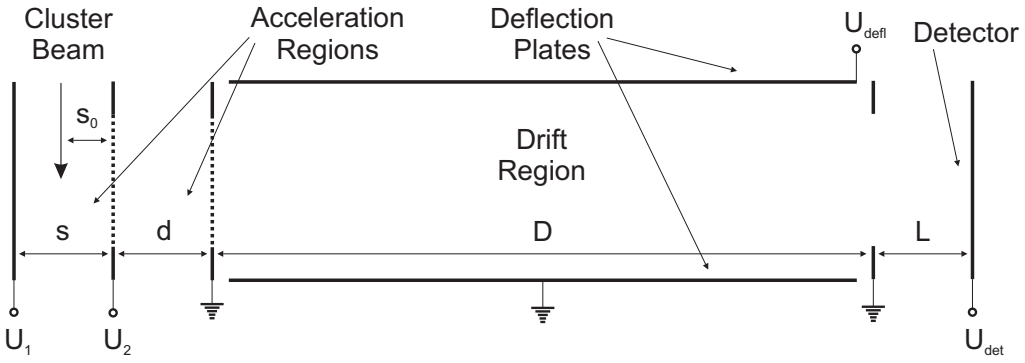

Figure 5.7: Schematic of the TOFMS used in the present work. The nomenclature is defined in Table 5.1 and the dimensions are given in Table 5.2.

Table 5.2: Dimensions of the TOFMS as shown in Figure 5.7.

First acceleration region		$s = 20\,\text{mm}$
Average ion starting point		$s_0 = 10\,\text{mm}$
Second acceleration region		$d = 20\,\text{mm}$
Drift region		$D = 417\,\text{mm}$
Post-acceleration region	for Daly detector	$L = 23\,\text{mm}$
	for MCP detector	$L = 20\,\text{mm}$

Four stainless steel rods are mounted on a flange where the drift region ends. This flange needs to be double-sided to enable the TOFMS to be attached to the system on one side and the detector to the TOFMS on the other side. The round backplate which forms one side of the first acceleration region is made from 1 mm brass as are the two annular plates which hold the grids between first and second acceleration region and between second acceleration region and drift tube. These meshes consist of 27 nickel wires per centimetre and have a transmissivity of 90%.[2] Silver paint was used to attach the meshes to the rings. The backplate and the rings are held in place by spacers which insulate them against the support rods and define the distances between all the elements.

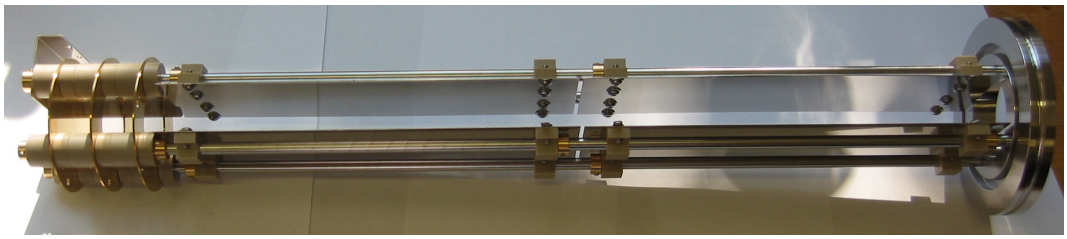

Figure 5.8: The acceleration regions and the drift tube of the TOFMS. The detector is not shown.

The acceleration voltages are supplied by two 5 kV power supplies[3] which are connected to two high-voltage switches[4] which drive the pulsed

[2] The manufacturer of the meshes is Buckbee Mears (type BM0070-01-N).

[3] Two types of power supplies were used for the experiments: Stanford Research PS350 (5 kV, 5 mA) and Spellman MP5 (5 kV, 2 mA).

[4] Behlke GHTS 60 (100 ns pulse delay time).

fields. The control pulses for the high-voltage switches are supplied by a pulse generator which was built by the local electronic workshop. The pulse length is continuously adjustable from 400 ns to 15 ms and the frequency from 10 Hz to 88 kHz. The second mesh is grounded by a connection to the support rods.

The deflection plates consist of four aluminium plates (two on each side) which are each 195 mm long, 54 mm wide and 0.5 mm thick. The distance between the two sides – which corresponds to the width of the flight tube – measures 23 mm. They are screwed onto spacers which are attached to the support rods. Using two plates instead of one per side allows the set-up of two independent deflection fields if required. The deflection voltage is supplied by a 300 V power supply.[5]

Optimisation of Parameters and Expected Resolution

Using the optimisation procedure discussed in Section 5.2.2 and the geometry of the system described above, the acceleration voltages can be optimised. For the values in Table 5.2, space focussing using condition (5.19) and expression (5.20) leads to $k \simeq 8.6$ where k is given as

$$k = \frac{E_s s_0 + E_d d}{E_s s_0} \tag{5.21}$$

Solving this equation for the ratio of the electric fields, E_d/E_s, leads to the expression

$$r_E = \frac{E_d}{E_s} = \frac{s_0}{d}(k-1) \simeq 3.8 \tag{5.22}$$

Setting the first voltage to 4500 V allows calculation of the second voltage:

$$U_2 = \frac{U_1}{1 + \frac{1}{r_E}} \simeq 3563\,\mathrm{V} \tag{5.23}$$

Once all the parameters are fixed, the theoretical resolution of the TOFMS can be determined according to Wiley-McLaren [7] which consists

[5] Spellman MS0.3 (300 V, 10 mA).

of space resolution

$$R_s = \left(\frac{m}{\Delta m}\right)_s \simeq 16k\left(\frac{s_0}{\Delta s}\right)^2 \tag{5.24}$$

and energy resolution

$$R_E = \left(\frac{m}{\Delta m}\right)_E = \frac{1}{4}\sqrt{\frac{E}{\Delta E}}\left(\frac{k+1}{\sqrt{k}} - \frac{\sqrt{k}-1}{k+\sqrt{k}}\frac{s}{s_0}\right) \tag{5.25}$$

where E is defined as $E = ze(E_s s_0 + E_d d)$. In these two equations, Δs stands for the initial space distribution and ΔE for the energy distribution. Δs corresponds to the diameter of the aperture at the exit of the ioniser which is 7 mm. ΔE can be estimated to be approximately 20 meV [11]. The total resolution is then given as

$$R_{\text{total}} = \left(\frac{1}{R_s} + \frac{1}{R_E}\right)^{-1} \simeq \left(\frac{1}{281} + \frac{1}{330}\right)^{-1} = 152 \tag{5.26}$$

5.3.2 Ioniser

As the clusters generated by the inert-gas source are neutral, they have to be ionised before reaching the spectrometer. The two most common ionisation methods are photoionisation using a laser or a UV lamp and electron ionisation [12]. For this study, electron impact ionisation is used where thermionic electrons are emitted from a heated filament and accelerated through a grounded grid forming a cylindrical anode cage as shown in Figure 5.9. Inside this cage, the electrons cross the cluster beam where they knock electrons off the clusters leading to positively charged particles. Depending on the type of atoms, the ionisation efficiency reaches a maximum for an electron energy between 20 and 100 eV [13]. If the energy is too high and the excess energy surpasses the binding energy of the clusters, fragmentation can occur. The resulting mass spectrum might therefore not correspond to the neutral mass distribution. There is also the possibility that slow electrons are captured by the clusters leading to negatively charged particles [14].

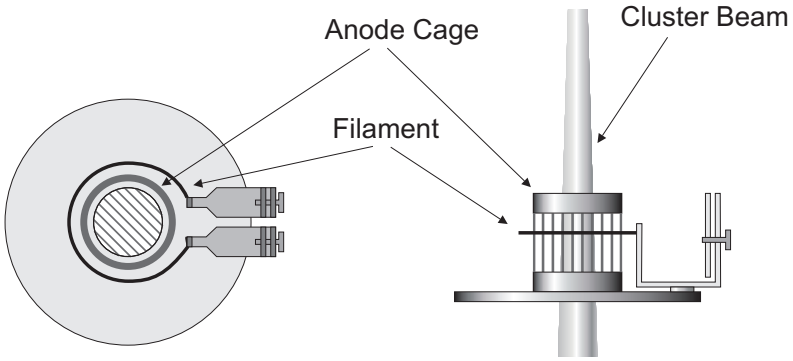

Figure 5.9: Schematic top view (left) and side view (right) of the ioniser. The shield which encloses the ioniser is not shown.

The filament is made of thoriated tungsten wire with 0.1 mm diameter.[6] Adding thorium lowers the work function from 4.54 eV for pure tungsten to 2.63 eV and also means that the maximum emission is reached at a lower temperature [15]. The power supply for the filament current floats at a voltage (usually between −30 and −70 V) to provide the electrons with the necessary energy.[7] The filament current is usually run at approximately 1.5 A. If the current is too high, electrons start to flow directly onto the grounded stainless steel shield which encloses the ioniser. This in turn decreases the potential applied to the filament as the power supply cannot cope with such a high current.

After being ionised, the clusters fly out of the ioniser through a grounded grid with a diameter of 7 mm. This diameter also defines the maximum space distribution in the first acceleration region.

5.3.3 Detector

There are several different techniques for charged cluster detection, all with their advantages and disadvantages. For the present study, two different

[6] The exact composition is 99.4% W and 0.6% Th (Goodfellow, type W 055250).

[7] For the filament current a DSE power supply (30 V, 5 A) was used and for the offset voltage a Spellman MS0.3 (300 V, 10 mA, negative polarity).

types of detectors were chosen: a Microchannel Plate (MCP) detector and a Daly detector. These two methods are presented below in detail.

MCP Detector

The MCP detector is an electron multiplier which consists of an array of fine channels joined together in a lead glass plate (see Figure 5.10) [12, 16]. There are between 10^4 to 10^7 channels with a diameter of 10–100 µm. The thickness of the plate is usually in the range of a few millimetres and the plate is coated on each side with a metallic layer. A positive potential difference is applied between the front and the back of the plate with a total resistance of the order of GΩ.

The walls of the channels are lined with a semiconducting layer. If a charged particle impinges on the entrance of a channel, it produces secondary electrons in the semiconducting layer. The secondary electrons are accelerated by the potential difference between the front and back of the plate and hit the channel walls again releasing more electrons leading to an avalanche effect. The resulting gain is on the order of 10^4 to 10^7. If the gain reaches a certain level, the high density of electrons on the back of the plate causes ionisation of residual gas molecules. These ions can then drift back to the front of the plate where they start a new electron cascade. To avoid this ion feedback, MCPs are often used in a so-called Chevron

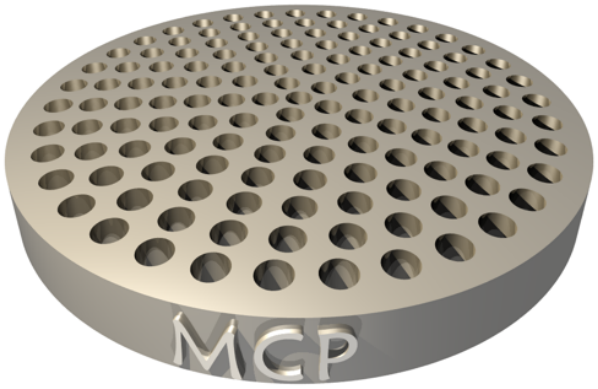

Figure 5.10: Illustration of an MCP (the dimensions are not to scale). After [16].

configuration as can be seen schematically in Figure 5.11. In this set-up, two MCPs with lower gain are installed in series with the channels of one plate at a bias angle relative to the channels of the other plate (the angles are typically $\pm 8°$). The two plates are separated by approximately 50 to 150 µm.

The main strengths of an MCP detector are the very high time resolution (< 100 ps) and the high gain (especially in the Chevron configuration). Additionally, it can detect positively as well as negatively charged particles and it can also be used for position-sensitive detection with a space resolution corresponding to the channel dimensions and spacings. The low dark-current is also an advantage. On the other hand, there are several restrictions: Firstly, there is a threshold velocity that a particle has to exceed to release an electron from the surface. This is a crucial disadvantage for the detection of heavy clusters in a TOFMS: as the kinetic energy of all ions in the drift tube is constant, the velocity decreases for heavy ions. In the literature, the velocity threshold is found to be around 2×10^5

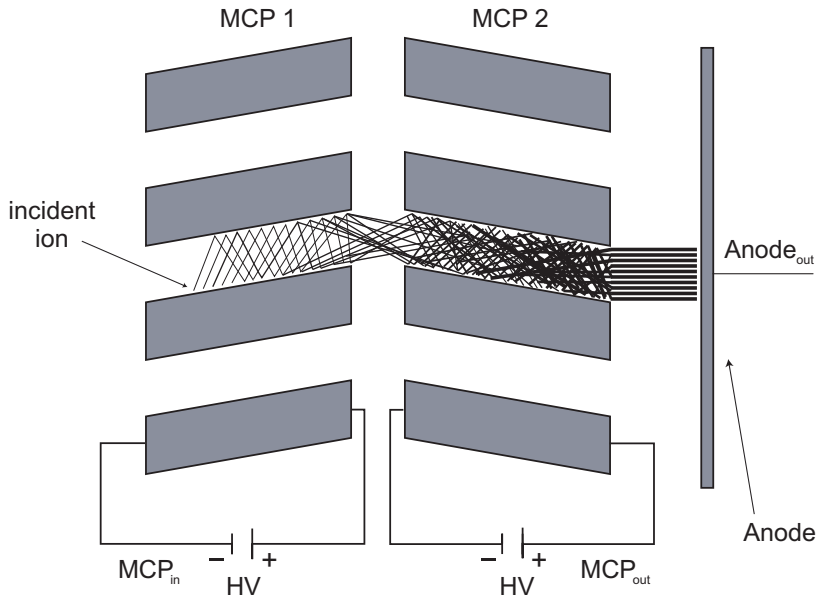

Figure 5.11: Schematic side view of an MCP in Chevron configuration (not to scale).

to $1\times10^{6}\,\mathrm{ms}^{-1}$ [17, 18]. However, in one study it was possible to detect clusters with a velocity as low as $1\times10^{3}\,\mathrm{ms}^{-1}$ using an MCP detector [19]. Secondly, MCP detectors have a limited lifetime because the gain drops as a function of the accumulated counts. Thirdly, MCPs are very fragile and can only be used under certain conditions. The vacuum has to be below $5\times10^{-5}\,\mathrm{Torr}$ and the detector has to be able to outgas properly before a voltage can be applied. It is particularly important that there is no water left in the channels as they are hygroscopic. Lastly, depending on the application, the dead-time might be an issue. A single channel cannot be excited more frequently than once in $10^{-2}\,\mathrm{s}$. However, as there is a large number of channels, the resulting dead-time is still only on the order of 10^{-7}–$10^{-8}\,\mathrm{s}$ [12].

It is noteworthy that MCP detectors are also sensitive to UV light, X-rays and gamma rays as well as electrons. Especially UV photons and electrons might pose a problem depending of the ionisation method used. MCP detectors are, however, not sensitive to visible light.

The MCP detector used in this study is a Chevron-type detector with an effective diameter of 14.5 mm.[8] The channel diameter is given as 10 µm and the average centre-to-centre distance between two channels as 12 µm. The bias angle is $12^{\circ}\pm1^{\circ}$. The recommended potential across the two plates is 1.8 kV and it can be run with either negative or positive high voltage. In the first case, $\mathrm{MCP}_{\mathrm{in}}$ is set to approximately $-1.91\,\mathrm{kV}$ which results in a voltage of about $-110\,\mathrm{V}$ on $\mathrm{MCP}_{\mathrm{out}}$ while the anode is on ground (see Figure 5.11 for definitions). In the second case, $\mathrm{MCP}_{\mathrm{in}}$ is on $+70\,\mathrm{V}$, $\mathrm{MCP}_{\mathrm{out}}$ on $+1.87\,\mathrm{kV}$ and the anode on $+1.91\,\mathrm{kV}$. The gain was measured by the manufacturer to be 5×10^{8} with a 2 kV potential drop across the plates and 1×10^{8} at 1.8 kV.

Daly Detector

The Daly detector is a scintillator detector and works on a similar principle to the MCP detector described in the last section [20]. Ions are accelerated by a strong negative electric field onto a metallic surface and knock out secondary electrons. These are accelerated by the same field and hit a

[8] The detector is from El-Mul Technologies Ltd, type C018VAF.

plastic scintillator where they generate photons. The photons, in turn, are converted into electrons in a photomultiplier tube (PMT) where the signal is amplified similar to an MCP.

The Daly detector used in the present study is based on an improved design of the original Daly detector [21]. In this design, a stainless steel cup – the so-called Even cup – is used instead of a plate (see Figure 5.12). A high negative potential is applied to the cup, typically in the order of −20 kV. To improve secondary electron emission, the bottom of the cup can be coated with a metal with high secondary emission yield (e.g. Al, Mg or CsI). The secondary electrons are accelerated by the same potential and fly through a side-window close to the bottom. In some studies, a static magnetic field was applied perpendicular to the incident ion beam to steer the electrons onto the scintillator [22, 23]. However, this is usually not necessary, as long as the face of the scintillator is grounded properly. To provide a well-defined ground potential for the electrons, a thin layer of aluminium is deposited onto the face of the plastic scintillator. In the scintillator, the electrons knock electrons off atoms which emit visible light photons – typically 5–10 per electron [21]. These photons strike the photocathode at the entrance to the PMT and release electrons which are multiplied by several dynode stages.

The main advantage of the Daly detector is its suitability for heavy ion detection. As the ions are accelerated in a high potential, they reach considerably higher velocities than in a conventional MCP set-up. In fact, the potential difference can easily be increased to even higher values as the currents involved are very low. Furthermore, all the components are comparatively inexpensive and robust. The detector is also suitable for use in a high vacuum system and has a very low dark-current [12]. Although it is possible to detect anions with the Daly design, it requires the face of the scintillator to be floating at a very high positive potential. In general, the only major drawback of the Daly detector is the necessity to use very high voltages.

The detector used in this work is shown in Figure 5.12. The stainless steel cup has an inner diameter of 12 mm and is 60 mm deep. The position of the window was found using a simulation procedure described below and the window itself has a diameter of 12 mm. The entry mesh

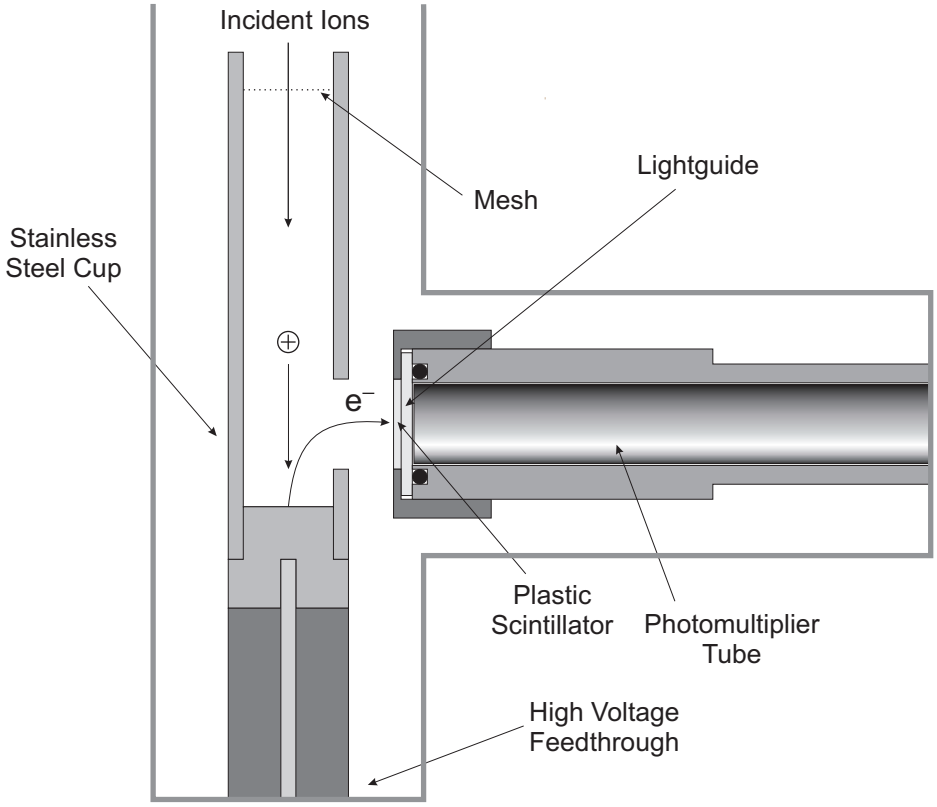

Figure 5.12: Schematic of the Daly detector used in this study.

is made from the same material used for the meshes of the acceleration regions described in Section 5.3.1. The cup is mounted on a high-voltage feedthrough which is connected to a 60 kV power supply[9]. For the experiments, the voltage was usually set to −15 kV. The distance between window and scintillator is 6 mm. The scintillator is made of plastic and shaped as a disc with 12 mm diameter and 1 mm thickness.[10] It is coated with a thin layer of aluminium (approximately 50 nm thick) and is glued onto a lightguide which is at the same time a vacuum window. The PMT[11] has eight dynode stages and is mounted outside the vacuum. The gain is

[9] Wallis Electronics Ltd, type R603/05 (60 kV, 500 µA, negative polarity).
[10] The scintillator is from Bicron, type BC-418 (1.4 ns decay time).
[11] The PMT is from Hamamatsu, type R1635-02 (0.8 ns rise time).

given as 2.4×10^6 at 1250 V potential difference between anode and cathode. During experiments, the potential difference was set to 1 kV where the gain is approximately 6.5×10^5.

5.3.4 Signal Processing

The same signal processing can be used for both detectors. The current output from the PMT or the MCP anode is fed into a fast preamplifier with a gain of 20.[12] From there it is transferred to an oscilloscope.[13] The oscilloscope uses the monitor output from the pulse generator or from the high-voltage switches as a trigger for the mass spectrum. To reduce the noise, the signal is averaged 128 times. The oscilloscope is connected via GPIB (IEEE-488.1) to a computer which allows the TOF spectra to be saved.[14] Since the oscilloscope used does not have enough memory to store multiple spectra, it was necessary to transfer them to the computer as quickly as possible. As the first solution using LabVIEW[15] turned out to be too slow, the data acquisition software used in the end was a programme written in C which makes use of National Instruments GPIB library for C.[16]

5.4 Ion Optics Simulation

While designing a TOFMS, it is difficult to predict the exact ion trajectories because of influences from secondary effects such as fringing fields and initial ion energies. It is also helpful to predict the outcome of a particular experiment and compare the prediction to the experimental data. This allows verification of whether the TOFMS is working as expected. It is therefore important to simulate the electric fields and ion flight paths to get a more accurate understanding of the TOFMS.

[12] The preamplifier is from Ortec, type 9326 (output rise time <1 ns).

[13] Tektronix TDS-1012 with TDS2CMA communications module.

[14] The oscilloscope is connected to the computer using a National Instruments PCI-GPIB card.

[15] LabVIEW is a graphical programming environment from National Instruments (http://www.ni.com/labview/).

[16] The programme tdslog.c from Tektronix was used as a template.

The most popular ion optics simulation software is SIMION 3D [24, 25] which was used in version 7.0 for this study.[17] The programme allows the definition of complex geometries consisting of different electrodes and a series of ions with individual starting positions and energies and will then calculate the respective trajectory for every single ion. The programme is very versatile, has a scripting interface to control it and can be adjusted to most cases. The procedure of a simulation is split up into several steps:

Defining the geometry: in the first step, a geometry with all the required electric fields has to be defined. This can be done either in 2D or in 3D. The 2D version requires less memory and CPU time but is less accurate. The design itself can either be done with the built-in drawing programme or by using the included geometry scripting language. If the design is complex and has to be changed often, it is advisable to use the scripting language. This also allows the geometry to be defined according to the exact dimensions of the TOFMS. Every electrode has to be defined individually and receives a temporary potential. There are several predefined geometric shapes which can be used and new elements can be made up of the union or difference between these basic shapes. It is also possible to define transparent wire meshes. Once the whole geometry definition is fixed, the geometry file has to be translated by SIMION.

Refining: subsequently, the potentials for every point between electrodes have to be calculated by solving the Laplace equation (for details, see [26]). Depending on the complexity of the geometry, this step can be time-consuming. It is therefore not practical to test different versions of a design which vary only slightly.

Defining the ions: in the next step, the mass, charge, starting position, initial energy including direction, and the time of birth for all ions have to be defined. This can either be done in groups of similar ions or for every ion individually. Defining ions in groups is done by setting the starting conditions for the whole group and then defining increments

[17] http://www.simion.com/

for individual parameters. For preliminary tests, it is more practical to define the ions in groups but for more thorough studies the individual definitions are more flexible. Defining ions individually can be done either manually inside SIMION or by editing a text file with all the parameters (manually or by using an external programme).

Running the simulation: after the geometry and the ions are defined, the electrodes have to be set to the desired voltages before the simulation is run producing a visual output of the ion trajectories. Optionally, all the parameters involved can be stored in a file. It is also possible to superimpose the potential energy surfaces of the electric fields onto the geometry. This helps to understand the effects of ion optical elements such as lenses and mirrors.

There is a powerful (albeit rather unintuitive) programming interface which allows so-called *user programs* to be written. These programmes can be used to change electric fields and ion starting parameters depending on run conditions. Programmes can also simulate the pulsing of the accelerating fields with a cluster beam entering the first acceleration region. For the present work, however, these user programmes were not used.

SIMION was used for several different purposes during this study: Firstly, it was used to help design the general set-up. An example of this process is shown in the next section. Secondly, it allowed calibration of the TOFMS spectra by comparing experimental data to simulation results. And thirdly, it was used to get an improved understanding of the influence of the initial velocity and the deflection plates on the cluster transmission.

5.4.1 Examples of Ion Optics Simulations

In a first step, the simulations were tested by letting gas ions fly through the TOFMS. An example of the resulting trajectories is shown in Figure 5.13. In this simulation, Ar ions with initial velocities of $150\,\mathrm{ms}^{-1}$ in the direction of the beam start from five different locations. The acceleration voltages are set to $U_1 = 4.5\,\mathrm{kV}$ and $U_2 = 3.563\,\mathrm{kV}$ as described in Section 5.3.1. The Daly detector is used and the Even cup is set to a potential of $-15\,\mathrm{kV}$. There

is no potential applied to the deflection plates. The ions spread out in the drift region due to the influence of the initial velocities and fringing fields caused by the ioniser. After leaving the flight tube, the high potential of the Even cup acts as a lens focussing the particles. The same simulations were run with N_2 and H_2O ions as well but the trajectories are indistinguishable. The flight times are of course different.

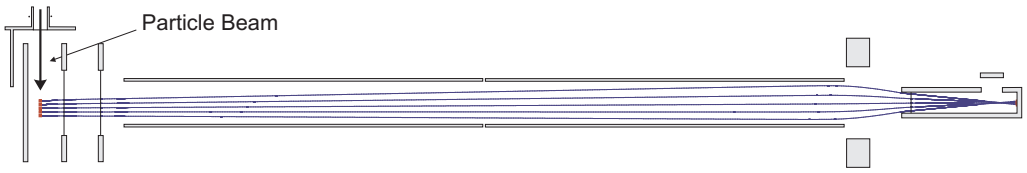

Figure 5.13: Simulation of Ar ion trajectories in the TOFMS. The voltages are set to $U_1 = 4.5\,\mathrm{kV}$, $U_2 = 3.563\,\mathrm{kV}$ and $U_{\mathrm{det}} = -15\,\mathrm{kV}$ on the Daly detector. The Ar ions start from five different positions along the centre of the beam axis with initial velocities of $150\,\mathrm{ms}^{-1}$ in the direction of the beam.

A similar procedure was followed to compare the experimental results to results from simulations. In this case, a large number of ions are started from different positions along the beam axis. For each set of parameters – such as acceleration voltages and deflection plate voltage – an average time of flight is determined. For some simulations, the transmission efficiency was determined by counting the number of particles which reached the detector. The results from these simulations will be shown in the next section where they are compared to the experimental TOF spectra.

Simulation of Electron Trajectories in Even Cup

The Even cup described in Section 5.3.3 was designed using the results from ion optics simulations. Especially the position of the side window can be optimised. Electrons are knocked off the metal surface which is on a high negative potential (typically between -15 and $-20\,\mathrm{kV}$) and accelerated onto the grounded scintillator face.

The simulation results in Figure 5.14 show the window in a good position. It is evident that the electrons experience a lensing effect which ensures that they all reach the scintillator. The diameter of the scintillator

could even be reduced without decreasing the detection performance. It can also be seen that the fringing field does not enter very far into the cup.

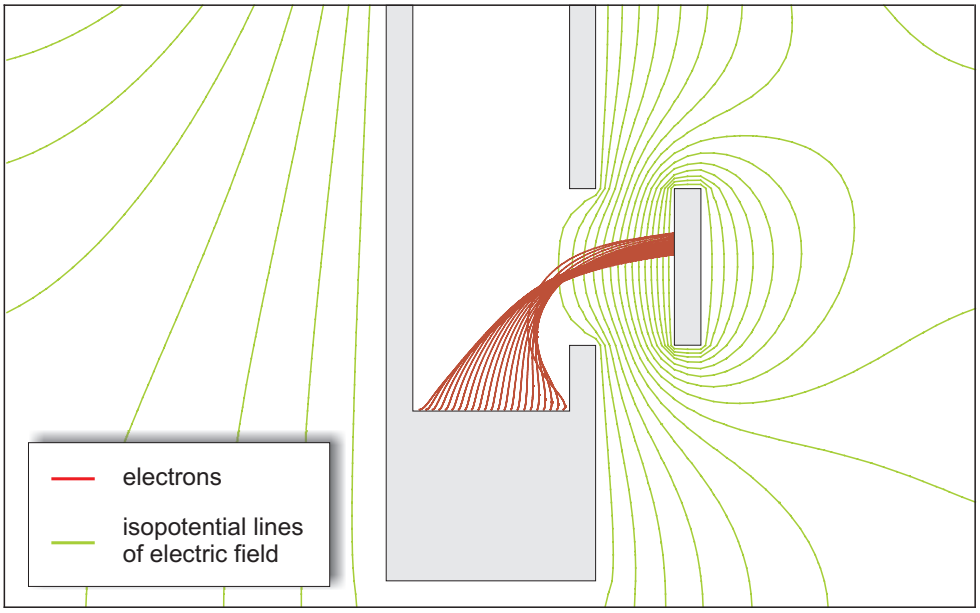

Figure 5.14: Simulation of electron trajectories from the Even cup to the scintillator. The voltage of the Even cup is set to −15 kV and the isopotential lines of the electric field are drawn every 1 kV. The incident clusters, the vacuum chamber and the high-voltage feedthrough are not shown to improve readability.

5.5 Experiments

In this section, the experimental results from the TOFMS studies are presented, divided into two parts: The first part contains the experiments which were done in the vacuum system that was used for the electron diffraction study described in Chapter 2. The second part covers the analysis of additional experiments undertaken by Dr Jim Partridge when the same TOFMS was mounted in a different system. The reason for this second study was the failure to record a cluster signal in the original set-up. Possible explanations will be discussed below. In the original set-up, it was only possible to test the TOFMS using residual gas and additional Ar and N_2. For the second part, the TOFMS had to be adjusted slightly. The changes will be presented below.

5.5.1 Experiments in the Original Set-up

All the experiments presented here were done using the set-up described in the previous sections. For some studies the MCP detector was used and for others the Daly detector. It will always be indicated which one was used for any particular experiment. In a first step, various tests using Ar and N_2 are described, followed by a section about the tests done with Sb and Bi clusters.

Ar and N_2 was let into the system through the gas inlet in the source chamber and the three nozzles which connect the source chamber to the diffraction chamber (see Section 2.1). This set-up is not ideal to create a collimated beam of Ar or N_2 gas as the light gas particles are expected to diverge strongly after leaving the third nozzle [27, 28]. Most of the residual gas in the chamber is not bound in the beam and lacks the directional velocity component necessary to fly through the ioniser and still reach the TOFMS. However, if residual gas reaches the acceleration region of the TOFMS, it is expected to have a broader initial energy component in the direction of the TOFMS and therefore show a decreased mass resolution than is expected for a cluster beam. Although the resulting gas intensity in the TOFMS is rather low, it is still possible to detect it.

To simplify the set-up, only one acceleration voltage was used for some

of the tests. In this case, the second acceleration region serves only as an extension of the drift region. As the TOFMS has not been optimised for the use of only one acceleration voltage, the resolution is decreased considerably as will be seen below.

Varying the Acceleration Voltages

For the first set of tests, only the first acceleration voltage was used, while the second voltage was set to ground. Ar gas is let into the chamber and the acceleration voltage is increased in steps of 0.5 kV from 2.0 to 4.5 kV. At each step, a TOF spectrum is recorded. The resulting spectra are shown in Figure 5.15. They all display two broad peaks with the right one being stronger. As expected, a higher acceleration voltage leads to shorter flight times, thereby shifting the peak positions to the left.

With such a series of spectra for different acceleration voltages, it is possible to test whether the TOFMS behaves as expected. Equation (5.6)

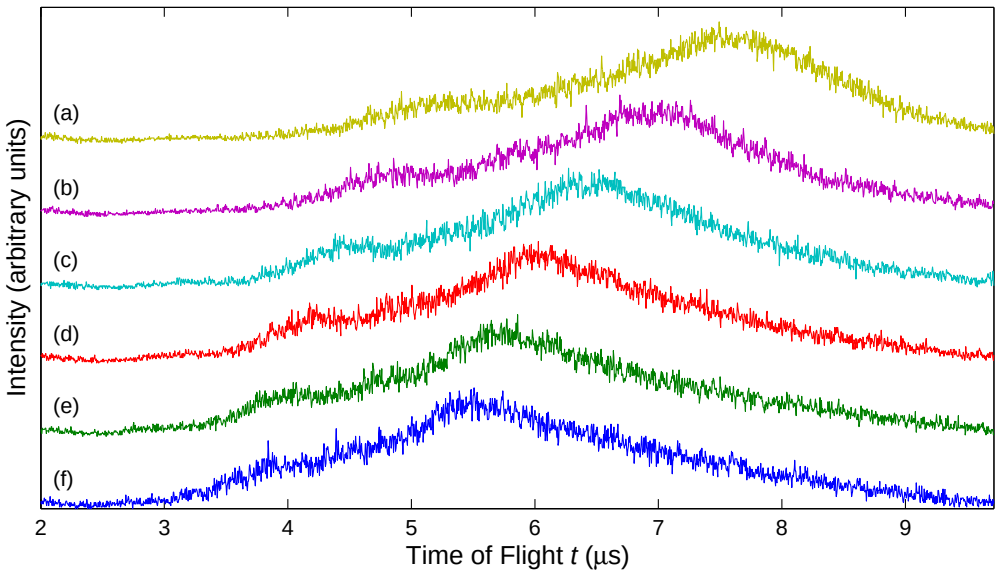

Figure 5.15: TOF spectra with varied acceleration voltages and Ar gas flow. The acceleration voltage is increased in steps of 0.5 kV from (a) 2.0 kV to (f) 4.5 kV. An Ar flow rate of 60 sccm was used for all spectra. The intensity of the spectra is normalised. Refer to Table 5.4 for details.

predicts that there is a linear relationship between the TOF for a particular $^{m}/_{z}$ ratio and the inverse square root of the acceleration voltage:

$$t = A \cdot \sqrt{U^{-1}} + B \tag{5.27}$$

If the positions of the two main peaks in Figure 5.15 are plotted against the inverse square root of the acceleration voltage, it can be compared to the values from SIMION simulations for various molecules as shown in Figure 5.16. Comparing the slope A for the experimental data to the value from the simulations allows the peaks to be assigned to certain masses (or more accurately mass-to-charge ratios). The slope of the main peak is determined to be 283 which is very close to the slope of the simulated data for Ar ($A \simeq 277$). This peak can therefore be attributed to Ar. The slope of the secondary (i.e. weaker) peak is given as 187 which is in good agreement with the simulated slope for H_2O ($A \simeq 185$). As mentioned previously, the offset B in the experimental patterns is due to experimental effects such as the finite rise-time of the pulsed fields as well as the delay time of electronics and detector.

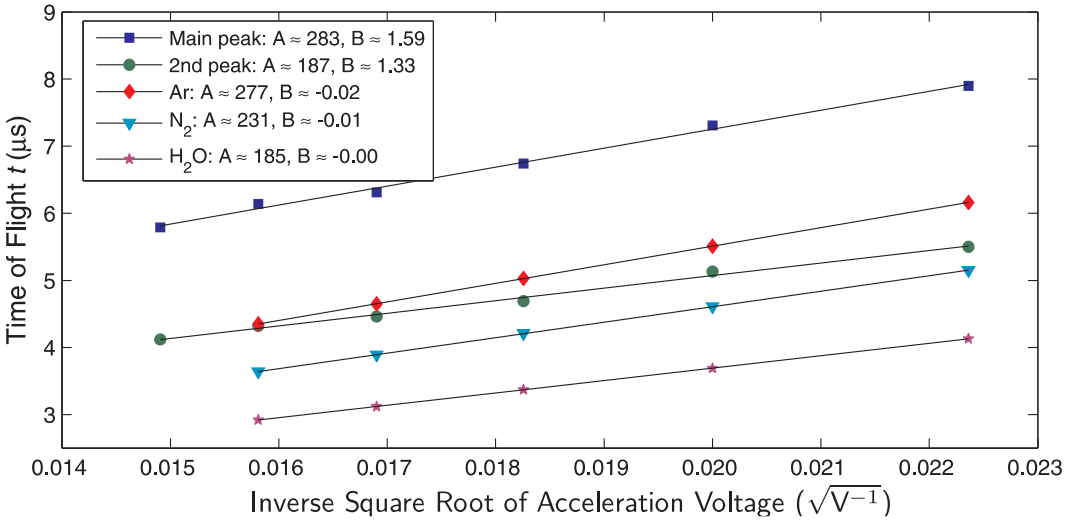

Figure 5.16: TOF versus inverse square root of the acceleration voltage for Ar. The peak positions of the main peak (■) and the secondary peak (●) from Figure 5.15 are compared to simulation results for Ar (♦), N_2 (▲) and H_2O (★). A and B correspond to the two fit parameters in (5.27).

The same procedure described above was repeated using a gas flow of 60 sccm N_2 instead of Ar. The acceleration voltage was again increased from 2.0 to 4.5 kV. The resulting TOF spectra of this run are shown in Figure 5.17. The main features of these spectra are similar to the ones seen in Figure 5.15, although the main peak is closer to the secondary peak.

If the peak positions of the two main peaks are plotted against the inverse square root of the acceleration voltage, it leads to the results shown in Figure 5.18. The slope of the data points for the main peak is determined to be 220 which agrees well with the simulation results for N_2 ($A = 231$). The slope for the secondary peak is given as 192 which matches the H_2O simulation ($A = 185$) as in the previous case.

Note that the absolute flight times differ considerably from the simulated times. Part of this effect can be explained by the timing delay of the detector and the electronics. However, this should not amount to a delay of almost 2 µs in the case of Ar and N_2.

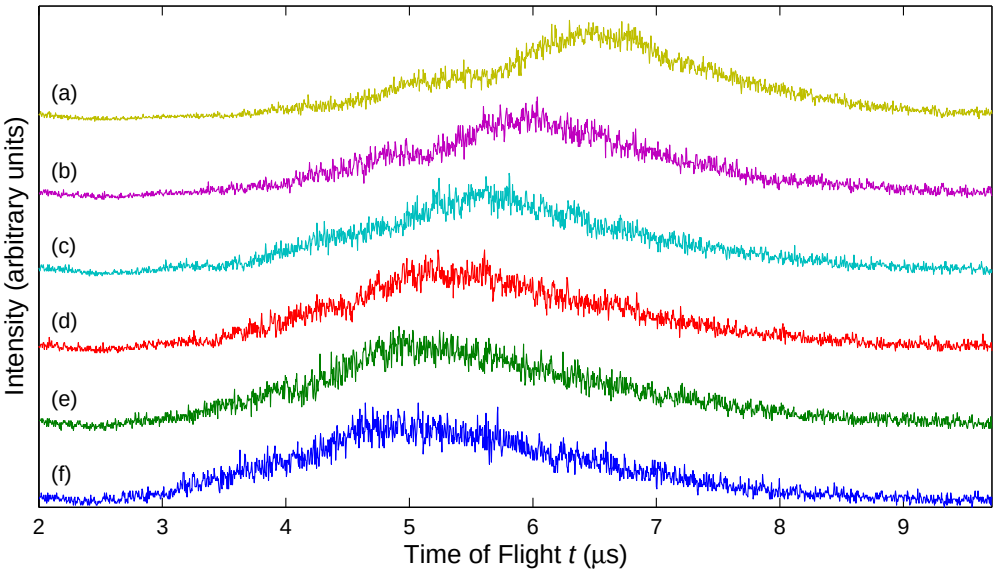

Figure 5.17: TOF spectra with varied acceleration voltages and N_2 gas flow. The acceleration voltage is increased in steps of 0.5 kV from (a) 2.0 kV to (f) 4.5 kV. An N_2 flow rate of 60 sccm was used for all spectra. The intensity of the spectra is normalised. Refer to Table 5.4 for details.

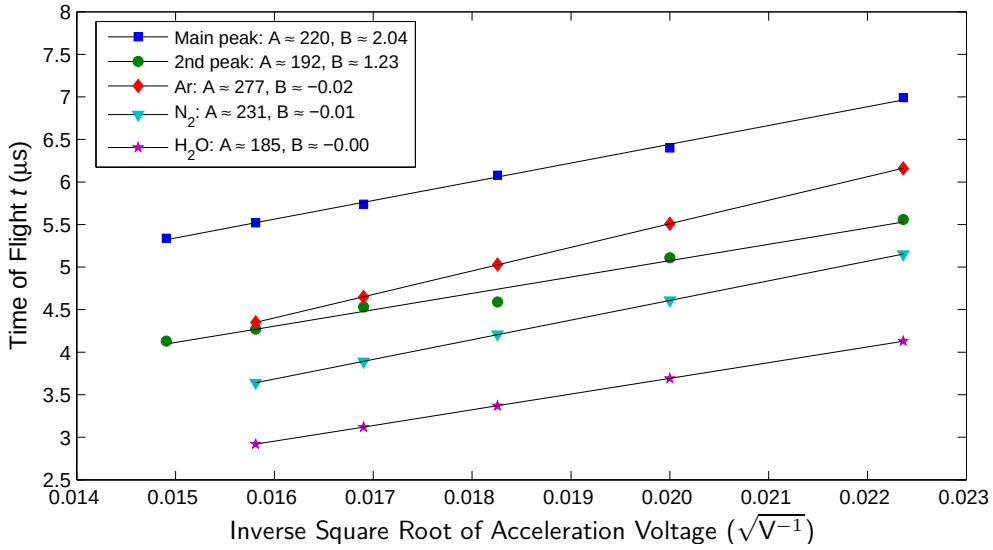

Figure 5.18: TOF versus inverse square root of the acceleration voltage for N_2. The peak positions of the main peak (■) and the secondary peak (●) from Figure 5.17 are compared to simulation results for Ar (♦), N_2 (▲) and H_2O (★). A and B correspond to the two fit parameters in (5.27).

Using both Acceleration Voltages

Since the TOFMS has not been optimised for the use of only one acceleration voltage, the spectra in the previous section have a very low resolution. If the second acceleration voltage is used, the resolution can be increased considerably. Figure 5.19 shows two spectra, one where only the first voltage was used (set to 4.5 kV) and a second one where both voltages were used ($U_1 = 4.5\,\text{kV}$ and $U_2 = 2.25\,\text{kV}$). For both spectra, an Ar flow was used. In the first case, the resulting spectrum is similar to the spectra presented in the last section. Adding the second acceleration voltage gives rise to a series of well-defined peaks.

The resolution of the second spectrum is high enough to calibrate it. If the mass-to-charge ratio of two or more peaks is known, a spectrum can be calibrated using (5.7). To determine which peak corresponds to which molecule, the following procedure was applied: by varying the amount of Ar and N_2 gas which is let into the system, the relative peak intensities change and it can be determined which peak corresponds to which molecule. The

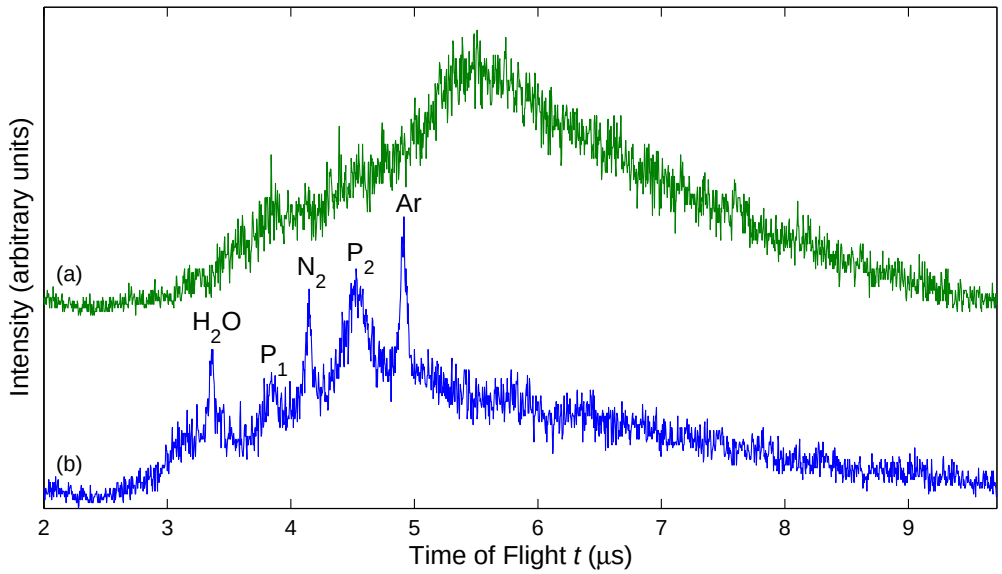

Figure 5.19: Simple mass spectra for Ar gas. Spectrum (a) was recorded using only the first acceleration region with $U_1 = 4.5\,\text{kV}$ while for the spectrum (b) $U_1 = 4.5\,\text{kV}$ and $U_2 = 2.25\,\text{kV}$ were used. In both cases an Ar flow rate of 60 sccm was used. The intensity of the two spectra is normalised. Refer to Table 5.4 for details.

peaks for Ar and N_2 are marked in Figure 5.19. While two peak positions are enough to calibrate the spectrum, adding a third peak position would decrease the uncertainty considerably. In a high-vacuum system there is always a certain amount of water. Since H_2O is lighter than Ar and N_2, its peak is expected at a shorter time of flight. It can therefore be assumed that the third well-defined peak corresponds to H_2O. This assumption has to be verified after calibration. Using the TOF of these three peaks, the slope A and offset B from (5.7) can be determined as shown in Figure 5.20.

It is evident that the linear fit matches the three data points well. The choice of the peak for H_2O is therefore justified. Using the values $A \simeq 0.745$ and $B \simeq 0.481$ from the fit allows calculation of the mass-to-charge ratio of the two unknown peaks P_1 and P_2 marked in Figure 5.19. The $^{m}/_{z}$ ratio for P_1 is given as 23.7 and for P_2 as 33.8. It is not clear what is responsible for the first peak. It can be assumed that the second peak consists at least partly of O_2. The fact that these two peaks are considerably broader than

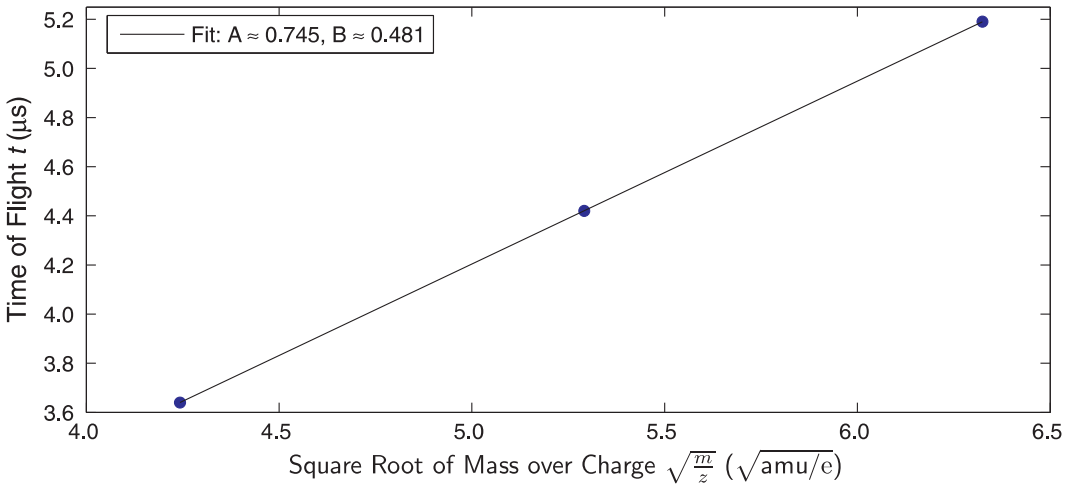

Figure 5.20: Calibration of the TOF spectrum from Figure 5.19 using (5.7).

the peaks for H_2O, Ar and N_2 indicates that these particles had a higher initial distribution either in starting position or initial energy.

It should be noted that the highest resolution when using both acceleration regions was not achieved with the optimised settings from Section 5.3.1. Instead of $U_1 = 4.5\,\text{kV}$ and $U_2 = 3.563\,\text{kV}$, the best settings were found to be $U_1 = 4.5\,\text{kV}$ and $U_2 = 2.25\,\text{kV}$ (note that this case is equivalent to using only one extended acceleration region). The reason for this behaviour might lie in the fact that in the first case, the electric field in the first acceleration region is considerably lower than in the second case and so, if the velocity of the gas in the direction of the beam is too high, the ions cannot reach the detector.

For the two sets of acceleration voltages discussed above, simulations were run to compare the resolution. For these simulations, Ar ions with an initial velocity of $150\,\text{ms}^{-1}$ along the beam axis were used. Contrary to the previous simulations, the starting positions were distributed along the TOFMS axis and not along the beam axis. The width of the starting positions corresponded to the width of the exit aperture of the ioniser (7 mm). Since the particle beam is densest along the centre of the beam axis, a normal distribution was used to determine the number of Ar particles per starting position. These particles were then accelerated through the virtual

TOFMS using the two sets of acceleration voltages discussed above. Plotting a histogram of their arrival times gives rise to a spectrum with only one peak corresponding to a conventional TOF spectrum. The spectra for the two sets of parameters are shown in Figure 5.21. As previously mentioned, the resolution of a spectrum can be determined by measuring the peak width (FWHM) and using (5.10). To determine the FWHM, a normal distribution was fitted to the TOF peak resulting in the values quoted in each figure. It is evident that the optimised parameters lead to a narrower peak and thereby an increased resolution compared to the parameters used in the experiments.

The same procedure can be repeated for the experimental spectrum shown in Figure 5.19(b). The peak positions and peak widths for H_2O, N_2 and Ar were determined by first removing the background and then fitting normal distributions to the three peaks. The resulting values are shown

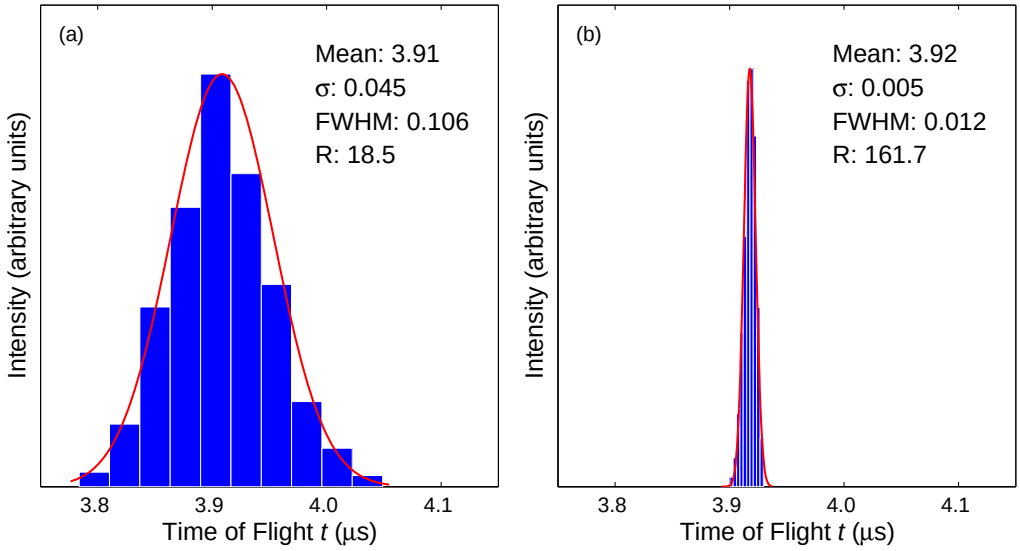

Figure 5.21: Comparison of simulated resolution for two sets of parameters. The acceleration voltages were set to (a) $U_1 = 4.5\,\text{kV}$ and $U_2 = 2.25\,\text{kV}$ and (b) $U_1 = 4.5\,\text{kV}$ and $U_2 = 3.563\,\text{kV}$. The superimposed curves are normal distribution fits to the data. The mean TOF and the standard deviation σ are the fit parameters. R is the resolution calculated using (5.10). Refer to the text for a detailed explanation.

in Table 5.3 where they are compared to the values from calculation and simulation.

It is worth mentioning that the simulation only took an initial spatial distribution into account. The energy distribution was disregarded. The experimental as well as the calculated resolution include both the space and the energy distribution. It is not obvious why the simulated resolution is worse than the experimental one.

Table 5.3: Comparison of resolution from experiment, calculation and simulation. The experimental resolution of the three peaks for H_2O, N_2 and Ar from the spectrum in Figure 5.19(b) is compared to the resolution from calculation and simulation. For experiment, calculation and simulation the acceleration voltages were set to $U_1 = 4.5\,\text{kV}$ and $U_2 = 2.25\,\text{kV}$. The experimental resolution was determined using (5.10). The calculated resolution is based on (5.26) using $\Delta s = 7\,\text{mm}$ and $\Delta E = 20\,\text{meV}$. The simulated value is based on the results shown in Figure 5.21.

Element	Peak Position (µs)	FWHM (µs)	Resolution
H_2O	3.64	0.056	32.6
N_2	4.42	0.049	45.4
Ar	5.19	0.064	40.8
		Average (experiment)	39.6
		Calculation	66.3
		Simulation	18.5

Changing from Ar to N_2 Gas Flow

More information about the peak positions in TOF spectra can be gained by switching from one gas to the other. These tests were performed using acceleration voltages set to $U_1 = 4.5\,\text{kV}$ and $U_2 = 2.25\,\text{kV}$. Initially, there was a gas flow of 60 sccm N_2 with no Ar contribution. In a second experiment, the N_2 gas flow was reduced to 30 sccm and an additional 30 sccm Ar was let into the system. Finally, the gas flow was switched to pure Ar with a flow rate of 60 sccm. The resulting three TOF spectra are shown in Figure 5.22. In the N_2 spectrum in Figure 5.22(a) two strong peaks are

visible. By comparing this spectrum to the spectrum in Figure 5.19(b) and the subsequent calibration, it is evident that these two main peaks can be attributed to H_2O and N_2. There is a broad peak visible between the two identified peaks. This peak was already observed in the spectrum in Figure 5.19(b). Adding Ar to the system gives rise to two additional peaks at higher flight times (see Figure 5.22(b)). Again using the knowledge of the aforementioned calibration, the more well-defined peak of the two can be attributed to Ar. As in the previous case, the origin of the broad peaks is not understood. If the gas flow is changed to pure Ar, the intensity of the N_2 peak and of the broad peak to the left is decreased (see Figure 5.22(c)). Both peaks are still clearly visible. Even if the gas flow is switched completely to Ar, the N_2 peak never fully vanishes for two reasons: firstly, there is always some N_2 available in the residual gas and secondly because the N_2 peak shares the m/z ratio with CO which is readily available as well.

It is now evident that the two broad peaks to the left of the N_2 peak

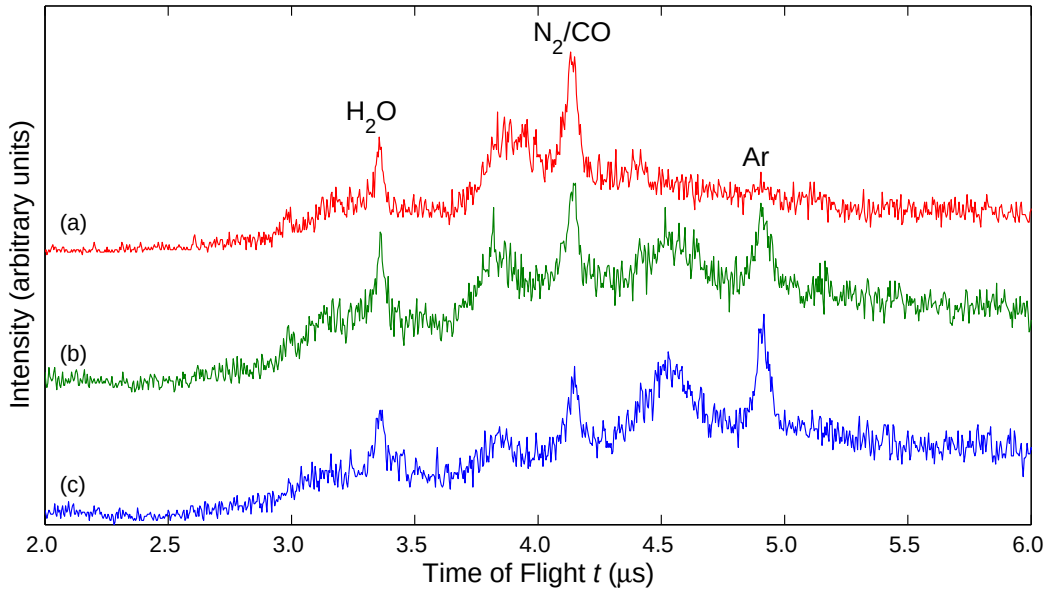

Figure 5.22: Influence of a changing gas flow on the TOF spectrum. The gas flow is changed in three steps from (a) 60 sccm N_2 to (b) 30 sccm N_2 and 30 sccm Ar to (c) 60 sccm Ar. The intensity of the spectra is normalised. Refer to Table 5.4 for details.

and the Ar peak are in some way connected to the main peaks. They always appear and disappear together with their main peak. As discussed in the previous section, the calibration led to m/z ratios which could not be attributed to any molecule which could be expected to present in a vacuum system. They do not match the ratios for doubly ionised Ar or N_2 either. The broadness of the peaks seems to indicate that the starting parameters of the particles are clearly different to the parameters for N_2 and Ar. It is possible that this phenomenon is caused by stray electrons ionising gas outside the ioniser.

Detector Comparison

All the tests so far were performed using the Daly detector. To check whether some of the previously mentioned effects could be due to the detector, further tests were performed using the MCP detector. In an initial step, the two detectors were compared directly. As changing the detector requires the system to be shut down, it was not possible to do the comparison in the same run. However, the conditions were similar, the only difference being a change in absolute gas flow rates (50 sccm N_2, 50 sccm Ar for the MCP and 30 sccm N_2, 30 sccm Ar for the Daly detector). The acceleration voltages were set to $U_1 = 4.5\,\mathrm{kV}$ and $U_2 = 2.25\,\mathrm{kV}$. The resulting TOF spectra are shown in Figure 5.23.

All the main features are shown in both spectra. The three strongest peaks are again due to H_2O, N_2 and Ar. The two broad peaks observed before are visible in both spectra as well. The most obvious differences are marked in Figure 5.23 with arrows. The spectrum of the MCP detector shows additional weak peaks for heavier masses. However, this discrepancy might also be due to different vacuum conditions. The two detectors are similar regarding the signal-to-noise ratio and they both display a strong background. The background of the Daly detector drops off more strongly for higher masses than the background of the MCP detector. It is not clear what the origin of this background is, but it might be due to stray electrons from the ioniser.

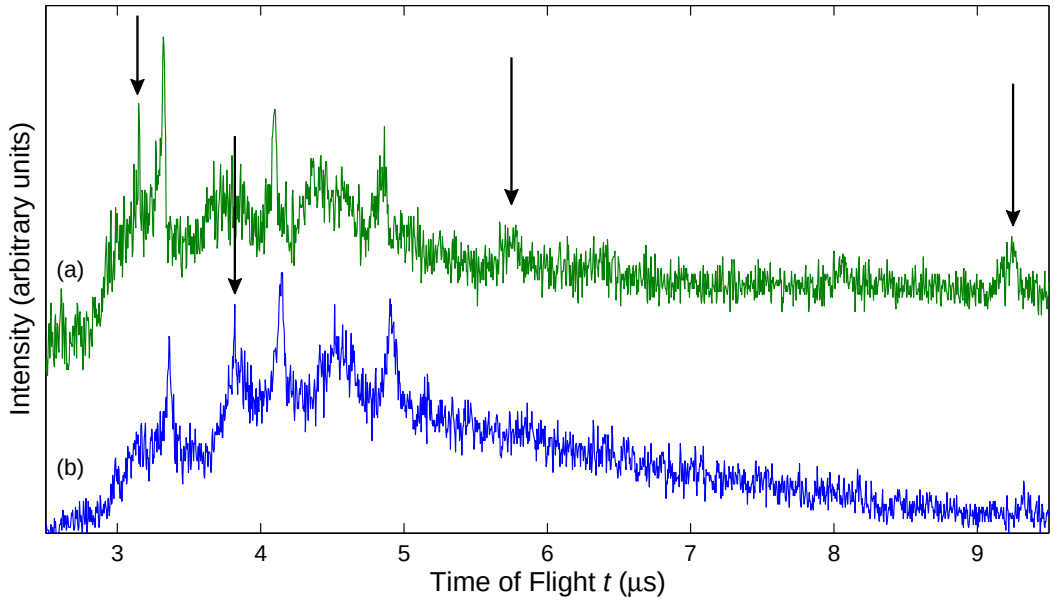

Figure 5.23: Comparison of (a) MCP detector and (b) Daly detector. The gas flow rates were (a) 50 sccm N_2, 50 sccm Ar; (b) 30 sccm N_2, 30 sccm Ar. The acceleration voltages were set to $U_1 = 4.5\,\text{kV}$ and $U_2 = 2.25\,\text{kV}$ for both spectra. The intensity of the two spectra is normalised. Refer to Table 5.4 for details.

Varying the Deflection Voltage

The deflection plates are mainly used to steer clusters with a high energy component in the direction of the beam axis onto the detector. However, they can also be used to test some of the functionality of a TOFMS using an Ar or N_2 gas flow. In these experiments, a constant Ar gas flow of 103 sccm was used. The two acceleration voltages were set to $U_1 = 4.5\,\text{kV}$ and $U_2 = 2.5\,\text{kV}$. Varying the voltage on the deflection plates changes the intensity of the detector signal. The deflection voltage was decreased in steps from 0 V to −70 V and a spectrum was recorded at each setting. The resulting spectra are shown in Figure 5.24. The first three spectra up to a deflection voltage of −20 V are very similar in intensity (Figure 5.24(a)–(c)). The intensity of the spectrum at −30 V is slightly decreased (Figure 5.24(d)). At −50 V the intensity is further decreased and only the strongest peak is still

visible (Figure 5.24(e)). The spectrum at −70 V does not show any peaks at all (Figure 5.24(f)).

When the deflection voltage on the plates closer to the source chamber is set to negative values, the particles are bent in the direction of the plates. At a given deflection potential, only particles within a range of energies are able to reach the detector. If the mass of the molecules in the beam is known, the particle velocity can be estimated. Figure 5.25 shows the dependence of the signal intensity on the deflection voltage and the particle velocity. The experimental data from Figure 5.24 is compared to simulated data from SIMION for Ar gas and different velocities. Note that there is no experimental data available for −40 and −60 V.

The wide range of initial velocities used as starting parameters for the simulations leads to a relatively narrow range of intensity distributions. It is therefore not possible to obtain definitive information about the particle beam velocity. Furthermore, the peak shape of the experimental

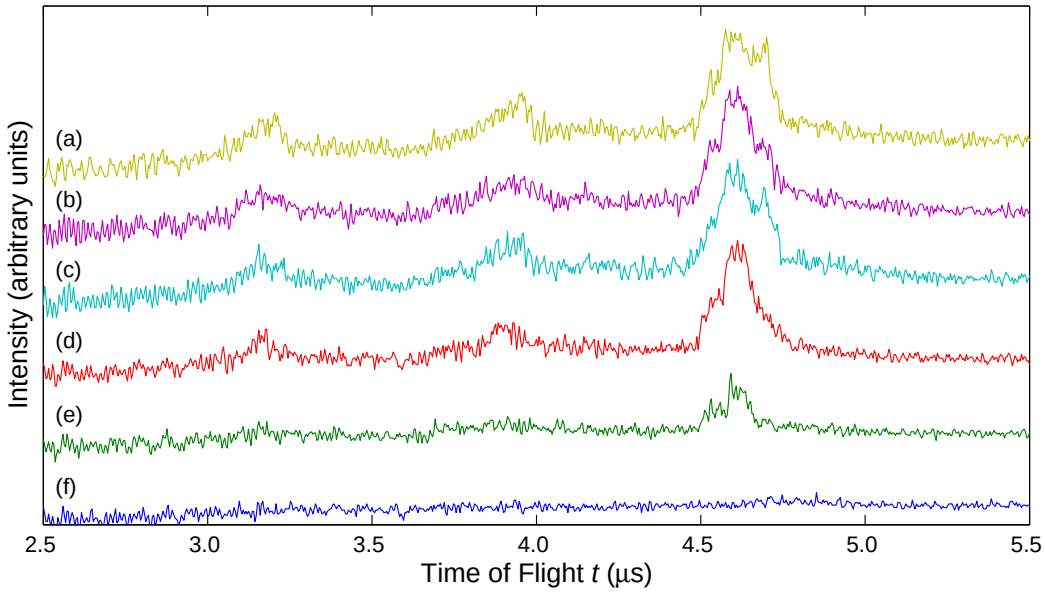

Figure 5.24: Influence of the deflection voltage on the mass spectra for cations. The deflection voltage is decreased from (a) 0 V to (f) −70 V (bottom). The main peak corresponds to Ar. The acceleration voltages were set to $U_1 = 4.5\,\mathrm{kV}$ and $U_2 = 2.5\,\mathrm{kV}$ and the Ar flow rate to 103 sccm. Refer to Table 5.4 for details.

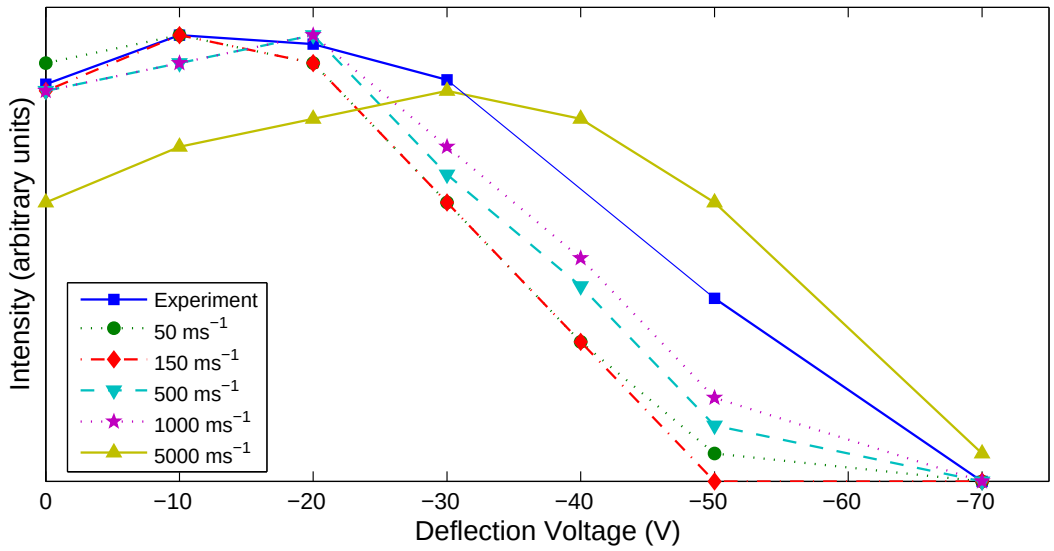

Figure 5.25: Dependence of signal intensity on deflection voltage and particle velocity. The experimental data from Figure 5.24 (■) is compared to simulated data for Ar gas with velocities of $50\,\mathrm{ms}^{-1}$ (●), $150\,\mathrm{ms}^{-1}$ (♦), $500\,\mathrm{ms}^{-1}$ (▼), $1000\,\mathrm{ms}^{-1}$ (★) and $5000\,\mathrm{ms}^{-1}$ (▲). The experimental data is scaled to match the maximum intensity of the simulated data.

intensity distribution curve does not fit any of the simulated peaks shapes. The maximum at $-10\,\mathrm{V}$ corresponds to the simulated curves for $50\,\mathrm{ms}^{-1}$ and $150\,\mathrm{ms}^{-1}$ but it does not drop off as quickly with higher deflection voltages. In this area it would fit a curve for particle velocities between $1000\,\mathrm{ms}^{-1}$ and $5000\,\mathrm{ms}^{-1}$. This observed behaviour cannot be explained by the Maxwell-Boltzmann velocity distribution alone, since there is virtually no contribution from particle velocities above $1000\,\mathrm{ms}^{-1}$ for Ar at room temperature.

As previously noted, if the electron energy is low enough (typically below 10 eV), it is possible to generate negatively charged particles through electron attachment. This is, however, not expected to happen at the ioniser voltage settings used for this study. As some experiments with Sb and Bi clusters indicated the existence of negatively charged particles, TOFMS tests were performed to check for gas anions. The MCP detector allows a change in polarity to detect anions; the polarity of the acceleration plates

can be changed easily. For these tests, an Ar gas flow of 100 sccm was used. Only the first acceleration voltage was used and it was set to −3.0 kV. The deflection voltage was first set to 0 V and then increased in steps of 10 V to 50 V. Four further spectra were recorded at 70 V, 100 V, 200 V and 300 V. The resulting spectra for anions are shown in Figure 5.26. In contrast to the studies with cations, the anion intensity is virtually zero when no deflection voltage is applied. Only when the deflection voltage is increased to approximately 30 to 40 V, a spectrum comparable to the cation spectra appears. According to the simulations and experiments discussed above, a deflection voltage of more than 70 V should lead to an almost complete extinction of the spectrum. For anions, this is only the case once the deflection voltage is increased to well over 100 V. While it has to be kept in mind that the polarity reversal of the TOFMS does not lead to the exact same set-up with opposite sign for all the potentials (in the positive polarity set-up, the face of the MCP is set to around +70 V compared to −1.91 kV for negative polarity), the conditions for anions in the set-up with negative acceleration voltages should be very similar to those for cations with positive voltages. There is no obvious explanation for the observed behaviour.

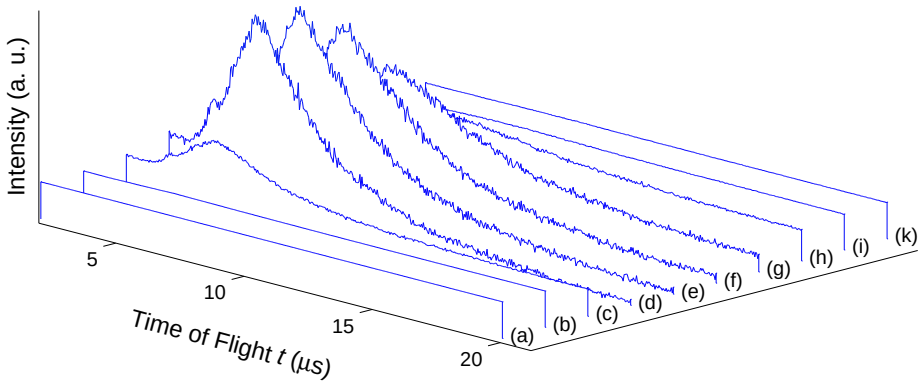

Figure 5.26: Influence of the deflection voltage on the mass spectra for anions. A negative acceleration voltage (first region only) and positive MCP detector polarity were used. The deflection voltage was increased from (a) 0 V to (k) 300 V. Refer to Table 5.4 for details.

Varying the Ioniser Voltage

As described in Section 5.3.2, the voltage applied to the ioniser filament determines the electron energy. The optimal electron energy depends on the type of molecules to be ionised. Each type has a characteristic electron impact ionisation cross section curve [13]. The maximum of this curve indicates the ideal electron energy to ionise this particular molecule. For Ar the maximum lies between 50 and 100 eV.

To test the ioniser, the voltage applied to the filament was varied and the signal intensity measured. For these tests, an Ar gas flow of 103 sccm was used and the acceleration voltage of the first region was set to 3.0 kV. The second voltage was not used. The spectra recorded for varying ioniser voltage are shown in Figure 5.27. The spectra show similar features but differ in intensity. The main peak shows a clear maximum for −41 V. For higher negative voltages, the intensity drops off. At −70 V the main peak has almost completely disappeared. The observed maximum at −41 V is clearly lower than the −50 to −100 V range expected for Ar [13].

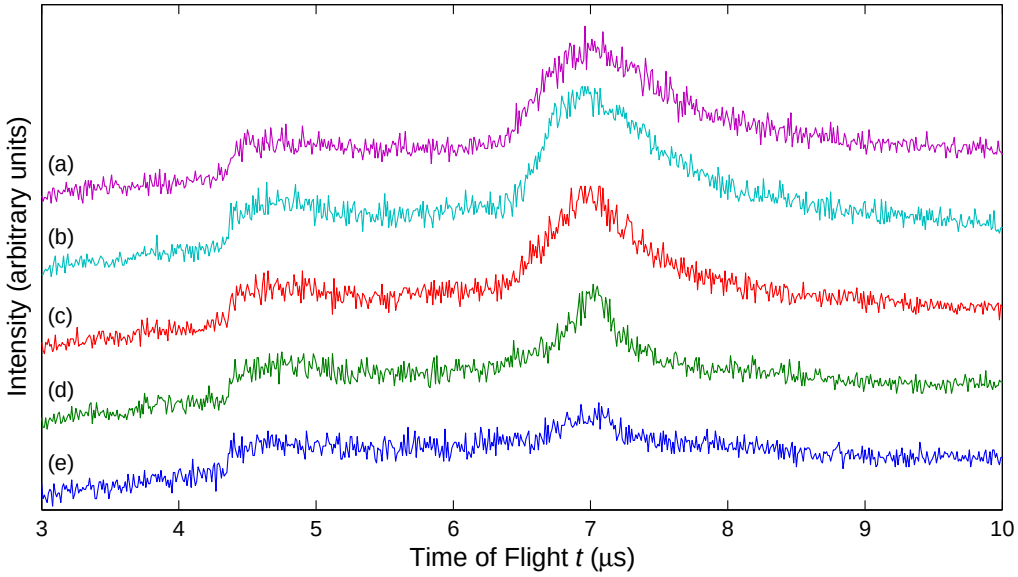

Figure 5.27: Effect of varying the ioniser potential on the TOFMS spectra. The ioniser voltage is decreased in steps of approximately 10 V from (a) −30 V to (e) −70 V. Refer to Table 5.4 for details.

Tests using Sb and Bi Clusters

Numerous tests with Sb and Bi clusters were carried out. A wide range of source parameters was tested, especially conditions known to produce small clusters. However, it was not possible to detect a cluster signal with the TOFMS.

To test whether the clusters are being ionised at all, a constant positive voltage was applied to the first acceleration region. The deposition rate measured on the deposition rate monitor (see Section 2.3) dropped considerably, as soon as the voltage was turned on. Changing the field strength allowed the deposition rate measured on the monitor to be controlled. This is a clear indication that the clusters are ionised and get deflected in the electric field. After removing the TOFMS, it was discovered that there was substantial cluster deposition on the backplate of the TOFMS and not on the first mesh as expected which meant that the clusters were anions and not cations. However, using the MCP detector on a positive potential and negative acceleration voltages did not allow any cluster signal in the TOFMS to be measured either.

Experimental Conditions for TOFMS Tests with Ar and N_2 Gas

In Table 5.4 the experimental conditions for all the tests presented in this section are displayed. The acceleration voltages used were all in the range from 2.0 to 4.5 kV (positive or negative polarity). Below 2.0 kV the signal-to-noise ratio was too low to record a spectrum. The upper limit was determined by the power supplies used as the switching of high voltages draws considerable currents. The range of deflection voltages used was 0 to −100 V for cation detection and 0 to 300 V for anion detection. Beyond this range, the intensity of the spectra became too weak to be recorded. The ioniser voltage which controls the electron energy was set to values between −40 and −70 V. This voltage, however, is influenced by the ioniser current as described in Section 5.3.2. At times, this voltage was observed to be drifting towards zero without the ioniser current being changed. This might have been due to some components charging up. The detectors were exchanged between tests to see whether some of the phenomena described

above were influenced by the choice of detector. There was no noticeable difference between the Daly detector and the MCP detector with the negative setting. The observed differences when using the MCP detector in its positive set-up were most likely due to effects in the ioniser.

Table 5.4: Experimental conditions for TOFMS tests in the original set-up as shown in Figure 5.19 to 5.27. (In the last column, $MCP^{\ominus/\oplus}$ indicates whether the MCP detector was used with negative or positive polarity.)

Fig.	Flow Rate (sccm)		Acc. Volt. (kV)		Defl. Volt. (V)	Ion. Volt. (V)	Detector
	Ar	N_2	U_1	U_2	U_{defl}	U_{ion}	
5.19(a)	60	–	4.5	–	–	−42	Daly
5.19(b)	60	–	4.5	2.25	–	−42	Daly
5.15(a)	60	–	2.0	–	–	−42	Daly
5.15(b)	60	–	2.5	–	–	−42	Daly
5.15(c)	60	–	3.0	–	–	−42	Daly
5.15(d)	60	–	3.5	–	–	−42	Daly
5.15(e)	60	–	4.0	–	–	−42	Daly
5.15(f)	60	–	4.5	–	–	−42	Daly
5.17(a)	–	60	2.0	–	–	−42	Daly
5.17(b)	–	60	2.5	–	–	−42	Daly
5.17(c)	–	60	3.0	–	–	−42	Daly
5.17(d)	–	60	3.5	–	–	−42	Daly
5.17(e)	–	60	4.0	–	–	−42	Daly
5.17(f)	–	60	4.5	–	–	−42	Daly
5.22(a)	0	60	4.5	2.25	–	−42	Daly
5.22(b)	30	30	4.5	2.25	–	−42	Daly
5.22(c)	60	0	4.5	2.25	–	−42	Daly
5.23(a)	50	50	4.5	2.25	–	−48	$MCP^{\ominus}$
5.23(b)	30	30	4.5	2.25	–	−42	Daly
5.24(a)	103	–	4.5	2.5	0	−40	$MCP^{\ominus}$
5.24(b)	103	–	4.5	2.5	−10	−40	$MCP^{\ominus}$
5.24(c)	103	–	4.5	2.5	−20	−40	$MCP^{\ominus}$
5.24(d)	103	–	4.5	2.5	−30	−40	$MCP^{\ominus}$
5.24(e)	103	–	4.5	2.5	−50	−40	$MCP^{\ominus}$
5.24(f)	103	–	4.5	2.5	−70	−40	$MCP^{\ominus}$
5.26(a)	100	–	−3.0	–	0	−61	$MCP^{\oplus}$
5.26(b)	100	–	−3.0	–	10	−61	$MCP^{\oplus}$
5.26(c)	100	–	−3.0	–	20	−61	$MCP^{\oplus}$
5.26(d)	100	–	−3.0	–	30	−61	$MCP^{\oplus}$
5.26(e)	100	–	−3.0	–	40	−61	$MCP^{\oplus}$
5.26(f)	100	–	−3.0	–	50	−61	$MCP^{\oplus}$
5.26(g)	100	–	−3.0	–	70	−61	$MCP^{\oplus}$
5.26(h)	100	–	−3.0	–	100	−61	$MCP^{\oplus}$
5.26(i)	100	–	−3.0	–	200	−61	$MCP^{\oplus}$
5.26(k)	100	–	−3.0	–	300	−61	$MCP^{\oplus}$
5.27(a)	103	–	3.0	–	–	−30	$MCP^{\ominus}$
5.27(b)	103	–	3.0	–	–	−41	$MCP^{\ominus}$
5.27(c)	103	–	3.0	–	–	−50	$MCP^{\ominus}$
5.27(d)	103	–	3.0	–	–	−60	$MCP^{\ominus}$
5.27(e)	103	–	3.0	–	–	−70	$MCP^{\ominus}$

5.5.2 Experiments on Palladium Clusters

This section presents an analysis of experiments undertaken by Dr Jim Partridge in a different vacuum system [29] but using the same TOFMS as described above. The system features a magnetron sputtering source [30, 31] which was used to produce palladium (Pd) clusters for the TOFMS experiments.

In the next paragraph, the differences between the two experimental set-ups are described followed by the results from the experiments. For a range of source conditions, TOF spectra were recorded while varying the acceleration and deflection voltages.

Experimental Set-Up

The experimental set-up of this system is similar to the one used for the previous experiments. Instead of an inert-gas aggregation source, a magnetron sputtering source is used [30, 31]. In this source, atoms are sputtered off a target by Ar ions from a plasma. Clusters are then formed by condensation in an inert gas flow in a similar process to the one described in Section 2.1. This method can be used to generate clusters from materials with a low vapour pressure at high temperatures which would be difficult to achieve in an IGA source. An additional advantage for the TOFMS study in particular is the fact that up to 80% of the clusters are ionised when leaving the source [30] (compared to below 1% efficiency for electron impact ionisation). Positively as well as negatively charged clusters are produced. The cluster production can be influenced by changing the inert gas flow rate, the type of inert gas and the power applied to the sputtering target (thereby strengthening the plasma and increasing the potential difference between plasma and target).[18]

As in the original set-up, the TOFMS is mounted perpendicular to the cluster beam. Due to the dimensions of the vacuum chamber, the flight tube had to be extended from 417 mm to 467 mm. All other parts of the TOFMS remained the same. The Daly detector was used for all cluster

[18] There are additional source parameters which were not changed in the present study, e.g. aggregation length and nozzle geometries.

experiments and it was always set to −15 kV. Only the first acceleration voltage was used as high resolution was not required and it was felt that the use of a single acceleration voltage would simplify the experiments.

Varying the Acceleration Voltage

In a first test, the acceleration voltage of the first region was varied. The source conditions for this particular run were 400 sccm Ar flow rate and 25 W sputtering power. The acceleration voltage was decreased in steps of 0.5 kV from 4.5 kV to 3.0 kV. At each step, a TOF spectrum was recorded. The resulting series of spectra is shown in Figure 5.28. Each individual spectrum represents the size distribution of Pd clusters in the beam. All spectra show one broad peak as their dominant feature. As expected, the peak position shifts to higher flight times as the acceleration voltage is decreased. The spectrum with the highest intensity is observed at 4.5 kV. Decreasing the acceleration voltage led to a drop in intensity, as can be seen from the increasing noise in the spectra in Figure 5.28(c) and (d).

As there is no calibration data available for these spectra, the method described in Section 5.5.1 has to be applied here: the mean TOF for each spectrum is plotted against the inverse square root of the acceleration voltage and a linear fit is calculated for these data points. The slope of this fit is proportional to the mean mass of the clusters. These results are compared to simulation data to determine the mass of the clusters in the experiment. In this section, it is assumed that the clusters are only singly charged. Strictly speaking, the values for the mass quoted below correspond to the m/z ratio.

The size distribution in a cluster beam is expected to follow a log-normal distribution [32]. To determine the mean TOF, it is therefore possible to fit a log-normal distribution to the experimental spectrum. As this distribution is not symmetric, the mean TOF is not equivalent to the TOF of the centre of the peak. The mean TOF for each spectrum obtained from log-normal fits and the corresponding linear fit are shown in Figure 5.29. This figure also displays the simulation data for Pd clusters with a diameter of 2, 3 and 5 nm (which correspond to cluster masses of approximately 30 500, 103 000, and 476 000 amu). The simulations were run as described in Sec-

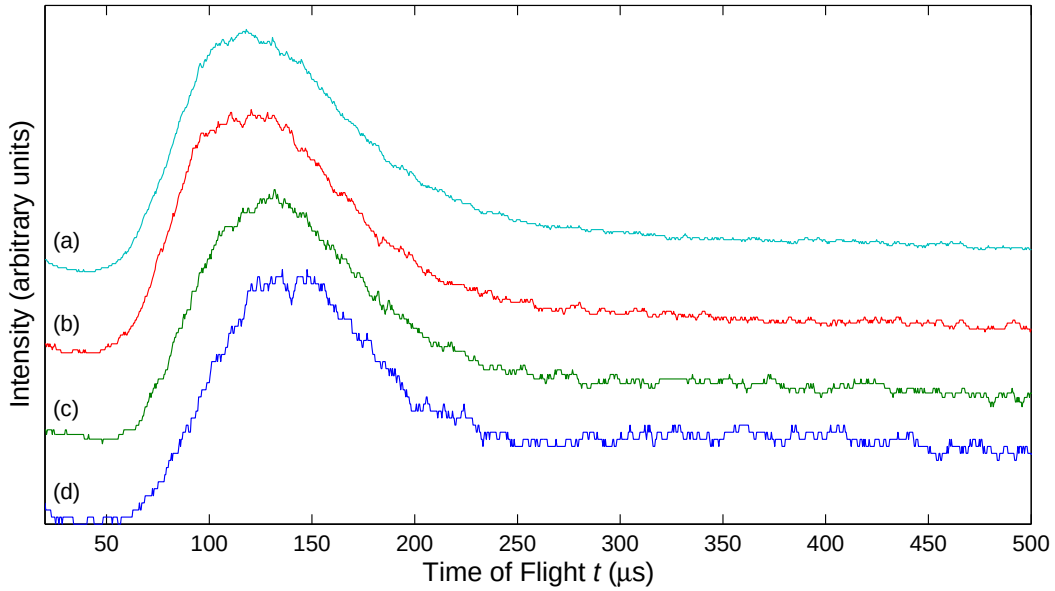

Figure 5.28: TOF spectra of Pd clusters with varied acceleration voltages. The acceleration voltage is decreased in steps of 0.5 kV from 4.5 kV at the top to 3.0 kV at the bottom. An Ar flow rate of 400 sccm was used for all spectra. The intensity of the spectra is normalised. Refer to Table 5.5 for details.

tion 5.5.1 with all the Pd clusters starting along the centre of the beam axis and measuring the flight times.

Using the fit parameters and the values for the simulations, the mean mass for the experimental data can be calculated as approximately 27 000 amu which corresponds to a diameter of 1.92 nm. The relationship between cluster mass and diameter was calculated assuming a spherical particle with the density of bulk Pd. While this method is inaccurate for small clusters consisting of less than approximately 100 atoms, it is expected to be a good estimate for larger clusters.

It is also possible to determine the average cluster mass in each spectrum individually by using the mean TOF determined by the fitting procedure described above and solving (5.17) for the mass. Results from this method are more prone to inaccuracies compared to the slope method as they depend on only one spectrum. If a spectrum is recorded with a low signal-to-noise ratio, it might be difficult to fit a log-normal distribution to

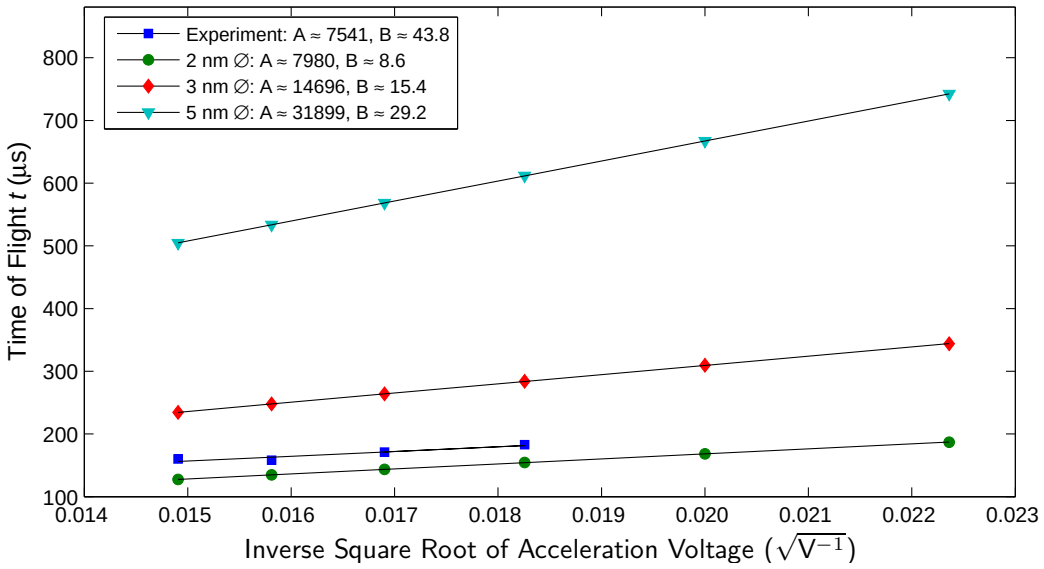

Figure 5.29: TOF versus inverse square root of the acceleration voltage comparing the experimental data from Figure 5.28 (■) to simulations for Pd clusters with diameters of 2 nm (●), 3 nm (♦) and 5 nm (▼). A and B correspond to the two fit parameters in (5.27).

the signal. The results from this method will be shown in a table at the end of the section.

It is noteworthy that the intensity of all the spectra in Figure 5.28 does not drop to zero for high flight times. It was observed that this background is visible for the whole length of the acceleration pulse. Unexpectedly, reducing the pulse length to shorter times (theoretically still sufficiently long for all clusters to leave the acceleration region) destroys the signal completely. It is not understood why the pulse length has to be longer than the total time-of-flight for the spectrum to be visible, but it is believed that this is due to an undiagnosed problem with the electronics.

For a second test, the source conditions were changed by replacing the Ar gas flow with He. The flow rate was left at 400 sccm and the sputtering power remained at 25 W. The acceleration voltage is again decreased in steps of 0.5 kV from 4.5 kV to 3.0 kV. The resulting spectra are shown in Figure 5.30. As in the first test the peak position also shifts to higher flight times for lower acceleration voltages. However, it is evident that the mean

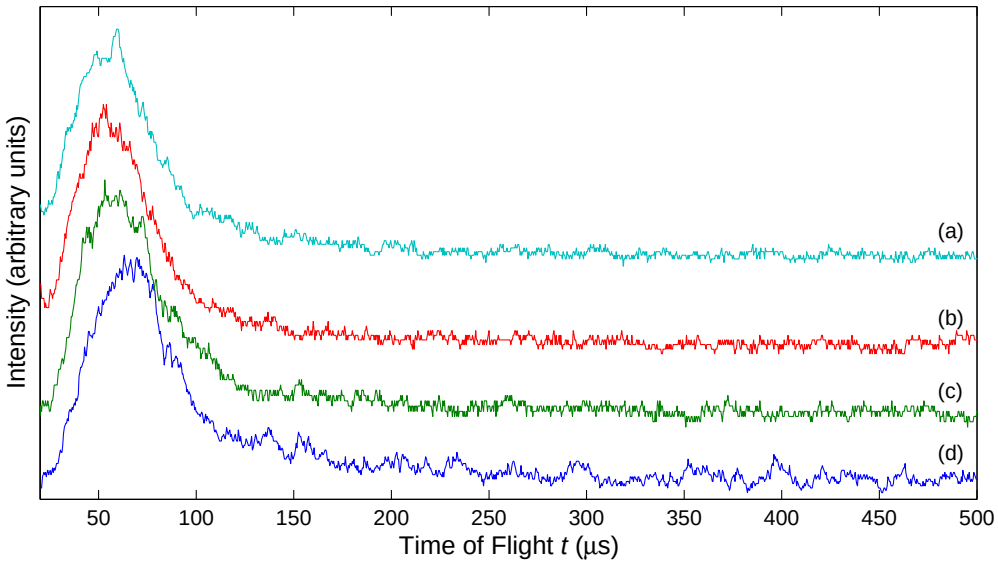

Figure 5.30: TOF spectra of Pd clusters with varied acceleration voltages. The acceleration voltage is decreased in steps of 0.5 kV from 4.5 kV at the top to 3.0 kV at the bottom. A He flow rate of 400 sccm was used for all spectra. The intensity of the spectra is normalised. Refer to Table 5.5 for details.

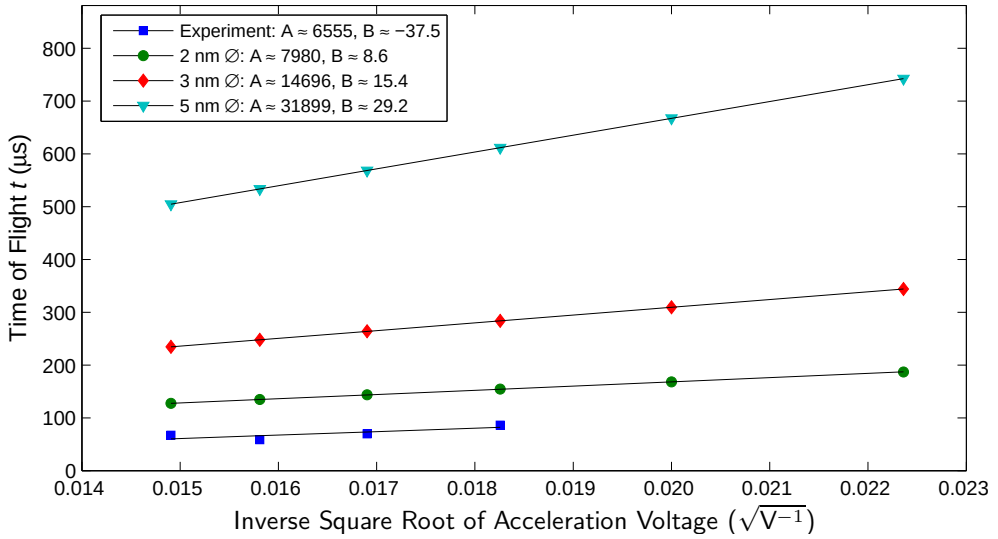

Figure 5.31: TOF versus inverse square root of the acceleration voltage comparing the experimental data from Figure 5.30 (■) to simulations for Pd clusters with diameters of 2 nm (●), 3 nm (♦) and 5 nm (▼). A and B correspond to the two fit parameters in (5.27).

flight times are noticeably shorter at each setting compared to the corresponding spectra in Figure 5.28. This is an indication that using He instead or Ar leads to smaller clusters (see Section 4.3.2 for a similar observation using the IGA source).

The fitting procedure described above was also applied to the second set of data to determine the mean TOF for each spectrum. These mean values are plotted against the inverse square root of the acceleration voltage and compared to the simulation data in Figure 5.31. The slope of the linear fit to the experimental data translates into a mean cluster mass of approximately 20 400 amu which corresponds to a cluster diameter of 1.75 nm. As expected, these values are considerably smaller than the values determined in the previous experiment.

Varying the Deflection Voltage

Depending on the cluster size and velocity, it is necessary to steer the clusters onto the detector using the deflection plates described above. The same deflection plates were used as in the original set-up which means that they did not cover the whole flight tube which was now longer. The wiring was changed so that a positive deflection voltage is required for positively charged clusters to reach the detector. At a given deflection voltage only clusters within a limited range of energies are allowed to reach the detector.

For this test, an Ar gas flow rate of 100 sccm was used and the source sputtering power was set to 10 W. The acceleration voltage was set to 3.5 kV for all runs. The deflection voltage was increased from 0 to 50 V and spectra were recorded at 0, 5, 10, 20 and 50 V. The resulting spectra are shown in Figure 5.32. The spectra all show one broad peak and the intensity decreases for increasing deflection voltage settings. At 50 V, there is almost no peak visible (Figure 5.32(e)).

The mean cluster masses are calculated for these spectra using (5.17) and shown in Table 5.5 at the end of this section. As expected, the mean TOF is slightly increased for higher deflection voltages as heavier clusters are able to reach the detector and lighter ones are bent into the plates.

The influence of the deflection voltage on the signal intensity can be compared to simulations as described in Section 5.5.1. A first series of

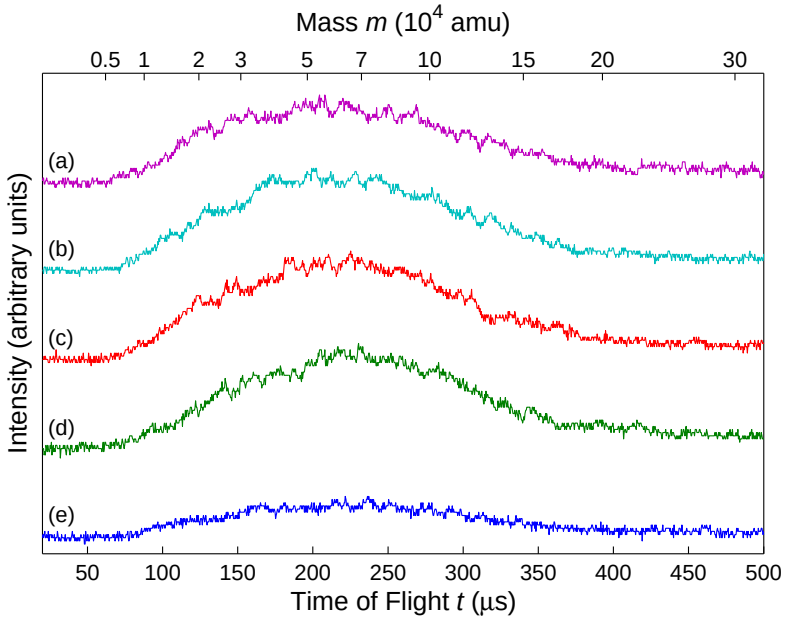

Figure 5.32: Influence of the deflection voltage on the mass spectra. The deflection voltage is increased from (a) 0 V to (e) 50 V. The mass scale was calibrated using (5.17). Refer to Table 5.5 for details.

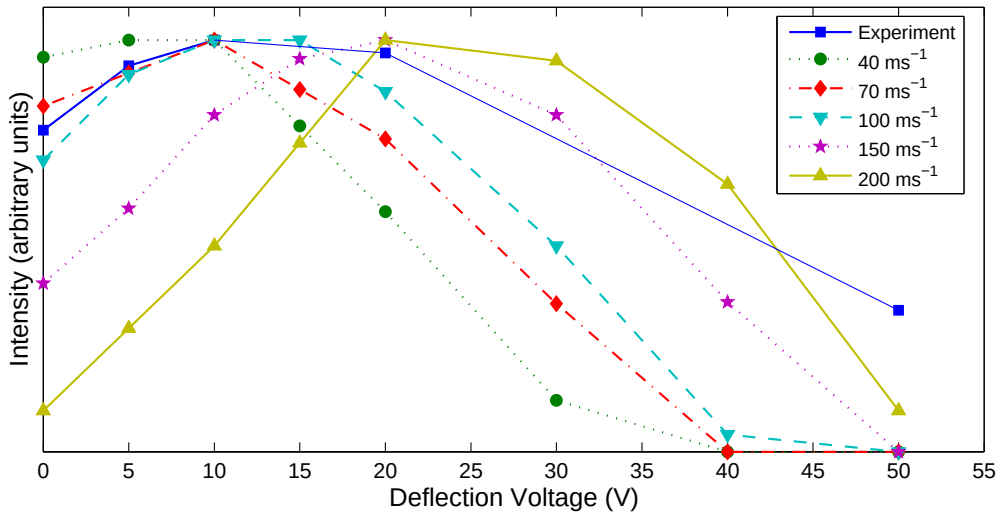

Figure 5.33: Dependence of signal intensity on deflection voltage and particle velocity. The experimental data from Figure 5.32 (■) is compared to simulated data for 2.5 nm Pd clusters with initial velocities of 40 ms^{-1} (●), 70 ms^{-1} (♦), 100 ms^{-1} (▼), 150 ms^{-1} (★) and 200 ms^{-1} (▲). All the data is scaled.

simulations was run with 2.5 nm Pd clusters with a mass of 59 500 amu and varied initial velocities in the beam direction. The results are displayed in Figure 5.33. For low deflection voltages, the experimental data agrees well with a cluster velocity of 100 ms^{-1}. For higher deflection voltages, however, the experimental signal intensity is too high and even the simulation for 200 ms^{-1} fails to match the remaining signal at a deflection voltage of 50 V.

This behaviour might be explained by the presence of larger clusters in the beam. Other experiments on the same system indicate that there is a wide size distribution and a rather narrow velocity distribution [33].

To test this assumption, a second series of simulations was run. In four independent simulations, Pd clusters with diameters of 2, 2.5, 3 and 5 nm, initial velocities of 100 ms^{-1} and starting positions along the beam axis were flown through the TOFMS. The acceleration voltage on the first plate was set to 3.5 kV. The deflection voltage was then increased from 0 to 50 V. The trajectories of the simulations with no deflection voltage are shown in Figure 5.34.

These simulations show clearly that the number of clusters which reach the detector declines rapidly for large clusters above 2.5 nm diameter. If no deflection voltage is used, clusters with a diameter of 5 nm do not reach the detector at all (Figure 5.34(d)). Figure 5.35 shows the dependence of the signal intensity on the deflection voltage. For clusters with a diameter of 5 nm an intensity is only recorded once the deflection voltage is increased to 15 V. At a deflection voltage of 50 V the intensity of the small clusters drops to zero, while there is still a considerable proportion of the signal from 5 nm clusters left.

The experimental intensities agree well with the simulated data for clusters between 2 and 3 nm for deflection voltages up to 30 V. The experimental intensity at a deflection voltage of 50 V seems to indicate that the beam also contains considerably larger clusters. However, the original TOF spectrum in Figure 5.32 does not show such a huge increase in cluster size for 50 V deflection voltage. It is therefore not clear where the contribution at higher deflection voltages comes from.

To test whether it is theoretically possible to detect clusters with a diameter of more than 5 nm, further simulations were run. For these simulations, Pd clusters with a diameter of 7 nm and an initial velocity of 150 ms^{-1}

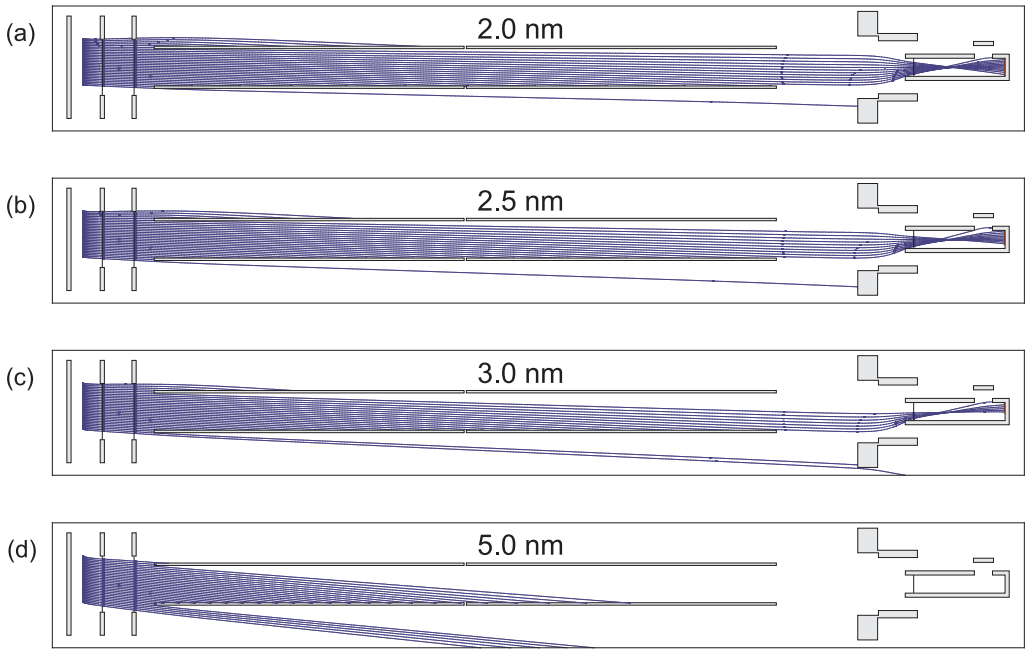

Figure 5.34: Trajectories of Pd clusters with different diameters. Pd clusters with initial velocities of 100 ms^{-1}, starting positions along the beam axis and diameters of (a) 2 nm, (b) 2.5 nm, (c) 3 nm and (d) 5 nm were flown through the TOFMS. The acceleration voltage was set to 3.5 kV and no deflection voltage was used.

were used [33]. The acceleration voltage was left at 3.5 kV. Figure 5.36 shows the ion trajectories for four different deflection voltage settings.

If the deflection voltage is set to 100 V or less, all the clusters hit the bottom deflection plate (Figure 5.36(a)). This is still the case at 105 V, although the clusters fly further into the flight tube (Figure 5.36(b)). If the deflection voltage is increased by only 1 V to 106 V, some of the clusters are bent past the detector and hit the side walls on the opposite side (Figure 5.36(c)). Further increasing the voltage to 125 V leads to a larger group of clusters being bent past the detector and ending up on the opposite deflection plate (Figure 5.36(d)). In these four simulations, not a single cluster was detected. It is therefore assumed to be impossible to detect clusters with diameters of considerably more than 5 nm in the current set-up, if the clusters have initial velocities of more than 100 ms^{-1}.

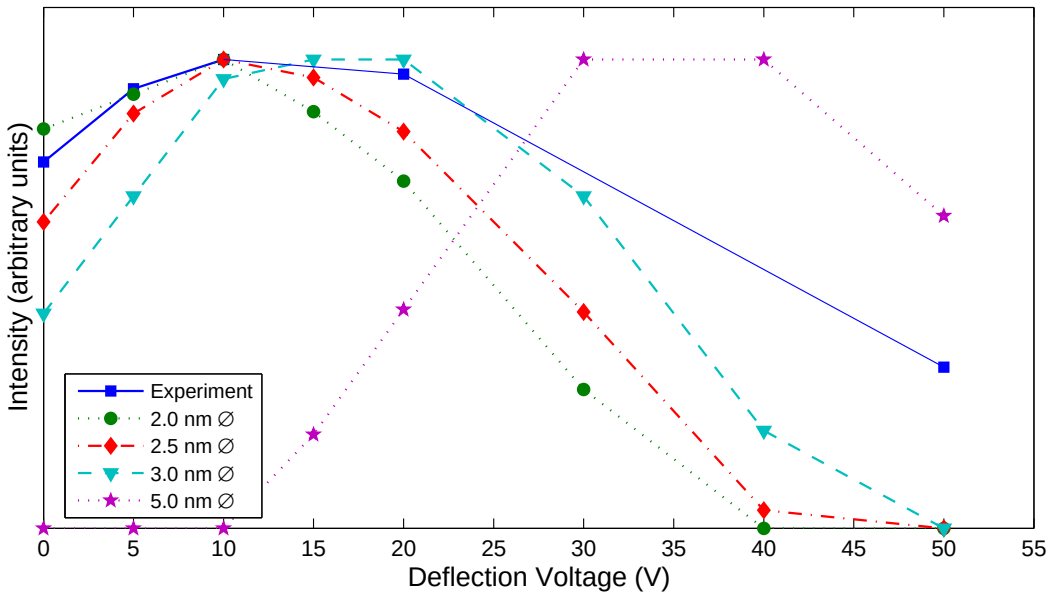

Figure 5.35: Dependence of signal intensity on deflection voltage and particle size. The experimental data from Figure 5.32 (■) is compared to simulated data for Pd clusters with initial velocities of 100 ms^{-1} and diameters of 2.0 nm (●), 2.5 nm (⧫), 3 nm (▼) and 5 nm (★). All the data is scaled to match the maximum intensity.

Note that the simulations and the experiments were run with the deflection plates on a constant potential. It is possible to ramp the deflection voltage linearly during the time the ions are in the drift tube [22]. If the ramp rate is chosen correctly, a wider range of particle masses can be deflected onto the detector compared to the set-up used in the present work. In a simpler approach, the deflection voltage can also be pulsed with a time delay relative to the acceleration pulse [22]. In this set-up, the faster (i.e. lighter) ions are already well down the drift tube when the deflection voltage is turned on and are therefore less deflected. The current set-up of the TOFMS does not allow the deflection voltage to be pulsed or ramped. However, this would not be too difficult to implement.

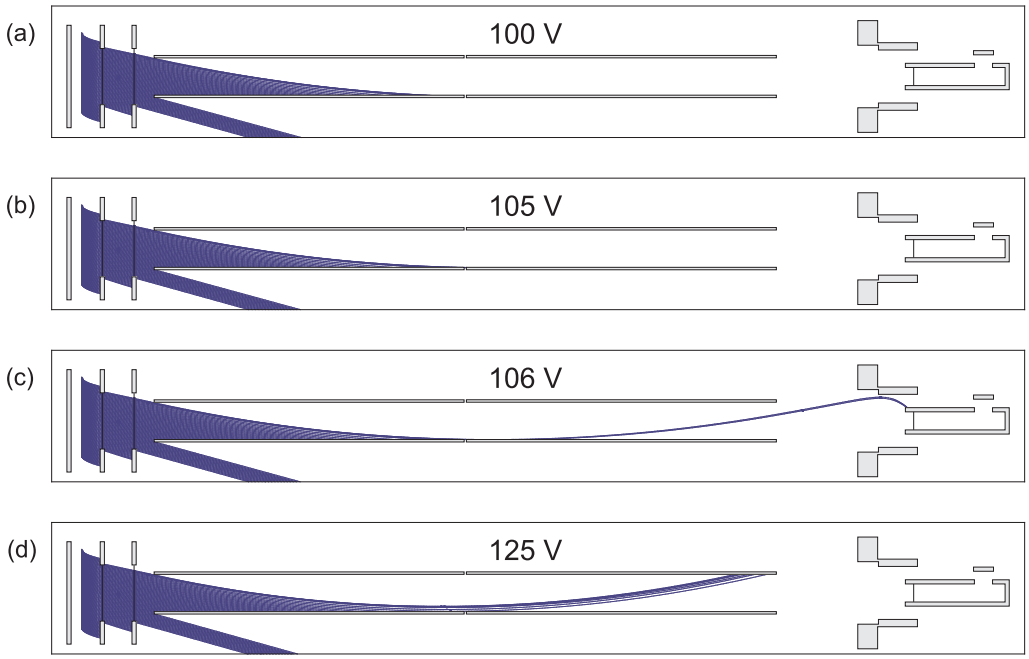

Figure 5.36: Trajectories of Pd clusters at different deflection voltage settings. Pd clusters with a diameter of 7 nm, initial velocities of 150 ms^{-1} and starting positions along the beam axis were used. The deflection voltage was increased from (a) 100 V to (b) 105 V to (c) 106 V and finally to (d) 125 V. The acceleration voltage was set to 3.5 kV.

Experimental Conditions for TOFMS Tests on Pd Clusters

In Table 5.5 the conditions and results for all the experiments presented in this section are displayed. Only the first acceleration voltage was used and it was set to values in the range of 1.5 to 5.0 kV. However, the TOF spectra at the lower end of this range have a low signal-to-noise ratio. The gas flow rates used were from 100 to 700 sccm for Ar and 100 to 400 sccm for He. For most experiments, only Ar was used. The sputtering power was varied between 5 and 30 W. Deflection voltages up to 50 V were tested which – for most experiments – was the limit where the signal vanished completely.

The average mass of the clusters was determined using two independent methods. The first method required the mean TOF at different acceleration voltages to be determined. Equation (5.27) was then fitted to the data

and the slope of the fit was compared to results from simulations. With this method a set of experiments leads to an average value for the cluster mass and only data with different acceleration voltages can be used. The second method involved solving (5.17) for the mass by using the experimental mean flight times. This second method leads to individual results for all runs. However, the results are less accurate, especially for spectra with a low signal-to-noise ratio.

The size results for the first group of experiments (Figure 5.28) are consistent, although the calculated mean cluster diameter differs from the diameter determined using the slope method. The results of the second group (Figure 5.30) indicate that using He as a cooling gas leads to considerably smaller clusters. The differences between the individual results are more pronounced and while the slope method leads to a smaller average diameter in the first case, in this run it leads to a larger diameter. For the third group (Figure 5.32), the mean cluster mass is expected to shift towards higher values for higher deflection voltages. This behaviour holds true for all but the last experiment. This deviation, however, is most likely due to the low signal intensity of this measurement. The average values for this run are not very meaningful as they are based on a series of increasing clusters sizes. The slope method could not be applied in this case, as it relies on a series of measurements with different acceleration voltages.

From Table 5.5, it is evident that the source conditions influence the cluster growth crucially. The TOFMS could therefore be used to characterise the source in detail. This would, however, go beyond the scope of the present study and is part of two further PhD theses to be submitted over the next few years.

Table 5.5: Experimental conditions for TOFMS tests on Pd clusters as shown in Figure 5.28, 5.30, and 5.32. The mean diameter values in the penultimate column are calculated from the mean mass values, while the values in the last column are determined using the slope method described earlier.

Fig.	Flow Rate (sccm) Ar	He	Power (W) P_S	Acc. Volt. (kV) U_1	Defl. Volt. (V) U_{defl}		Mean Mass (amu)	Mean Diameter (nm) calculated	slope method
5.28(a)	400	–	25	4.5	–		42 971	2.24	
5.28(b)	400	–	25	4.0	–		37 230	2.15	
5.28(c)	400	–	25	3.5	–		37 920	2.16	
5.28(d)	400	–	25	3.0	–		37 065	2.14	
						Average	39 130	2.17	1.92
5.30(a)	–	400	25	4.5	–		7603	1.26	
5.30(b)	–	400	25	4.0	–		5179	1.11	
5.30(c)	–	400	25	3.5	–		6404	1.19	
5.30(d)	–	400	25	3.0	–		8391	1.30	
						Average	6894	1.21	1.75
5.32(a)	100	–	10	3.5	0		67 339	2.61	
5.32(b)	100	–	10	3.5	5		69 679	2.63	
5.32(c)	100	–	10	3.5	10		73 295	2.68	
5.32(d)	100	–	10	3.5	20		77 640	2.73	
5.32(e)	100	–	10	3.5	50		65 449	2.58	
						Average	70 680	2.65	–

5.6 Conclusions and Suggested Improvements

In the present chapter, the fundamentals of TOF mass spectrometry as well as the design and testing of such a device are presented. TOF mass spectrometry is a powerful tool to study molecular beams due to its high duty cycle and wide mass range. Additionally, designs such as the reflectron mass spectrometer and the Wiley-McLaren TOFMS discussed above are able to reach high mass resolutions which were not possible in conventional TOF mass spectrometry.

The particular TOFMS design presented in this chapter is an orthogonal-acceleration Wiley-McLaren TOFMS which uses deflection plates along the drift tube to steer the heavy ions onto the detector. With a drift length of less than 0.5 m it is relatively short, however, since it was designed to characterise large clusters, a high resolution was not required. There are two detectors which can be used interchangeably, an MCP detector and a Daly detector. The main advantages of the Daly detector over the MCP detector are its robustness, its simple design and a high post-acceleration voltage capability which improves the detectability of heavy clusters. High post-acceleration potentials can also be used with an MCP detector. In this case, however, the set-up is more complex. Furthermore, the MCP detector is very fragile and requires at least high-vacuum conditions. An advantage of the MCP detector is the switchable polarity which allows the detection of positively as well as negatively charged ions. The Daly detector in its present set-up can only detect positively charged particles.

The design of the TOFMS has been tested by ion optics simulations using SIMION. These simulations help to understand the characteristics of a TOFMS, facilitate the detailed design of the spectrometer components and also allow the comparison between experiments and simulations. It has to be stressed, however, that the simulations are unable to accurately predict all the details of a TOFMS as the situation is complicated by fringing fields, non-ideal grids and other higher order phenomena.

While the TOFMS was successfully tested on Pd clusters in a new deposition system, it was unable to detect clusters in the electron diffraction apparatus. In the latter system, it was only possible to test the TOFMS

performance using gas molecules such as Ar and N_2. The two main reasons for this failure are thought to be a malfunctioning ioniser as well as the unexpectedly high cluster energies. In the next section the differences between the electron diffraction system and the new deposition system are discussed to explain why the TOFMS did not work as expected in the original set-up. Furthermore, a series of possible improvements are proposed which would enable the TOFMS to be used in the original electron diffraction system.

5.6.1 Suggested Improvements

The main difference between the electron diffraction system and the more recently built deposition system is the fact that the sputtering source in the latter produces clusters which are ionised already, whereas the inert-gas aggregation source of the original system produces only neutral clusters and depends on an additional ioniser. The ioniser is most likely the weakest point of the present set-up. A further difference between the two systems is the ability of the sputtering source to produce small clusters – at least for Pd. Assuming a cluster beam velocity of around $150\,\mathrm{ms}^{-1}$ – which is reasonable judging by the results from the experiments with the deflection plates – simulations indicate that it is impossible to detect Pd or Sb clusters with a diameter of 7 nm or more. Previous studies on Ag and Cu clusters showed cluster diameters of well below 10 nm using the IGA source [34–39], however, the latest study on Bi clusters found diameters in the order of 10 nm [40]. It would therefore be important to find a way of producing a wider range of cluster sizes (especially smaller clusters) before further testing could be undertaken in the electron diffraction apparatus. Smaller clusters would also be of greater interest because of possible structural changes and quantum size effects.

Below is a list of suggested improvements to the TOFMS to allow its use in the original set-up and to increase its resolution:

Ioniser: although the ioniser is working for Ar and N_2 gas and further tests on Bi and Sb indicate that it manages to ionise at least a part

of the cluster beam, it does not work as expected. The following list addresses some of the shortcomings:

- The high abundance of negatively charged particles at high electron energies is not understood. Electron impact ionisation usually leads to a very low number of negatively charged particles and only for very low electron energies.
- The fact that negatively charged particles can only be detected once the deflection voltage is set to a certain potential, might also be attributed to the ioniser. It is possible that malfunctioning of the ioniser leads to a charging-up of the deflection plates.
- Additionally, there are very high leakage currents which do not allow the desired electron energy to be achieved.
- The grid at the exit of the ioniser is too coarse and blocks out a considerable part of the beam.

High cluster energies: clusters with a high kinetic energy in the direction of the cluster beam are very difficult to direct towards the detector. However, several improvements can be suggested:

- The most obvious solution would be not to use orthogonal acceleration but to have the TOFMS on axis with the cluster beam. However, this is impossible in the present vacuum system as the area further downstream is blocked off by a turbo pump. Furthermore, having the mass spectrometer on axis would severely decrease its resolution due to high initial energies in the direction of the TOFMS.
- If the TOFMS is mounted perpendicular to the beam, shortening and widening the flight tube and enlarging the detector would improve the detectable mass range [41]. A shorter flight tube, however, would decrease the resolution but not as much as mounting the TOFMS on-axis. However, a shorter flight tube is not possible in the current system geometry.
- Instead of mounting the TOF orthogonally, it could also be inclined in the direction of the cluster beam so that the clusters

would follow their spontaneous drift trajectory. A drawback of this design is the fact that the ideal angle is mass-dependent (in the same way that the ideal deflection voltage is mass dependent). Due to the set-up of the vacuum system, this design would be difficult to implement.

- A similar but more compact solution is the tilting of the acceleration plates in such a way that the electric fields are pointing slightly against the original beam direction [42]. In this approach the deflection happens already in the acceleration regions and not only in the flight tube as it is the case with deflection plates. The tilting angle is mass-dependent and the maximum angle is limited depending on the geometry of the acceleration regions. Once this limit is reached, deflection plates could be used in addition to bend even heavier ions onto the detector.
- Increasing the acceleration voltages would also help to steer heavier clusters onto the detector. However, a practical limit is probably reached at approximately 10 kV as the switching of high voltages is complex and requires expensive equipment. The limit of the present equipment is 5 kV.
- Instead of using deflection plates to steer the clusters in the right direction, it is possible to use a quadrupole lens [43]. The downside of this method is its mass-dependence.

Resolution: there are several possible improvements to be made to increase the resolution of the TOFMS. It should be noted, however, that the resolution is considered not to be of great importance for the study of heavy clusters.

- The most efficient improvement is to eliminate some of the causes of low resolution, e.g. initial space and energy distribution. Initial space distribution can be diminished by inserting an ion-optical lens between ioniser and acceleration region.
- Fringing fields decrease the resolution and should therefore be minimised. A possible solution is the use of additional electrodes

between the acceleration regions set to the correct potential by voltage dividers [22, 23].

- Several studies have shown that field distortions around meshes reduce the resolution [3, 44]. This effect is worse if the incident angle of ions is not exactly 90° as it is the case in an oa-TOFMS. A possible solution is the use of arrays of parallel wires aligned in the direction of the cluster beam instead of meshes [3].
- Deflection plates are also considered to be a cause of a loss of resolution [45]. Deflection plates can either be replaced by one of the alternatives discussed above or can be used with a time delay after the ions enter the drift tube as the loss in resolution is caused by fringing fields at the entry to the drift region [22]. This time delay also increases the detectable mass range if it is timed properly as the lighter – and therefore faster – ions experience less deflection than the heavier ones.
- Extending the drift tube would also increase the resolution. The most practical way of achieving this, is the use of a reflectron [4]. In a reflectron, ions are reflected in a retarding field. Ions with higher energies penetrate this field further than ions with lower energies. In addition to almost doubling the length of the drift tube, this design also decreases the effect of initial energy distribution (see Section 5.2.2).
- Insulators tend to charge up leading to distortions of the electric fields. It is best to have no insulators in the vicinity of the ion beam or even enclose the acceleration fields completely [46].

Efficiency: improving the efficiency is important when a low intensity cluster beam is under study.

- Although the meshes used in this study have a transmission coefficient of 0.9, three meshes in series reduce the transmission to 73%. If rapid potential changes are eliminated, it is possible to have a design without any meshes [46].
- Improving the conversion efficiency of the Daly detector would

increase the efficiency. As discussed in Section 5.3.3 this could be achieved by coating the base of the cup with Al or Mg.

- The detection efficiency of both detectors decreases with decreasing cluster velocity which limits the detectability of heavy ions. Increasing the post-acceleration potential increases the detection efficiency [19].
- The duty cycle of the TOFMS could be increased if an oscilloscope was employed which was capable of processing a larger number of averages (the present model is only able to average 128 spectra) and storing several averaged spectra before transferring them to the computer.

To summarise, the following changes to the current TOFMS design are crucial to be able to detect clusters in the electron diffraction set-up. The most important change would be the replacement of the ioniser. Using higher acceleration voltages and a wider flight tube would help to steer the clusters onto the detector. If the width of the flight tube is extended, the detector might have to be enlarged as well. Shielding the TOFMS would also be important in reducing external influences such as stray electrons and fringing fields.

References

[1] I. Howe, D. H. Williams, and R. D. Bowen, *Mass Spectrometry*, McGraw-Hill, 2nd edition, 1981.

[2] K. Downard, *Mass Spectrometry*, Royal Society of Chemistry, 2004.

[3] M. Guilhaus, D. Selby, and V. Mlynski, Mass Spectrom. Rev. **19**, 65 (2000).

[4] B. A. Mamyrin, V. I. Karataev, D. V. Shmikk, and V. A. Zagulin, Sov. Phys. JETP **37**, 45 (1973).

[5] W. C. Wiley and I. H. McLaren, Rev. Sci. Instrum. **26**, 1150 (1955).

[6] M. Guilhaus, J. Mass Spectrom. **30**, 1519 (1995).

[7] W. C. Wiley and I. H. McLaren, Rev. Sci. Instrum. **26**, 1150 (1955).

[8] J. Coles and M. Guilhaus, Trends Anal. Chem. **12**, 203 (1993).

[9] R. J. Cotter, editor, *Time-of-flight mass-spectrometry*, volume 549 of *ACS Symposium Series*, Washington DC, 1994, American Chemical Society.

[10] G. Sanzone, Rev. Sci. Instrum. **41**, 741 (1970).

[11] A. Fielicke, *Reaktivitätsstudien an Metalloxidclustern in der Gasphase: Bismutoxid-Clusterkationen als aktive Zentren bei der Alkenoxidation*, PhD thesis, Humboldt-Universität zu Berlin, 2001.

[12] P. Milani and S. Iannotta, *Cluster Beam Synthesis of Nanostructured Materials*, Springer Series in Cluster Physics, Springer-Verlag, 1999.

[13] P. L. Bartlett and A. T. Stelbovics, Phys. Rev. A **66**, 012707 (2002).

[14] R. L. Johnston, *Atomic and Molecular Clusters*, Masters Series in Physics and Astronomy, Taylor & Francis, 2002.

[15] A. L. Reimann, *Thermionic Emission*, chapter 3, Chapman & Hall, 1934.

[16] J. L. Wiza, Nucl. Instrum. Meth. **162**, 587 (1979).

[17] R. Beuhler and L. Friedman, Chem. Rev. **86**, 521 (1986).

[18] R. A. Baragiola, E. V. Alonso, and A. O. Florio, Phys. Rev. B **19**, 121 (1979).

[19] U. Zimmermann, N. Malinowski, U. Näher, S. Frank, and T. P. Martin, Z. Phys. D: Atom. Mol. Cl. **31**, 85 (1994).

[20] N. R. Daly, Rev. Sci. Instrum. **31**, 264 (1960).

[21] D. Bahat, O. Cheshnovsky, U. Even, N. Lavie, and Y. Magen, J. Phys. Chem. **91**, 2460 (1987).

[22] W. A. de Heer and P. Milani, Rev. Sci. Instrum. **62**, 670 (1991).

[23] F. Chandezon, B. Huber, and C. Ristori, Rev. Sci. Instrum. **65**, 3344 (1994).

[24] D. A. Dahl, J. E. Delmore, and A. D. Appelhans, Rev. Sci. Instrum. **61**, 607 (1990).

[25] D. A. Dahl, Int. J. Mass Spectrom. **200**, 3 (2000).

[26] D. A. Dahl, SIMION 3D *Version 7.0 User's Manual*, Idaho National Engineering and Environmental Laboratory, Idaho Falls, 2000.

[27] P. Liu, P. J. Ziemann, D. B. Kittelson, and P. H. McMurry, Aerosol Sci. Technol. **22**, 293 (1995).

[28] P. Liu, P. J. Ziemann, D. B. Kittelson, and P. H. McMurry, Aerosol Sci. Technol. **22**, 314 (1995).

[29] R. Reichel, *Nanocluster Devices*, PhD thesis, University of Canterbury, 2006, to be published.

[30] H. Haberland, M. Karrais, M. Mall, and Y. Thurner, J. Vac. Sci. Technol. A **10**, 3266 (1992).

[31] H. Haberland *et al.*, J. Vac. Sci. Technol. A **12**, 2925 (1994).

[32] J. Söderlund, L. B. Kiss, G. A. Niklasson, and C. G. Granqvist, Phys. Rev. Lett. **80**, 2386 (1998).

[33] A. Ayesh *et al.*, to be submitted to Rev. Sci. Instrum.

[34] M. Flüeli, *Observation des Structures Anormales de Petites Particules d'Or et d'Argent par Microscopie Eléctronique à Haute-Résolution et Diffraction d'Eléctrons par un Jet d'Agrégats d'Argent*, PhD thesis, Ecole Polytechnique Fédérale de Lausanne, 1989.

[35] B. D. Hall, *An Installation for the Study of Unsupported Ultrafine Particles by Electron Diffraction with Application to Silver: Observation of Multiply Twinned Particle Structures*, PhD thesis, Ecole Polytechnique Fédérale de Lausanne, 1991.

[36] B. D. Hall, M. Flüeli, R. Monot, and J.-P. Borel, Phys. Rev. B **43**, 3906 (1991).

[37] D. Reinhard, *Croissance et Stabilité d'Agrégats d'Argent et de Cuivre, Etudiés en Jets Moléculaires par Diffraction d'Electrons à Haute Energie*, PhD thesis, Ecole Polytechnique Fédérale de Lausanne, 1996.

[38] D. Reinhard, B. Hall, D. Ugarte, and R. Monot, Phys. Rev. B **55**, 7868 (1997).

[39] D. Reinhard, B. D. Hall, P. Berthoud, S. Valkealahti, and R. Monot, Phys. Rev. Lett. **79**, 1459 (1997).

[40] A. Wurl, *Electron Diffraction Studies of Unsupported Bismuth Clusters*, PhD thesis, University of Canterbury, 2003.

[41] T. Hihara and K. Sumiyama, J. Vac. Sci. Technol. B **17**, 1923 (1999).

[42] C. W. S. Conover, Y. J. Twu, Y. A. Yang, and L. A. Bloomfield, Rev. Sci. Instrum. **60**, 1065 (1989).

[43] T. Bergmann, H. Goehlich, T. P. Martin, and H. Schaber, Rev. Sci. Instrum. **61**, 2585 (1990).

[44] T. Bergmann, T. P. Martin, and H. Schaber, Rev. Sci. Instrum. **60**, 347 (1989).

[45] M. Guilhaus, J. Am. Soc. Mass. Spectrom. **5**, 588 (1994).

[46] U. Even and B. Dick, Rev. Sci. Instrum. **71**, 4415 (2000).

Chapter 6

Conclusions and Outlook

This thesis consists of two main parts: In the first part, the structure of antimony (Sb) clusters was studied using electron diffraction. In the second part, a time-of-flight mass spectrometer (TOFMS) was designed and tested to determine the size distribution of the clusters.

Electron diffraction on unsupported particles is an ideal method to study the structure of clusters, since it avoids several problems related to conventional methods (microscopy and diffraction on supported samples). The main advantages are the ability to study the clusters *in situ* and in real time without removing them from the vacuum system or depositing them on a substrate, the short exposure to the electron beam, as well as the ability to study an almost unlimited range of materials.

During the diffraction studies on Sb clusters transitions between three different structures were observed: an amorphous structure, a crystalline structure and a structure corresponding to Sb_4. The transitions between these phases depended on the source temperature, the source inlet gas flow rate and the cooling gas composition (Ar and He were used as cooling gas). The amorphous structure was observed for low source temperatures and low Ar gas flow rates. Increasing temperature or flow rate led to the appearance of crystalline structures. When using He as the source cooling gas, a similar evolution was observed: for low flow rates and pure He the

diffraction patterns showed the characteristics of Sb_4. Increasing the flow rate or adding Ar to the cooling gas led to the same crystalline structure mentioned previously. In the range of source temperatures tested, there was no transition observed when only He was used for cooling.

To analyse the diffraction patterns, theoretical patterns from model structures were calculated using the Debye equation. The model structures were based on the rhombohedral structure of bulk Sb with different crystal habits as well as Sb_4 and liquid Sb. The morphologies and size distributions of deposited clusters were studied under an FE-SEM. For crystalline particles, the size information was then compared to the values obtained by analysing the diffraction patterns.

All crystalline diffraction patterns were similar in appearance and the crystalline structure was in good agreement with the rhombohedral structure of bulk Sb. The crystalline particles show a huge variety of different morphologies and sizes. According to the FE-SEM results, the mean cluster diameters were between 15 and 130 nm which is considerably larger than the Bi clusters produced on the same system during a previous study. The mean sizes for crystalline particles followed two clear trends: an increase in source temperature led to larger clusters, while an increase in gas flow rate reduced the average size. Applying the Scherrer equation to the crystalline patterns led to radically different mean sizes between 3.0 and 5.7 nm. This obvious discrepancy is most likely due to the presence of lattice defects in the clusters which would lead to individual domains. It is worth mentioning that most size trends described above were not observed for the Scherrer results.

The amorphous diffraction patterns did not match the calculated patterns for liquid clusters. They did, however, agree with diffraction patterns for amorphous Sb thin films, although the bond length and bond angle showed deviations. The FE-SEM study revealed that the amorphous clusters all had a spherical shape and a narrow size distribution. The mean values were all between 27 and 45 nm.

The Sb_4 diffraction patterns were found to be in good agreement with calculated patterns based on a theoretical model. Instead of a homogeneous film as expected for Sb_4 deposition, the FE-SEM images showed individual particles with average sizes between 18 and 35 nm. If the cluster

coverage on the samples was high enough, these particles tended to coalesce. Judging by these morphologies, it has to be assumed that there are particles consisting of randomly oriented Sb_4 units in the cluster beam. The diffraction pattern from such particles would be indistinguishable from the pattern for individual Sb_4 units. To our knowledge, such a structure has not been observed before.

For further electron diffraction studies on Sb or other elements, the following issues should be addressed: First of all, despite all efforts, it was not possible to produce clusters with average diameters below 10 nm. In previous studies on the same system, mean cluster sizes well below 10 nm were achieved. It is not known whether this is an issue related to Sb or whether the source geometry could be adjusted to influence the particle size. Improving the source cooling by using liquid N_2 instead of water might help reducing the cluster size as well. In general the lack of control over cluster parameters such as size and temperature is an important issue. If, however, large clusters continue to be observed in future studies, it could be worth investing in developing a framework for calculating diffraction patterns according to the dynamic diffraction theory. This would also allow calculated patterns to be fitted to the data of larger clusters. Furthermore, it might shed a new light on the issue of differing size information from the Scherrer equation and the microscopy data. Finally, the availability of a theoretical potential for Sb would enable the development of a model using molecular dynamics simulations. All these steps combined would lead to a dramatically improved understanding of the structure of Sb particles in particular and of clusters in general.

The second part of the thesis was focussed on the design and development of a TOFMS. A TOFMS is an invaluable tool for characterising the cluster beam and would help to solve the size discrepancy issue mentioned above. A Wiley-McLaren TOFMS was built in collaboration with Dr Bernhard Kaiser from the Humboldt University in Berlin. The design featured an electron impact ioniser, a drift region of 0.5 m length, deflection plates to steer the beam and two detectors which could be used interchangeably: an MCP and a Daly detector. The direction of the TOFMS was chosen to

be perpendicular to the cluster beam axis to improve resolution but also because of constraints due to the geometry of the vacuum system.

The TOFMS was unable to detect clusters in the original set-up. It was only possible to record spectra for gas molecules such as Ar and N_2. The TOFMS was, however, successfully used to detect clusters in a new vacuum system which uses a magnetron sputtering source. The main difference between these two systems is the fact that the sputtering source produces clusters which are mostly ionised already, whereas the inert-gas aggregation source of the original system produces only neutral clusters and depends on an additional ioniser. The ioniser is most likely the weakest point of the whole design, as various unexpected effects were observed. A further difference between the two systems is the ability of the sputtering source to produce small clusters. Ion optics simulations undertaken for our design indicate that it is very difficult to steer Sb clusters with diameters larger than 10 nm onto the detector in the current set-up. Since almost all the clusters observed in the diffraction study were larger than 10 nm, it is not surprising that it was impossible to detect a cluster signal. The following improvements are suggested to allow the TOFMS to be used in its original set-up: The first step would be to replace the ioniser with a model which has been fully tested and is known to have a high ionisation efficiency for clusters, in order to solve the issue of the observed excess of negatively charged particles. In a next step, measures would be taken to ensure that the clusters reach the detector. This can be achieved by increasing the acceleration potential, enlarging the space between the deflection plates, increasing the size of the detector or possibly tilting the acceleration plates.

List of Figures

List of Tables

Acronyms and Abbreviations

AC	Alternating current
Ag	Silver
Al	Aluminium
amu	Atomic mass unit
Ar	Argon
As	Arsenic
Au	Gold
Bi	Bismuth
Cu	Copper
DC	Direct Current
fcc	Face-centred cubic
FE-SEM	Field emission scanning electron microscope
FWHM	Full width at half maximum
Ge	Germanium
GPIB	General purpose interface bus
hcp	Hexagonal close-packed
H_2O	Water
He	Helium
HRTEM	High resolution transmission electron microscope
IGA	Inert-gas aggregation source
LDA	Linear diode array
MCP	Microchannel plate
N	Nitrogen
P	Phosphorus
Pb	Lead
Pd	Palladium
PMT	Photomultiplier Tube
RDF	Radial distribution function

rms	Root mean square
Sb	Antimony
sccm	Standard cubic centimetres per minute
SEM	Scanning electron microscope
SiO_2	Silicon dioxide
SiN	Silicon nitride
TEM	Transmission electron microscope
TlCl	Thallium chloride
TOF	Time-of-flight
TOFMS	Time-of-flight mass spectrometer
Zn	Zinc

Acknowledgements

First and foremost I would like to thank my supervisor, Prof Simon Brown, for his support and guidance throughout the whole project.

I would also like to thank Dr Bernhard Kaiser for travelling halfway around the world with a box full of scuba-diving gear (aka TOFMS components) and for helping me with the design and development of the mass spectrometer. Furthermore, the support of our two (former and present) postdocs, Dr Alan Dunbar and Dr Jim Partridge, was crucial during many stages of my thesis.

This thesis would not have been possible without the help from Dr Andreas Wurl. Not only did he introduce me to the mysteries of our ancient equipment and his precious new detector at the beginning of my project, but he was also still available to answer questions long after he had left the University and New Zealand.

The expertise and experience of our workshops was also invaluable for the project in general but particularly for the development of the TOFMS. Special thanks go to Ross Ritchie, Graeme McDonald, Owen Caughley, Wayne Smith, and Graeme Kershaw.

I would also like to thank Dr Richard Tilley from Victoria University, Wellington, for making the HRTEM available to me and teaching me how to use it. Thanks to Helen Devereux and Gary Turner from the Department of Electrical and Computer Engineering for helping me with the FE-SEM.

Who could get through a PhD thesis without getting distracted by office mates at times? Thanks to Dr Michael Hyslop, Dr Andreas Wurl, Monica Schulze, Shelley Scott, René Reichel, Ahmad Ayesh, David McCarthy, David MacKenzie and Toby Matthewson for all the fun and discussions about life, the universe and everything.

Financial support from the University of Canterbury, the MacDiarmid Institute as well from the Freiwillige Akademische Gesellschaft, Basel and the Theodor Engelmann Foundation is also greatly appreciated.

Last but not least, I would like to thank my parents for supporting me for the last 30 years and of course Esther for putting up with me, for encouraging me when the going got tough and for all the proof-reading.